NOTICE

AVIS

The quality of this microform is heavily dependent upon the quality of the original thesis submitted for microfilming. Every effort has been made to ensure the highest quality of reproduction possible.

If pages are missing, contact the university which granted the degree.

Some pages may have indistinct print especially if the original pages were typed with a poor typewriter ribbon or if the university sent us an inferior photocopy.

Reproduction in full or in part of this microform is governed by the Canadian Copyright Act, R.S.C. 1970, c. C-30, and subsequent amendments.

La qualité de cette microforme dépend grandement de la qualité de la thèse soumise au microfilmage. Nous avons tout fait pour assurer une qualité supérieure de reproduction.

S'il manque des pages, veuillez communiquer avec l'université qui a conféré le grade.

La qualité d'impression de certaines pages peut laisser à désirer, surtout si les pages originales ont été dactylographiées à l'aide d'un ruban usé ou si l'université nous a fait parvenir une photocopie de qualité inférieure.

La reproduction, même partielle, de cette microforme est soumise à la Loi canadienne sur le droit d'auteur, SRC 1970, c. C-30, et ses amendements subséquents.

Canada

UNIVERSITY OF ALBERTA

SPECTROCHEMICAL STUDIES OF THE ICP AND THE GDD USING A FOURIER TRANSFORM SPECTROMETER

by

TIEBANG WANG

A Thesis

submitted to the Faculty of Graduate Studies and Research

in partial fulfillment of the requirements for the Degree

of Doctor of Philosophy

Department of Chemistry

Edmonton, Alberta

Spring, 1992

Canadä

UNIVERSITY OF ALBERTA

RELEASE FORM
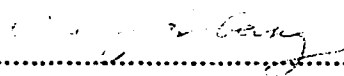
NAME OF AUTHOR: Tiebang Wang

TITLE OF THESIS: Spectrochemical Studies of the ICP and the GDD using a Fourier transform spectrometer.

DEGREE: Ph.D.

YEAR THIS DEGREE GRANTED: 1992

....
(signed)

#1,
10630-83 Ave.,
Edmonton, Alberta
T6E 2E2
(403) 433-0711

Date: ....

UNIVERSITY OF ALBERTA

FACULTY OF GRADUATE STUDIES AND RESEARCH

The undersigned certify that they have read, and recommend to the Faculty of Graduate Studies and Research for acceptance, a thesis entitled SPECTROCHEMICAL STUDIES OF THE ICP AND THE GDD USING A FOURIER TRANSFORM SPECTROMETER submitted by TIEBANG WANG in partial fulfillment of the requirements for the degree of Doctor of Philosophy.

Dr. G. Horlick (supervisor)

Dr. J. A. Plambeck

Dr. L. Li

Dr. A. Hunter

Dr. E. H. Pinnington

Dr. R. R. Williams (external examiner)

Date: ....

This thesis is dedicated to my parents

and my wife

Abstract

The ICP is capable of generating large quantities of spectrochemical information about the elemental composition of a sample. The Fourier transform spectrometer (FTS), with its excellent simultaneous multielement measurement capabilities, wide spectral range coverage, accurate wavelength axis and very high resolution, should allow more complete utilization of the information provided by the ICP.

As a tool for the measurement of emission from the ICP and the glow discharge device (GDD), some of the most important capabilities of the FTS system have been explored in this thesis.

Two of the most important fundamental properties - excitation temperature, ionization temperature of the pure argon ICP and mixed-gas (argon-air, argon-helium, argon-nitrogen and argon-oxygen) ICP's as a function of the observation height and the composition of the mixed-gases have been measured. Electron number density in a pure argon ICP as a function of the observation height and forward power has been evaluated.

The spectral characters of the ICP and the GDD in the UV and visible spectral regions for selected samples have been examined with the FTS as the measurement system. The excitation temperatures of the two sources have also been measured and compared.

To counteract the dynamic range and base line noise limitations of the FTS system, a system based on the front-end wavelength pre-selection of the LECO Plasmarray™ spectrometer, and a simple pre-dispersion system with fiber optic coupling to the FTS have been characterized. Wavelength pre-selection is accomplished using pre-dispersion with a 0.5 M concave grating

polychromator. The results have been very successful.

The powerful information gathering capability of the FTS system has also been demonstrated by measuring the argon emission from the ICP and the GDD in the visible and near-IR spectral regions (300-1300 nm) and the measured wavelengths of the argon emission have been compiled.

Acknowledgements

TABLE OF CONTENTS

LIST OF TABLES

LIST OF FIGURES

Chapter 1

Introduction

Analytical atomic spectroscopy can be described as a continual search for the so called "ideal" source and the "ideal" spectrometer. The ideal spectrochemical measurement system might be described as possessing the following characteristics: wide total spectral range; simultaneous and comprehensive wavelength coverage over any selected band pass; high accuracy of wavelength measurements; high spectral resolution up to full resolution of the physical line widths in the source; good sensitivity; high accuracy and wide linear dynamic range for spectral intensity measurements; applicable to both steady and transient signals; able to provide a permanent record; intelligent decision making capability; and ease of operation at reasonable cost.

1-1. Analytical atomic spectroscopy

The origins of analytical atomic spectroscopy can be traced back to the time when Newton studied basic optics. In 1672, he separated the color components of white light into its spectrum using a prism. Further significant developments in the field of atomic spectroscopy did not occur until 1800 when Herschel recognized infrared radiation beyond the limits of the visible spectrum. Fraunhofer invented the first diffraction grating in 1821. Herschel and Talbot observed the spectra of salts in flames in 1821, and Wheatstone began to observe spectra of metals in electrical sparks in 1835. Kirchoff and Bunsen cataloged the flame spectra of cesium and rubidium in

1

1861. Spectral studies were extended into the ultraviolet in 1862 by Stokes. In 1868, Angstrom published an extensive table of lines in the solar spectrum. In 1883, quantitative analysis by atomic emission spectroscopy was demonstrated by Hartley, and in 1885 the Balmer series in the hydrogen spectrum was recorded. By the late nineteenth century, Rowland had developed concave gratings. In 1880 Michelson invented the interferometer and established the basic concepts of Fourier transform spectrometry.

At this time, atomic spectroscopy was an empirical science, lacking theoretical foundation. The theoretical explanations did not appear until the twentieth century. In 1913, the Bohr model of the atom provided a rationale for the converging line series in the hydrogen spectrum, but could not be successfully applied to more complex atomic systems than hydrogen.

The development of the photomultiplier tube (PMT) for photoelectric detection in spectroscopic instrumentations resulted from the technological impetus of World War II, and in 1950 monochromators of the Czerny-Turner design using plane gratings and PMT detectors began to be utilized.

Emission, absorption, and fluorescence are the three major branches of atomic spectroscopy. Atomic emission spectroscopy (AES) was the first to develop as an useful analytical tool. The emission spectra of alkali elements were easily observed visually in flames. Later developments in photography led to the employment of photographic plates as detectors for emission spectra generated in flames, arcs and sparks. This technique was useful for both qualitative and quantitative analysis.

Atomic emission, generated by flames, arcs, or sparks and detected photographically or photoelectrically, continued to play the major role for

analytical atomic spectroscopy through the entire first half of the twentieth century until the introduction of analytical atomic absorption spectroscopy (AAS) in 1955 by Alkamade [1] and Walsh [2, 3]. The increased sensitivity, selectivity, and spectral simplification of the technique caused a revolution in analytical spectroscopy. In the period from 1965 to 1980, atomic absorption was the most prominent technique for elemental analysis. Development of flameless atomizers such as graphite furnaces increased the attainable sensitivity and further promoted the success of the technique.

Although atomic fluorescence spectroscopy (AFS) was studied as early as 1902, it was the last of the three major branches of atomic spectroscopy to emerge on the analytical chemistry stage. In 1962, Winefordner and Vickers [4] discussed the principles of applying AFS to analytical spectroscopy. Although AFS is potentially very promising, acceptance in the analytical laboratory has been sluggish due to the lack of significant advantages over the already popular AAS techniques and due to the requirement of high intensity line sources. The advent of lasers in the 1960's has greatly enhanced the capabilities of the AFS technique but the high expense has restricted development to research more than practical applications.

1-2. Inductively coupled plasma

Despite the tremendous success and popularity that AAS techniques have been enjoying, a growing renaissance in atomic emission has evolved, and AES is again regaining it former position of prominence in the analytical laboratory. This has been caused by the increased demand for multielement analysis with a wide range of concentration levels of different elements in the sample. This demand could not be met by AAS but has been by the

development of the inductively coupled plasma (ICP) as an excitation source. Initial studies of the analytical applicability of the ICP were conducted independently by Greenfield [5] in 1964 and by Fassel [6] in 1965. This source eliminates many of the limitations of previous excitation sources, such as flames, arcs, and sparks, for AES and it possesses many unique and favorable additional characteristics.

Traditional excitation sources have included combustion flames, arcs, and sparks. Flames are limited by relatively low temperatures; as a result, it is difficult to analyze refractory elements or elements with relatively high excitation energies. In addition, combustion products and flame gases give rise to both chemical and spectral interferences. Arcs and sparks are capable of higher excitation temperatures, but the nature of the electrical discharge is strongly affected by the matrix of the samples. Minor variations in sample composition cause variations in the excitation conditions, thus making a close matching of samples and standards or the use of an internal standard indispensable.

The ICP excitation source is an electrodeless argon plasma operated at atmospheric pressure and sustained by inductive coupling to a radio frequency (RF) electromagnetic field. Argon gas flows tangentially into the plasma torch consisting of three concentric quartz tubes that are surrounded by three or four turns of an induction coil connected to a RF generator. The standard RF frequency is 27.12 megahertz (MHz), and the power output is generally from 1.0 to 3.0 KW. The high frequency current flowing in the induction coils generates oscillating magnetic fields whose lines of force are axially oriented inside the quartz tubes and follow closed elliptical paths outside the quartz tubes. The induced magnetic fields in turn induce electrons

in the gas to flow in closed annular paths inside the tube space. This electron flow is called the eddy current, and the electrons are accelerated by the time-varying magnetic field, meeting resistance to flow such that resistive or Ohmic heating and additional ionization result. Since argon is initially neutral and non-conducting, the plasma must be initiated by "seed electrons" most commonly achieved by a brief Tesla discharge. The plasma forms instantaneously and is subsequently self-sustaining.

The samples, most commonly in solution form, are aspirated by a nebulizer system, and a fine liquid aerosol is transported up through the central tube by a flow of argon carrier gas (nebulizer gas). The temperature in this analyte channel is high enough for the samples to become volatilized, desolvated, atomized, ionized, excited, and subsequently to emit radiation.

There are many advantages of the ICP as an excitation source for analytical atomic spectroscopy: high quality multielement analysis may be realized in either a sequential or simultaneous mode with very little compromise in experimental or operational parameters because the optimal conditions for most elements are practically identical. The higher temperature of the ICP compared to combustion flames allows the determinations of refractory elements such as phosphorus, tungsten, zirconium, and uranium. Working curves established with the ICP demonstrate high linear dynamic range, generally being linear over four to five orders of magnitude on the concentration scale. Self-absorption is generally negligible because the sample stream is physically slender and the analyte behaves as an optically thin emitting source. This high linear dynamic range allows simultaneous determinations of major, minor, and trace constituents in the same sample without dilution or separate

determinations. Excellent detection limits are achieved [7, 8] with the ICP. Detection limits obtained with this technique are generally better than for flame atomic absorption, arc, or spark, but not always competitive with graphite furnace atomic absorption. Finally, excellent accuracy and precision have been demonstrated using the ICP.

Although initially considered to be virtually absent, interelement effects (matrix effects) have been shown to be greatly reduced but not totally eliminated in the ICP in later studies.

1-3. Glow discharge device (GDD)

Different types of glow discharge devices have been used for a long time as radiation sources in atomic spectroscopy. Not only because of their abilities to excite atomic spectra but also because of the volatilization processes involved, they have been found to be interesting alternatives to arc and spark sources operated at atmospheric pressure.

In 1968 the first practical glow discharge device for spectrochemical analysis with a flat cathode was described by Grimm [9]. In his device the sample, which must be electrically conductive, is taken as the cathode and the discharge is restricted to the sample surface.

In general, the glow discharge is a simple two-electrode device, filled with a rare gas (Ar, Ne) to about 0.1 to 10.0 torr. A few hundred to over one thousand volts applied across the electrodes causes breakdown of the gas and formation of the ions, electrons, and other species that make the glow discharge useful in analytical chemistry. Fig. 1 is a simplified sketch that
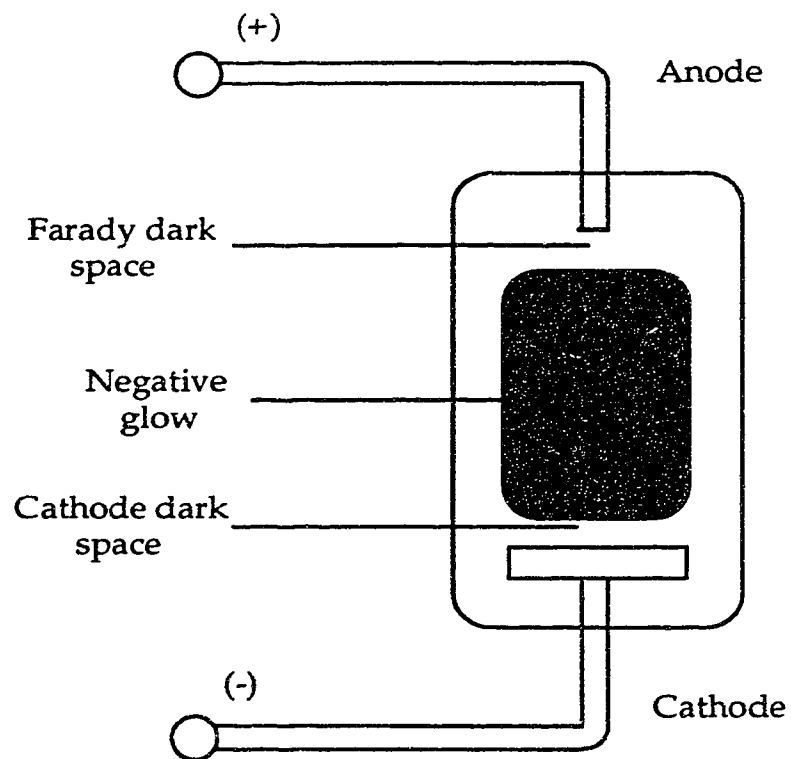
Fig. 1. Basic layout of a planar diode glow discharge showing the cathode dark space and the negative glow.

shows the basic components and discharge regions. The sample to be analyzed serves as the cathode; the anode material is not particularly critical.

The sample is atomized into the discharge by a process called sputtering. Positive ions and fast neutrals strike the cathode sample, penetrating a few atomic distances before losing their momentum. Some atoms at the surface receive sufficient energy through these collisions to overcome their binding and are normally ejected as neutral atoms, although a small percent may come off as ions. Glow discharge analytical methods are based on the utilization of this large sputtered neutral population.

Only two zones in the GDD concern us: the cathode dark space and the negative glow. As shown in Fig. 1, the cathode dark space is a thin layer that shows relatively little light emission from electron atom collisions because of the high energy of the accelerated electrons. By contrast, the negative glow is a region of bright emission arising from excitation of atoms by lower energy electrons that have been slowed by inelastic collisions. This bright emission is generally measured by end-on observation.

Apart from conducting metallic samples, non-conducting powders can also be analysed with the glow discharge device. They can be mixed with a metal powder and the mixture can be briquetted into sample pellets. By using appropriate techniques, vacuum-tight and mechanically stable pellets can be obtained even with small amounts of sample. Analysis can be performed by calibrating with synthetic samples.

Coupled to various emission spectrometers, glow discharge device-atomic emission spectrometry (GDD-AES) can be performed. Discharges

under reduced pressure, from the point of view of sample volatilization and excitation, have unique features as radiation sources for atomic emission spectrometry. When the sample is cooled, material volatilization is solely based on cathodic sputtering. It is also possible to adjust the cathode temperature carefully by regulation of the discharge current and/or external heating. The latter provides ideal conditions for the selective volatilization of elements or species from a complex matrix. The discharge gas is nearly always a noble gas which, moreover, because of its high ionization energy, also permits an efficient excitation of elements with high excitation energy. In most cases argon is used as the filler gas, as the heavier noble gases are expensive and their ionization energies are lower.

Despite the fact that the problem of quantification has not been satisfactorily resolved, GDD-AES is already used for solving many practical problems, particularly in metallurgy.

As the material volatilized in a glow discharge device is, to a large extent, present as a vapour cloud of free atoms, glow discharges are suitable atom reservoirs for atomic absorption and atomic fluorescence work.

Apart from their use as sources for optical atomic spectrometry, glow discharge devices also have been recognized as being powerful ion sources for inorganic mass spectrometry.

1-4. Fourier transform spectroscopy

The search for the ideal spectrometer has historically included the development and application of spectrographs, monochromators, polychromators and photodiode array spectrometers. Each of these types of

spectrometer has unique advantages to offer analysts, but each also has its own characteristic set of limitations. Fourier transform spectroscopy is a viable alternative to the optical atomic emission measurement systems. Research in this area has been going on for over the last two decades [10-19]. Since then several other research groups in the United States and Europe have developed an interest in Fourier transform spectroscopy (FTS) in spectral regions other than the mid- and far-infrared and commercial instrumentation has been developed. Presently spectrochemical studies with the FTS measurement system coupled to the inductively coupled plasma and glow discharge device is underway in our laboratory. In the following sections, the basic principles of FTS will be discussed and the "pros and cons" of the FTS technique including what it can do for atomic emission spectroscopy will be presented.

1-4-1. FTS - basic principles

Analytical atomic spectroscopists usually work with wavelength-dispersive instrumentation. A wavelength-dispersive spectrometer spreads radiation of different wavelengths spatially, and the spectrum is recorded either by sequential scanning or by recording more than one pre-determined wavelengths of interest using a number of different detectors, one for each wavelength of interest. In contrast, in a Fourier transform spectrometer system, there is no spatial separation; radiation of all wavelengths is recorded simultaneously with a single detector.

In order to discuss the Fourier transform technique, a method called "multiplexing" should be mentioned. Multiplexing is a method of
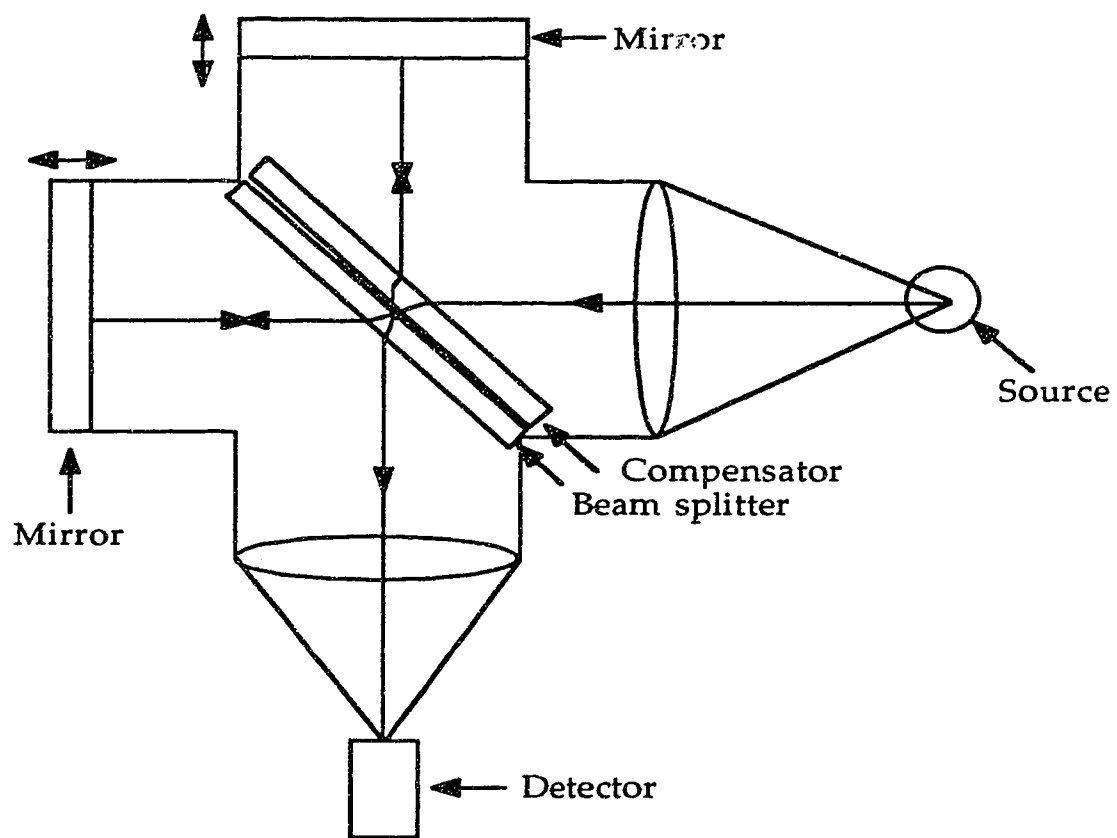
Fig. 2. Simplified schematic diagram of a Michelson interferometer.

information processing. Independent pieces of information are encoded so that they can be simultaneously transmitted or received over common information pathways. The multiplexed information must later be decoded so that each independent piece of information is uniquely and correctly recovered. In analytical spectroscopy, the independent pieces of information are the intensities of light at various frequencies emitted by the source. The interferometer encodes this information in the form of an interferogram. The computer decodes the information by performing the Fourier transform.

A Fourier transform spectrometer is based on the design and operational principles of a Michelson interferometer, as shown in Fig. 2. Before going into the interferometer, light from the source has to be collimated by the collimating optics. A beam splitter divides the collimated beam into two parts, which travel along the two arms of the interferometer and are reflected by mirrors back to the beamsplitter and recombined. The resulting beam is then focused on to a single detector. If one or both of the mirrors move, the optical paths in the two arms are not equal. Constructive and destructive interference then occur in the recombined beam, according to the optical path difference and the frequencies of light from the source. If the mirrors move as a function of time, then each frequency of light present in the source is modulated, and the time-varying signal at the detector is a record of the modulation of all the frequencies present in the source. This time-varying signal, which is the time domain half of a Fourier transform pair, is called the interferogram. The mathematical process of the Fourier transform yields the frequency domain half of the pair, known more familiarly as the spectrum.

1-4-2. FTS - The "pros"

Before the FT technique was applied to the ultraviolet and visible spectral regions, FTS methods were firmly established in infrared (IR) region. Most of the characteristics of FTS-IR are directly transferable to FTS in the ultraviolet and visible spectral regions.

FTS facilitates the direct measurement of a broad spectral range. This arises from the fact that as a multiplex instrument, the Fourier transform spectrometer simultaneously records all the spectral information within the selected band pass. This is unmatched by any of the direct reader or monochromator based measurement systems. The spectral region measured is limited only by the detector response and the efficiency limits of the optical components of the interferometer. Therefore, the transformed spectrum includes all the emission lines from atomic and molecular species in the source, as well as the background and base-line characteristics of the spectrum. The total spectral information within that selected band pass is comprehensively recorded by the spectrometer and permanently available stored in the interferogram or the transformed spectrum. Unlike wavelength-dispersive systems, such as the polychromator or monochromator which require that only a few analytical wavelengths be pre-selected, Fourier transform systems allow the selection of the wavelengths for analysis to be made at any time before, during, or after the acquisition of the spectral information. Thus, the selection can be based on an examination of the content of the actual spectrum, and the maximum flexibility of choice is allowed.

Qualitative analysis is therefore easily realized, as the comprehensive emission spectrum of all species in the source will be recorded within the selected band pass. Thus spectral interferences are usually easily identified, as the presence of key lines of elements can alert the analyst or even the computer to possible interferences at other wavelengths. Computerized cross-reference wavelength tables can be utilized for an initial qualitative analysis as well as for the warning of a possible potential spectral interference. Alternate line selection in the event of spectral interferences is usually available, as all the emission lines of all the analytes were recorded in the selected band pass. The computer system can also be used to cross-reference potential spectral interferences based on the initial qualitative survey and to suggest the the best interference-free lines for the analysis, based on the stored reference spectra and the actual sample composition.

Because all the spectral information within the band pass is available, it is also possible to develop new data processing methods using more than one of the emission lines of an analyte for quantitative analysis. A method of "multiple line analysis" can be used to improve the sensitivity of, for instance, ICP-FTS or GDD-FTS. The idea is to construct calibration curves and calculate detection limits using the "accumulated intensity" of all the major lines of a species instead of just a single line as normally done. Dr. Greg King, a graduate from this research group, constructed a Fe calibration curve with 15 Fe emission lines [20]. The calibration curve showed excellent linearity, and a gain in detection limit by a factor of 1.42 was realized. Using only the 3 most intense lines among the 15 lines, further improvement was achieved. It should be pointed out that this method only works for elements with several strong emission lines.

Another feature of the FTS technique is high resolution, which is relatively easy to achieve in a very compact instrumental system compared to wavelength-dispersive spectrometers [21, 22]. The resolution of the FTS system is determined ultimately by the optical path difference in the two arms of the interferometer which is related to the distance the moving mirror has travelled.

The Fourier transform spectrometer developed and built in this research group has a 2 cm maximum optical retardation (0.5 cm^{-1} nominal resolution) [23]. Sections of spectra measured with our ICP-FTS measurement system are given in Fig. 3, Fig. 4, and Fig. 5 illustrating the practical resolution capability of the system.

Fig. 3 shows the baseline resolved B I 249.678 nm and B I 249.773 nm lines. The spectrum was derived from an interferogram measured at an optical retardation equivalent to 16,384 periods of the He-Ne reference laser fringes - only one fourth of the maximum resolving power of the instrument.

Sections of an ICP spectrum of a solution containing 960 µg/ml As and 40 µg/ml Cd are given in Fig. 4. From Fig. 4.a to Fig. 4.c, the limiting aperture in front of the PMT detector was decreased from 1.0 mm in diameter to 0.25 mm in diameter which improves the resolution.

The spectrum shown in Fig. 5.a was derived from an interferogram (obtained with the same solution as in Fig. 4) equivalent in length to 16,384 periods of the He-Ne reference laser fringes, while the spectrum shown in
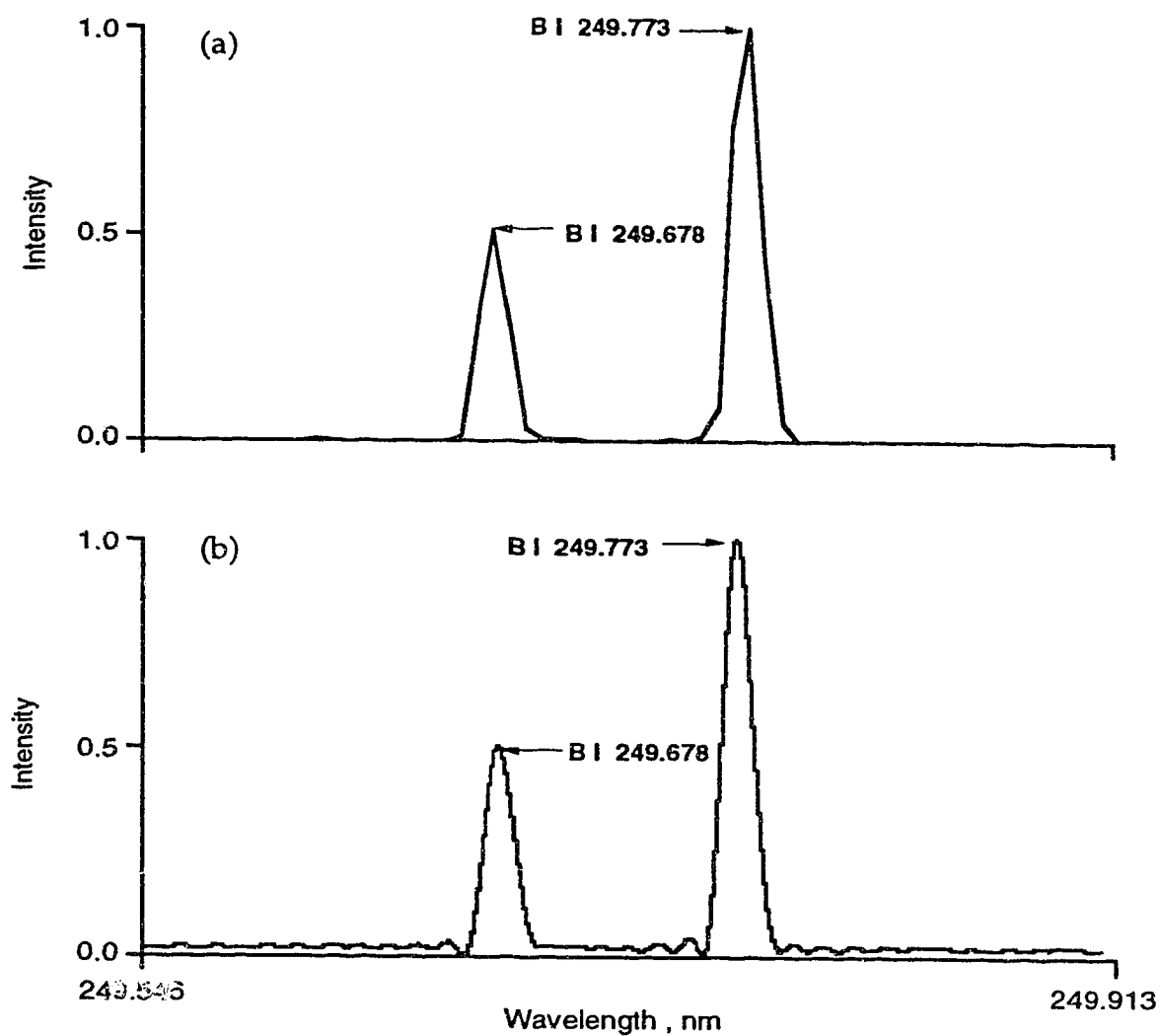
Fig. 3. A 0.4 nm segment of the 16 k spectrum of 1000 µg/ml boron solution (a) and the zero-filled spectrum of the same solution (b) illustrating the resolution of B I 249.678 nm and B I 249.773 nm lines.
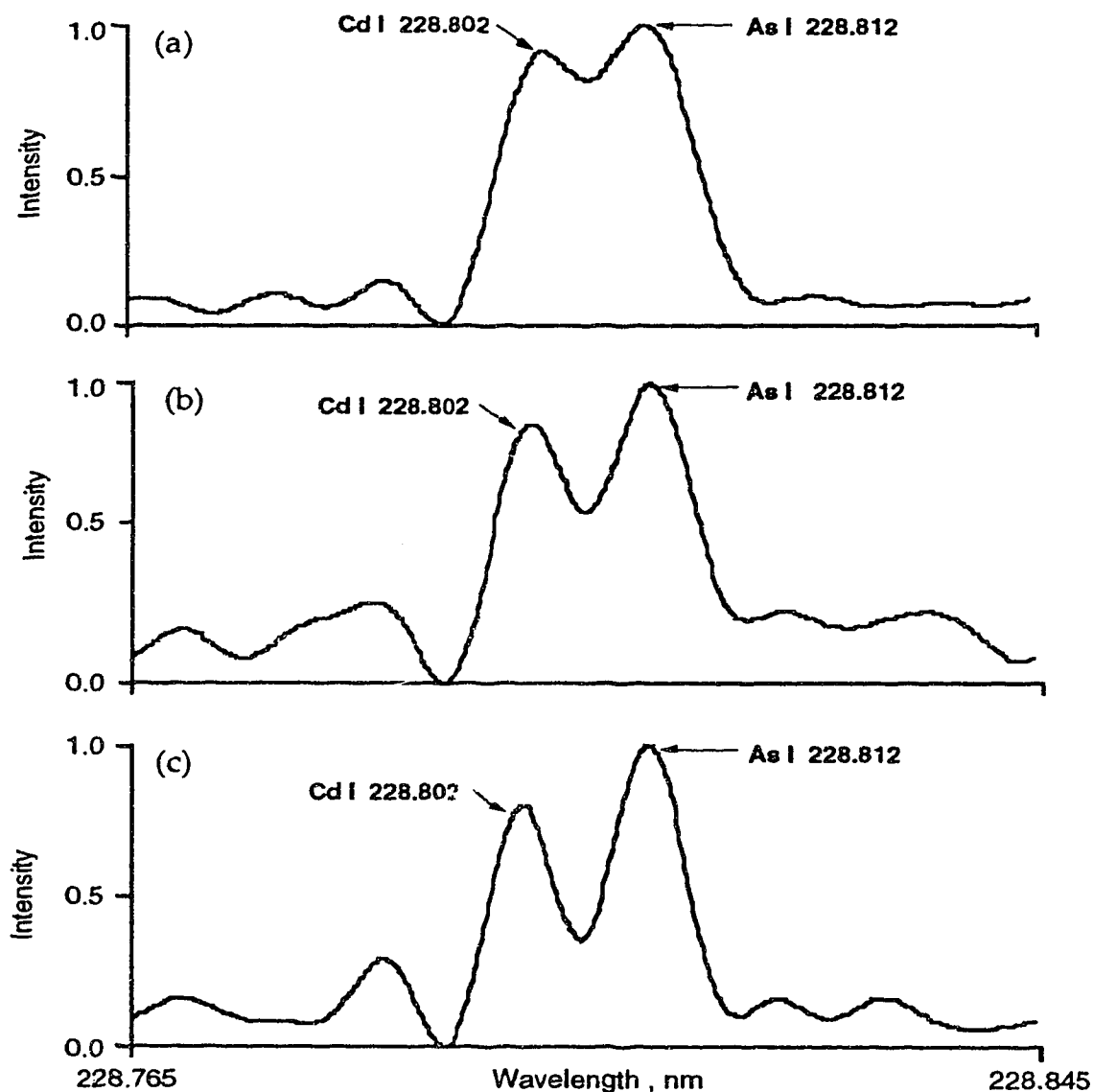
Fig. 4. A 0.08 nm segment of the zero-filled 16 k spectrum of a solution containing 960 μg/ml As and 40 μg/ml Cd with a limiting aperture of 1.0 mm (a) 0.5 mm (b) and 0.25 mm in diameter (c) in front of the detector illustrating the practical resolution capability of the spectrometer.
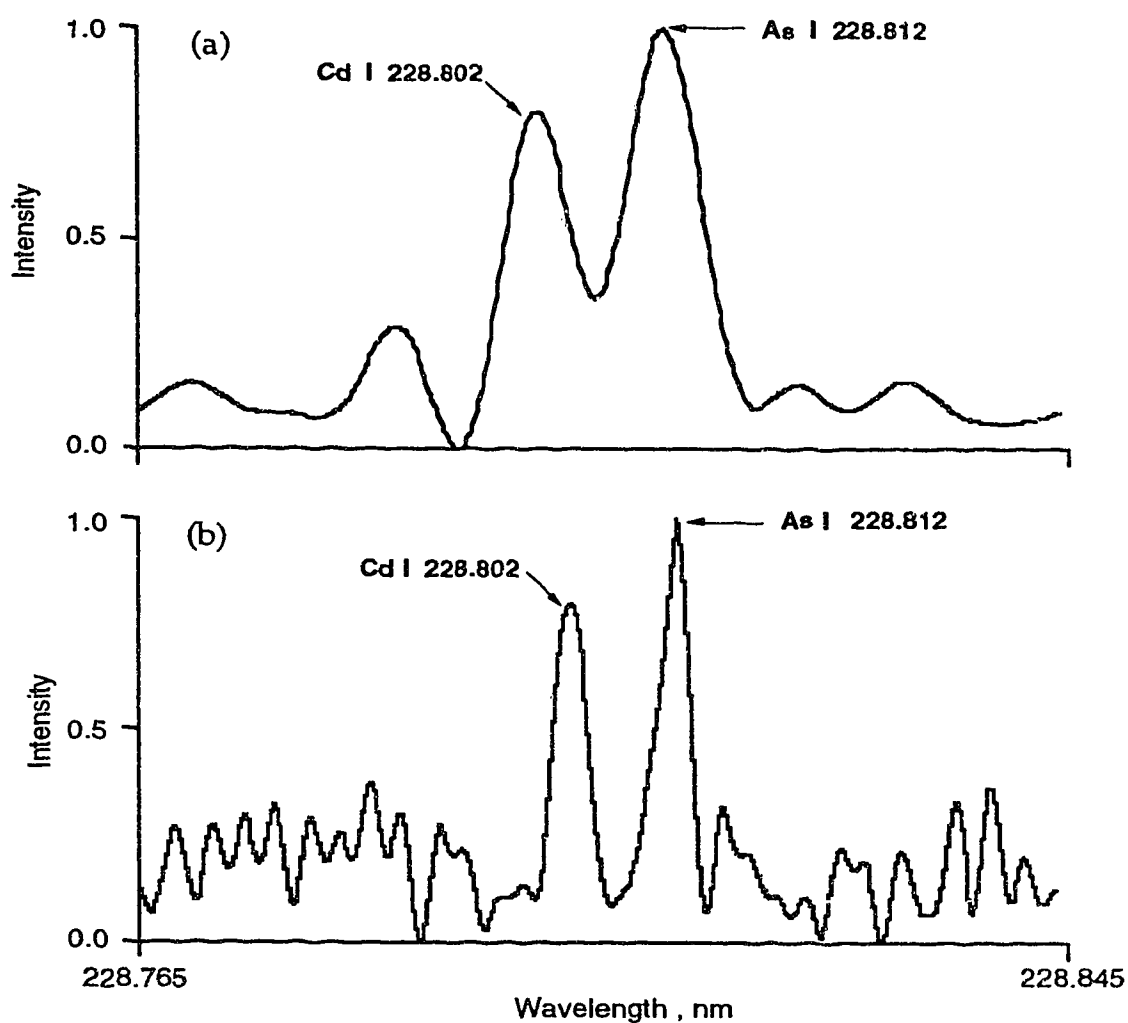
Fig. 5. A 0.08 nm segment of the zero-filled 16 k (a) and 64 k (b) spectrum of a solution containing 960 μg/ml As and 40 μg/ml Cd illustrating the resolution of Cd I 228.802 nm and As I 228.812 nm lines.

Fig. 5.b was derived from an interferogram equivalent in length to 65,536 periods of the reference He-Ne laser fringes, the maximum resolution capability of our system. The Cd I 228.802 nm and As I 228.812 nm lines (which are only 10 pm apart) are fully baseline resolved in the spectrum shown in Fig. 5.b.

High resolution was previously considered very difficult and costly to achieve using wavelength-dispersive instruments [24]. The development of Fourier transform spectrometers for the ultraviolet and visible spectral regions now provides the analytical chemist with the opportunity to work with high resolution and high quality spectra in a practical system.

High resolution reduces the number of spectral interferences in a given analysis. This greatly simplifies many analytical problems, especially those involving very complex spectra such as those of the rare earth and actinide elements. It is also possible that some tedious and time-consuming sample pre-treatment and separation steps may be eliminated. High resolution is also very valuable for basic research and spectrophysical studies of an excitation source such as the ICP or the GDD. If the resolution is high enough to fully resolve the physical line widths and shapes in the source without distortion or broadening due to the instrumental function (a conservative guide line to follow is that this is achieved when the FTS resolution R is at least three times smaller than the physical line width), then the ability to measure line widths and shapes provides information for the study of excitation and energy transfer mechanisms.

Unlike the direct reader or monochromator, the resolution of the interferometer can easily be adapted to the application by changing the length

of the mirror drive. The tradeoff for high resolution is the increased number of data points in the acquired interferogram, and the increased computation time and memory space necessary for the data processing.

An important advantage of the FTS technique is the high degree of accuracy in the measurement of wavelengths, which is a big problem with both the direct reader and monochromator type spectrometers. Only a single internal laser (usually a He-Ne laser) is required to calibrate the entire scale of the spectrum. The accuracy of the wavelengths (or wavenumbers) is limited only by the accuracy with which the wavelength of the laser is known, and by the alignment of the optics in the interferometer system.

By virtue of the three combined advantages the FTS technique offers (spectral range, wavelength resolution, and wavelength accuracy), one obvious application is for compiling spectral atlases for sources such as the ICP and the GDD. An atlas that is specific to the ICP and GDD is required because almost all the previous wavelength tables were derived from arc and spark sources. Dr. G. King [20] has measured the wavelengths of spectral lines of 21 elements that are excited in the ICP.

With the three advantages available, it is possible to automate the interpretation of the spectra measured. A computer can be used to extract all the spectral lines in a spectrum and present them to the analytical chemist along with tentative assignments. This could alleviate or even eliminate the tedious task of examining peak by peak the entire spectrum. Lines could be assigned simply by matching wavelengths with a database of known lines. The assignments are tentative because other factors such as aliasing and spectral interferences can lead to more than one assignments for a single line.

An expert system has been developed in this research group [20] to automatically identify spectral lines, which was tested on standard steel samples and the system correctly assigned to each line the element that was responsible for that line.

Another practical application would be to subtract stored single element spectra from a multi-component spectrum. This "spectral stripping" technique could be used to simplify sample spectra to make interpretation easier. Spectral stripping is only achievable with FTS technique because of its ability to measure comprehensively the entire spectrum with absolute wavelength accuracy. This also requires reproducible alignment of the optics in the interferometer, which is still very difficult to do manually.

1-4-3. FTS - The "cons"

There are two sides to everything. Any technique or method has both features and problems.

Whereas the realisation of the multiplex advantage was a major factor in the utility of Fourier transform spectrometry in the infrared spectral region, the application of FTS in the ultraviolet and visible spectral regions may, in most cases, actually involve a multiplex disadvantage, which should be carefully considered in the development of ICP-FTS or GDD-FTS. The multiplex advantage is a gain in signal-to-noise ratio in the FTS spectrum compared with that achieved for a comparable measurement time by a sequential scanning wavelength-dispersive spectrometer. This advantage arises in detector-noise limited situations (which commonly occur in the infrared spectral region): that is, the limiting noise is that associated with the

detector and is independent of the signal intensity. In the ultraviolet and visible spectral regions, the detector, usually a photomultiplier tube or a photodiode, is not the noise limiting factor. With the ICP in this spectral region, for instance, the noise limiting factor is either signal shot noise, for which there is neither a signal-to-noise ratio advantage nor a disadvantage in FTS, or source flicker noise, for which there is a signal-to-noise ratio disadvantage in FTS. In the later cases, the noise level at the detector is dependent on the signal intensity. As FTS is a multiplex technique, all the source emission intensity is recorded simultaneously at a single detector. In the Fourier transform process, the noise at any given frequency in the source is distributed throughout the resulting spectrum.

One other problem in FTS, both in the infrared and in the ultraviolet and visible spectral regions, is the dynamic range limitations. This limitation occurs for a very weak signal in the presence of an intense one. The intensity of the weak signal, because the dynamic range is limited by the strong signal, may fall below the resolution of analog-to-digital converter (ADC) required to acquire the interferogram. The weak signal consequently may not be distinguished from the noise in the baseline of the spectrum. And the source noise from strong emission lines may increase the overall baseline noise level in the transformed spectrum and thereby degrade the detection limits for other analytical species in the sample. As a result, detection limits in ICP-FTS or GDD-FTS are definitely dependent on the total sample composition.

1-5. Thesis objectives

In summary, in comparison with wavelength-dispersive measurement systems, the FTS measurement system has a simultaneous, comprehensive

wavelength coverage, an unparalleled accurate and precise wavelength axis, and high resolution with a relatively compact instrumental system. On the other hand, dynamic range limitations and signal-to-noise ratio disadvantages are problems which must be considered in an FTS measurement system for the ultraviolet and visible spectral regions. As a qualitative tool, the FTS system is far superior to other measurement methods coupled to both the inductively coupled plasma (ICP) and the glow discharge device (GDD).

It can be seen that Fourier transform spectroscopy coupled to sources such as the ICP and the GDD offers both powerful measurement potential and unique measurement problems for the analytical chemist. No new technique ever completely replaces those already in use, but rather provides a complementary method with some advantages and some inherent limitations. The multiplex approach is relatively new to analytical atomic spectroscopy community. Before its measurement potential is fully understood and realised, its unique characteristics must be carefully examined and considered.

The objectives of this thesis ·· · to explore and take full advantage of the FTS system and to counteract its limitations.

In Chapter 3, fundamental studies of pure-argon and mixed gas plasma discharges are carried out. The emission spectra of 8 thermometric species are measured in pure argon, argon-air, argon-helium, argon-nitrogen, and argon-oxygen mixed-gas ICP discharges. Excitation and ionization temperatures of those thermometric species whose emission spectra are in the ultraviolet spectral region are thus measured simultaneously based on the intensities

extracted from the corresponding spectra. Excitation and ionization temperatures of those thermometric species whose emission spectra fall in the visible spectral region are obtained in the same way. H_β emission line profiles are measured together with the emission spectra of the thermometric species in the pure argon ICP and the effect of forward power on the electron number density is examined. The effect of the types of torches, RF forward power, types of nonargon gases and the percentages of the nonargon gases mixed into the argon ICP on the excitation and ionization temperature profiles are investigated. Detection limits for selected elements are also measured simultaneously or separately in various mixed gas plasma discharges.

In Chapter 4, attempts are made to counteract the multiplex disadvantage and the dynamic range limitations in the ICP-FTS system. The front-end of the LECO PLASMARRAY™ echelle/photodiode array spectrometer (without the echelle grating and the PDA) is used as the "masking" or "windowing" device to limit the optical bandpass into the interferometer to a few small regions such that emission lines of interest are passed and unwanted emission lines are blocked, or just one small region around the spectral position of the desired information is selected. As a result, the possibility of dynamic range limitations and a multiplex disadvantage due to the strong emission in other spectral regions will be diminished.

Using the three major spectral measurement advantages that the FTS technique offers, the spectral characters of brass, stainless steel, and low alloy steel samples excited in the ICP and the GDD are evaluated and compared in Chapter 5. The excitation temperatures in the ICP and the GDD are also calculated and compared.

Finally, in Chapter 6, argon emission from 300 nm to 1300 nm excited in both the ICP and the GDD in the visible and near IR spectral regions is measured interferometrically and the corresponding wavelength tables are compiled.

Chapter 2

Temperature and electron number density measurements

2-1. Introduction

The inductively coupled plasma (ICP) is a highly effective and useful source for atomic emission spectroscopy. The plasma source temperature is considerably higher than that obtained with flames, thus enhancing atomization, ionization and excitation processes and reducing many chemical interferences. A knowledge of the fundamental properties of an inductively coupled plasma such as temperature and electron number density, which govern the excitation mechanisms, is of importance for an understanding of ICP's and for their efficient use for analytical purposes.

Various authors have already measured temperatures and electron number densities in an argon ICP [25-62]. The results are summarized in Table 1. The disagreement between different studies results from different operating conditions and calculation parameters such as (1) r. f. frequency, (2) r. f. input power, (3) argon gas flow rates, (4) sample uptake rate, (5) observation height, (6) torch geometry, (7) gf values from different sources and (8) others.

There are a number of methods for the measurement of temperature and electron number density. In this chapter, only some of the most commonly-used methods will be discussed: the "Boltzmann plot" method and the line pair intensity ratio method for the measurement of excitation

Table 1. Temperature measured by different authors

Excitation temperature

Fe I	5300-7100 [44]	5200-6600 [46]	4500-5100 [50]	
	3900-5700 [51]	5009-8500 [52]	6500 [53]	4800 [55]
	4899-5104 [57]	4000-7000 [58]	4000-7500 [59]	
Ti I	3500-4900 [60]	4100-5400 [50]	4400-5700 [51]	
	4000-5200 [60]			
Ti II	5200-6200 [44]	5000-7000 [41]	4000-8500 [49]	
	4600-5400 [50]	4400-5000 [51]	7000 [54]	
Ar I	4000-4600 [35]	4800-5100 [51]	5187-5283 [57]	
V II	4500-5200 [50]			
V I	6142 [50]			
Ni I	5039 [57]			
Co I	4392 [57]			
Mn I	4500 [60]			
Mn II	7000-8000 [60]			
W I	3900-4600 [60]			
W II	4600-4900 [60]			
Sc II	7800-10000 [60]			
Ca II	7800 [55]			
Mo I	5500-6500 [62]			

Rotational temperature

OH	2030-2570 [55]	3000 [60]	3700-3800 [61]	
N_2^+	4500-5600 [50]	3600-4250 [55]	4300 [60]	5050-6100 [61]
C_2	6100 [41]			
CN	3500-5400 [35]			
BO	5000 [36]			

Ionization temperature

Mg II 279.6/Mg I 285.2	7100-7300 [51]	5900-8000 [52]
Mg II 280.2/Mg I 285.2	7000-7300 [51]	
V(380 line pairs)	6000-7400 [51]	
Ca II 396.8/Ca I 422.7	5600-8100 [52]	
Ca II 393.4/Ca I 422.7	6000-7000 [49]	
Cd II 226.5/Cd I 228.8	5600-8100 [52]	
Zn II 206.1/Zn I 213.9	6100-7700 [52]	
Fe II 258.8/Fe I 252.3	6000-8200 [52]	
Ba II 493.4/Ba I 553.5	5600-8400 [52]	
Ti II 450.1/Ti I 451.2	5200-6199 [52]	

temperature; the ion line to neutral atom line intensity ratio method for the determination of ionization temperature; rotational temperature measurement using N_2^+ first negative system; and electron number density measurement using the Stark effect broadening of the H_β line.

2-2. Plasma temperatures and measurement methods

Species in a plasma, such as neutral atoms, ions, molecules, and electrons, are distributed over many energy states such as translational, rotational, vibrational, electronic, and ionization states. Each state can be defined by its own temperature. When this temperature is the same for all states, the system is said to be in thermal equilibrium, and that temperature value truly defines the energy of the system. A statement of temperature is a way to describe the energies of the various species. Spectroscopic methods are popular for the measurement of plasma temperatures primarily because the measurements do not disturb the system and, if the temperature is very high, they may be the only applicable methods. The theories and methods used for the measurement of excitation, ionization and rotational temperatures will be described in the following sections.

2-2-1. The measurement of T_{exc} using the "Boltzmann plot" method

For a homogeneously radiating gaseous layer of thickness d, intensity I and emissive power J [63]

$$I = J \times d \qquad\qquad \text{Equation 2-1}$$

J represents a quantity that is directly and exclusively related to the number of radiative transitions per sec in unit volume. If the number of transitions per sec per cm^3 leading to the emission of a light quantum hv is equal to N, we have the relation

$$J = \frac{1}{4\pi} Nh\nu \qquad\qquad \text{Equation 2-2}$$

replacing J in Equation 2-1 by Equation 2-2, we have

$$I = \frac{d}{4\pi} Nh\nu \qquad\qquad \text{Equation 2-3}$$

the absolute intensity of the spectral line emitted in the transition from p state to q state can be written as [63]

$$I_{pq} = \frac{d}{4\pi} A_{pq}N_p h\nu_{pq} \qquad\qquad \text{Equation 2-4}$$

or

$$I_{pq} = \frac{d}{4\pi} A_{pq} \times N_p h \frac{c}{\lambda_{pq}} \qquad\qquad \text{Equation 2-4.a}$$

where d is the depth of the source, A_{pq} the transition probability, N_p the concentration or density of atoms in the higher level p, h is Planck's constant, c the velocity of light, ν_{pq} the frequency, λ_{pq} the wavelength of the transition. For a system in thermal equilibrium, at temperature T, the concentration or density of atomic level p follows a Boltzmann distribution [64, 65]

$$N_p = N_0 \frac{g_p}{Z(T)} \exp(\frac{-E_p}{kT}) \qquad\qquad \text{Equation 2-5}$$

where N_0 is the total number density of the atoms, g_p the statistical weight of the level p, Z(T) the partition function of the atom, E_p the excitation energy of the level p, and k is the Boltzmann constant. The temperature governing this energy population is defined as the excitation temperature T_{exc}. Replacing N_p in Equation 2-4.a by Equation 2-5, we have:

$$I_{pq} = \frac{d}{4\pi} N_0 \frac{g_p}{Z(T)} A_{pq} h \frac{c}{\lambda_{pq}} \exp(\frac{-E_p}{kT})$$

Equation 2-6

Rearranging Equation 2-6 we have:

$$\frac{I_{pq}\lambda_{pq}}{g_p A_{pq}} = \frac{dN_0hc}{4\pi Z(T)} \exp(\frac{-E_p}{kT})$$

Equation 2-6.a

the logarithmic form of Equation 2-6.a is

$$\log \frac{I_{pq}\lambda_{pq}}{g_p A_{pq}} = \log \frac{dN_0hc}{4\pi Z(T)} + \frac{-E_p}{2.303kT}$$

Equation 2-6.b

From Equation 2-6.b, we can see that log ($I\lambda/gA$) is a linear function of the excitation energy E_p

$$\log \frac{I_{pq}\lambda_{pq}}{g_p A_{pq}} \propto E_p$$

Equation 2-7

The plot resulting from this linear function is the so called "Boltzmann plot." The slope (-1/2.303kT) is related to the excitation temperature and is equal to -0.625/T when E_p is in cm^{-1} and equal to -5040/T when E_p is in eV. In Equation 2-7, A_{pq} is sometimes replaced by the absorption oscillator strength f using the relationship

$$g_p A = C\, g_q\, f/\lambda^2 \qquad\qquad \text{Equation 2-8}$$

where g_q is the statistical weight of the lower level q, C is equal to 6.67×10^{13} if λ is in nanometers, thus we have

$$\log \frac{I_{pq}\,\lambda_{pq}^3}{g_p\, f} \propto E_p \qquad\qquad \text{Equation 2-9}$$

In order to measure an excitation temperature using this method, transition probabilities or oscillator strengths for several lines of an elemental species are required. The selection of a set of spectral lines should be based on three major factors [48]. First, reliable transition probabilities must be available [51, 66], second, the spectral lines should be close together to avoid calibration of the detector systems, third, lines with a wide range of excitation energies of the upper levels should be utilized to enhance the precision of the temperature measurement. The line sets for different thermometric species and the parameters used in this thesis are listed in Table 2. Iron is typically chosen as the thermometric species for this graphical "Boltzmann plot" method for several reasons. The complex spectrum provides many available spectral lines. Transition probabilities or oscillator strengths of iron are generally considered more reliable than for most other elements. Iron lines are easily identified since the iron spectrum is a traditional wavelength standard. Lastly, because iron is so often chosen for temperature determinations by spectroscopic methods, comparisons with results published in different studies are facilitated.

There have been problems associated with the accuracy of the transition probabilities or oscillator strengths available. A classic reference for iron is the work of Corliss and Tech [67] whose compilation lists transition probabilities and oscillator strengths for 3288 lines of iron I between 210 and 990 nm. Although this work continues to be a common reference source for these values, a later publication [68] stated that a systematic error existed in that first compilation and provides information to allow the reader to calculate revised values. Attempts have been made in later work to improve on the accuracy and precision of the experimental techniques used to determine the transition probabilities or oscillator strengths values for iron. The results of these later experiments are included in the work of Gary and Kock [69], Bridges and Wiese [70], Wolnick et al. [71], Huber and Parkinson [72] , Banfield and Huber [73], Bridges and Kornblith [74], Reif et al. [75] and Blackwell et al. [76].

The complications of the "Boltzmann plot" method are: (1) the assumption of thermal equilibrium or local thermal equilibrium in the source so that the Boltzmann expression applies (2) the possibility of self-absorption in the source which alters the observed line intensities and leads to erroneous results (3) the lack of and/or the lack of access to reliable gf or gA values and (4) others. In spite of evidence against the existence of local thermal equilibrium (LTE) in the ICP, most researchers continue to apply spectroscopic methods based on the "Boltzmann plots" for the determination of excitation temperatures in the ICP. This possible deviation from local thermal equilibrium could be one of the causes of the discrepancies among temperatures measured with different thermometric species and other

Table 2. Emission line data employed for the measurement of excitation temperature

Species	λ(nm)	$gA(10^8\,s^{-1})$	E_p (cm^{-1})
Fe II	258.588	6.64	38626
	261.187	8.71	38626
	260.709	6.63	39030
	275.574	21.1	44190
	273.955	15.4	44432
	271.441	3.86	44755
	266.466	26.5	64834
	266.663	24.1	65076
Fe I	385.991	0.796	25885
	371.994	1.79	26853
	382.043	6.16	33062
	361.876	5.09	35642
	360.886	4.16	35884
	381.584	8.15	38142
Ti II	324.198	4.0	30873
	323.904	5.78	30959
	323.657	8.79	31114
	322.284	2.55	31114
	323.452	11.6	31301
	321.706	2.28	31301
	323.966	8.58	39603
	322.86	8.06	39675
	323.228	7.66	39927
	321.827	16.9	43741
	322.424	20.27	43781
Ar I	425.118	0.0267	116660
	430.01	0.159	116999
	427.217	0.2064	117151
	426.629	0.1325	117184
	434.517	0.0819	118407
	433.534	0.0924	118460
	433.356	0.253	118469
	425.936	0.366	118871

temperature-related unusual behaviors as will be seen in Chapter 3. The problem of self-absorption in the ICP is generally considered to be negligible except for the alkali elements at high concentrations. The possible formation of metal oxides and nitrides in the ICP could also lead to erroneous intensity values, and thus resulting in inaccurate temperature measurements, as will be discussed in Chapter 3.

2-2-2. The measurement of T_{exc} using the line pair intensity ratio

Another commonly-used and simpler method to determine excitation temperature is to measure the ratio of two line intensities I_1 and I_2 of an element in the same ionization state. A or f values can be used and T can be deduced from Equation 2-6, namely,

$$T = \frac{0.625\,(E_{p2} - E_{p1})}{\log \frac{I_1}{I_2} - \log \frac{g_{p1}A_{pq1}\lambda_{pq2}}{g_{p2}A_{pq2}\lambda_{pq1}}} \qquad \text{Equation 2-10}$$

Several thermometric species have been used: titanium with Ti I 390.48/392.45 [77], Ti II 310.62/313.08 and 333.21/334.03 [78], Ti II 322.28/322.42 [44, 79], iron with Fe I 391.67/391.72 [24], Fe I 381.58/382.44 [49], Fe I 382.54/382.44 [80], zinc with Zn I 307.59/328.23 [81], strontium with Sr II 407.77/430.54 [82], calcium with Ca II 393.36/373.69 [56, 83]. The line pairs and the parameters used in this thesis are listed in Table 3.

The criteria in selecting lines or line pairs are similar to those listed in "Boltzmann plot" method. This method is subject to the same complications as the "Boltzmann plot" method. On the other hand, this method is very

Table 3. Emission line data employed for evaluation of excitation temperature via two line method

Species	λ(nm)	gA(10^8 s^{-1})	E_p (cm^{-1})
Fe I	382.588	26.18	33507
Fe I	382.444	1.253	26140
Fe I	381.584	66.15	38175
Ti II	334.034	2.6	30837
Ti II	333.211	17	40027
Ti II	322.424	7.03	43781
Ti II	322.284	2.08	31114

useful to follow the relative variation of the excitation temperature when one or several parameters of the source are modified. In Chapter 5, this method will be used to calculate and compare the excitation temperatures of the ICP and the GDD.

2-2-3. Ionization temperature

The distribution of the different species in an ICP can be described by a mass action law that is a function of the temperature. Ionization in the ICP can be described by the following equation:

$$M_a \rightleftarrows M_i^+ + e^-$$

If neutral atoms M_a and ions M_i^+ are collisionally equilibrated, their concentration ratio is given by the Saha equation [64, 65]

$$\frac{n_i n_e}{n_a} = \frac{(2\pi mkT)^{3/2}}{h^3} \frac{2Z_i}{Z_a} \exp\left(\frac{-E_i}{kT}\right) \qquad \text{Equation 2-11}$$

where n_a is the number density of the neutral atoms, n_e the electron number density, n_i the number density of the ions, m the mass of the electron, E_i the ionization potential, Z_a and Z_i the respective partition functions. The coefficient 2 is the statistical weight of the electron and h and k are the Planck and Boltzmann constants, respectively. We can calculate the constant in Equation 2-11

$$\frac{2\times(2\pi mk)^{3/2}}{h^3} = \frac{2\times(2\times3.14\times9.109\times10^{-28}g\times1.38\times10^{-16})^{3/2}}{(6.626\times10^{-27}erg/s)^3} = 4.83\times10^{15}$$

so we have:

$$\frac{n_i n_e}{n_a} = 4.83 \times 10^{15} \, T^{3/2} \, \frac{Z_i}{Z_a} \exp\left(\frac{-E_i}{kT}\right)$$

Equation 2-12

or

$$\frac{n_i}{n_a} = \frac{4.83 \times 10^{15}}{n_e} \, T^{3/2} \, \frac{Z_i}{Z_a} \exp\left(\frac{-E_i}{kT}\right)$$

Equation 2-12.a

Recall Equation 2-6, the equation for the intensity of emission by atoms. Ion line emission intensity can be described in the same way:

$$I_{ipq} = \frac{d}{4\pi} N_i \frac{g_{ip}}{Z_i(T)} A_{ipq} \, h\frac{C}{\lambda_{ipq}} \exp\left(\frac{-E_{ip}}{kT}\right)$$

Equation 2-13

where E_{ip} is the energy of the emitting state of the ion. Dividing Equation 2-13 by Equation 2-6, we have:

$$\frac{I_{ipq}}{I_{apq}} = \frac{N_i}{N_0} \frac{Z(T)g_{ip}\lambda_{apq}}{Z_i(T)g_{ap}} \frac{A_{ipq}}{\lambda_{ipq}A_{apq}} \exp\left[\frac{-(E_{ip}-E_p)}{kT}\right]$$

Equation 2-14

n_i/n_a in Equation 2-12.a is equal to N_i/N_0 in Equation 2-14, so we can replace N_i/N_0 in Equation 2-14 by Equation 2-12.a, we have:

$$\frac{I_{ipq}}{I_{apq}} = \frac{A_{ipq}g_{ip}}{\lambda_{ipq}} \times \frac{\lambda_{pq}}{g_{ap}A_{apq}} \frac{4.83 \times 10^{15}}{n_e} T^{3/2} \exp\left[\frac{-(E_{ip}-E_{ap}+E_i)}{kT}\right]$$

Equation 2-15

T in Equation 2-15 is the ionization temperature, which can be determined from the spectral line intensity ratio of an ion line to an atom line of the same element. Equation 2-15 can be solved numerically using Newton-Raphson iteration method to obtain the ionization temperature. Seven elements with lines whose transition probabilities are known with moderate accuracy from the recent literature are often selected as thermometric species, viz. Mg [84], Ca [84], Zn [85, 86], Cd [85, 86], Ti [87, 88], Ba [89], and Fe [67, 73, 90, 91]. The lines and other parameters needed in the ionization temperature calculations are listed in Table 4. The line pairs were selected on the grounds of similarity of excitation energy and closeness of wavelength. Of course, an electron number density value, n_e, is required for the calculation of the ionization temperature. This can be obtained experimentally using the Stark broadening theory (which will be described in section 2-4-2 and 2-4-3) or you can assume a "reasonable value" using the best results in the literature. The ionization potentials, E_i, for each element can be found in almost every chemistry textbook.

This method, which depends on the measurement of the relative intensities of an atom and ion line of a suitable thermometric species, has similar disadvantages as the method for the determination of excitation temperature using the "Boltzmann plot" method.

The ionization temperatures of 5 thermometric species in various mixed-gas plasma discharges will be calculated using this method in Chapter 3.

Table 4. Emission line data employed for the evaluation of the ionization temperature

Species	λ(nm)	E_p (cm^{-1})	gA(10^8 s^{-1})
Mg II	279.553	35761	10.72
Mg I	285.213	35051	14.85
Ca II	396.847	25192	2.92
Ca I	422.673	23652	6.54
Cd II	226.502	44136	5.02
Cd I	228.802	43692	15.035
Zn II	206.191	48481	6.575
Zn I	213.856	46745	18.91
Fe II	258.588	38660	8.009
Fe I	252.285	39626	29.125
Ba II	493.409	20262	1.91
Ba I	553.548	18060	3.45
Ti II	450.127	31207	1.393
Ti I	451.274	28896	0.95

2-2-4. Rotational temperature

Similarly to excitation and ionization temperatures, a rotational temperature can also be deduced in the same way. We start from Equation 2-4 once again

$$I_{pq} = \frac{d}{4\pi} A_{pq} N_p h \nu_{pq}$$

Equation 2-4

we also know that [40, 92],

$$A \propto \nu_{pq}^2$$

Equation 2-16

so we have [61]

$$I_{pq} \propto N_p \nu_{pq}^4$$

Equation 2-17

Because we are now considering the emission intensity of a rotational line emitted from a diatomic molecule, the number of molecules N_J in the rotational level J should replace N_p in Equation 2-17

$$I_J \propto N_J \nu_J^4$$

Equation 2-17.a

the number of molecules in each of the rotational states is proportional to the Boltzmann factor $e^{-E/kT}$, where E for a rotator at rotational state J is given by [92]

$$E = h/(8\pi^2 cI) \, J(J+1) \, hc = BJ(J+1) \, hc$$

Equation 2-18

where I is the moment of inertia of the rotator, $B=h/(8\pi^2 cI)$ is called the rotational constant. For most practical cases (the quantum number of the angular momentum $\Lambda=0$, rigid rotator), the number of molecules N_J in rotational state J can be related to the Boltzmann factor by

$$N_J \propto (2J+1) \exp[-BJ(J+1) hc/kT]$$ Equation 2-19

the appearance of the factor (2J+1) accounts for the fact that, according to quantum theory, each state of an atomic system with total angular momentum J consists of 2J+1 levels which coincide in the absence of an external field. Similar to Equation 2-5, we have

$$N_J = \frac{N_0}{Q_r} (2J+1)\exp[-BJ(J+1) hc/kT]$$ Equation 2-20

where Q_r is the state sum or partition function.

The variation of the intensity of the lines in a rotation-vibration band as a function of J is given essentially by the thermal distribution of the rotational levels; that is, to a first approximation, the intensity is proportional to Equation 2-20. In this approximation it is assumed that the transition probability is the same for all lines of a band. Actually there is a slight dependence on J and ΔJ which in the case of $\Lambda= 0$ (that is, when only P and R branch appear) can be taken into account by using in Equation 2-20 (J'+J"+1) in place of (2J+1); (J'>J"). Furthermore it should be noted that the J value of initial state must be used in the exponential term, that is, in emission J'. Combining Equation 2-17.a and Equation 2-20, we have the emission intensity of a rotational line emitted from a diatomic molecule

$$I_J = \frac{C v^4}{Q_r} (J'+J''+1)\exp[-BJ'(J'+1) \ hc/kT] \qquad \text{Equation 2-21}$$

Rearranging Equation 2-21, we have:

$$\ln\frac{I_J}{(J'+J''+1)} = \ln\frac{C v^4}{Q_r} - BJ'(J'+1) \ hc/kT \qquad \text{Equation 2-21.a}$$

or

$$\log\frac{I_J}{(J'+J''+1)} = \log\frac{C v^4}{Q_r} - BJ'(J'+1) \ hc/(2.303kT) \qquad \text{Equation 2-21.b}$$

now it is possible to determine the rotational temperature from the slope of the curve $\log (I_J/ \ J'+J''+1)$ versus $J'(J'+1)$. The value of the slope is

$$-Bhc/2.303 \ kT = 1.296/T \qquad \text{Equation 2-22}$$

in the case of N_2^+ [30, 51, 56] which is one of the most popular molecular species used in rotational temperature measurement, the first negative system $^2\Sigma - {^2\Sigma}$ corresponds to the emission of two branches R and P with $J'=J''+1$ for the R branch and $J'=J''-1$ for the P branch, J'' being the assignment of lower state. We have:

R branch: $(J' + J'' + 1) = 2 (j''+ 1)$ $J' (J' + 1) = (J'' + 1)(J'' + 2)$

P branch: $(J' + J'' + 1) = 2 J''$ $J' (J' + 1) = J'' (J'' - 1)$

The assignments of the rotational lines as a function of J'' are based on the works of Childs [93] and Coster and Brons [94]. Due to the even-odd alternation [92], line intensity with odd J'' must be multiplied by 2. Parameters of the lines of the first negative system of N_2^+ for rotational

temperature measurement are listed in table 5. The next step is to measure the intensities of those lines listed in table 5. Then we can calculate log (I/ J'+J"+1) (which is log [I/ 2 (J"+1)] for R branch, and log (I/ 2 J") for P branch) and draw these data points against J'(J'+1) (which is (J" + 1)(J" + 2) for R branch, and J" (J" - 1) for P branch), a nearly straight line will be obtained. Finding the slope of this line, we can calculate the rotational temperature using Equation 2-22.

An effective resolving power of at least 30,000 is necessary for this method [50].

Other molecular species can also be used for this purpose, such as OH [49, 55, 95-97], CN [35] , BO [38] and C_2 [95, 41].

Rotational temperature is not actually measured in this thesis, the discussion given here is only for the sake of completeness.

2-3. Electron number density measurements

Electrons are most likely the species responsible for excitation and ionization in the plasma. Many of the recent attempts to develop a model of fundamental processes in the analytical inductively coupled plasma have placed increasing emphasis on using electron number density as a key defining parameter. Rate model calculations require an accurate value for electron number density to enable the calculation of rate constants for most collisional-radiative processes. Some research groups [98, 99] have advocated the use of n_e as the fundamental basis of the local thermal equilibrium (LTE) model of the ICP, such as those of Lovett [100] and Hasegawa and Haraguchi [101].

Table 5. Line assignments and parameters of the first negative system of N_2^+

	P Branch		R Branch	
J''	λ (nm)	J''(J''- 1)	λ (nm)	(J''+ 1)(J''+ 2)
6			390.49	56
7			390.40	72
8			390.29	90
9			390.19	110
10			390.08	132
11			389.97	156
12			389.85	182
13			389.73	210
16			389.33	306
18	391.35	306	389.04	380
20	391.30	380	388.74	462
21	391.29	420	388.58	506
22	391.25	462		
23	391.20	506		
24	391.15	552		
25	391.10	600		
26	391.04	650		
27	390.97	702		
28	390.91	756		
29	390.84	812		
30	390.76	870		
31	390.68	930		
32	390.60	992		
33	390.51	1056		
34	390.41	1122		
35	390.31	1190		

2-3-1. Pressure broadening

The atom and ion emission line profiles of species which are embedded in a dense gas or plasma, will be determined by the extent of interactions of the emitters with the surrounding charged or neutral particles. This type of line broadening is generally known as pressure broadening. From the practical point of view, the pressure broadening can be further subdivided into

    a. Holtzmark or Resonance broadening

    b. Lorentz broadening

    c. Stark broadening

Depending on whether the broadening is caused by interaction with (a) atoms of the same kind, (b) atoms or molecules of different kinds or (c) charged particles. Since ions and electrons (charged particles) are present in the ICP in sufficiently high concentration, spectral lines from the ICP are broadened mostly by the interaction between the emitting atoms and the local electric field generated by the surrounding ions and electrons. This is the so called Stark broadening [102-104]. Because of its importance in plasma diagnostics, the following discussion will be limited only to Stark broadening.

2-3-2. Stark broadening

Stark broadening is caused by the action of charged particles, that is electrons and ions. According to the types of particles, two extreme theories

have been used to describe the experimental line profile. In the quasi-static theory, the perturbers are almost stationary because of their mass (that is, ions). The perturbation is constant over the whole emission process. The electrical field causes a symmetrical splitting of the line into several components. In the impact theory [105], fast-moving perturbers (that is, electrons) are considered. For a long time, broadening caused by electron was considered negligible, but several experiments indicated their role. Therefore a more refined Stark broadening model for hydrogen-like atoms was developed which takes simultaneously into account the electrons and the ions. Several groups of workers have been involved: Griem, Kolb, and Shen [102, 104, 106], Kepple and Griem [105], and Vidal, Cooper and Smith [107].

2-3-3. Measurement of n_e using H_β line

The theory and application of Stark broadening methods for the determination of n_e in plasmas has been discussed extensively [102-104]. Atomic hydrogen Balmer lines are most frequently employed for these calculations because of the availability of extensive tabulations of Stark broadening parameters for the complete line profiles [102, 104, 107] and because the theory is somewhat simpler to apply and more accurate than that for multielectron atomic species. The H_β line (486.13 nm) is often selected for the measurements because: (a) it is free from spectral interference by plasma components; (b) the range of half-widths anticipated and the relative intensities observed are sufficiently large to allow accurate measurement at various observation heights in the ICP; (c) extensive Stark data are available for the complete line profile encompassing a broad range of values and temperatures; and (d) greater accuracy is generally associated with Stark

ca.culations for the H_β line than for other atomic hydrogen lines. The precision obtained with the Stark calculation from the H_β line is approximately 5%. The H_β line profile measured with the Fourier transform spectrometer in this laboratory is shown in Figure 6.

Several Stark effects are observed. From the central frequency v_0 several components are located at a distance depending on the electrical field F

$$\Delta v = aF + bF^2 \qquad\qquad \text{Equation 2-23}$$

when $\Delta v = aF$, the linear Stark effect is observed; when $\Delta v = bF^2$, the quadratic Stark effect is observed. The full width at half-maximum $\Delta\lambda$ is related to the electron number density n_e by

$$\Delta\lambda = C(n_e ,T) \, n_e^a \qquad\qquad \text{Equation 2-24}$$

with the linear Stark effect, $a=2/3$, and with the quadratic effect, $a=1$. The linear effect applies to H, in contrast to Ar, where the quadratic effect should apply. Usually, the parameter C depends only weakly on n_e and temperature. The hydrogen may come from the decomposition of the aqueous solution nebulized into the ICP or a small amount (1% or less) of H can be added (either mixed with the outer gas or with the carrier gas). Because of the absence of the unshifted Stark component at high n_e, H_β exhibits a central dip. For $n_e = 2.4\times10^{15}$ cm^{-3} , the dip theoretically should be 40%. But practically, the value is smaller.
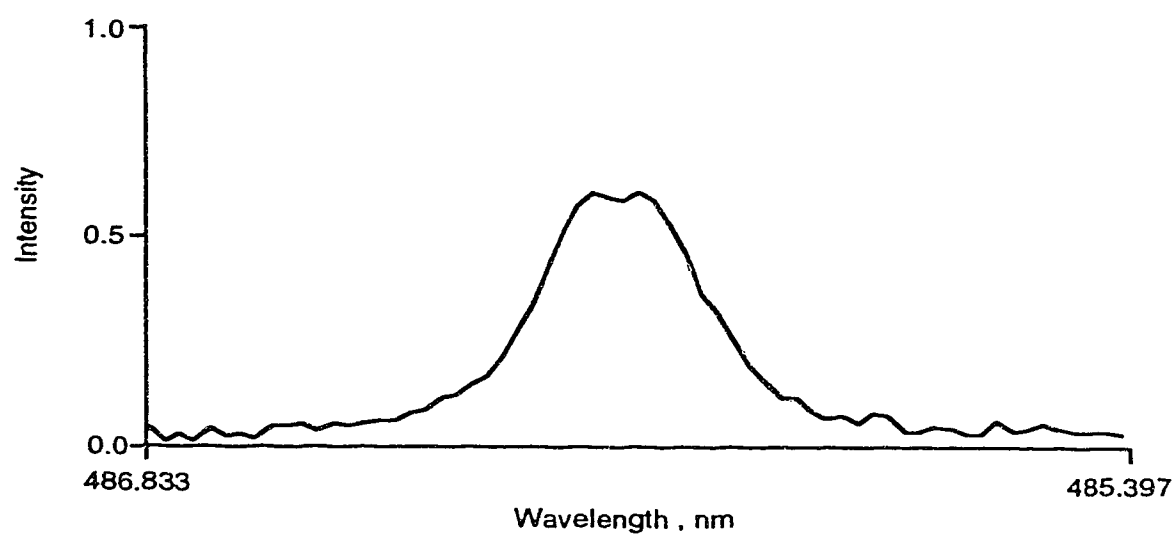
Fig. 6. Experimental profile of H_β emission measured by FTS spectrometer.

According to Griem [102], the combined widths due to both ion and electron broadening should scale quite closely as the two-thirds of the electron density. This suggests writing the electron density as

$$n_e = C(n_e, T)\Delta\lambda^{3/2} \qquad\qquad \text{Equation 2-25}$$

Values of the coefficient $C(n_e, T)$ for the line can be found in the book by Griem [104] (p 538). After you have this coefficient and halfwidth value, the calculation is very straight forward. It is very important to mention that the temperature contribution to $C(n_e, T)$ is negligible in comparison to the contribution by n_e, therefore the temperature term may be dropped; and the Doppler contribution to the halfwidth broadening should be taken into account, and can be calculated from the following equation

$$\Delta\lambda_{1/2} = 7.10 \times 10^{-7}\lambda_0 \, (T/M)^{1/2} \qquad\qquad \text{Equation 2-26}$$

where $\Delta\lambda_{1/2}$ is the Doppler width, λ_0 is the wavelength at the center of the line and M is the atomic weight, and T the temperature expressed in K. It should be noted that thermal Doppler broadening is most profound for lines of light elements and at high temperatures. As a matter of fact, at high temperature (T>10,000 K) and at low electron density ($<10^{14}$ cm^{-3}), line broadening due to the Stark effect becomes insignificant, and the line shapes will be increasingly dominated by Doppler broadening effects. Therefore, for a low electron density and high temperature plasma source, the line profile must be deconvoluted to remove the thermal Doppler broadening contribution. It is most fortunate that the electron densities in the ICP source determined from the measurement of the line are in the range of 10^{14} to 10^{16}

cm^{-3}. Therefore, a Doppler broadening contribution can be ignored for the measurements of the halfwidths under normal plasma operating conditions. Some improved theories on the determination of electron density using H$_\beta$ line have been published [105, 108-110].

To avoid the use of hydrogen, electron number densities can be determined from the Stark effect on some argon lines [64] such as Ar I 549.5 and 565.0 nm, although the line-broadening is not so large compared to the values obtained with H$_\beta$.

This method does not require the assumption of thermal equilibrium for the ICP. Consequently, the H$_\beta$ Stark method is considered to be more reliable than other spectroscopic methods used to determine electron number density such as continuum intensity method [111] and Inglis-Teller method [112-115].

In Chapter 3, the effects of forward power and observation height on the electron number densities in a pure argon ICP discharge ignited with a "long" torch and a "normal" torch will be examined using the method described in this section.

2-4. Conclusion

Excitation temperature, ionization temperature, and electron number density can be measured by spectroscopic methods as described in this chapter. Errors in these measurements associated with these methods are caused by the inaccuracy in the transition probabilities or oscillator strengths currently available in the literatures, and the possible formation of oxides and/or nitrides in the source used. Another complication is that some of the

methods described here require that the measured system be in thermal equilibrium or local thermal equilibrium (LTE), which is not true in the real world in most cases. However, these methods are very useful to follow the relative variations of the excitation temperature, ionization temperature, and electron number density when one or several parameters of the system are modified.

Chapter 3

Fundamental studies of argon and mixed-gas ICP's

3-1. Introduction

Inductively coupled plasmas (ICP's) operated at atmospheric pressure are commonly used as vaporization-atomization-excitation-ionization sources in analytical atomic emission spectrometry (AES), atomic florescence spectrometry (AFS), and mass spectrometry (MS). Argon-supported ICP discharges exhibit several advantages for spectrochemical analysis. Because of ease of operation and a power requirement lower than that for other support gases such as air, nitrogen, oxygen, and hydrogen, most laboratory ICP discharges are sustained in pure argon. This relative ease of operation and reduced power requirement are partly attributed to lower thermal conductivity, lower heat capacity, and lower electrical resistivity of argon, compared to other support gases.

The choice of argon as the support gas for ICP spectrometry poses several limitations. From an analytical viewpoint, the exciting species in an argon ICP can not provide sufficient energies to promote electronic transitions in atomic and ionic levels of high excitation energies, such as those of the halogens. Certain elements such as sulfur and phosphorus, having useful spectral lines in the near UV-visible region, are subject to spectral interferences by argon lines [116, 117]. Thus, a high-resolution vacuum monochromator, with a purged optical path, is required to observe alternative lines in the vacuum UV region. If nonresonant lines in the near

IR region are used, the complex background spectrum of the argon ICP discharge limits selection of suitable lines for determinations of certain elements, especially the nonmetals [118, 119]. From an economical point of view, argon is more expensive compared to air, nitrogen and oxygen, thus increasing the running cost of the ICP facility, especially in regions where argon gas is not produced locally. To reduce the argon consumption, the utilization of various low-gas-flow torches have been investigated, and at least three commercial versions of these torches have been introduced into the marketplace by various manufacturers. Although the utilization of low-gas-flow torches has resulted in a significant reduction in argon gas-flow requirements, no improvements in the detection powers of the corresponding plasmas have been realized; in some of the cases, detection limits measured at spectral lines occurring at wavelengths less than 250 nm have been inferior to those of a conventional argon ICP discharge [120, 121].

The above analytical and economical limitations for Ar ICP discharges have been a stimulus for many investigations of mixed gas, molecular gas, and helium ICP discharges. Although plasma formation at atmospheric pressure was observed to be the easiest in a flowing stream of argon, once the discharge is formed, argon gas mixtures containing various amount of air, helium, nitrogen, oxygen and hydrogen could also be used. The major impact of mixed-gas and molecular-gas ICP's is their superior ability to decompose refractory particles and to operate with higher solvent and analyte loading compared to an argon ICP, thus extending the domain of samples which could be handled effectively in practice. Both the mixed-gas and molecular-gas ICP discharges possess excellent potentials for the direct analysis of solids [122-124]. And it is claimed that helium ICP discharges are especially beneficial

for exciting high-excitation energy lines that are either not intense enough or not observed at all in the argon ICP discharges.

In almost all the studies of mixed-gas plasmas, foreign gases (non-argon gases) are introduced into either the coolant gas or nebulizer gas of an argon ICP discharge. Among molecular gases used in the coolant gas of the ICP discharge, nitrogen has been the one most commonly used [125-160]. An oxygen coolant has been used to generate an argon-oxygen ICP discharge [127, 147, 149, 150]. Power requirements were similar, but a larger apparent volume was observed as compared to an argon-nitrogen plasma [147, 148]. Argon-air ICP discharges, with air as the coolant gas, have also been formed [143, 127, 147, 149, 150]. In general, the argon-air plasma was shorter than an argon ICP discharge, but a brighter, longer, conical plasma was observed for the argon-air ICP discharge compared to the argon-nitrogen ICP discharge using pure nitrogen as the coolant gas. An argon-helium ICP discharge with 70% helium and 30% argon as the coolant gas was operated in the Fassel torch [126, 146-149]. The argon-helium plasma was slightly smaller but significantly less intense than the argon discharge. Introduction of more than 70% helium into the coolant will extinguish the plasma [127, 147-150].

In terms of analytical performance, the argon-nitrogen ICP has been investigated more extensively than other mixed gas ICP discharges. Montaser et al. [144] have clearly demonstrated that introduction of 5 to 20% nitrogen in the coolant of an argon-nitrogen ICP discharge enhances both the net analyte and background intensities. They also concluded that, while the background, the net intensity, and the S/B (signal-to-background ratio) values decrease sharply for ion lines as the coolant gas flow approaches 100% nitrogen, the opposite trend is found for the neutral atom lines of medium excitation

energies. The above conclusions achieved from the studies of Montaȿer et al have been reconfirmed by Choot and Horlick [148-150], who also introduced air, helium, nitrogen, and oxygen into the coolant flow of the Fassel torch. Their results iɩdicate that, mixed-gas plasmas exhibit maximum intensities at an observation height of 10 mm above the load coil, where the analyte intensity in the mixed gas plasmas are a factor of 2 to 3 greater than that of an argon ICP discharge. More importantly, Choot and Horlick [149] also found that when air, pure nitrogen, pure oxygen, or a mixture of 70% helium and 30% argon was used in the coolant gas of the plasma, the S/N (signal-to-noise ratio) values measured for three high-excitation-energy cadmium lines, even at a forward power of up to 2.3 kW, were inferior, by a factor of 3 to 4, to those achieved for an argon ICP discharge.

To interpret the above-mentioned results, and to obtain basic data for plasma modeling, diagnostic studies of the plasmas are essential. As mentioned in Chapter 2, the most important criteria used to access fundamental properties of analytical ICP's are temperatures and electron number densities. These properties can provide insight on the various reaction mechanisms prevailing in the plasmas, the extent of departure from local thermodynamic equilibrium, and the role of different species in exciting the analytes. Relatively few investigators have reported the temperature or electron number density for their plasmas, no data are available on comprehensive and systematic studies of argon-air, argon-helium, argon-nitrogen, and argon-oxygen mixed gas ICP discharges. In this chapter, the excitation temperatures of Fe II, Fe I and Ti II, the ionization temperatures of Mg, Fe, Cd, Ca, and Zn as the function of the observation height and the percentage of foreign gases (0, 5, 10, 20, 50, 100% of air, nitrogen and oxygen; 0,

5, 10, 20, 50% of helium in the coolant) are measured. The effect of 20% nitrogen in the nebulizer gas introduced into a argon-sustained ICP discharge on temperature profiles of selected thermometric species is examined in comparison with the results obtained with a pure-argon plasma discharge. Finally the electron number density in a pure argon ICP discharge as a function of forward power and observation height are also investigated. All lines and parameters used in this study were given in Chapter 2.

As pointed out by Montaser et al [161], temperatures must be measured on a single ICP facility before a viable comparison of the data for various mixed-gas plasmas can be made. Only then can the influence of generator frequency, torch design, and detection systems on the data be eliminated. In this study, the excitation temperatures of Fe II, Fe I and Ti II, the ionization temperatures of Mg, Fe, Cd, Ca, and Zn would have been measured simultaneously by nebulizing a single multi-element solution into the plasma discharge, if the 1P28 detector had had a good response in the UV region. As a result, the excitation temperatures of Fe II (derived from 8 lines) and the ionization temperatures of Mg, Fe, Cd, and Zn were measured simultaneously and then the excitation temperatures of Fe I (derived from 6 lines), Ti II (derived from 11 lines) and the ionization temperature of Ca were also measured from another single spectral measurement.

3-2. Experimental

3-2-1. ICP source

The ICP system used to generate and sustain the plasma discharge was a model HFP-2500D 2.5 kW r. f. generator (Plasma Therm Inc. Kreston, N. J.).

This generator is of a crystal controlled type operating at a frequency of 27.12 MHz. It allows power output be varied from 0 to 2.75 kW. The system also includes a model AMN-2500E automatic matching network. Power from the r. f. generator is coupled to the ICP source via this automatic matching network. This automatic matching network automatically adjusts the impedance of the system in order to establish and sustain a stable plasma discharge. This is particularly convenient when we need to introduce nonargon gases into the plasmas. The three turn load coil surrounds the top of the plasma torch and serves to couple r. f. power to the plasma source. Plasma operating conditions and various gas flow rates are listed in Table 6. All samples were introduced as aerosols using a glass concentric nebulizer (model TR-30-A2, J. E. Meinhard Associates, Santa Ana, California).

3-2-2. Plasma torch

The basic design of the torches used in this study are shown in Fig. 7. They are similar to that originally suggested by Fassel [6]. The one with the extended outer tube is 30 mm longer compared to the "normal" one. The two torches will be referred to as "long" and "normal" torch later in this chapter. The temperature and electron number density profiles obtained with these two types of torches will be compared in this chapter. When mixed-gas plasmas were studied, only the "normal" torch was used in this work. They are all constructed from three concentric quartz tubes. The outer tube, 18 mm i.d., is the coolant tube, which serves to introduce the coolant and plasma supporting gas into the plasma. Ordinarily, pure argon is introduced tangentially into this tube. In this study, mixtures of argon-air, argon-helium,

Table 6. Plasma running conditions

Forward power	1.0 - 2.0 kW
Reflected power	< 0.05 kW
Frequency	27.12 MHz
Viewing zone	a) 100% Ar, 5 - 20 mm above load coil
	b) mixed-gases, 2 - 10 mm above load coil
Coolant gas	a) Ar, 15 l/min
	b) Ar mixed with 5%, 10%, 20%, 50%, 100% air, nitrogen, and oxygen, 15 l/ min
	c) Ar mixed with 5%, 10%, 20%, 50% helium, 15 l/min
Auxiliary gas	a) Ar, 0.9 l/min
	b) mixed gas, 1.1 l/min
Nebulizer gas	Ar, mixed gases, 1.1 l/min
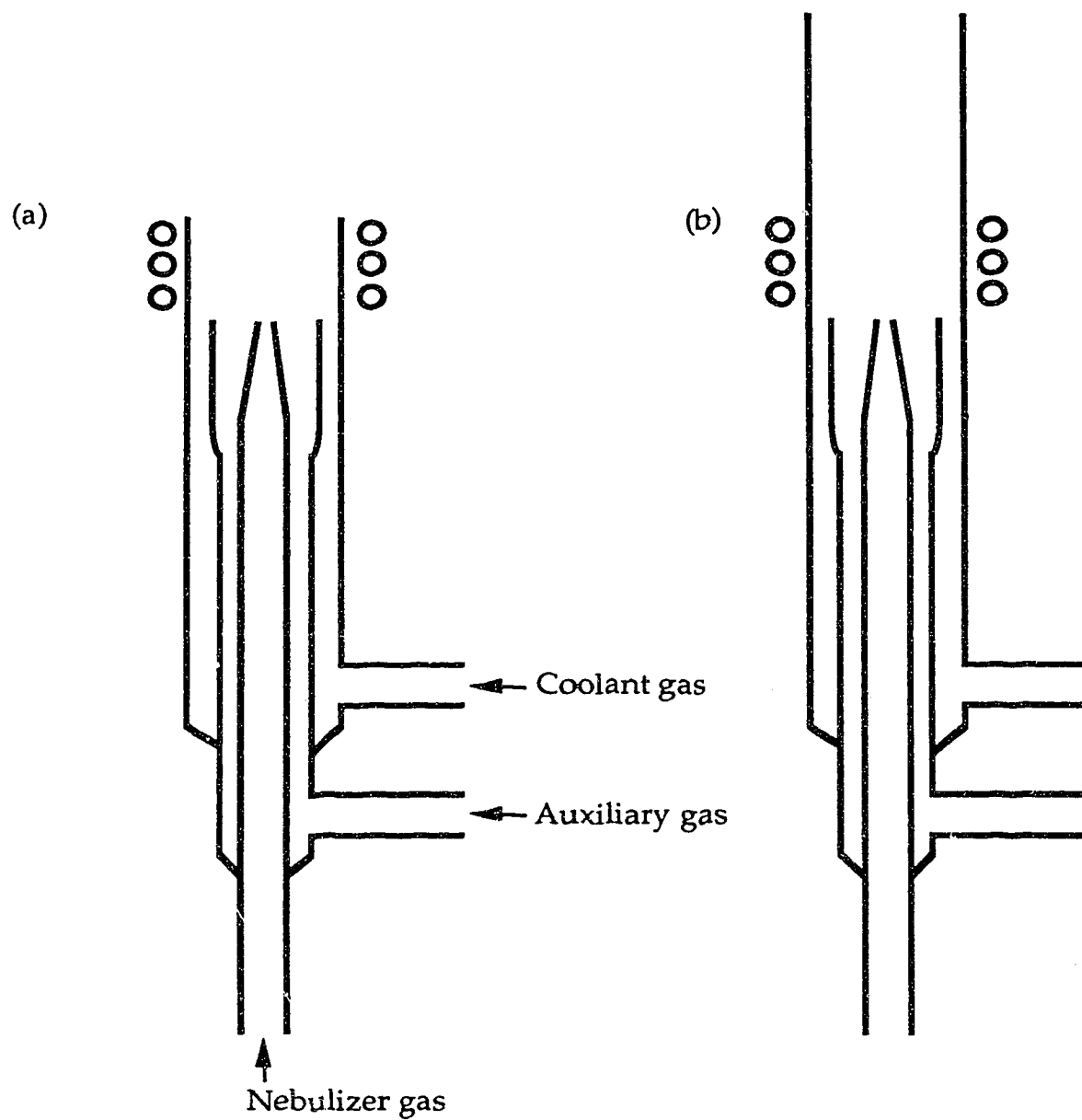
Fig. 7. ICP torches (a) normal Fassel torch, (b) Fassel torch with extented outer tube (long torch).

argon-nitrogen, and argon-oxygen were also introduced into this tube. The middle tube is known as the auxiliary gas tube. The auxiliary gas, introduced into the plasma tangentially, serves to lift the plasma slightly and prevent the central tube from melting. The central or aerosol tube is used to feed the sample aerosols into the center of the plasma discharge. The sample aerosols are carried by the nebulizer gas through this tube. Normally, both auxiliary and nebulizer gases are all argon. In part of this study, 20% of the argon in the nebulizer gas was replaced by nitrogen as well.

3-2-3. The optical system

The current Fourier transform spectrometer (FTS) used in this study was redesigned and improved by Bruce Todd [23]. The key component - the Michelson interferometer has two mirrors - the fixed and moving mirrors arranged 90° to each other and a beamsplitter 45° between them.

A block diagram of the FTS measurement system is shown in Fig. 8. The inductively coupled plasma, Michelson interferometer, and all the related optics are mounted on an optical rail bed. The radiation from the plasma was collimated by a quartz lens at a distance of its focal length (30 cm) onto a circular aperture with a 2.5 mm diameter. The collimated beam is divided by the beamsplitter to produce two beams that travel to the fixed and moving mirror of the interferometer. Both beams are reflected and combined. The combined beams interfere - the extent of the interference depending upon the position of the moving mirror. When the moving mirror moves to a position such that the optical path difference between the two beams is zero, the reflected beams would interfere constructively. A maximum signal would
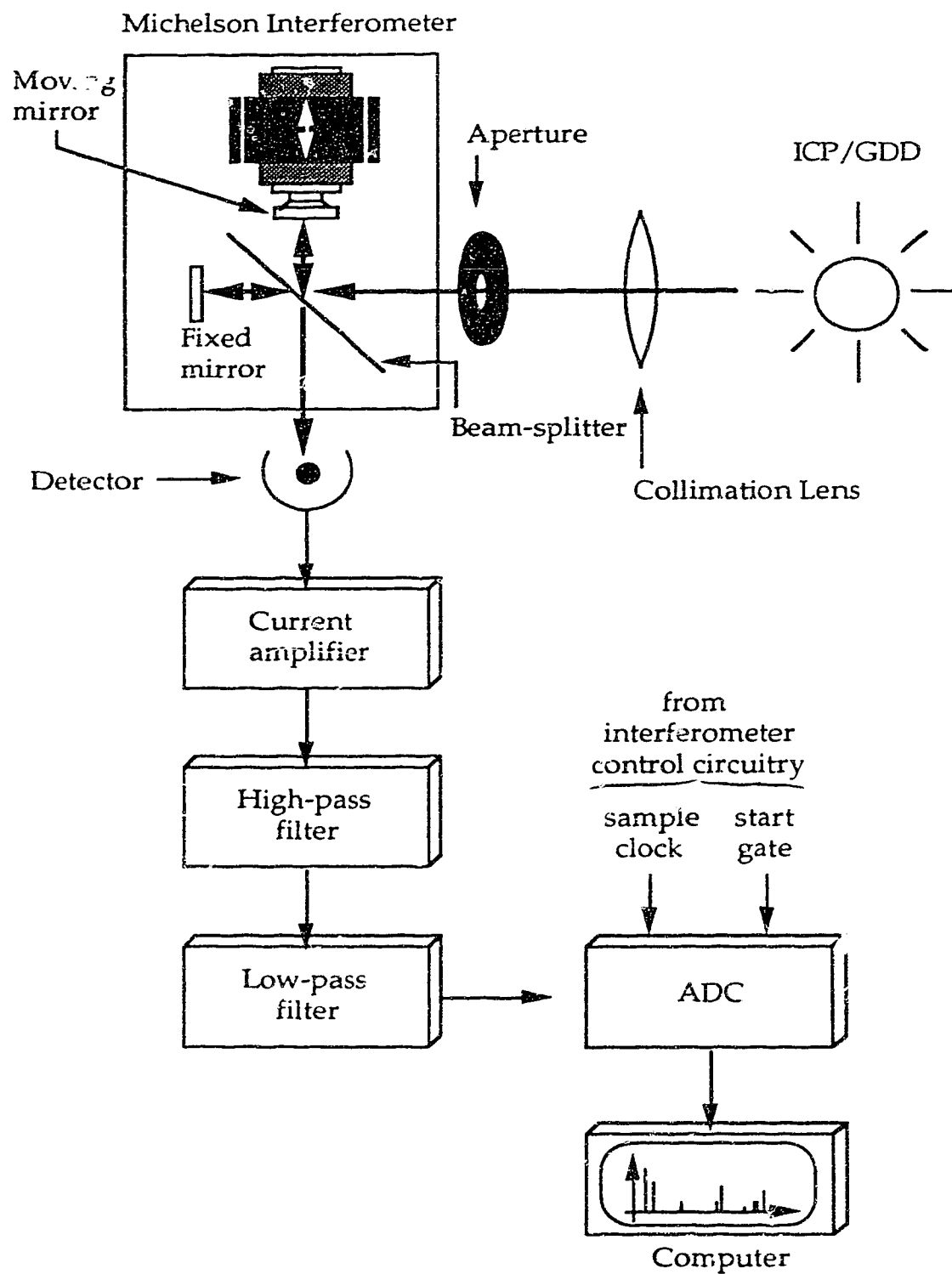
Fig. 8. Block diagram of the FTS measurement system.

be detected by the detector at this moment. If the moving mirror is at a position such that the optical path difference between the two arms of the interferometer is $\lambda/2$, the two reflected beams would undergo total destructive interference. None of the radiation from the plasma would reach the detector at this position. For any position of the moving mirror in between, varying degrees of interference are detected. This intensity oscillation is the so called "interferogram" of the source radiation. The amplitude and frequency of the detector output waveform are directly proportional to those of the electric field component of the incident radiation. Fourier transformation of the interferogram will give the spectrum of the source radiation. The interferogram obtained by nebulizing 1000 μg/ml B solution into the plasma and its resultant spectrum are given in Fig. 9. The "single line" when expanded is actually the boron doublet shown earlier in Figure 3.

Two detectors were used for this study. The ultraviolet measurements were made with a R166 solar-blind photomultiplier tube (PMT), while a 1P28 PMT was utilized for the visible spectral region measurements. Both PMT's were operated at 660 V. The interferogram measurement electronics consisted of a Keithley model 427 high speed current amplifier, a Krohn-Hite filter, which serves to remove high frequency noise and low frequency modulation components as well as leakage from the auxiliary channels into the analog sample interferogram signal.

The data acquisition portion of the control electronics generates a sample clock for the analog to digital convertor (ADC) and a start pulse at the
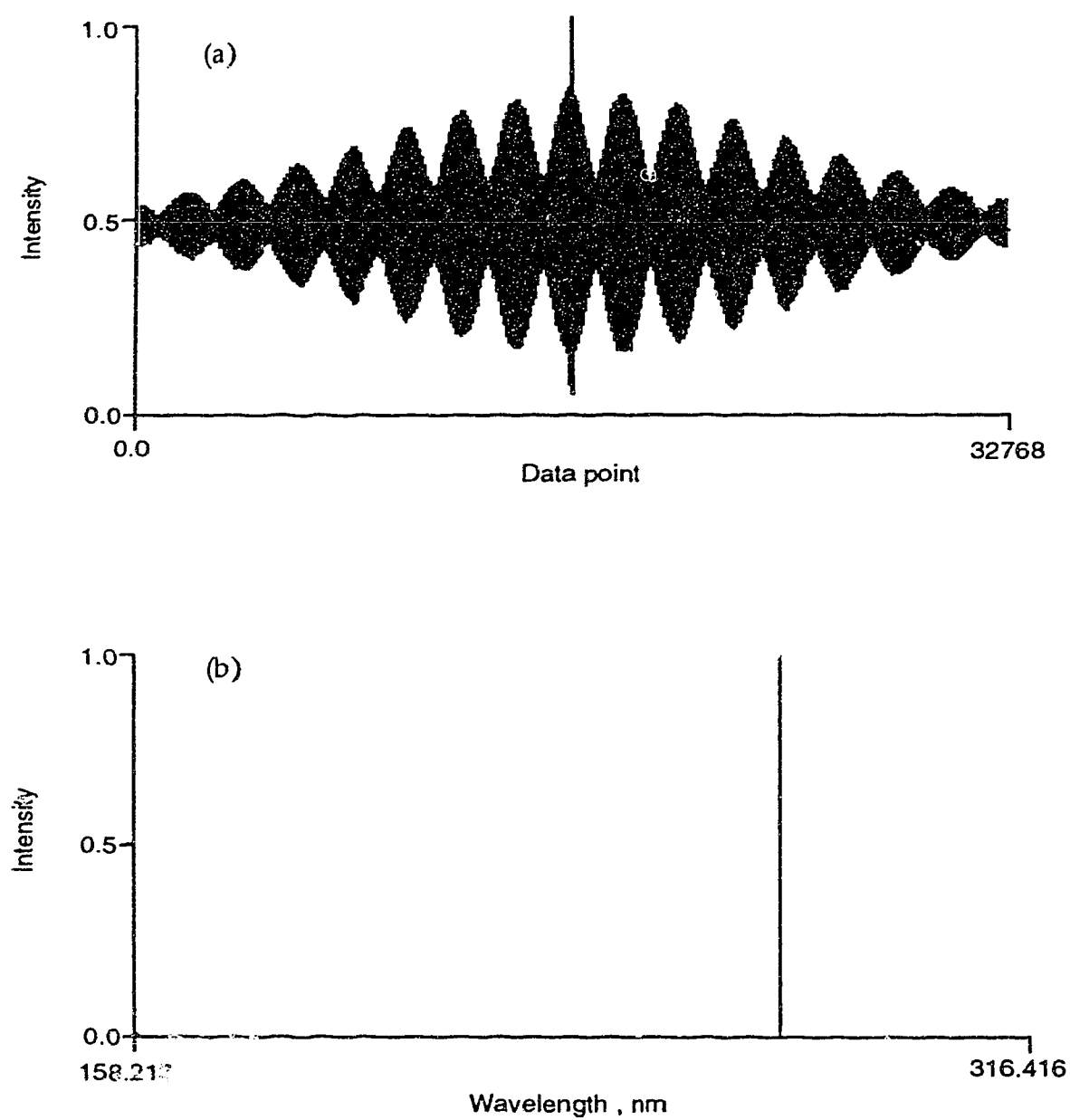
Fig. 9. Interferogram obtained from 1000 µg/ml boron (a), and the resultant spectrum (b).

beginning of each scan. This sample clock is derived from the interferogram of a He-Ne laser.

The current data system used with the FTS system is an Apple Macintosh II computer [162].

For each spectrum, 32 interferograms were co-added. All the spectra obtained in this chapter were calculated from 64 k interferograms sampled with a frequency 4 times of that of the clock derived from the He-Ne laser. The acquired interferograms were directly Fourier-transformed without any additional processing to yield the resultant spectra.

The measurement system was carefully aligned using a He-Ne laser so that the emission intensity from the middle of the central channel would be directed to the interferometer. The He-Ne laser was also used for observation height adjustments. Emission from different heights above the load coil was observed by raising or lowering the whole torch assembly.

3-2-4. Solution preparation

A single multi-element solution was used throughout this study for both UV and visible spectral regions. It was prepared from 1000 µg/ml commercial stock solutions. The elements used and their concentrations are listed in Table 7.

Table 7. Elements and concentrations used in acquiring their spectra

Element	Concentration (μg/ml)
Ca	25.0
Cd	100.0
Fe	500.0
Mg	12.5
Ti	50.0
Zn	250.0

3-3. Effect of forward power and types of torches on electron number density and temperature profiles

3-3-1. Argon ICP

As discussed in Chapter 2, electron number density can be calculated from the halfwidth of the H_β line. The H_β line profile was measured using the FTS system together with other lines used in the calculation of excitation temperatures, and ionization temperatures for all the thermometric species that have emission in the visible region. The purpose of this study is to investigate the relative change in electron number density as the observation height and forward power are varied along the middle of the central aerosol channel - the analytical reg. However, no Abel inversion was applied to the data obtained in this study.

The electron number density profiles were measured at 4 different positions above the load coil (5 mm, 10 mm, 15 mm, and 20 mm), and at 5 different forward powers (1.0 kW, 1.25 kW, 1.5 kW, 1.75 kW, and 2.0 kW) for a "normal" Fassel torch and a Fassel torch with an extended outer tube. The complete electron number density profiles are presented in Fig. 10. The profiles were obtained for a pure argon plasma, and the plasma running conditions were as listed in Table 6. Unfortunately, with 5% or more foreign gases introduced in the plasma, the H_β line became too weak to enable a good measurement of the halfwidth. As a result, no attempts were made to measure electron number density for mixed gas plasmas.

The values of the electron number density at various heights and forward powers range from 0.5 x 10^{15} to 6.0 x 10^{15} cm^{-3} and are in good agreement with those reported in the literature [42, 434, 48, 114].

It is not surprising to see that, with an increase in forward power, electron number density increases steadily at all the observation heights and for both the long and normal torches, since more energy is put into the plasma discharge, more electrons should be released from Ar atoms and analyte atoms present in the system. It is also interesting to notice that, with an increase in observation height, the electron number density value decreases. Choot [147] also observed an overall decrease in the magnitude of electron number density with increasing observation height, but also found that the value of the electron number density in the middle of the central aerosol channel (the region observed here) increased initially as the observation height was increased from 2 to 10 mm above the load coil, then it decreased gradually after 10 mm observation height. The difference can be explained by the fact that (a) Choot [147] Abel inverted his data, so the value of the electron number density is the "radial" electron number density, whereas, those in this study were not Abel inverted. (b) The entrance slit of the monochromator used by Choot [147] was set at 10 microns, whereas, the limiting aperture size (the circular aperture just in front of the detector) of the FTS system used in this study was 1 mm in diameter. That is to say, the observing zone in the plasma was 100 times bigger in diameter than in Choot's study. Thus only an "overall" trend of the electron number density profile is obtained here averaged over a larger zone of the plasma.
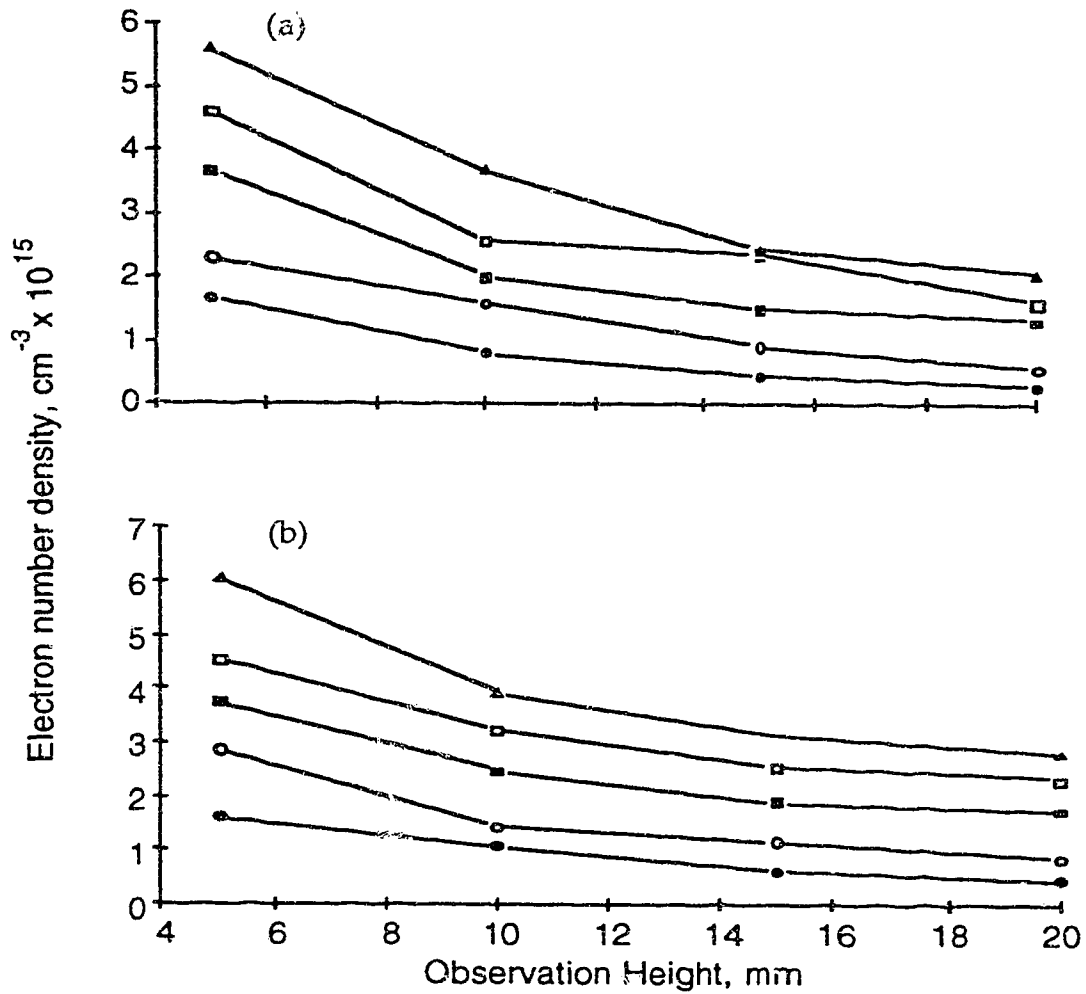
Fig. 10. Effect of forward power and observation height on electron number density in an argon plasma measured with a long torch (a) and a normal torch (b).

(▲) 2.00 kW   (□) 1.75 kW   (▣) 1.50 kW

(○) 1.25 kW   (●) 1.00 kW

Visually, the plasma discharge with a long torch had a bigger apparent volume compared to the plasma discharge with a normal torch. Logically it is assumed that the plasma discharge with a long torch should have lower value of electron number density, if the same amount of energy is put into the discharge (at the same power). By examining the electron number density profiles obtained with a long torch - Figure 10 (a) and the electron number density profiles obtained with a normal torch - Figure 10 (b), it can be seen that the magnitudes of all the electron number density profiles with a normal torch are slightly higher than those corresponding profiles obtained with a long torch at the same power. It also seems that at lower forward powers, the difference gradually diminishes.

The excitation temperature profiles were measured at 4 different positions above the load coil (5 mm, 10 mm, 15 mm, and 20 mm for Fe II and Fe I; for Ti II 10 mm, 15 mm, and 20 mm), and at 5 different forward powers (1.0 kW, 1.25 kW, 1.5 kW, 1.75 kW, and 2.0 kW) for a pure argon ICP discharge with a long torch as well as with a normal torch. The excitation temperature profiles derived from the emission intensities of 8 Fe II lines, 6 Fe I lines, and 11 Ti II lines are presented in Fig. 11, Fig. 12, and Fig. 13, respectively. As discussed in Chapter 2, these excitation temperature calculations were based on the "Boltzmann plot" method. The details of these calculations will not be repeated here.

All these data show a steady increase in excitation temperature with increasing forward power for all the three thermometric species, at any observation height, for both the normal torch and the long torch.

The next interesting thing to notice is that the excitation temperature profiles obtained with a normal torch peak at about 10 mm above the load coil (excitation temperature profiles calculated from 8 Fe II line are the exception, they peak at about 5 mm above the load coil), whereas, the excitation temperature profiles obtained with a long torch peak at about 15 mm above the load coil (excitation temperature profiles calculated from 8 Fe II lines are the exception, they peak at about 10 mm above the load coil). This trend, that excitation temperature profiles obtained with a long torch peak about 5 mm higher above the load coil than those obtained with a normal torch, can be explained by the observation of the physical appearance of the plasma discharges obtained with these two kinds of torches. The plasma discharge obtained with a long torch does have a much longer plasma than that obtained with a normal torch. It is reasonable to suggest that the longer plasma results in the "hottest spot" being pushed up by 5 mm or so.

In terms of maximum temperature obtainable, the data in Figures 11-13 show different behaviors when the excitation temperature profiles measured using a long torch are compared with those measured using a normal torch. In Figure 11 (except at 1.0 kW), the maximum excitation temperatures of Fe II obtainable measured when a long torch is used are higher than the corresponding temperatures measured when a normal torch is used. This is contradictory to the observation that the plasma discharge with a long torch has a larger apparent volume. In Figure 12, the maximum excitation temperature of Fe I at 1.75 kW and 2.0 kW measured with a long torch agree well with those measured with a normal torch. But the maximum excitation temperatures at 1.0 kW, 1.25 kW and 1.5 kW measured with a long torch are higher than the corresponding temperatures measured with a normal torch.
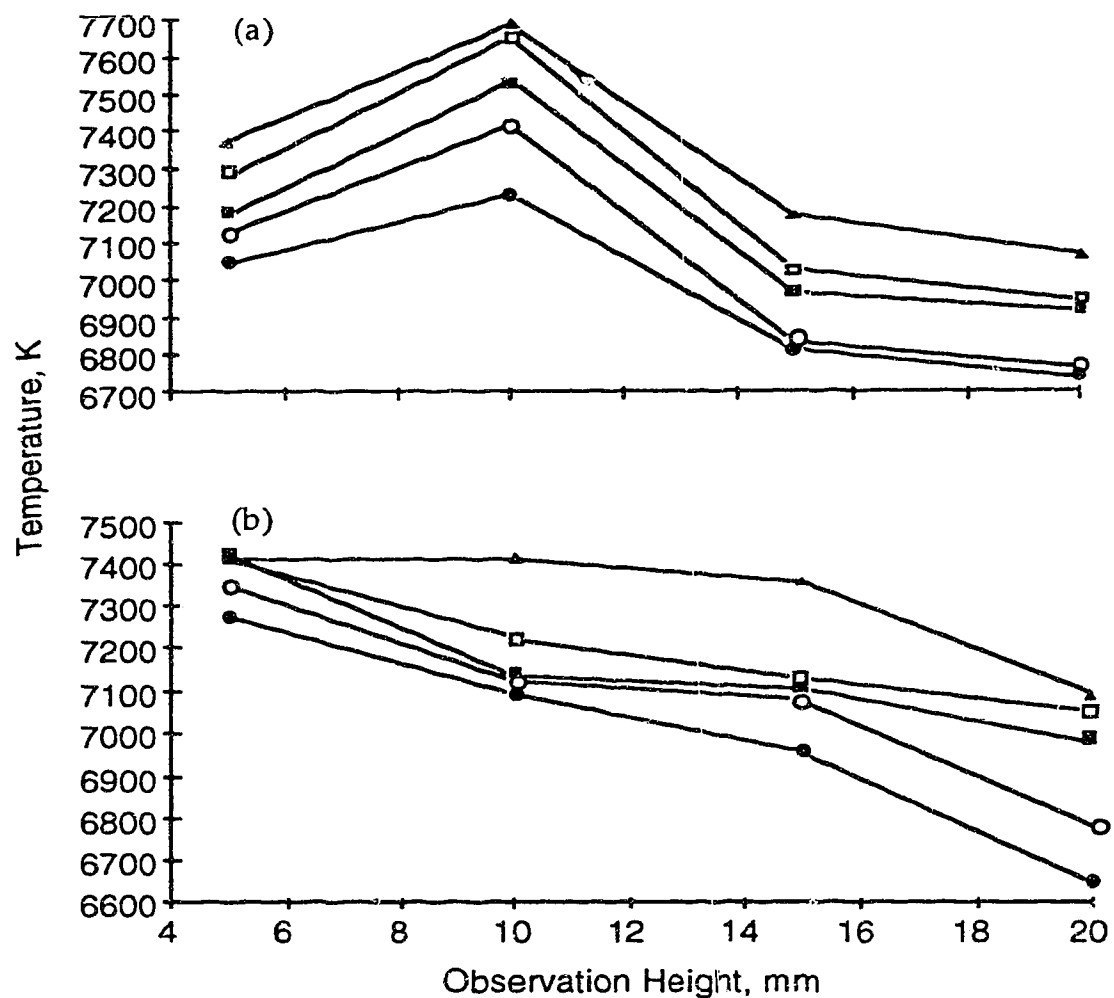
Fig. 11. Effect of forward power and observation height on excitation temperatures derived from 8 Fe II lines in an argon plasma with a long torch (a) and a normal torch (b).

(▲) 2.00 kW   (□) 1.75 kW   (■) 1.50 kW
(o) 1.25 kW   (●) 1.00 kW
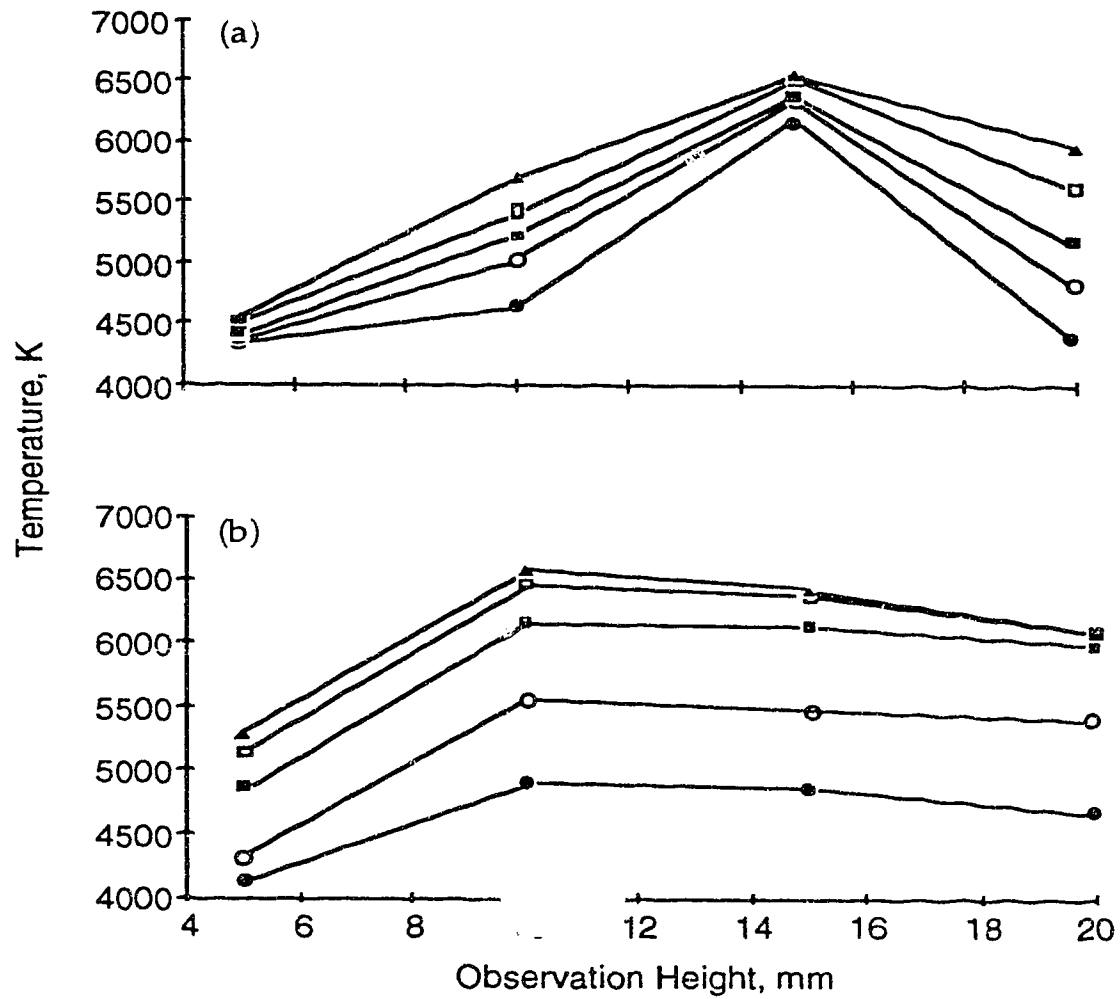
Fig. 12. Effect of forward power and observation height on excitation
temperatures derived from 6 Fe I lines in an argon plasma
with a long torch (a) and a normal torch (b).

(▲) 2.00 kW   (□) 1.75 kW   (■) 1.50 kW
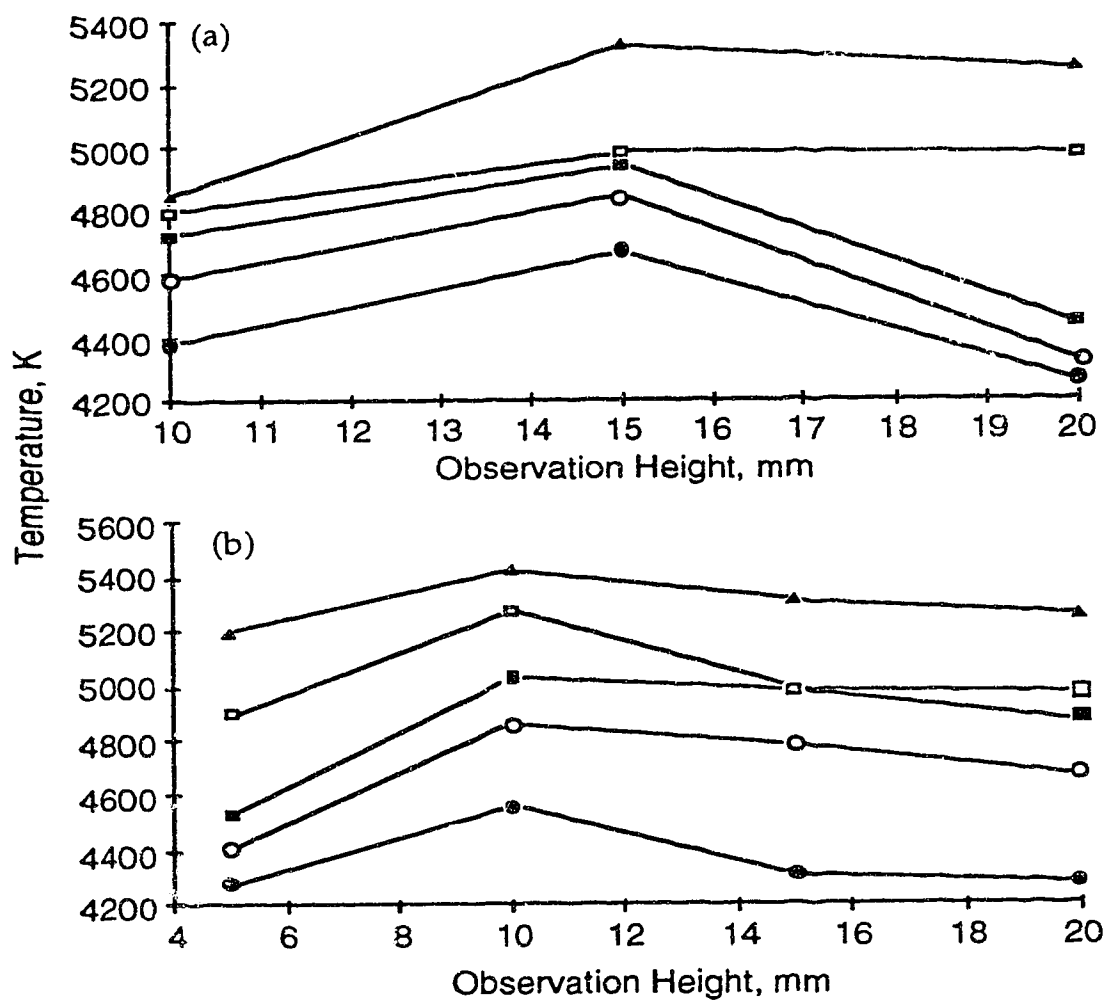
(o) 1.25 kW   (●) 1.00 kW

Fig. 13. Effect of forward power and observation height on excitation temperatures derived from 11 Ti II lines in an argon plasma with a long torch (a) and a normal torch (b).

(▲) 2.00 kW   (□) 1.75 kW   (■) 1.50 kW

(o) 1.25 kW   (●) 1.00 kW

In Figure 13, the maximum excitation temperatures of Ti II at 1.25 kW, 1.50 kW, 1.75 kW, and 2.0 kW measured using a normal torch are higher than the corresponding temperatures measured using a long torch. However, the opposite is observed at 1.0 kW for Ti II, i.e., the maximum excitation temperature with a long torch is a little bit higher than that measured with the normal torch.

It is also interesting to look at the temperature values for those data points at 5 mm (10 mm in Fig. 13.a) above the load coil. The temperature values measured using a normal torch at 5 mm above the load coil change faster with increasing forward power than those measured with a long torch at 5 mm (10 mm in Fig. 13.a) above the load coil. Excitation temperatures calculated from 8 Fe II lines are, once again, exceptions.

Comparing the three thermometric species, the excitation temperatures measured with Fe II are higher than that measured with Fe I, and the excitation temperatures measured with Ti II give the lowest values.

The ionization temperature profiles were also measured at four different positions above the load coil (5 mm, 10 mm, 15 mm, and 20 mm) and at five different forward powers (1.0 kW, 1.25 kW, 1.5 kW, 1.75 kW, and 2.0 kW) for a pure argon plasma discharge using 5 thermometric species with a long torch as well as a normal torch. The calculations of the ionization temperatures of these 5 thermometric species are based on the ionic line to neutral atom line intensity ratio method, as discussed in Chapter 2. The complete ionization temperature profiles for Ca, Cd, Fe, Mg, and Zn are presented in Figures 14-18.
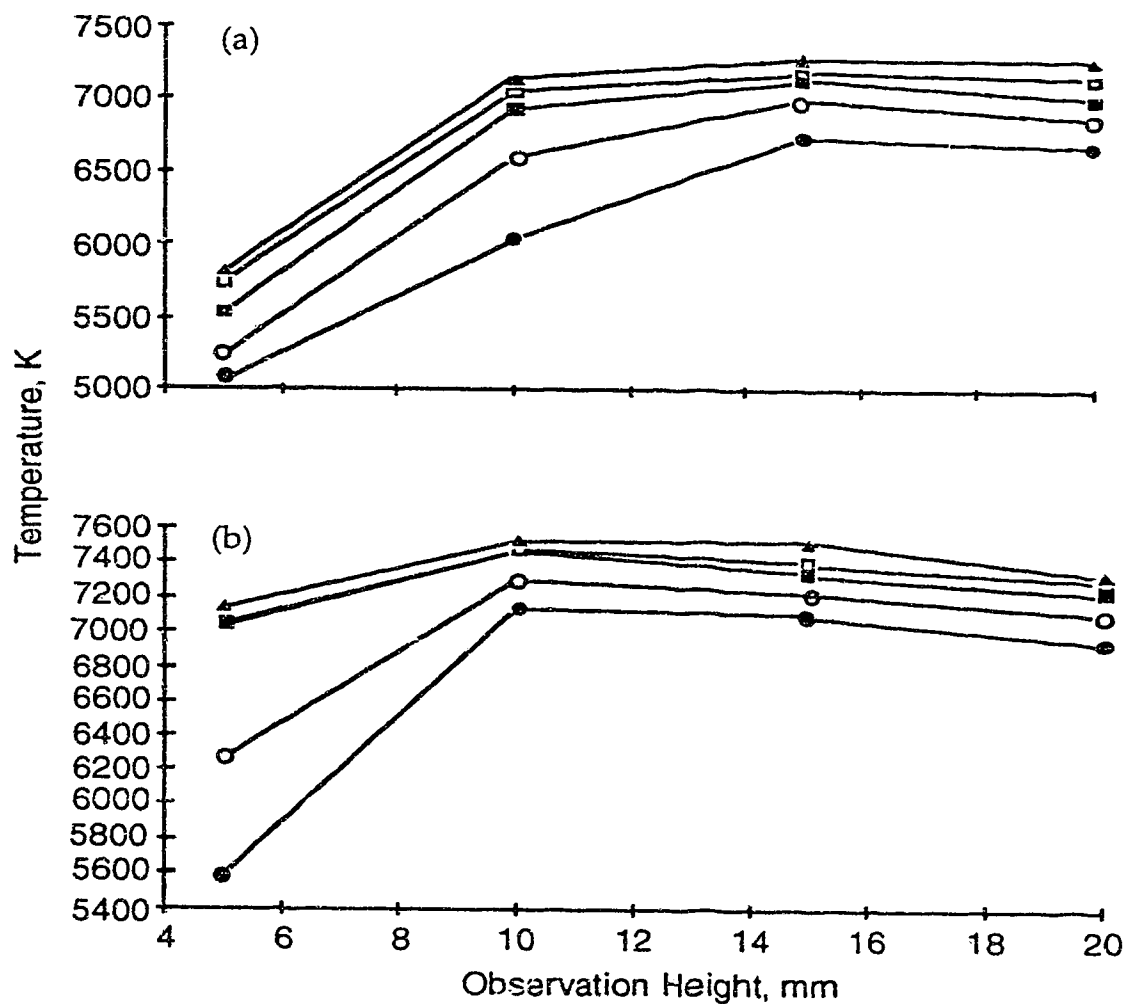
Fig. 14. Effect of forward power and observation height on ionization temperatures of calcium derived from the ratio of Ca II 396.847 to Ca I 422.673 in an argon plasma with a long torch (a) and a normal torch (b).

(▲) 2.00 kW (□) 1.75 kW (■) 1.50 kW
(o) 1.25 kW (●) 1.00 kW
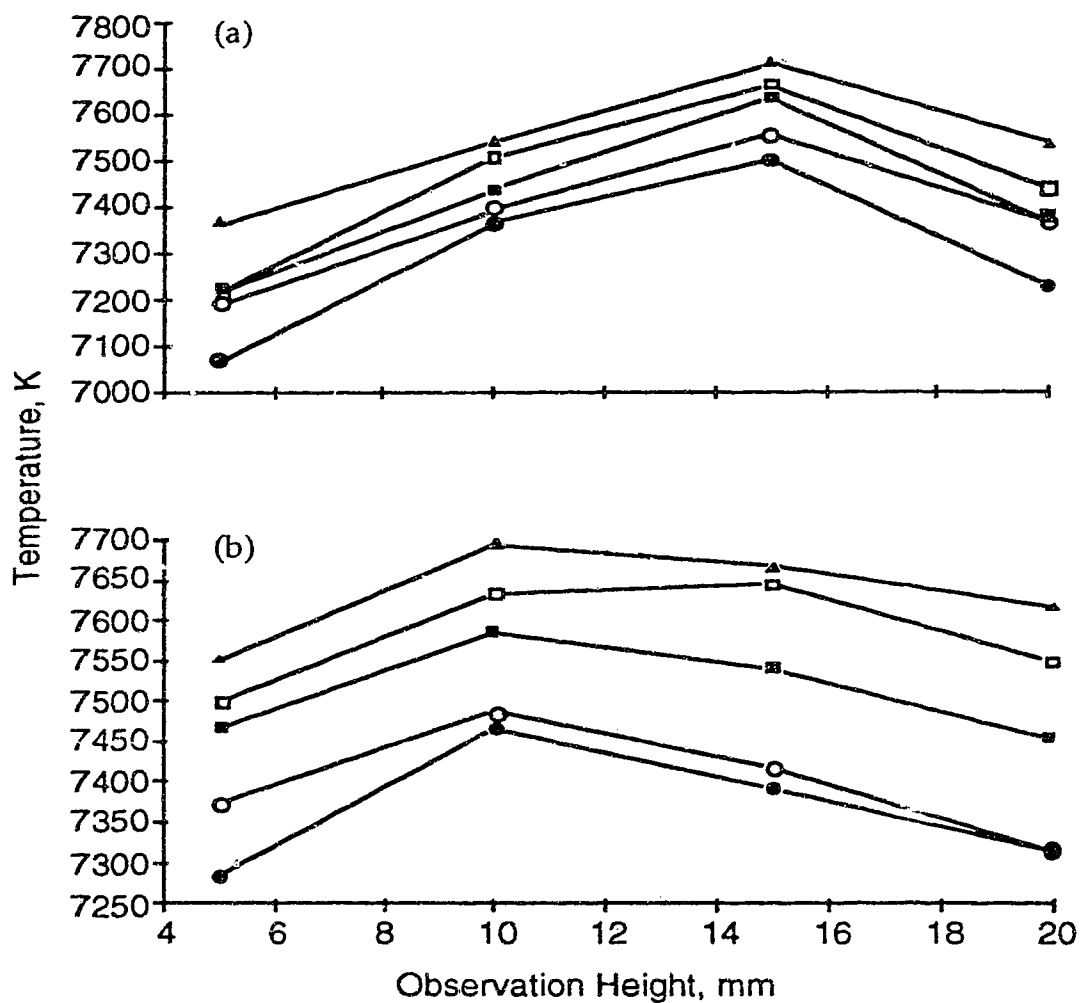
Fig. 15. Effect of forward power and observation height on ionization temperatures of cadmium derived from the ratio of Cd II 226.502 to Cd I 228.802 in an argon plasma with a long torch (a) and a normal torch (b).

(▲) 2.00 kW   (□) 1.75 kW   (■) 1.50 kW
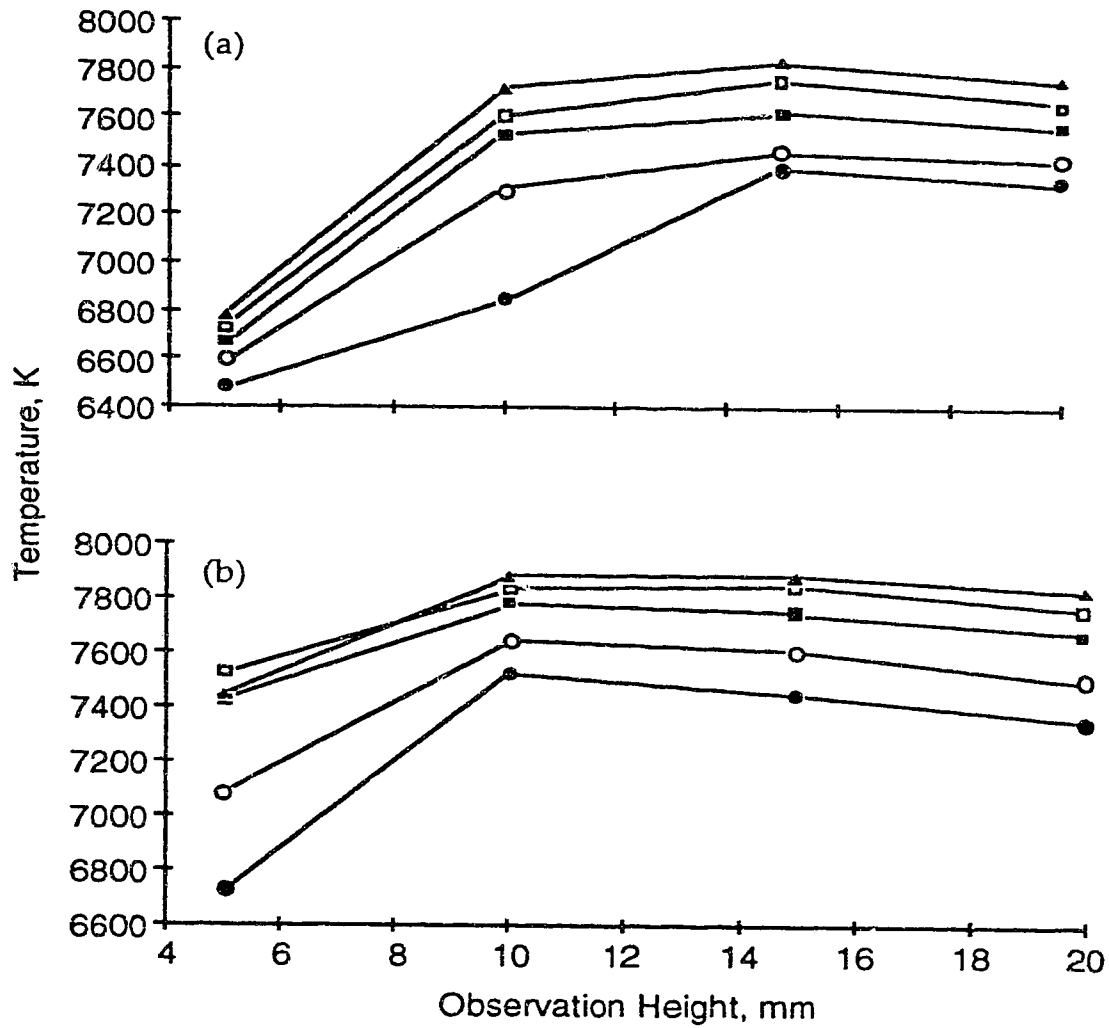
(o) 1.25 kW   (●) 1.00 kW

Fig. 16. Effect of forward power and observation height on ionization temperatures of iron derived from the ratio of Fe II 228.588 to Fe I 252.285 in an argon plasma with a long torch (a) and a normal torch (b).

(▲) 2.00 kW (□) 1.75 kW (■) 1.50 kW
(o) 1.25 kW (●) 1.00 kW
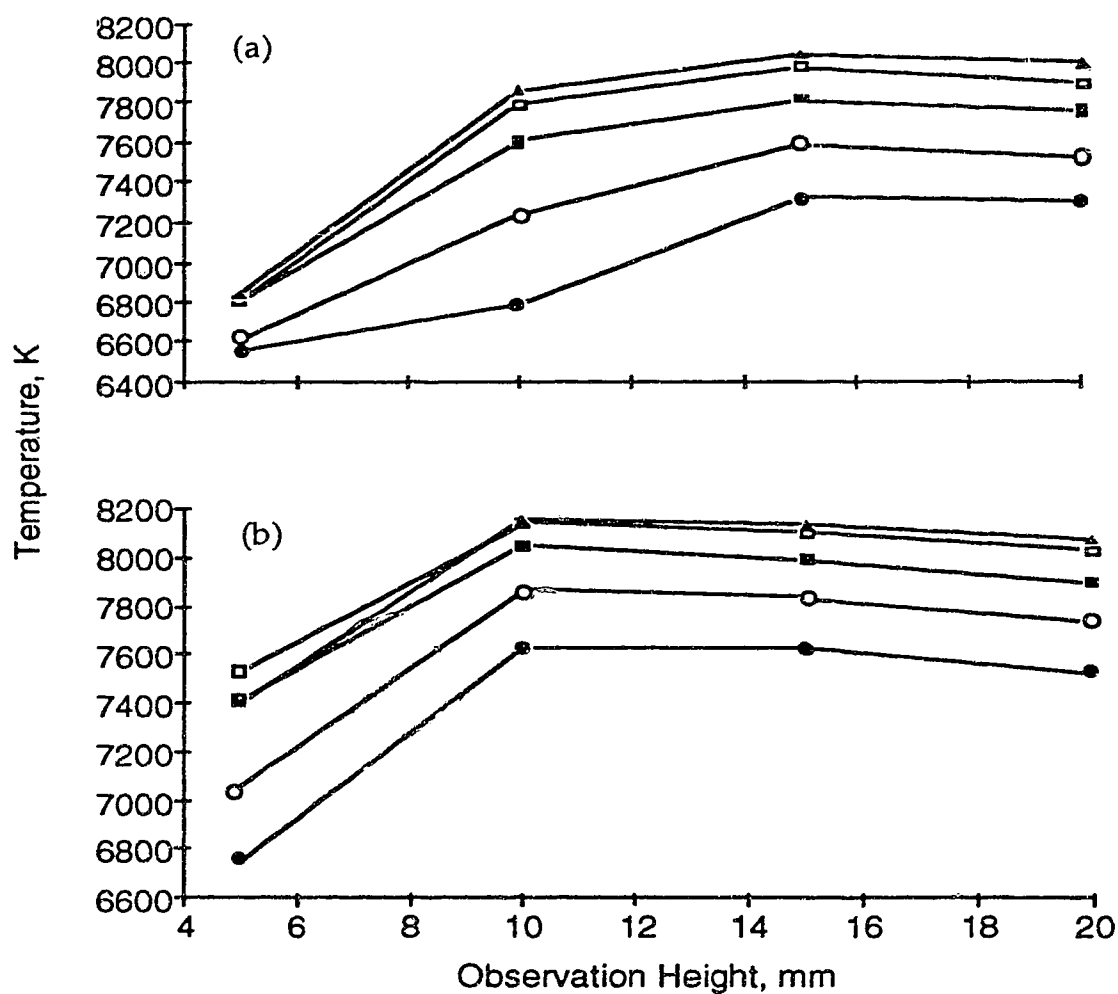
Fig. 17. Effect of forward power and observation height on ionization temperatures of magnesium derived from the ratio of Mg II 279.553 to Mg I 285.213 in an argon plasma with a long torch (a) and a normal torch (b).

(▲) 2.00 kW   (◻) 1.75 kW   (■) 1.50 kW
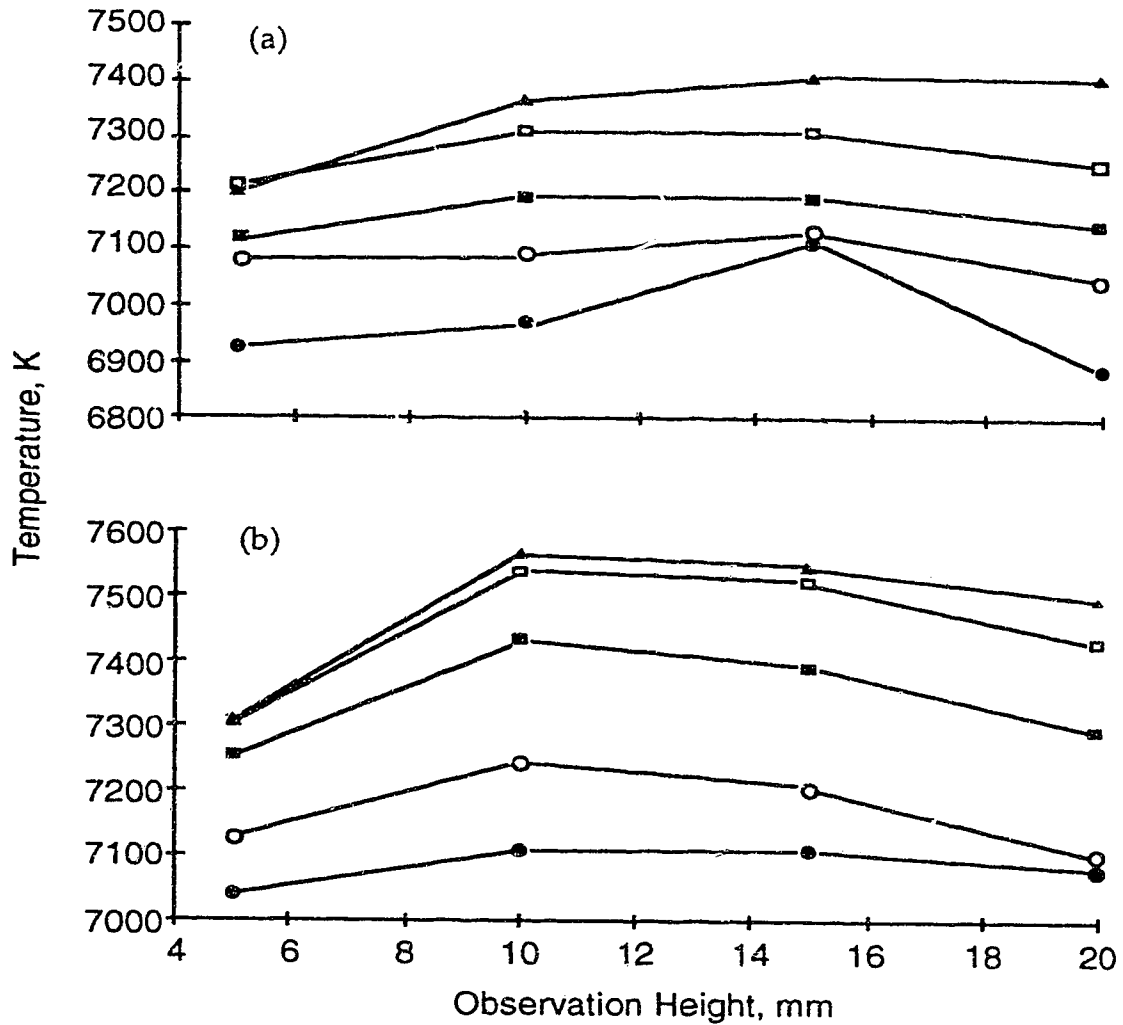
(o) 1.25 kW   (●) 1.00 kW

Fig. 18. Effect of forward power and observation height on ionization
temperatures of zinc derived from the ratio of Zn II
206.191 to Zn I 213.856 in an argon plasma with a long torch
(a) and a normal torch (b).

(▲) 2.00 kW   (□) 1.75 kW   (■) 1.50 kW
(o) 1.25 kW   (●) 1.00 kW

For all the thermometric species, their ionization temperatures increase with increasing forward power under all operating conditions.

All the ionization temperature profiles obtained with a long torch peak at 15 mm above the load coil, whereas, those measured with a normal torch peak at 10 mm above the load coil. Similar behavior was observed when excitation temperatures were measured under the same operating conditions (Fig. 11, Fig. 12, and Fig. 13), although, excitation and ionization temperature calculations are based upon two totally different methods.

In terms of maximum temperatures, the ionization temperatures measured with Ca (Fig. 14), Fe (Fig. 16), Mg (Fig. 17), and Zn (Fig. 18) using a normal torch are higher than those corresponding temperatures measured using a long torch. This observation supports the reasoning that the plasma discharge with a long torch has a bigger apparent volume, and the same amount of energy is distributed over a larger space. The ionization temperatures measured with Cd, however, show the opposite trend.

Also similar to what was observed when excitation temperatures were measured, at 5 mm above the load coil (the left side of the temperature profiles), the ionization temperatures measured with a normal torch show a more dramatic change with forward power than those measured with a long torch. Once again, the ionization temperatures measured with Cd give the only exception. Further diagnostic studies are needed to interpret the results observed.

Comparing the 5 thermometric species, the peak ionization temperature measured with Mg has the highest value. The order for the

ionization temperatures measured with the rest of the 4 thermometric species is: Fe > Cd > Zn > Ca. In general, the ionization temperatures measured with these 5 thermometric species are in very good agreement with each other under the same experimental conditions.

3-3-2. Ar ICP with 5% nitrogen in the coolant

The excitation and ionization temperature profiles for the 8 thermometric species used in last section were measured in an argon plasma discharge with 5% nitrogen introduced into the coolant stream using both a normal torch and a long torch. The plasma running conditions were as listed in Table 6. It should be noticed that the auxiliary gas flow rate was increased from 0.9 l/min to 1.1 l/min (as also done later when systematic studies were carried out on mixed-gas plasma discharges with 5% or more nonargon gases in the coolant stream and/or other flows) in order to lift the plasma slightly and prevent the tubes (particularly the central aerosol tube) from melting. Because the effect of forward power on excitation and ionization temperatures seemed to be straight forward from early observations, the forward power in this study was fixed at 1.5 kW. The excitation temperature profiles of Fe II, Fe I, and Ti II in an argon ICP with 5% nitrogen in the coolant are presented in Fig. 19, Fig. 20, and Fig. 21, respectively. The ionization temperature profiles for Ca, Cd, Fe, Mg, and Zn under the same operating conditions are shown in Fig. 22. For all the three thermometric species, the excitation temperature profiles obtained using a long torch (Fig. 19.a, Fig. 20.a, and Fig. 21.a) peak at about 8 mm above the load coil, whereas, those obtained using a normal torch (Fig. 19.b, Fig. 20.b, and Fig. 21.b) peak at about 4 mm
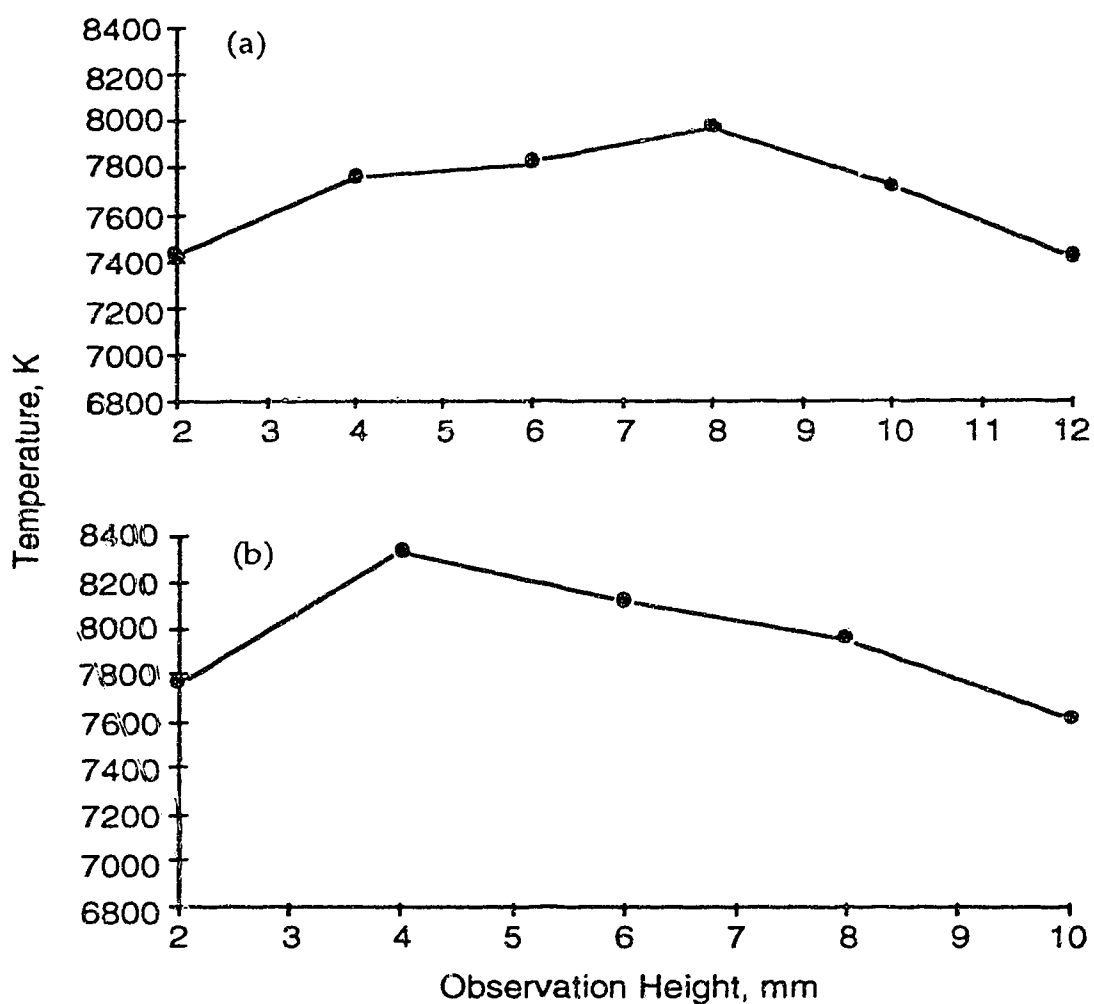
Fig. 19. The excitation temperature profiles of iron derived from 8 Fe II
lines in an argon ICP with 5% nitrogen in the coolant gas at
1.5 kW using a long torch (a) and a normal torch (b).
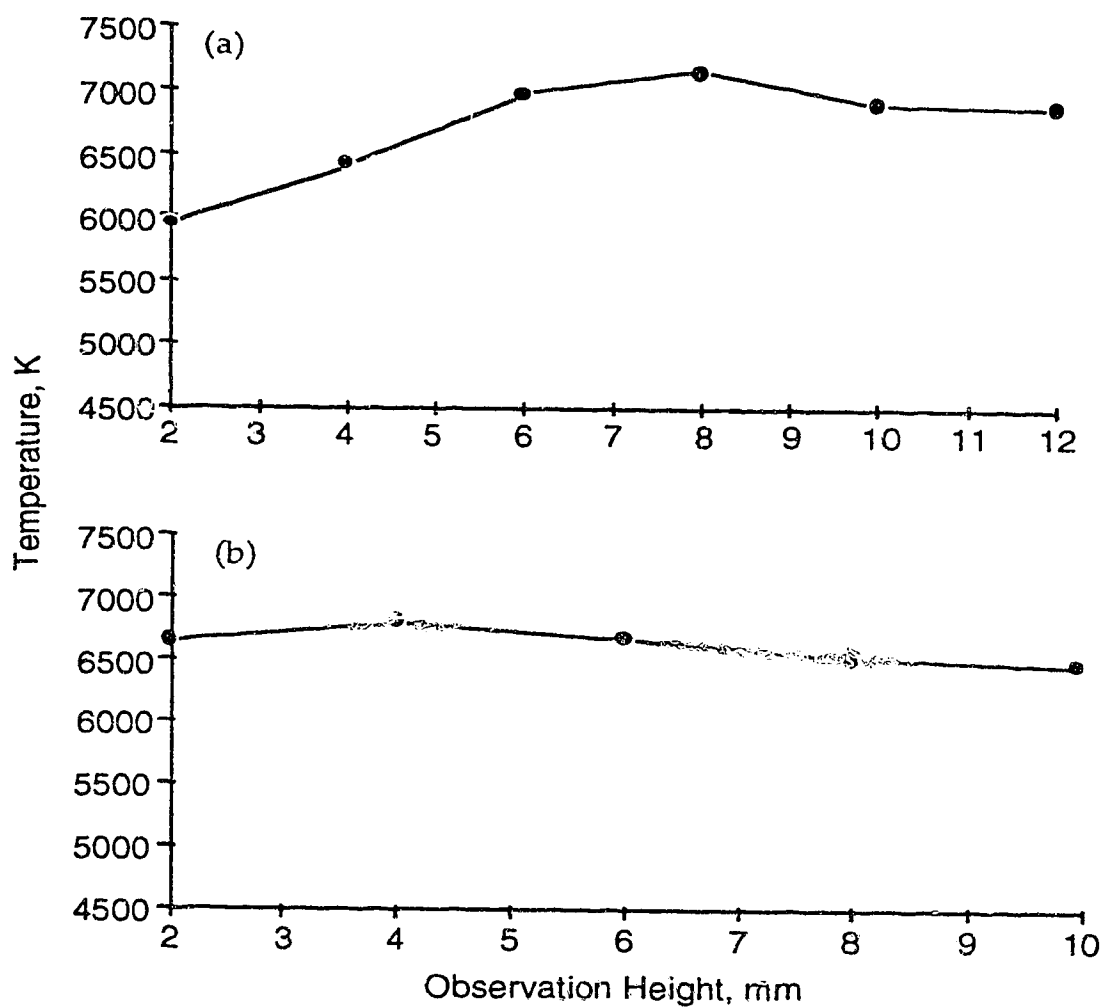
Fig. 20. The excitation temperature profiles of iron derived from 6 Fe I lines in an argon ICP with 5% nitrogen in the coolant gas at 1.5 kW using a long torch (a) and a normal torch (b).
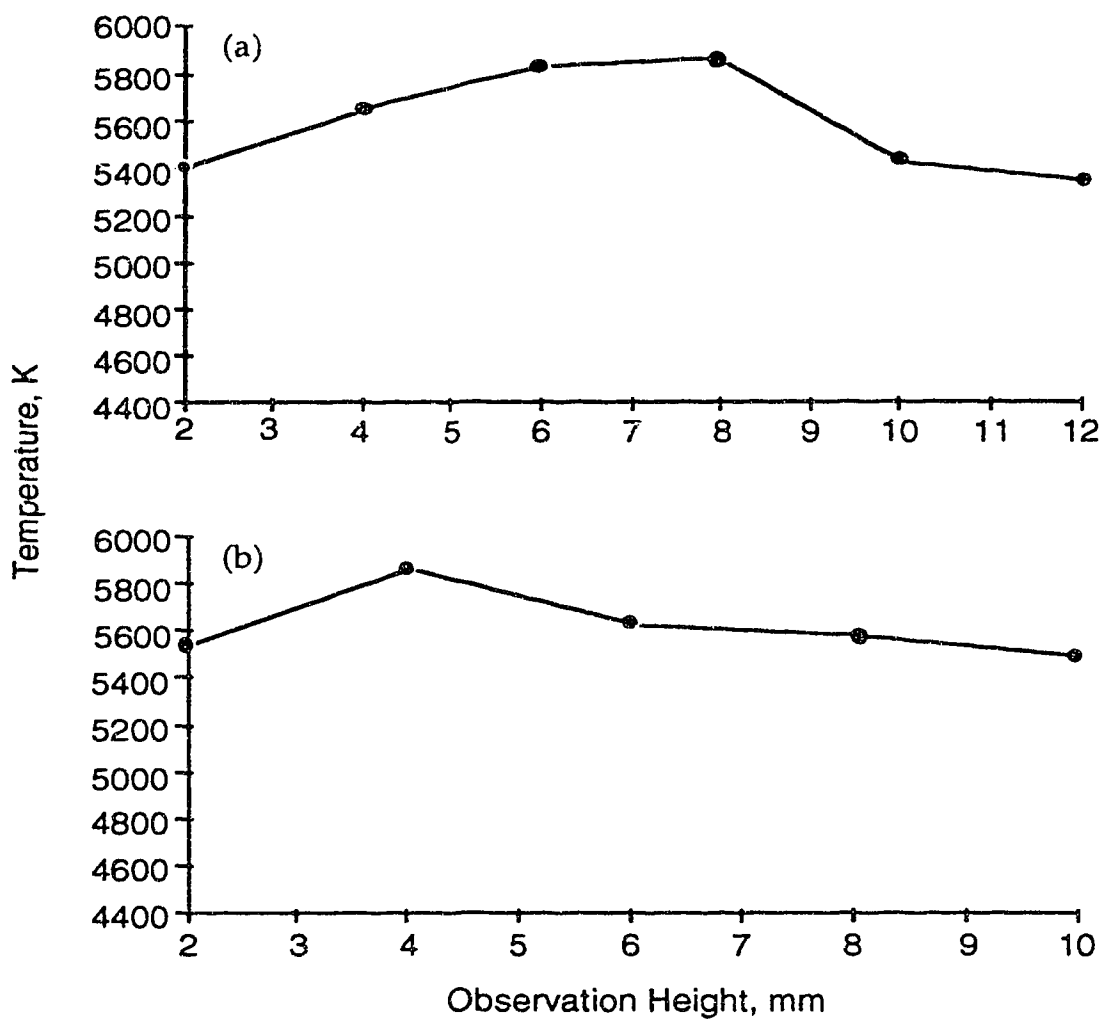
Fig. 21. The excitation temperature profiles of titanium derived from 11
Ti II lines in an argon ICP with 5% nitrogen in the coolant
gas at 1.5 kW using a long torch (a) and a normal torch (b).
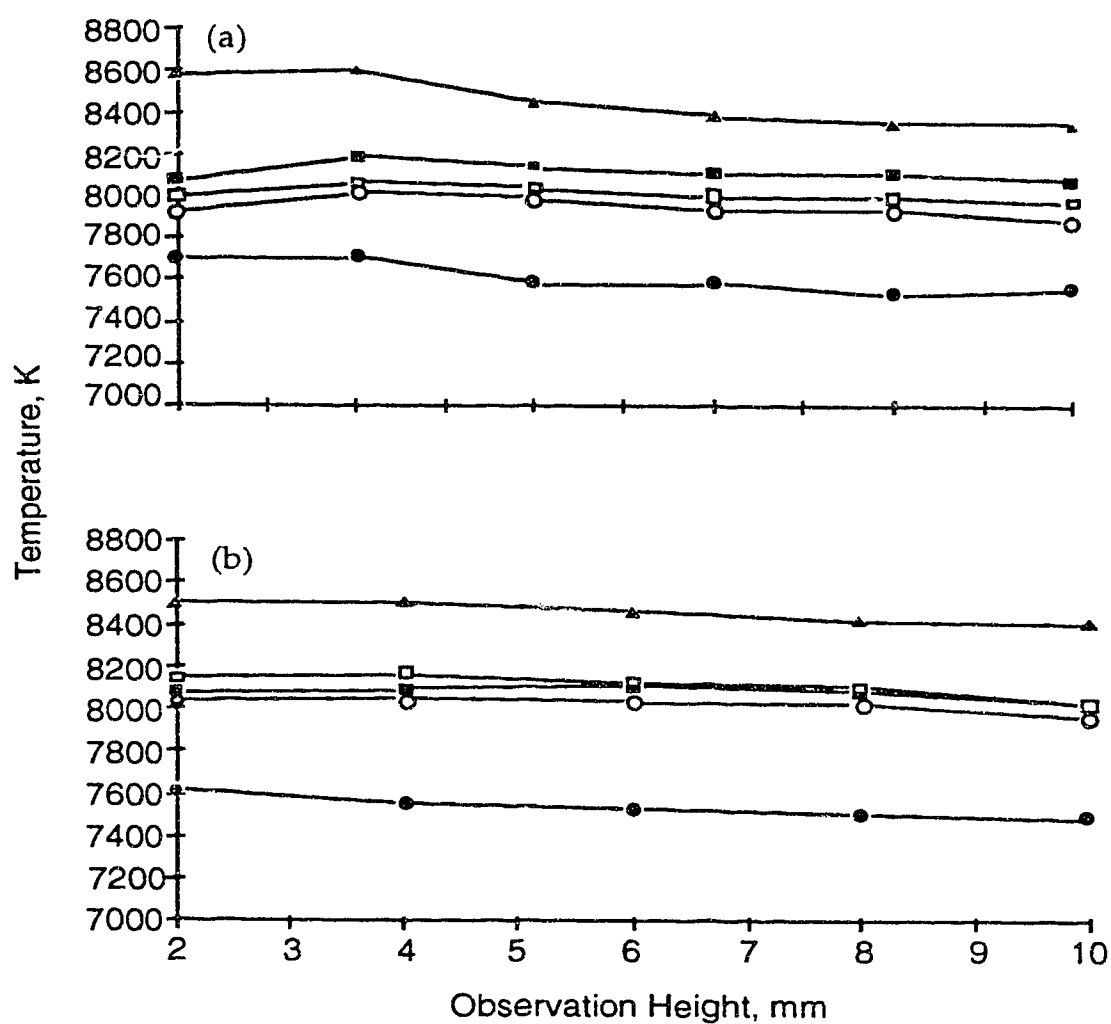
Fig. 22. The ionization temperature profiles of 5 thermometric species in an argon ICP with 5% nitrogen in the coolant gas at 1.5 kW, using a long torch (a) and a normal torch (b).

(▲) Mg   (□) Cd   (■) Fe

(○) Zn   (●) Ca

above the load coil. This is similar to what was observed using a long torch and a normal torch in a pure argon plasma discharge except that the temperature maxima are lower by about 6 mm for this 5% nitrogen cooled plasma.

As shown in Fig. 19, the excitation temperatures of Fe II measured with a normal torch are higher by about 400 K compared to those measured with a long torch. In Fig. 20, the excitation temperatures of Fe I measured with a normal torch seem to be higher only when the observation height is below 6 mm. Above 6 mm , the temperatures measured with a long torch appear to be higher. In Fig. 21, the overall magnitudes of the excitation temperature profiles obtained with a normal torch are also a little bit higher than those for the long torch.

Comparing the three thermometric species, the order for the excitation temperature is: Fe II > Fe I > Ti II.

The ionization temperature profiles obtained with a long torch (Fig. 22.a) are similar to those obtained with a normal torch (Fig. 22.b) for all the 5 thermometric species. For both torches, ionization temperatures change very little with increasing observation height, although almost all the curves just barely show maxima at about 4 mm above the load coil. The values of the ionization temperatures measured using a long torch are in good agreement with the corresponding temperature values measured using a normal torch. For Fe, Cd, and Zn, their ionization temperatures, which range from 8000 to 8200 K, are always in close agreement with each other. As in a pure argon plasma discharge, Mg gives the highest ionization temperature values and Ca, the lowest values.

The temperature increases relative to a pure argon ICP due to the introduction of 5% nitrogen in the coolant will be discussed later when 5% or more nitrogen and other nonargon gases are introduced into the coolant.

3-4. Effect of observation height on temperatures

The excitation and ionization temperature profiles for all the 8 thermometric species were measured at 5 different positions above the load coil (2 mm, 4 mm, 6 mm, 8 mm, and 10 mm), at a constant forward power of 1.5 kW, when 5%, 10%, 20%, 50%, and 100% nonargon gases were introduced into the coolant. From now on throughout the rest of the chapter, all the measurements were carried out using a normal torch. The temperature profiles of argon-air, argon-helium, argon-nitrogen, and argon-oxygen ICP discharges are shown in Fig. 23, Fig. 24, Fig. 25, and Fig. 26, respectively.

3-4-1. Argon-air mixed-gas plasmas

In Fig. 23, it is interesting to observe the excitation and ionization temperature changes with observation height when 5%, 10%, 20%, 50%, and 100% air were introduced into the coolant. Although almost all the temperatures start dropping right from 2 mm above the load coil, the excitation temperatures derived from 6 Fe I lines (Fig. 23.a), 8 Fe II lines (Fig. 23.b), 11 Ti II lines (Fig. 23.c), and the ionization temperatures of Cd (Fig. 23.e), Fe (Fig. 23.f), Mg (Fig. 23.g), and Zn (Fig. 23.h) change very slightly with increasing observation height when only 5%, 10%, and 20% air were introduced into the coolant. When 50% of the argon in the coolant was replaced by air, only the ionization temperature of Ca (Fig. 23.d) still does
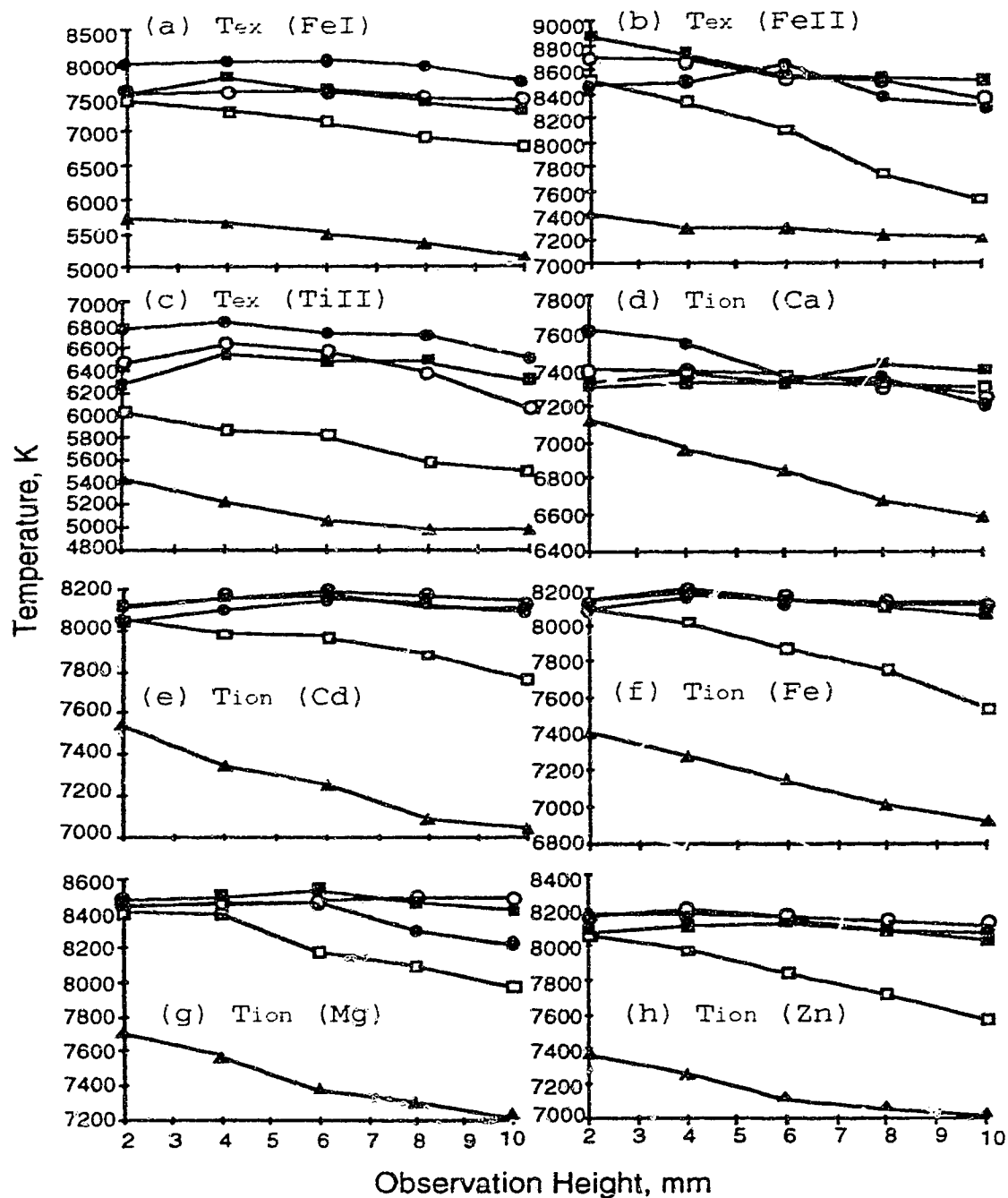
Fig. 23. Effect of observation height on temperatures of 8 thermometric
species in argon-air ICP's running at 1.5 kW with varying
amount of air in the coolant stream.

(●) 5% air   (o) 10% air   (■) 20% air
(□) 50% air (▲) 100% air
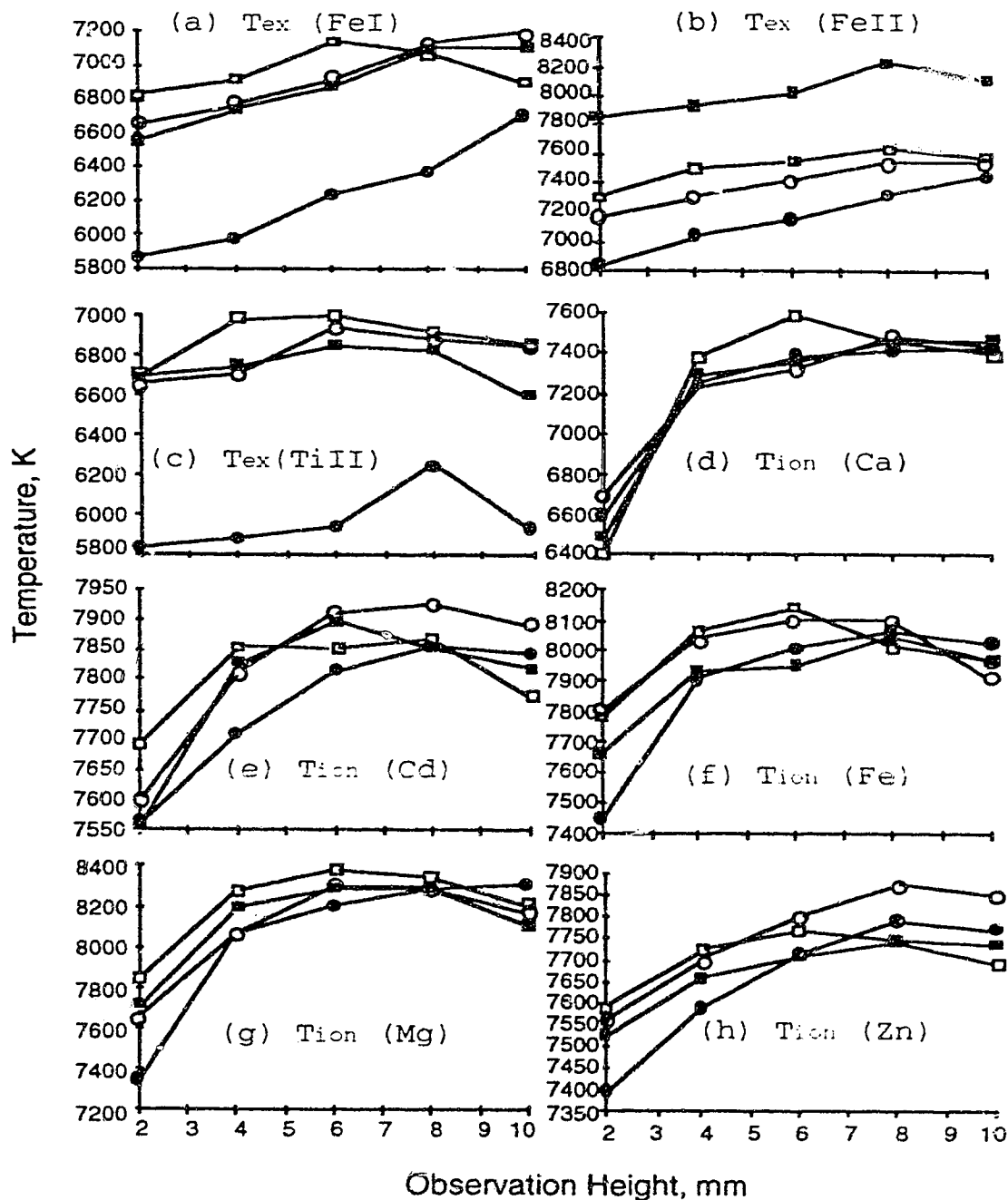
Fig. 24. Effect of observation height on temperatures of 8 thermometric species in argon-helium ICP's running at 1.5 kW with varying amount of helium in the coolant stream.

(●) 5% He (o) 10% He (■) 20% He
(□) 50% He
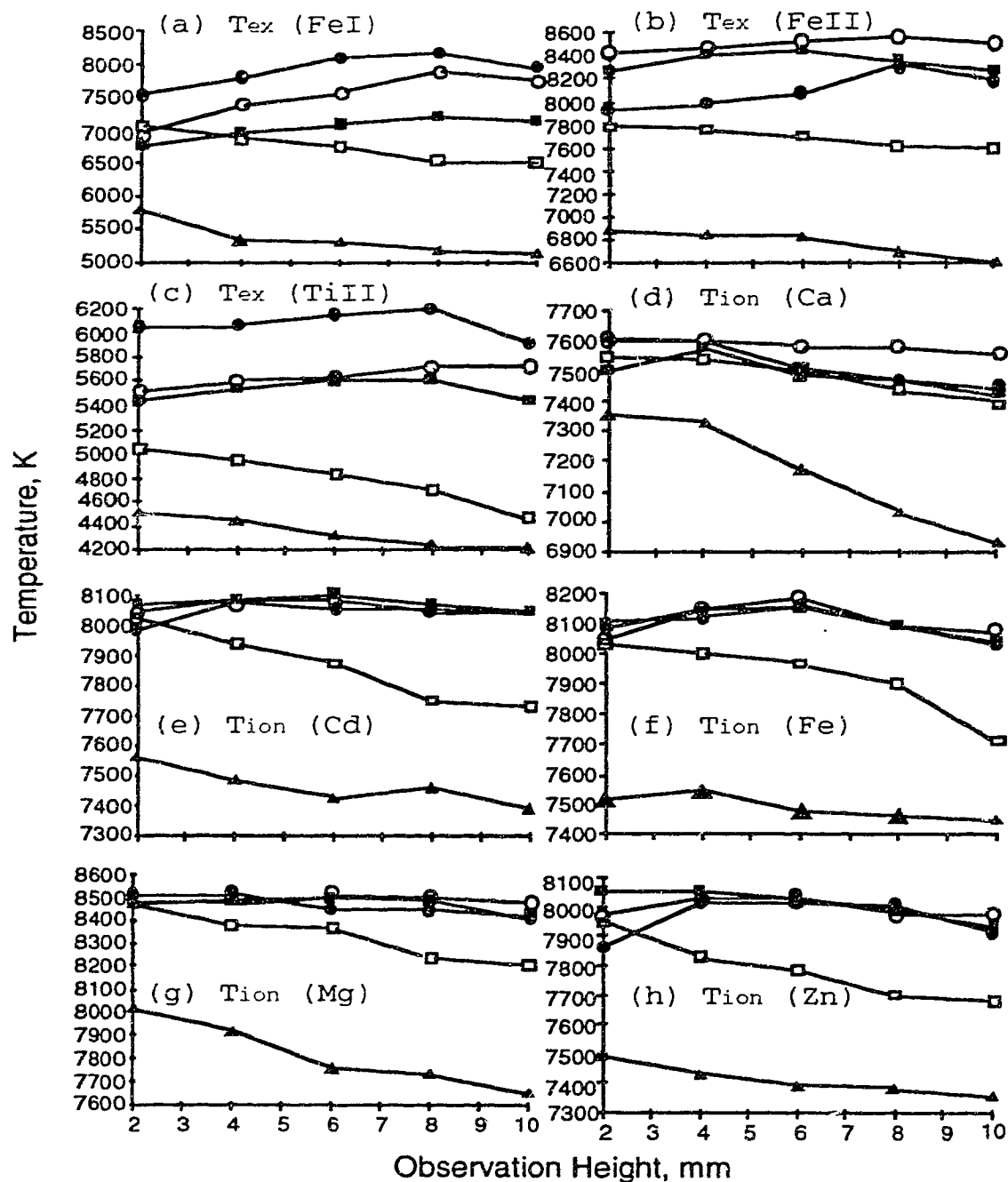
Fig. 25. Effect of observation height on temperatures of 8 thermometric
species in argon-nitrogen ICP's running at 1.5 kW with
varying amount of nitrogen in the coolant stream.

(●) 5% nitrogen (o) 10% nitrogen (■) 20% nitrogen
(□) 50% nitrogen (▲) 100% nitrogen

(a) Tex (FeI)

(b) Tex (FeII)

(c) Tex (TiII)

(d) Tion (Ca)

(e) Tion (Cd)

(f) Tion (Fe)

(g) Tion (Mg)

(h) Tion (Zn)

Temperature, K

Observation Height, mm
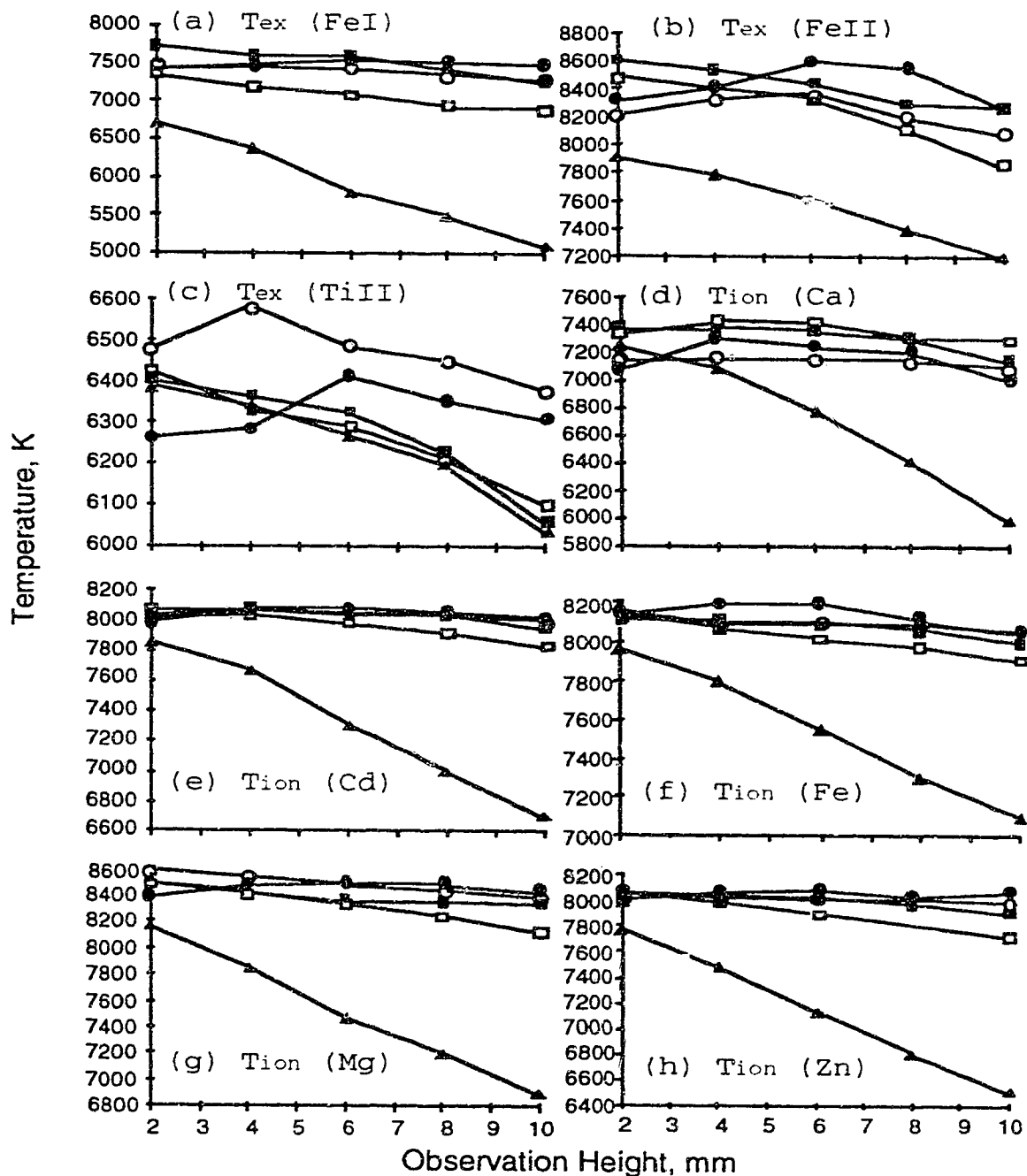
Fig. 26. Effect of observation height on temperatures of 8 thermometric species in argon-oxygen ICP's running at 1.5 kW with varying amount of oxygen in the coolant stream.

(●) 5% oxygen (○) 10% oxygen (■) 20% oxygen
(□) 50% oxygen (▲) 100% oxygen

not show any significant change with observation height, the temperatures for the rest of the 7 thermometric species start dropping very sharply when 50% and 100% air were introduced into the coolant stream. The excitation temperatures drop by 500 K to 900 K from 2 mm to 10 mm above the load coil, and ionization temperatures by 300 K to 600 K when 50% air was present in the coolant. When argon in the coolant was completely replaced by air, all the temperatures drop by 400 K to 700 K from 2 mm to 10 mm above the load coil. The only exception is the excitation temperature derived from 8 Fe II lines, it drops only slightly from 2 mm to 10 mm above the load coil. The temperature change with the amount of air introduced in the coolant and the comparison of temperature values obtained with different thermometric species will be discussed in section 3-6-1.

3-4-2. Argon-helium mixed-gas plasmas

In Fig. 24, the temperature change of all the 8 thermometric species with increasing observation height when 5%, 10%, 20%, and 50% helium were introduced into the coolant is illustrated. It seems that the behavior of helium in the coolant is totally different from that of the air. Almost all the temperature profiles show maxima at about 6 mm or 8 mm above the load coil; only the excitation temperatures of Fe I (Fig. 24.a) and Fe II (Fig. 24.b) still have not reached their maxima yet at 10 mm above the load coil when 5% argon in the coolant was replaced by helium.

Another interesting trend that can be observed is, when more and more helium is introduced into the coolant, the temperature profile maxima move to a lower and lower observation height above the load coil. In most

cases, when only 5% helium is present in the coolant, temperature profiles peak at about 8 mm, 10 mm or even higher above the load coil; when 10% and 20% helium is present in the coolant, the temperature profile maxima move down by about 2 mm; when 50% helium is in the coolant, the temperature profile maxima move down by about another 2 mm. Once again, the behavior of the excitation temperature profiles derived from 8 Fe II lines (Fig. 24.b) is a little bit different. In this case, the excitation temperature profile with 5% helium in the coolant peaks at 10 mm or higher above the load coil, while, those profiles with 10%, 20%, and 50% helium in the coolant peak at about 8 mm above the load coil. The temperature value change as a function of the amount of helium introduced into the coolant and the comparison of temperature values obtained with different thermometric species will be discussed in section 3-6-2.

3-4-3. Argon-nitrogen mixed-gas plasmas

In Fig. 25, the temperature change with the observation height measured from 2 mm to 10 mm above the load coil when 5%, 10%, 20%, 50%, and 100% nitrogen was introduced into the coolant stream of an argon plasma discharge is illustrated. It is not difficult to see that temperature profiles in Fig. 25 show a lot of similarities to those in Fig. 23 when 5% to 100% air was introduced into the coolant. When only 5%, 10%, and 20% argon in the coolant was replaced by nitrogen, the excitation and ionization temperatures change very slowly (if any) with increasing observation height. When 50% and more nitrogen were introduced, not only do the overall magnitudes of temperature for all the 8 thermometric species take a big drop, but also the temperatures decrease much more dramatically with observation

height. These were also observed when various amounts of air were introduced into the coolant. The temperature value change with the amount of nitrogen introduced and the comparison among different thermometric species will be discussed in section 3-6-3.

3-4-4. Argon-oxygen mixed-gas plasmas

The temperature profiles shown in Fig. 26 were measured and plotted in the same way as in Fig. 23 to Fig. 25, except that the nonargon gas is oxygen. Fig. 26, compared to Fig. 23 and Fig. 25, also shows similar behavior, but is somewhat different. In most cases, only when 100% argon in the coolant was replaced by oxygen, do the excitation and ionization temperatures begin to decrease very sharply - by 1000 K to 1400 K from 2 mm to 10 mm above the load coil. While when 5% to 50% oxygen was introduced into the coolant, most temperature profiles show relatively small change with increasing observation height.

In Fig. 26.b, with 10%, 20%, and 50% oxygen in the coolant, the excitation temperature drop for Fe II is also quite obvious from 2 mm to 10 mm above the load coil. In Fig. 26.c, with 20%, 50%, and 100% oxygen introduced, three almost parallel temperature profiles result. In other words, the excitation temperatures derived from 11 Ti II lines drop in almost the same rate - about 400 K from 2 mm to 10 mm above the load coil.

The discussion on the changes in temperature with the amount of oxygen in the coolant and the comparison among temperature values obtained using different thermometric species will be delayed until section 3-6-4.

3-4-5. Argon plasma with 20% nitrogen in the nebulizer

Researchers have introduced different nonargon gases into the nebulizer stream of pure argon-supported ICP discharges [144, 147-148] and the analytical performance has been evaluated [147-148].

In this study, temperature profiles were measured for those thermometric species whose emissions fall between the 200 nm to 300 nm range (only a solar-blind R166 PMT was needed) at 5 different positions above the load coil (10 mm, 12 mm, 14 mm, 16 mm, and 18 mm), and at a constant forward power of 1.5 kW. After the normal argon supported ICP discharge was initiated, nitrogen was gradually introduced into the nebulizer stream until 20% of the argon in the nebulizer was replaced by nitrogen and total flow rate of the nebulizer gas was 1.1 l/min. The complete temperature profiles are provided in Fig. 27.

Comparing the data in Fig. 27.a and those in Fig. 11.b, totally different temperature profiles are seen. The temperature profile at 1.5 kW in Fig. 11.b shows a drop of about 200 K from 10 mm to 18 mm above the load coil, while a temperature increase of about 300 K from 10 mm to 18 mm above the load coil is shown by the data in Fig. 27.a. The maximum temperature reached is about 500 K higher in the later case. Comparing the data in Fig. 27.b with the corresponding temperature profiles in Fig. 15.b, Fig. 16.b, Fig. 17.b, and Fig. 18.b, the replacement of 20% of the argon by nitrogen in the nebulizer stream has also shown some dramatic effect. The maximum temperature appears at 18 mm (may be higher) above the load coil, whereas the temperature peaked
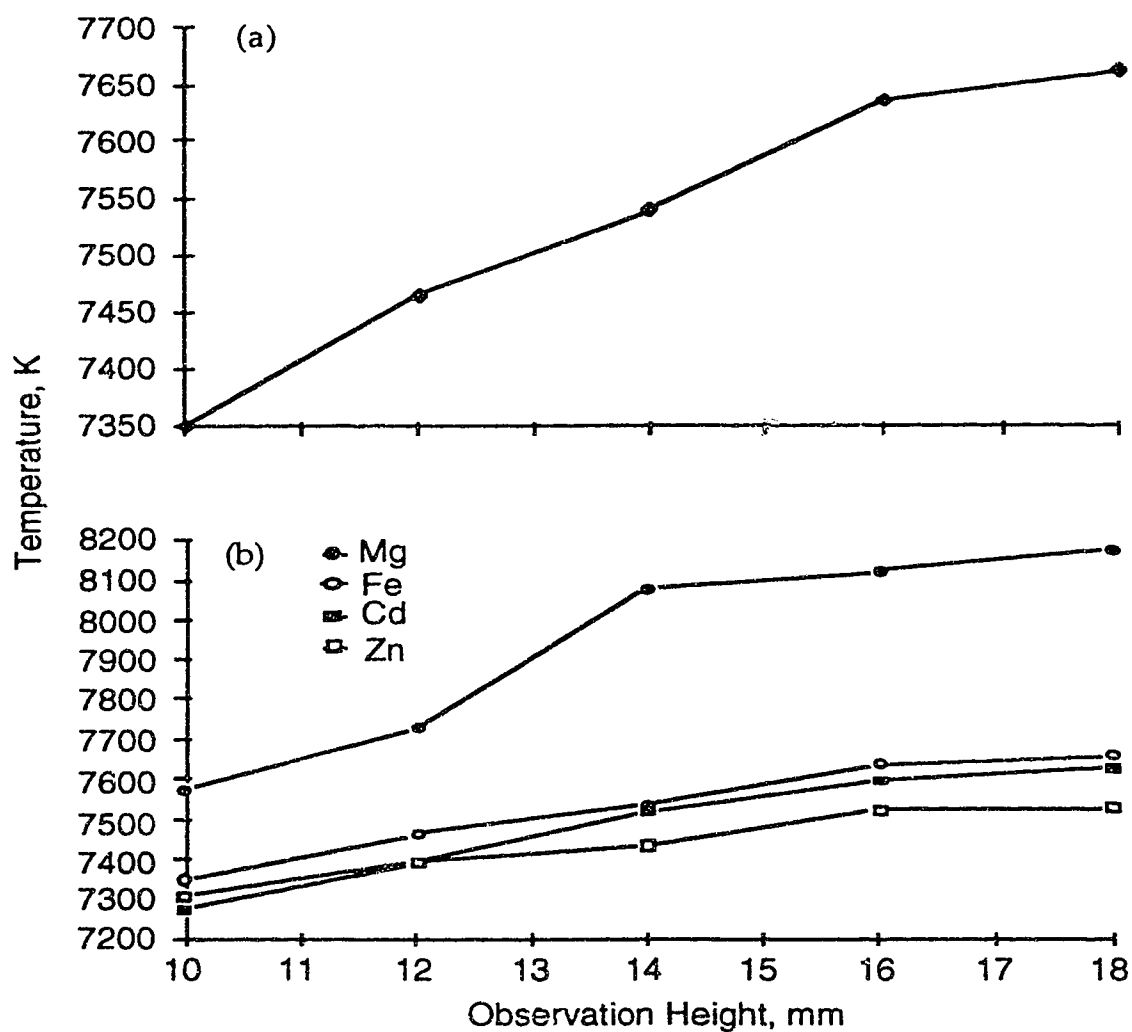
Fig. 27. Effect of 20% nitrogen in the nebulizer stream on excitation and ioni-
zation temperatures in an argon plasma at 1.5 kW: (a) excitation
temperature measured using 8 Fe II lines. (b) ionization temperatures
for 4 thermometric species.

at about 10 mm above the load coil when a pure argon plasma was used as shown in Fig. 15.b, Fig. 16.b, Fig. 17.b, and Fig. 18.b. However, unlike the excitation temperature of Fe II in Fig. 27.a, it is not possible to reliably state whether the temperatures here are higher or lower compared to those obtained in a normal pure argon ICP discharge. It is safe to say, though, that no dramatic temperature change is expected when 20% argon in the nebulizer is replaced by nitrogen. But with this replacement, it seems that the "hottest spot" along the central aerosol channel is pushed up by about 8 mm.

3-5. Effect of different foreign gases of the same percentage

From now on, attention will be focused on the change in the magnitudes of different temperatures when the composition of the coolant is varied. Bar graph plots will be used to illustrate the temperature variations throughout the rest of the chapter. All the temperatures were measured at five positions above the load coil (2 mm, 4 mm, 6 mm, 8 mm, and 10 mm) and at a constant forward power of 1.5 kW. These temperatures measured at all observation heights will be compared against corresponding temperatures obtained in a pure argon plasma discharge run at 1.5 kW, with an observation height of 14 mm above the load coil.

3-5-1. 5% foreign gases

Presented in Fig. 28 are the excitation and ionization temperatures of all 8 thermometric species measured in plasma discharges with 5% air, 5% helium, 5% nitrogen, and 5% oxygen in the coolant stream from 2 mm to 10 mm above the load coil. These temperatures are compared against those

(a) 2 mm above the load coil

(b) 4 mm above the load coil

(c) 6 mm above the load coil

(d) 8 mm above the load coil

(e) 10 mm above the load coil

Temperature, K

100% Ar   5% air   5% He   5% N₂   5% O₂

Composition of mixed gases
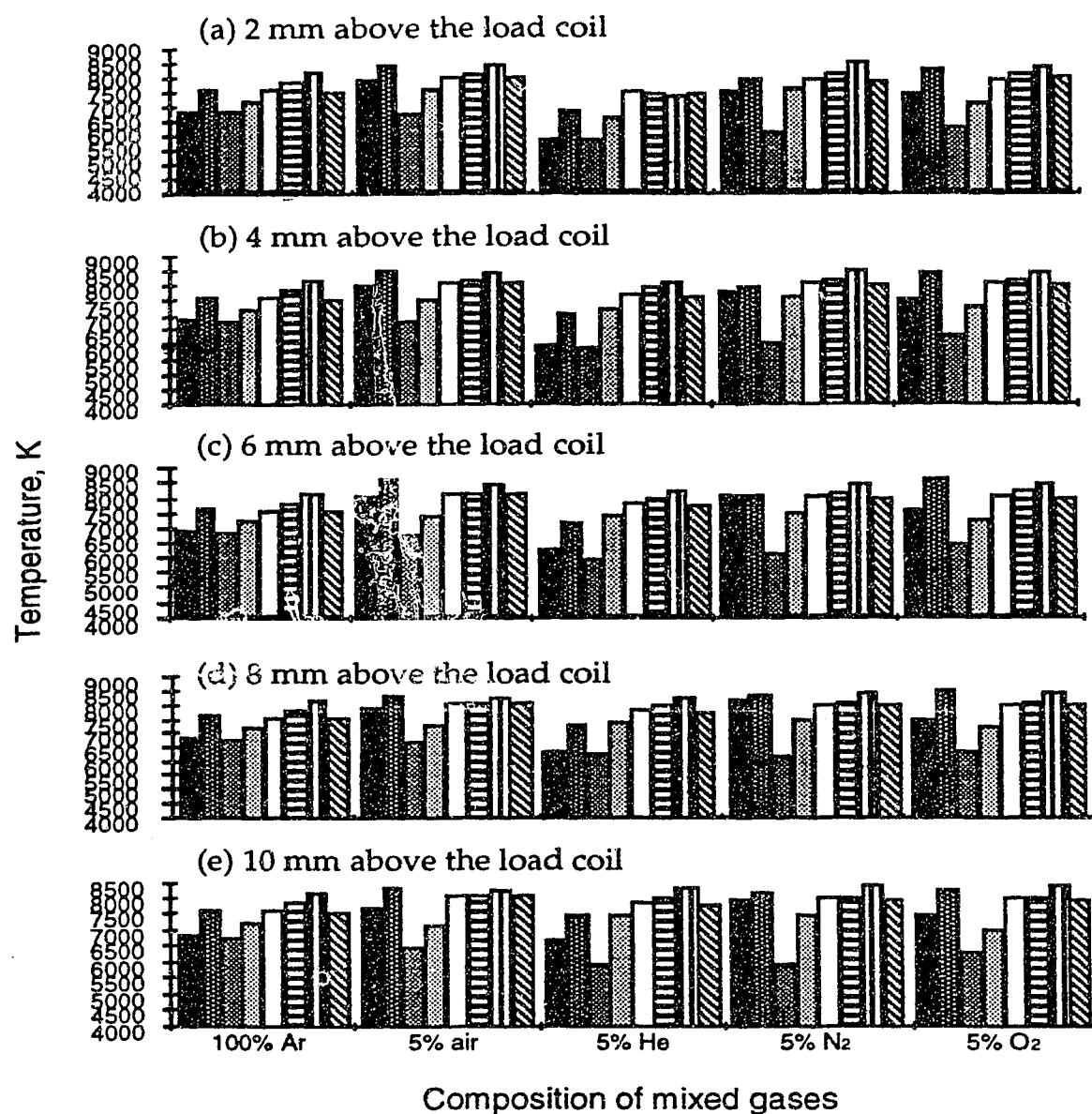
Fig. 28. Effect of 5% nonargon gases on temperatures of different thermo-
metric species   at various observation heights.

( ) Tex from 6 Fe I lines   ( ) Tex from 8 Fe II lines

( ) Tex from 11 Ti II lines   ( ) Tion from Ca II/Ca I

( ) Tion from Cd II/Cd I   ( ) Tion from Fe II/Fe I

( ) Tion from Mg II/Mg I   ( ) Tion from Zn II/Zn I

Fig. 29. Maximum temperatures obtainable for different thermometric species in argon plasma discharges with 5% nonargon gases in the coolant regardless of observation height.

(■) Tex from 6 Fe I lines   (▦) Tex from 8 Fe II lines
(▨) Tex from 11 Ti II lines   (▱) Tion from Ca II/Ca I
(□) Tion from Cd II/Cd I   (▤) Tion from Fe II/Fe I
(▥) Tion from Mg II/Mg I   (▧) Tion from Zn II/Zn I

corresponding temperatures measured in a 100% argon plasma discharge at 14 mm above the load coil and at a constant forward power of 1.5 kW.

At 2 mm above the load coil (Fig. 28.a), the general trend is that the excitation and ionization temperatures measured in a plasma with 5% air in the coolant have the highest values, and those measured in a plasma with 5% helium in the coolant give the lowest values. The order for the temperatures measured in different mixed-gas plasma discharges containing 5% nonargon gases is: argon-5% air ≥ argon-5% nitrogen > argon-5% oxygen > pure argon > argon-5% helium. The temperatures measured in plasma discharges with 5% air and 5% nitrogen in the coolant generally give comparable values. However, the excitation temperature of Fe II measured in the pure-argon plasma discharge shows roughly an equivalent value to that measured in a plasma discharge containing 5% air in the coolant. Both these values are higher than those measured in plasma discharges with 5% nitrogen, oxygen, and helium in the coolant. Compared to the temperatures measured in the pure-argon plasma discharge, the temperatures measured in an argon plasma discharge containing 5% air, nitrogen, and oxygen are higher by 500 K to over 1300 K in most of the cases; whereas, the temperatures measured in the plasma discharge containing 5% helium in the coolant are lower by about 200 K to 900 K. The excitation temperatures of Ti II show different behavior: the temperatures measured in plasma discharges containing 5% nitrogen and 5% oxygen give lower values than those measured in a pure-argon plasma discharge.

At 4 mm and 6 mm above the load coil (Fig. 28.b, Fig. 28.c), the same trend as observed at 2 mm above the load coil still prevails. But at 6 mm

above the load coil, the ionization temperatures of Ca and Cd measured in the plasma discharge containing 5% helium in the coolant are higher than those measured in the pure-argon plasma discharge.

At 8 mm and 10 mm above the load coil (Fig. 28.d, Fig. 28.e) the excitation temperatures of Fe I and Fe II, the ionization temperatures Cd and Mg still show the same trend as at 2 mm above the load oil. For the rest of the 4 thermometric species, the pure-argon plasma discharge and/or the argon plasma discharge containing 5% helium in the coolant show higher temperatures than those measured in plasma discharges containing 5% other nonargon gases in the coolant. At 8 mm above the load coil, for instance, the order of excitation temperatures of Ti II measured in various mixed-gas plasma discharges is: pure argon > argon-5% air > argon-5% helium $\geq$ argon-5% nitrogen $\geq$ argon-5% oxygen. At 10 mm above the load coil, the order for ionization temperatures of Ca is: argon-5% nitrogen > argon-5% helium > pure argon > argon-5% air $\geq$ argon-5% oxygen. This trend at 8 mm and 10 mm above the load coil is consistent with the previous observation that the maxima of the temperature profiles measured in a pure-argon plasma discharge (Fig. 12 to Fig. 18) and in the argon plasma discharge with 5% helium in the coolant (Fig. 24) appear at about 10 mm above the load coil or higher.

The graphs in Fig. 29 provide a "summary" of the data in Fig. 28. In this figure, only the maximum temperatures chosen from various observation heights are plotted. The trend for the maximum temperatures obtainable regardless of observation height is basically as follows: plasma discharges with 5% air, 5% nitrogen, and 5% oxygen in the coolant give comparable temperature values; these values are higher than those measured

in a pure-argon plasma discharge and in a plasma discharge containing 5% helium in the coolant by a few hundreds to over one thousand Kelvin. Comparing the temperatures measured in a pure-argon plasma discharge with those measured in an argon plasma discharge with 5% helium in the coolant, it is of interest to notice that for excitation temperatures, the order is: pure argon > argon-5% helium; whereas, for ionization temperatures, the order is: argon-5% helium > pure argon.

3-5-2. 10% foreign gases

Presented in Fig. 30 are the excitation and ionization temperatures of all the 8 thermometric species measured in plasma discharges with 10% air, 10% helium, 10% nitrogen, and 10% oxygen in the coolant from 2 mm to 10 mm above the load coil.

Introduction of 10% nonargon gases in the coolant does not make a lot of differences compared to the case when 5% nonargon gases were introduced. For the excitation temperatures of Fe I and Fe II, the ionization temperatures of Cd, Fe, Mg, and Zn from 2 mm to 10 mm above the load coil, argon-10% air, argon-10% nitrogen, and argon-10% oxygen plasma discharges also give comparable temperature values. These values are higher than those measured in the pure-argon plasma discharge and the argon plasma discharge with 10% helium in the coolant.

At 2 mm above the load coil, a pure-argon plasma discharge gives higher temperature values than those measured in a plasma discharge with 10% helium in the coolant; from 4 mm to 10 mm above the load coil, the opposite is true.

Fig. 30. Effect of 10% nonargon gases on temperatures of different thermometric species at various observation heights.

(▓) Tex from 6 Fe I lines

(▓) Tex from 11 Ti II lines

(□) Tion from Cd II/Cd I

(▥) Tion from Mg II/Mg I

(▓) Tex from 8 Fe II lines

(▨) Tion from Ca II/Ca I

(☰) Tion from Fe II/Fe I

(▧) Tion from Zn II/Zn I

Fig. 31. Maximum temperatures obtainable for different thermometric species in argon plasma discharges with 10% nonargon gases in the coolant regardless of observation height.

(▓) Tex from 6 Fe I lines   (▓) Tex from 8 Fe II lines
(▓) Tex from 11 Ti II lines   (▓) Tion from Ca II/Ca I
(□) Tion from Cd II/Cd I   (▤) Tion from Fe II/Fe I
(▥) Tion from Mg II/Mg I   (◪) Tion from Zn II/Zn I

The excitation temperatures derived from 11 Ti II lines demonstrate some unusual behavior at all 5 positions above the load coil. The temperatures measured in the pure-argon plasma discharge and the plasma discharge with 10% helium in the coolant indicate higher temperatures than those measured in plasma discharges containing 10% air, 10% nitrogen, and 10% oxygen in the coolant.

At 2 mm and 4 mm above the load coil, the order for the ionization temperature of Ca is: argon-10% nitrogen > argon-10% air > argon-10% oxygen > pure argon > argon-10% helium. Whereas, from 6 mm to 10 mm above the load coil the order becomes: argon-10% nitrogen > argon-10% helium > argon-10% air > argon-10% oxygen > pure argon.

The graphs in Fig. 31 provide a "summary" of the data in Fig. 30. In this figure, the maximum obtainable temperatures regardless of observation height for all the 8 thermometric species are compared. For 6 of the 8 thermometric species, plasma discharges with 10% air, 10% nitrogen, and 10% oxygen in the coolant have comparable temperatures. These temperatures are higher than those measured in the pure-argon plasma discharge and the argon plasma discharge with 10% helium in the coolant. For the excitation temperature of Ti II, the order is: argon-10% helium > pure argon > argon-10% air > argon-10% oxygen > argon-10% nitrogen. For the ionization temperature of Ca, the order is: argon-10% nitrogen > argon-10% helium > argon-10% air > argon-10% oxygen > pure argon.

3-5-3. 20% foreign gases

Excitation and ionization temperatures of all the 8 thermometric species were also measured when 20% of the argon in the coolant was replaced by air, helium, nitrogen, and oxygen. The results are shown in Fig. 32.

There are still no significant changes compared to the cases when 5% and 10% nonargon gases were in the coolant. For almost all the thermometric species, the order of temperatures obtained with 20% non argon gases in the coolant is: argon-20% air $\geq$ argon-20% nitrogen $\geq$ argon-20% oxygen $>$ argon-20% helium $\geq$ pure argon at all observation heights. From 2 mm to 10 mm above the load coil, the excitation temperature of Ti II shows the following order: pure argon $>$ argon-20% helium $>$ argon-20% air $\geq$ argon-20% oxygen $>$ argon-20% nitrogen. Only at 10 mm above the load coil (Fig. 32.e), the ionization temperature of Ca shows the highest value with 20% helium in the coolant among the temperatures of Ca measured in 20% other nonargon gases. At 2 mm above the load coil (Fig. 32.a), the order for the ionization temperature of Ca is: argon-20% nitrogen $>$ argon-20% air $>$ argon-20% oxygen $>$ argon-20% helium $\geq$ pure argon.

The graphs in Fig. 33. provide a summary of the data in Fig. 32. As in Fig. 31, the maximum obtainable temperatures regardless of observation height for all the 8 thermometric species are provided. The 8 thermometric species can be divided into three groups according to the orders of temperature when 20% nonargon gases were in the coolant. The first group

(a) 2 mm above the load coil

(b) 4 mm above the load coil

(c) 6 mm above the load coil

(d) 8 mm above the load coil

(e) 10 mm above the load coil

Temperature, K

100% Ar   20% Air   20% He   20% N₂   20% O₂

Composition of mixed gases

Fig. 32. Effect of 20% nonargon gases on temperatures of different thermometric species at various observation heights.

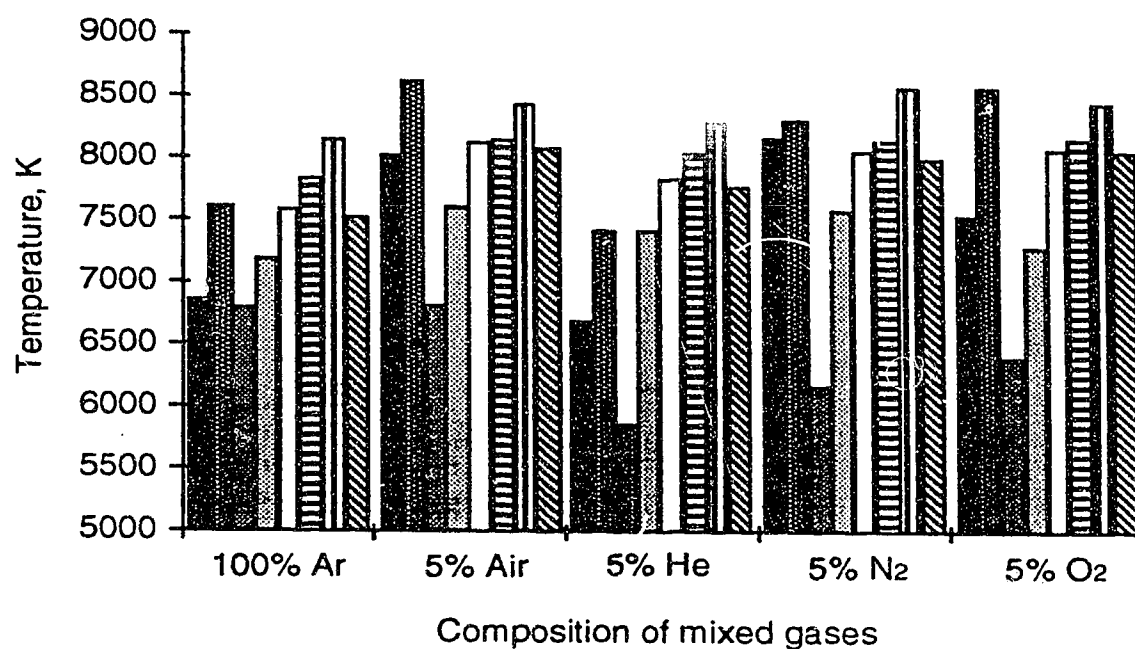(■) Tex from 6 Fe I lines   (▩) Tex from 8 Fe II lines

(▨) Tex from 11 Ti II lines   (□) Tion from Ca II/Ca I

(□) Tion from Cd II/Cd I   (▤) Tion from Fe II/Fe I

(▥) Tion from Mg II/Mg I   (▧) Tion from Zn II/Zn I
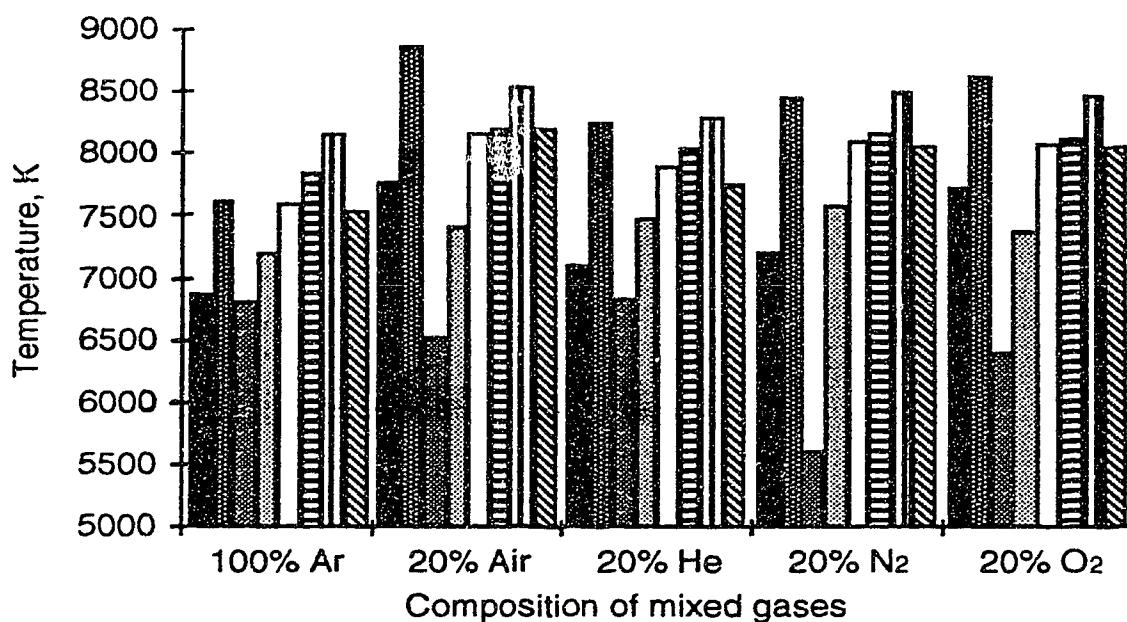
Fig. 33. Maximum temperatures obtainable for different thermometric species in argon plasma discharges with 20% nonargon gases in the coolant regardless of observation height.

(■) Tex from 6 Fe I lines   (▦) Tex from 8 Fe II lines

(▨) Tex from 11 Ti II lines   (▣) Tion from Ca II/Ca I

(□) Tion from Cd II/Cd I   (▤) Tion from Fe II/Fe I

(▥) Tion from Mg II/Mg I   (▧) Tion from Zn II/Zn I

includes Fe I and Fe II, the order for their excitation temperature is: argon-20% air > argon-20% oxygen > argon-20% nitrogen > argon-20% helium > pure argon. The second group includes two thermometric species showing unusual behavior: Ti II and Ca. The order for the excitation temperature of Ti II is: argon-20% helium > pure argon > argon-20% air > argon-20% oxygen > argon-20% nitrogen; the order for the ionization temperature of Ca is: argon-20% nitrogen > argon-20% helium > argon-20% air > argon-20% oxygen > pure argon. The third group contains the rest of the 4 thermometric species-Cd, Fe, Mg, and Zn, the order for their ionization temperatures is: argon-20% air > argon-20% nitrogen > argon-20% oxygen > argon-20% helium > pure argon.

3-5-4. 50% foreign gases

Excitation and ionization temperatures of all the 8 thermometric species measured with 50% nonargon gases in the coolant are shown in Fig. 34. At 2 mm and 4 mm above the load coil (Fig. 34.a, Fig. 34.b), the basic trend observed before still holds true, i.e., argon-air, argon-nitrogen, and argon-oxygen mixed-gas plasma discharges demonstrate higher temperatures compared to pure argon and argon-helium plasma discharges. At 6 mm and above the load coil, for most of the thermometric species, a pure-argon plasma discharge and an argon plasma discharge with 50% helium in the coolant begin to show higher and higher temperatures compared to other mixed-gas plasma discharges at the same observation height. Particularly at 8 mm and 10 mm above the load coil (Fig. 34.d, Fig. 34.e), an argon-50% helium mixed-gas plasma discharge shows the highest temperatures in most of the
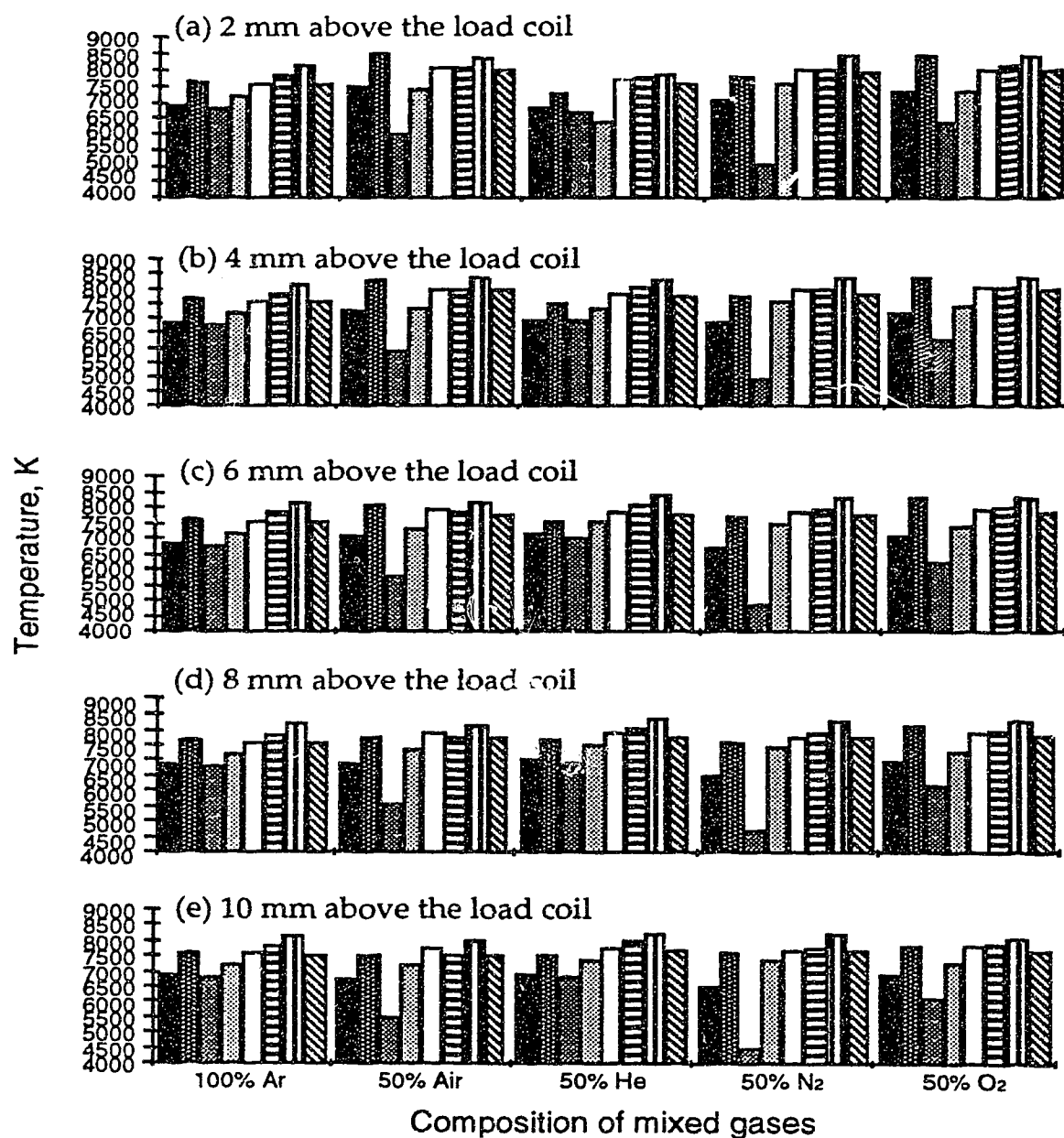
Fig. 34. Effect of 50% nonargon gases on temperatures of different thermometric species at various observation heights.

(▨) Tex from 6 Fe I lines   (▨) Tex from 8 Fe II lines
(▨) Tex from 11 Ti II lines   (▨) Tion from Ca II/Ca I
(☐) Tion from Cd II/Cd I   (▤) Tion from Fe II/Fe I
(▥) Tion from Mg II/Mg I   (▧) Tion from Zn II/Zn I
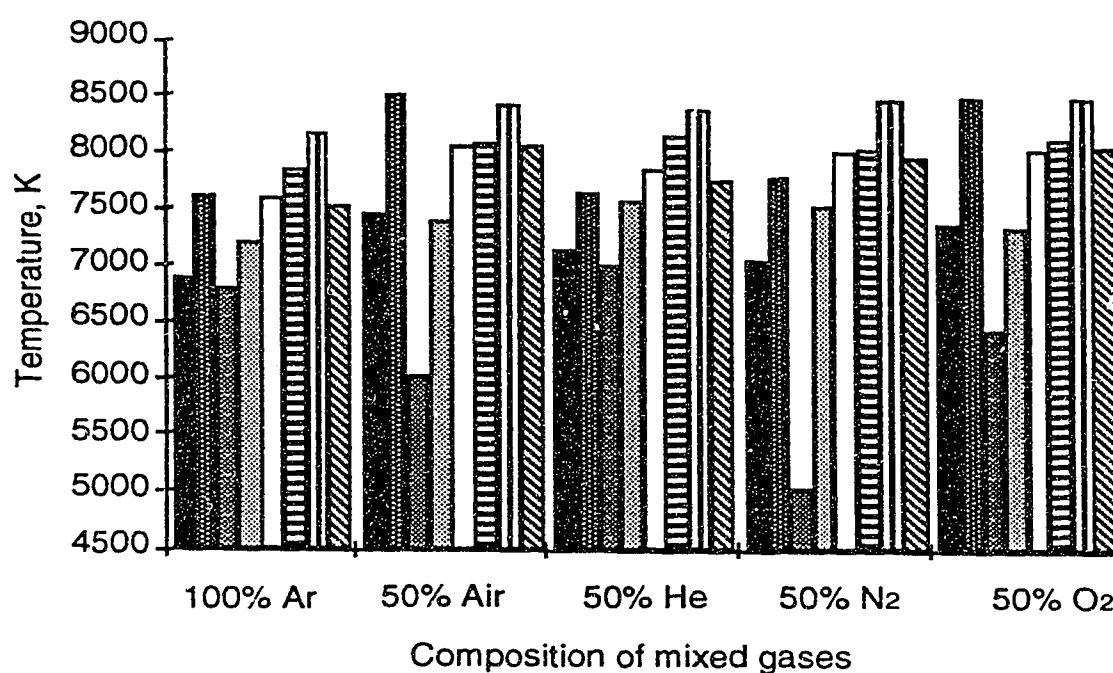
Fig. 35. Maximum temperatures obtainable for different thermometric species in argon plasma discharges with 50% nonargon gases in the coolant regardless of observation height.

(■) Tex from 6 Fe I lines   (▦) Tex from 8 Fe II lines

(▨) Tex from 11 Ti II lines   (▥)Tion from Ca II/Ca I

(□) Tion from Cd II/Cd I   (▤) Tion from Fe II/Fe I

(▥) Tion from Mg II/Mg I   (▧) Tion from Zn II/Zn I

cases. This can be explained by the previous observation that temperatures measured in plasma discharges containing 50% air, 50% nitrogen, and 50% oxygen decreased with increasing observation height right from 2 mm above the load coil (Fig. 23. Fig. 25, Fig. 26) and the plasma discharge with 50% helium in the coolant had temperature profiles with maxima at about 8 mm above the load coil (Fig. 24).

If we only compare the maximum obtainable temperatures regardless of observation height as shown in Fig. 35, similar results are observed as before when temperatures were compared at each individual observation height. For the excitation temperatures of Fe I, Fe II, the ionization temperatures of Cd, Mg, and Zn, plasma discharges with 50% air, 50% nitrogen, and 50% oxygen in the coolant have comparable temperature values. These values are higher than those measured in a pure-argon plasma discharge and an argon-50% helium plasma discharge. For the rest of the three thermometric species, although the order is not exactly the same, one thing in common about the excitation temperatures of Ti II and the ionization temperatures of Ca, and of Fe is that an argon-50% helium plasma discharge has the highest temperatures among these argon-50% nonargon gas plasma discharges.

3-5-5. 100% foreign gases

Presented in Fig. 36 are the temperatures measured at the same 5 positions above the load coil as before when argon in the coolant stream was totally replaced by air, nitrogen, and oxygen. As mentioned earlier, more than
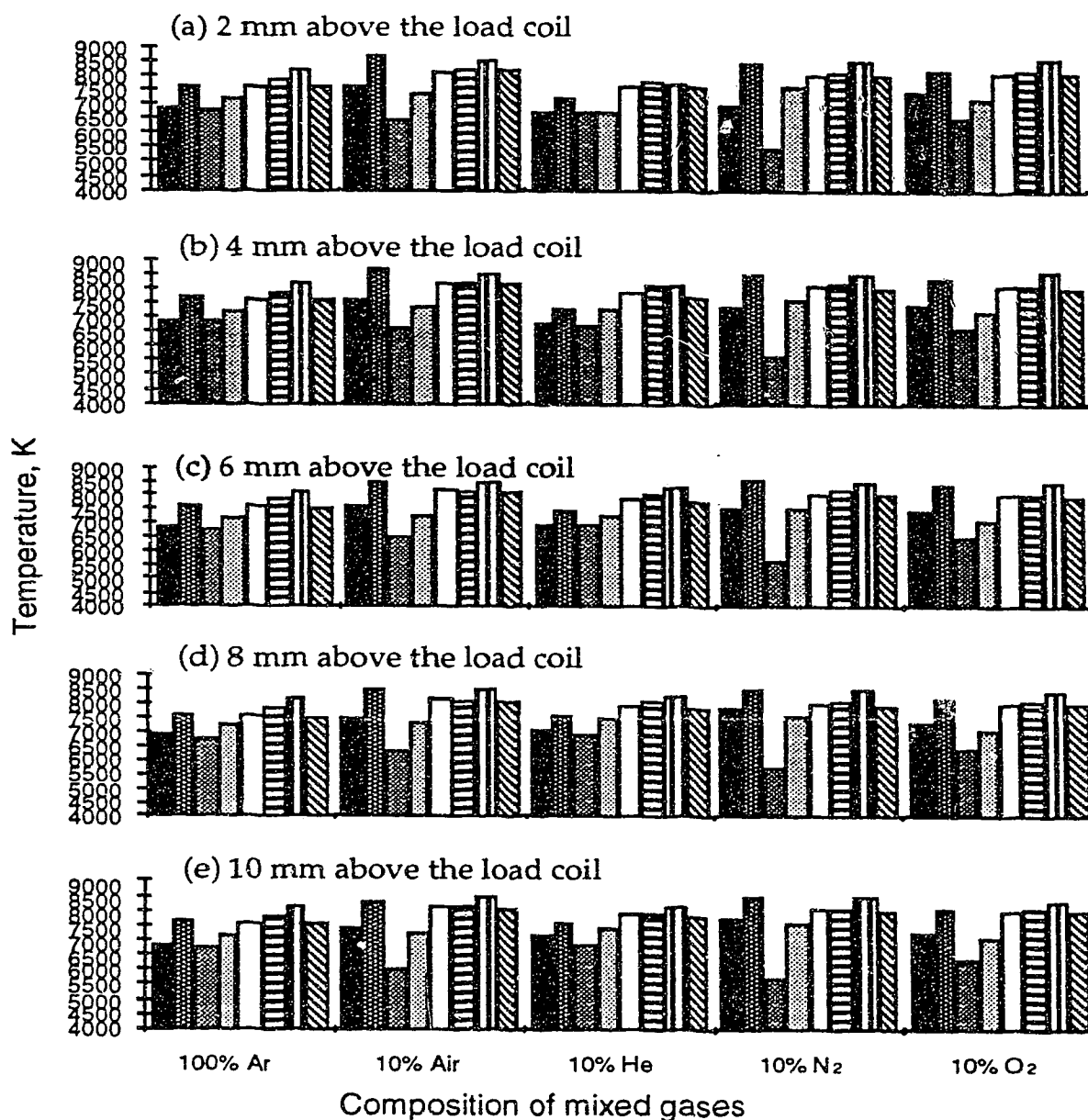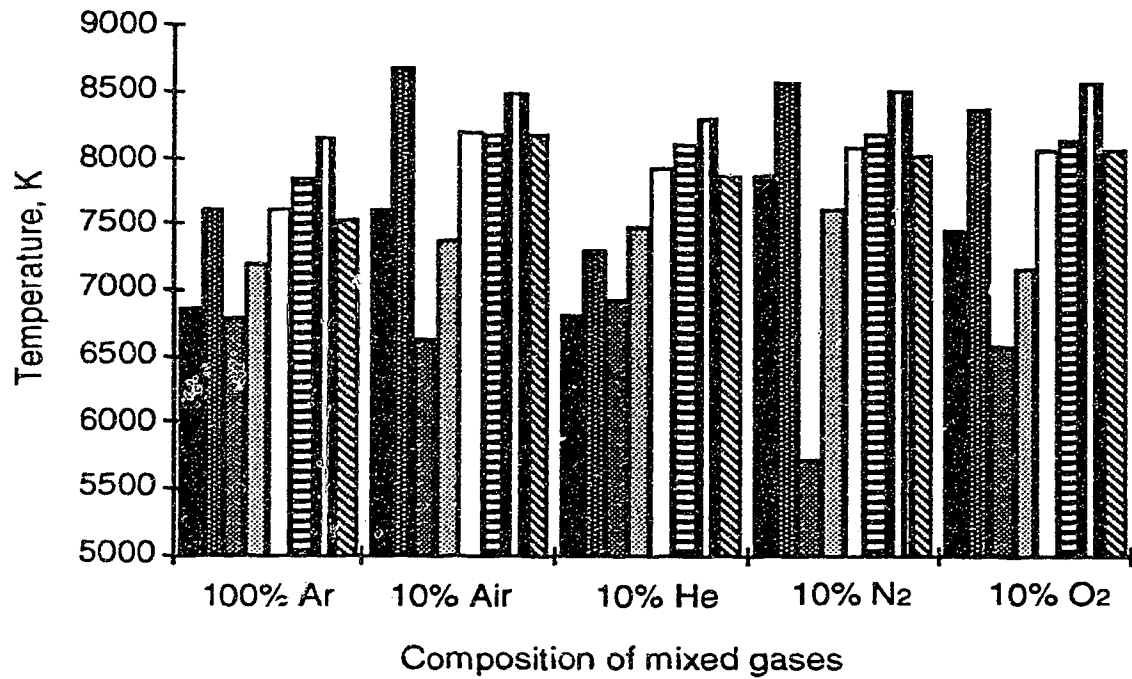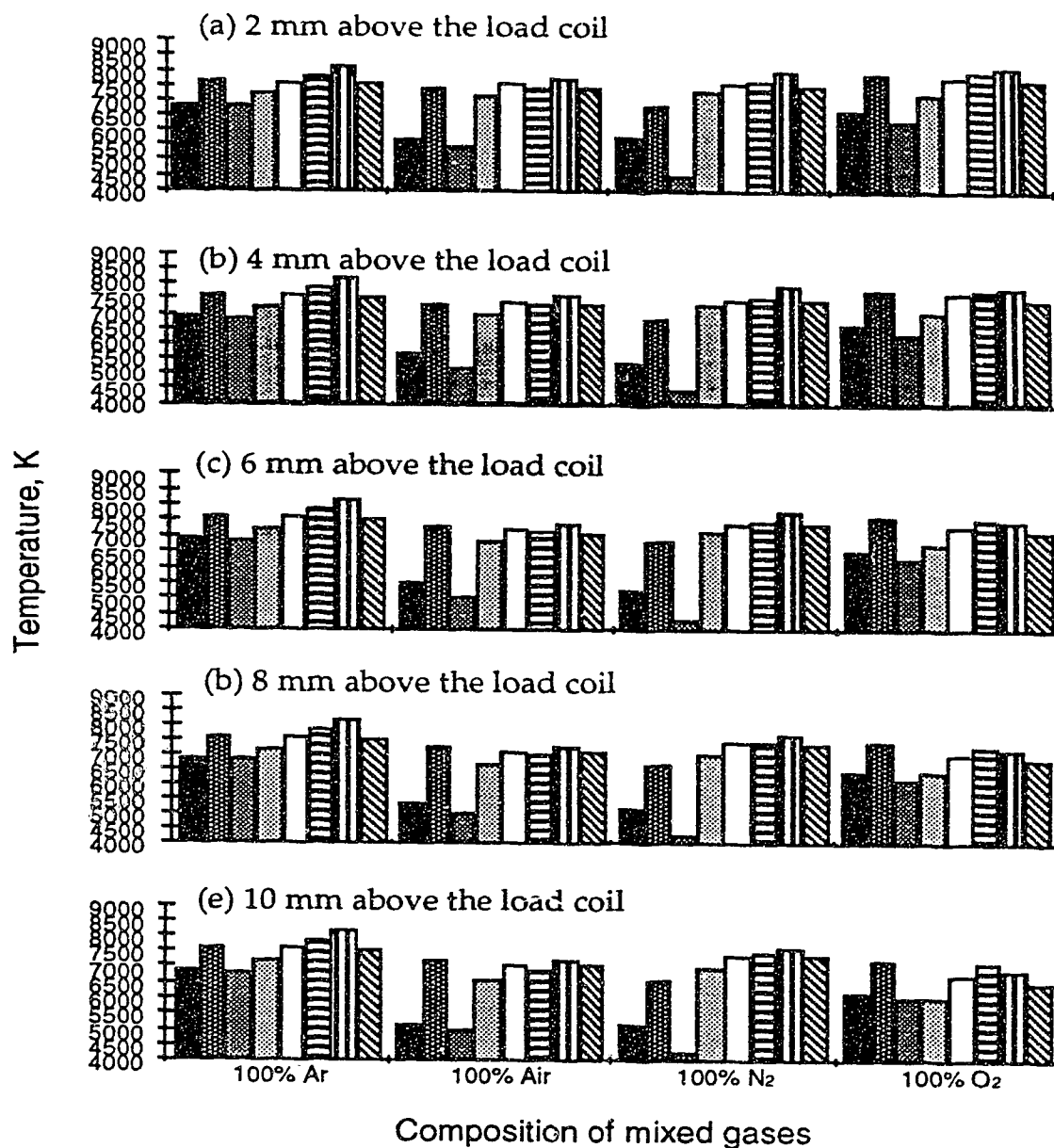
Fig. 36. Effect of 100% nonargon gases on temperatures of different thermo-
metric species at various observation heights.

( ) Tex from 6 Fe I lines   ( ) Tex from 8 Fe II lines
( ) Tex from 11 Ti II lines   ( ) Tion from Ca II/Ca I
( ) Tion from Cd II/Cd I   ( ) Tion from Fe II/Fe I
( ) Tion from Mg II/Mg I   ( ) Tion from Zn II/Zn I
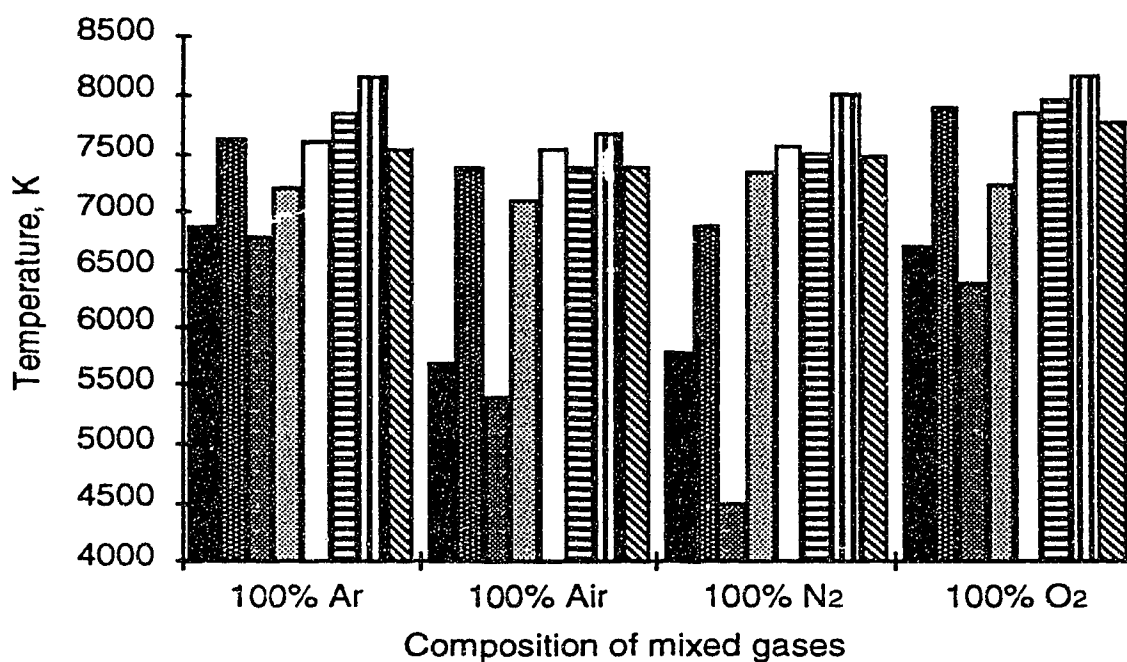
Fig. 37. Maximum temperatures obtainable for different thermometric species in argon plasma discharges with 100% nonargon gases in the coolant regardless of observation height.

(■) Tex from 6 Fe I lines   (▦) Tex from 8 Fe II lines

(▨) Tex from 11 Ti II lines   (▤) Tion from Ca II/Ca I

(□) Tion from Cd II/Cd I   (▤) Tion from Fe II/Fe I

(▥) Tion from Mg II/Mg I   (▨) Tion from Zn II/Zn I

70% helium in the coolant will extinguish the plasma discharge, therefore no results for 100% helium were obtained.

As mentioned at the beginning of section 3-5, the temperatures in a pure-argon plasma discharge shown throughout this chapter were measured at 14 mm above the load coil, that is, at the "hottest" spot along the central aerosol channel. Whereas, all temperatures took a "big drop" when argon in the coolant was totally replaced by air, nitrogen, and oxygen as seen in section 3-4. As a result, a pure-argon plasma discharge has (almost exclusively) the highest temperatures for all the 8 thermometric species from 2 mm to 10 mm above the load coil among pure argon, pure air, pure nitrogen, and pure oxygen plasma discharges. For some thermometric species, only at low observation heights does the plasma discharge with 100% oxygen in the coolant tend to show higher temperatures than those measured in the pure-argon plasma discharge. It can be concluded that, in terms of temperatures, there is no advantage in using 100% air, 100% nitrogen, and 100% oxygen in the coolant.

If we only consider the maximum temperatures obtainable regardless of observation height as in Fig. 37, a slightly different picture appears. For half of the thermometric species, a pure-argon plasma discharge has the highest temperatures. For the other half of the thermometric species, a plasma discharge with 100% oxygen in the coolant demonstrates the highest temperatures. As we noticed in Fig. 36, these "highest" temperatures were only observed at low observation heights.

3-6. Effect of the amount of nonargon gases in the coolant

The same sets of data as used in the last two sections are employed and rearranged in this section such that the effect of increasing amount of nonargon gases on the excitation and ionization temperatures of the 8 thermometric species from 2 mm to 10 mm above the load coil can be illustrated.

3-6-1. Argon-air mixed-gas plasmas

As shown in Fig. 38, at all positions above the load coil (therefore, there is no need to discuss results at each individual observation height), the temperatures increase by a few hundred to over a thousand degrees when 5% of the argon in the coolant was replaced by air. When 10% and 20% of the argon was replaced by air, there is no significant change in temperature values compared to the case when 5% air is in the coolant. When 50% air is in the coolant, a significant drop in temperature can be observed. At this point, only the excitation temperature of Ti II becomes lower than that of a pure argon plasma discharge, the temperatures of the rest of the 7 thermometric species are still higher than those measured in a pure-argon plasma discharge at all observation heights. When argon in the coolant is totally replaced by air, a dramatic drop in temperatures occurs. This time, the temperatures for all the thermometric species at all observation heights are lower by a few hundred to nearly two thousand degrees compared to those measured in a pure-argon plasma discharge.

If we only plot the maximum temperatures chosen from various

Fig. 38. Effect of increasing the amount of air in the coolant on the temperatures of different thermometric species in argon-air mixed-gas plasma discharges at various heights at 1.5 kW.

(■) Tex from 6 Fe I lines   (▨) Tex from 8 Fe II lines

(▨) Tex from 11 Ti II lines   (▣) Tion from Ca II/Ca I

(□) Tion from Cd II/Cd I   (▤) Tion from Fe II/Fe I

(▥) Tion from Mg II/Mg I   (▧) Tion from Zn II/Zn I

Fig. 39. Effect of increasing the amount of *air* in the coolant on the maximum temperatures obtainable of different thermometric species in argon-air mixed-gas plasma discharges at 1.5 kW.

(■) Tex from 6 Fe I lines   (▦) Tex from 8 Fe II lines

(▨) Tex from 11 Ti II lines   (▥) Tion from Ca II/Ca I

(□) Tion from Cd II/Cd I   (▤) Tion from Fe II/Fe I

(▥) Tion from Mg II/Mg I   (▧) Tion from Zn II/Zn I

observation heights, the same trend as observed in Fig. 38 still persists as is shown in Fig. 39. The only exception is the excitation temperature of Ti II, which begins to drop gradually when more than 5% air was present in the coolant. When 5% to 50% air were introduced into the coolant, a temperature increase of up to 1400 K is achievable relative to that measured in a pure-argon supported plasma discharge for the rest of the 7 thermometric species.

3-6-2. Argon-helium mixed-gas plasmas

As shown in Fig. 40, when 5%, 10%, 20%, and 50% of the argon in the coolant was replaced by helium, some interesting results were observed. At 2 mm above the load coil, all the thermometric species show the same behavior. When 5% helium was introduced into the coolant, all the temperatures measured were lower than those in the pure-argon plasma discharge. When 10% helium was mixed into the coolant, the temperatures began to increase, although for most of the thermometric species they were still lower than the corresponding temperatures in the pure-argon plasma discharge. When the amount of helium in the coolant was increased to 20% and 50%, no noticeable change in temperatures for most of the thermometric species was observed compared to the case when 10% helium was in the coolant. However, the excitation temperature of Fe II did increase sharply when 20% helium was in the coolant and drops by about 600 K when the amount of helium in the coolant was increased to 50%.

From 4 mm to 10 mm above the load coil, only the three excitation temperatures indicate the same behavior with increasing amount of helium

Fig. 40. Effect of increasing the amount of helium in the coolant on the temperatures of different thermometric species in argon-helium mixed-gas plasma discharges at various heights at 1.5 kW.

(▓) Tex from 6 Fe I lines   (▦) Tex from 8 Fe II lines

(▨) Tex from 11 Ti II lines   (▤) Tion from Ca II/Ca I

(☐) Tion from Cd II/Cd I   (▤) Tion from Fe II/Fe I

(▥) Tion from Mg II/Mg I   (▧) Tion from Zn II/Zn I
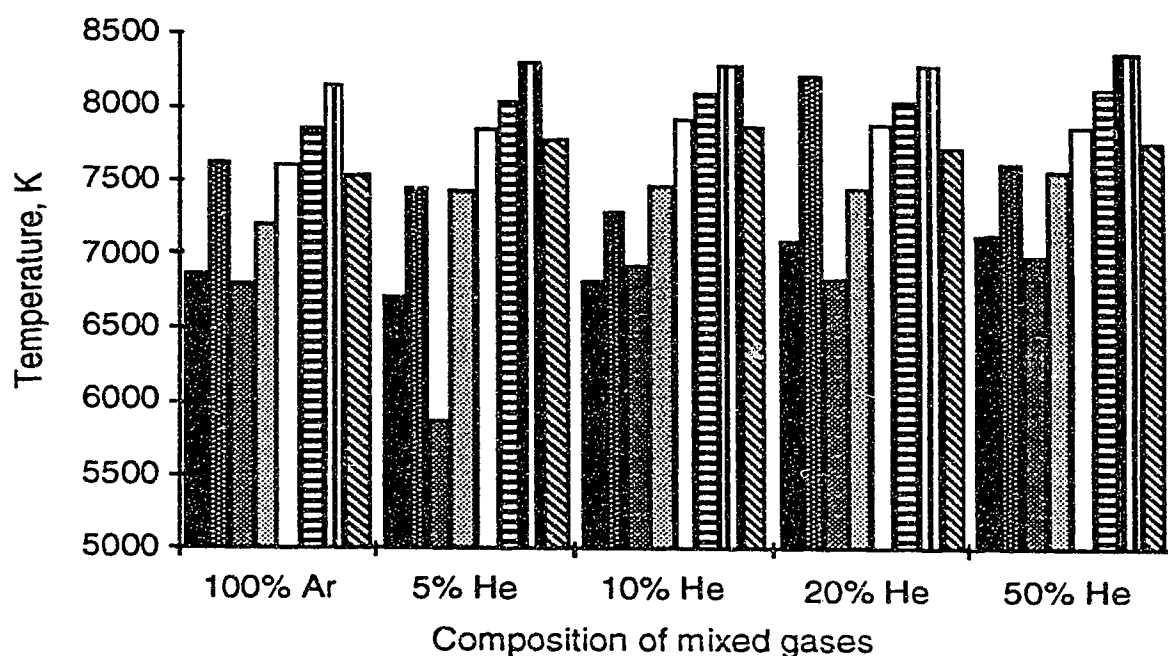
Fig. 41. Effect of increasing the amount of helium in the coolant on the maximum temperatures obtainable of different thermometric species in argon-helium mixed-gas plasma discharges at 1.5 kW.

( ) T_{ex} from 6 Fe I lines   ( ) T_{ex} from 8 Fe II lines

( ) T_{ex} from 11 Ti II lines   ( ) T_{ion} from Ca II/Ca I

( ) T_{ion} from Cd II/Cd I   ( ) T_{ion} from Fe II/Fe I

( ) T_{ion} from Mg II/Mg I   ( ) T_{ion} from Zn II/Zn I

in the coolant as at 2 mm above the load coil. For the five ionization temperatures, a totally different trend is observed. With 5% helium in the coolant, all the ionization temperatures already show higher temperatures than those in a pure-argon plasma discharge. With 10%, 20%, and 50% helium in the coolant, the temperatures either increase gradually or remain basically unchanged.

The maximum temperatures chosen from all observation heights when the amount of helium in the coolant was increased from 0% to 50% are shown in Fig. 41. All the excitation temperatures still show the same behavior as observed in Fig. 38 from 4 mm to 10 mm above the load coil. It is easily seen that at high observation heights, some gain in temperature can be achieved, although these increases in temperatures are only minimal (100 to 300 degrees) with the introduction of helium into the coolant.

3-6-3. Argon-nitrogen mixed-gas plasmas

As presented in Fig. 42, these bar graph plots reflect the changes in temperatures as the amount of nitrogen in the coolant was increased from 5% to 100%. As expected, argon-nitrogen mixed-gas plasma discharges are very similar to argon-air plasma discharges. Actually, for 7 of the 8 thermometric species, exactly the same behavior as seen in argon-air mixed-gas plasma discharges is observed. With the introduction of 5% nitrogen in the coolant, increases in temperature from a few hundred to over a thousand degrees are realized. Further increase in the amount of nitrogen to 10% and 20%, generates no noticeable changes. With the amount of nitrogen increased to
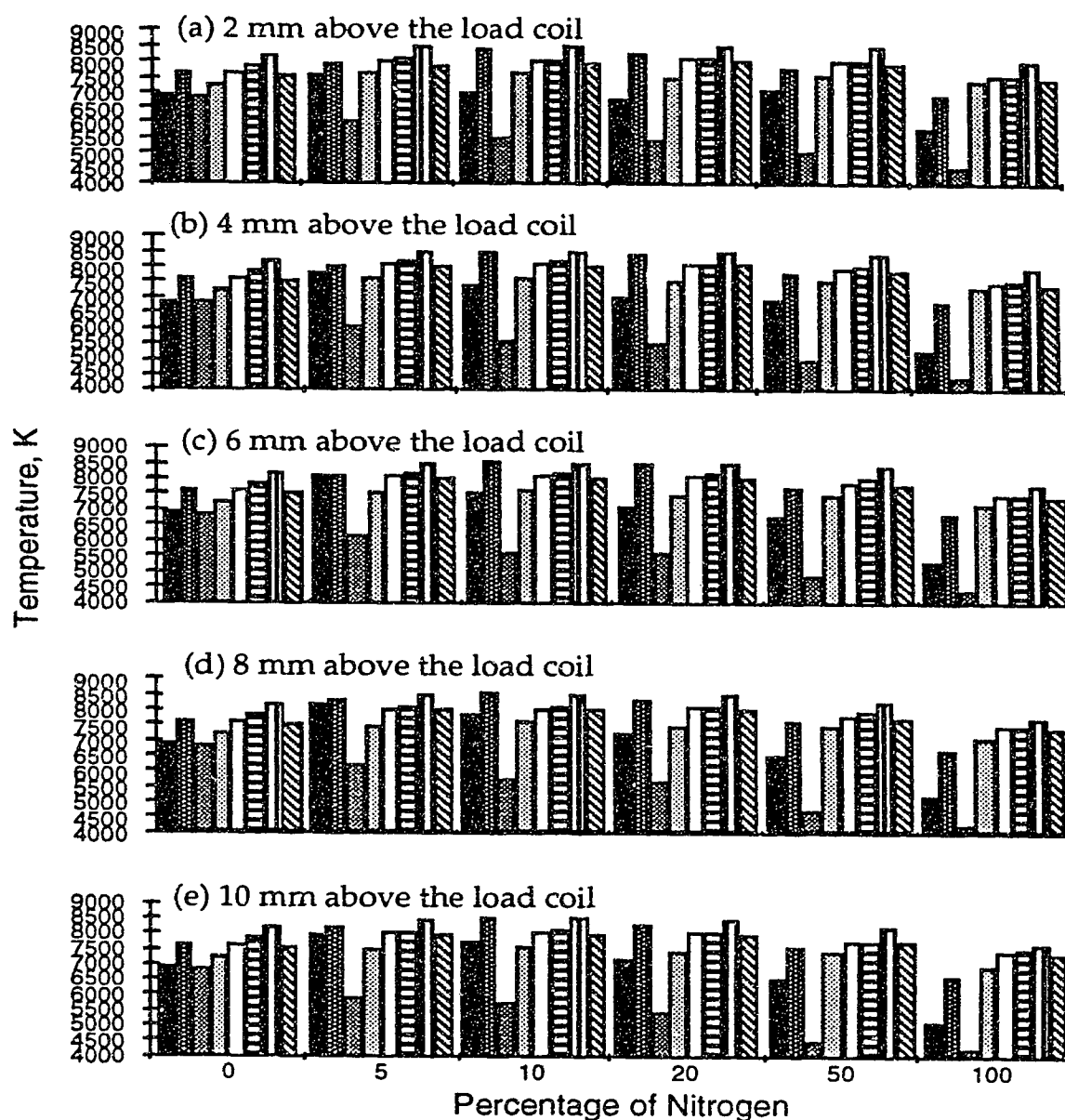
Fig. 42. Effect of increasing the amount of nitrogen in the coolant on the temperatures of different thermometric species in argon-nitrogen mixed-gas plasma discharges at various heights at 1.5 kW.

(■) Tex from 6 Fe I lines   (▦)Tex from 8 Fe II lines

(▨) Tex from 11 Ti II lines   (▤)Tion from Ca II/Ca I

(□) Tion from Cd II/Cd I   (▤) Tion from Fe II/Fe I

(▥) Tion from Mg II/Mg I   (▧) Tion from Zn II/Zn I
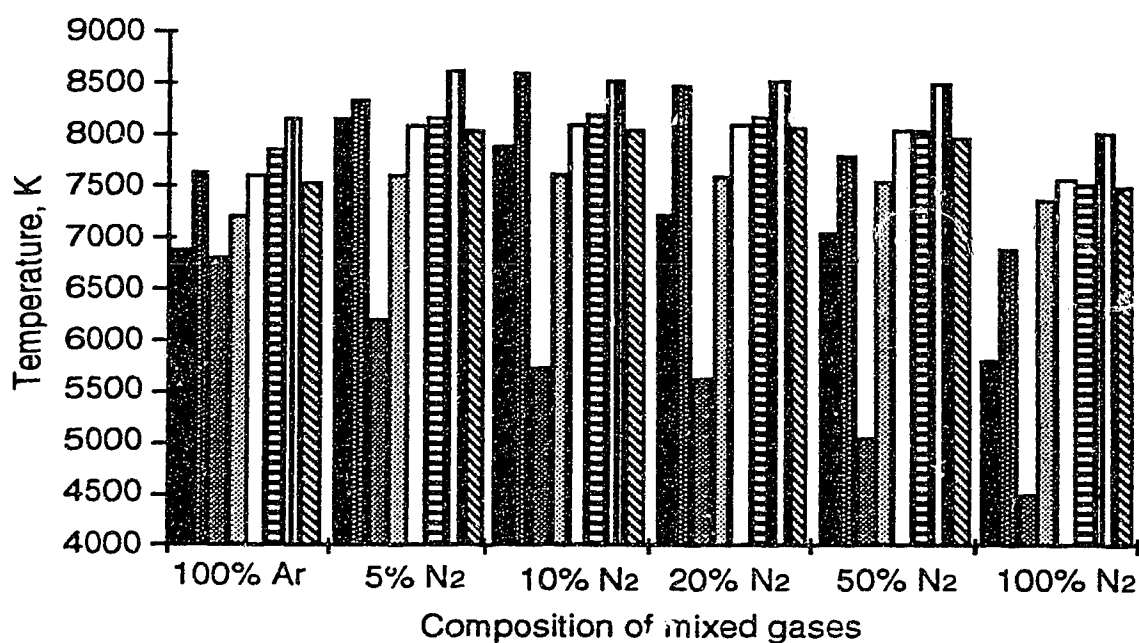
Fig. 43. Effect of increasing the amount of nitrogen in the coolant on the maximum temperatures obtainable of different thermometric species in argon-nitrogen mixed-gas plasma discharges at 1.5 kW.

(■) T_{ex} from 6 Fe I lines   (▦) T_{ex} from 8 Fe II lines

(▨) T_{ex} from 11 Ti II lines   (▣) T_{ion} from Ca II/Ca I

(□) T_{ion} from Cd II/Cd I   (▤) T_{ion} from Fe II/Fe I

(▥) T_{ion} from Mg II/Mg I   (▧) T_{ion} from Zn II/Zn I

50%, drops in temperatures for all the thermometric species begin to be very obvious. Dramatic decreases in temperature are observed when argon in the coolant is completely replaced by nitrogen.

It is hard to understand that the excitation temperature of Ti II keeps decreasing at all observation heights with the increase in the percentage of nitrogen in the coolant.

Nothing particularly new can be said about the data in Fig. 43 - the summary figure of the data in Fig. 42. It indicates temperature increases of up to 1300 K with the replacement of less than 50% argon in the coolant by nitrogen.

3-6-4. Argon-oxygen mixed-gas plasmas

As provided in Fig. 44, the temperatures measured from 2 mm to 10 mm above the load coil with 5% to 100% argon in the coolant being replaced by oxygen basically show the same behavior as argon-air and argon-nitrogen mixed-gas plasma discharges. There is no need to repeat how the temperatures vary with increasing amount of oxygen here. However, there is also something unusual about the excitation temperatures derived from the 11 Ti II lines. At all observation heights, the excitation temperatures of Ti II are slightly lower than those measured in the pure-argon plasma discharge with 5% oxygen in the coolant; then they begin to increase gradually when the amount of oxygen in the coolant is increased to 10%; when 20% to 100% oxygen was introduced, the temperatures of Ti II basically remained unchanged.
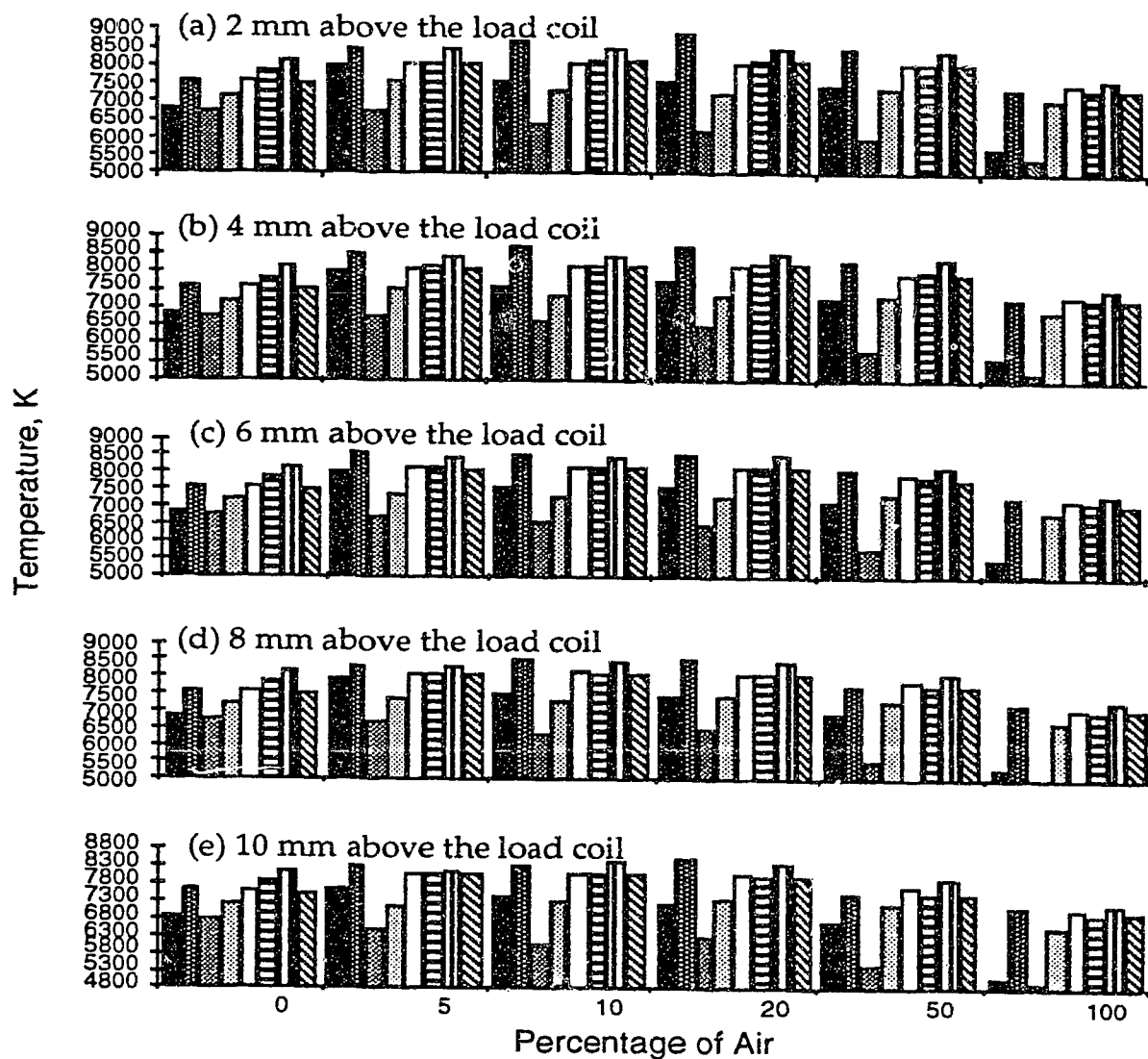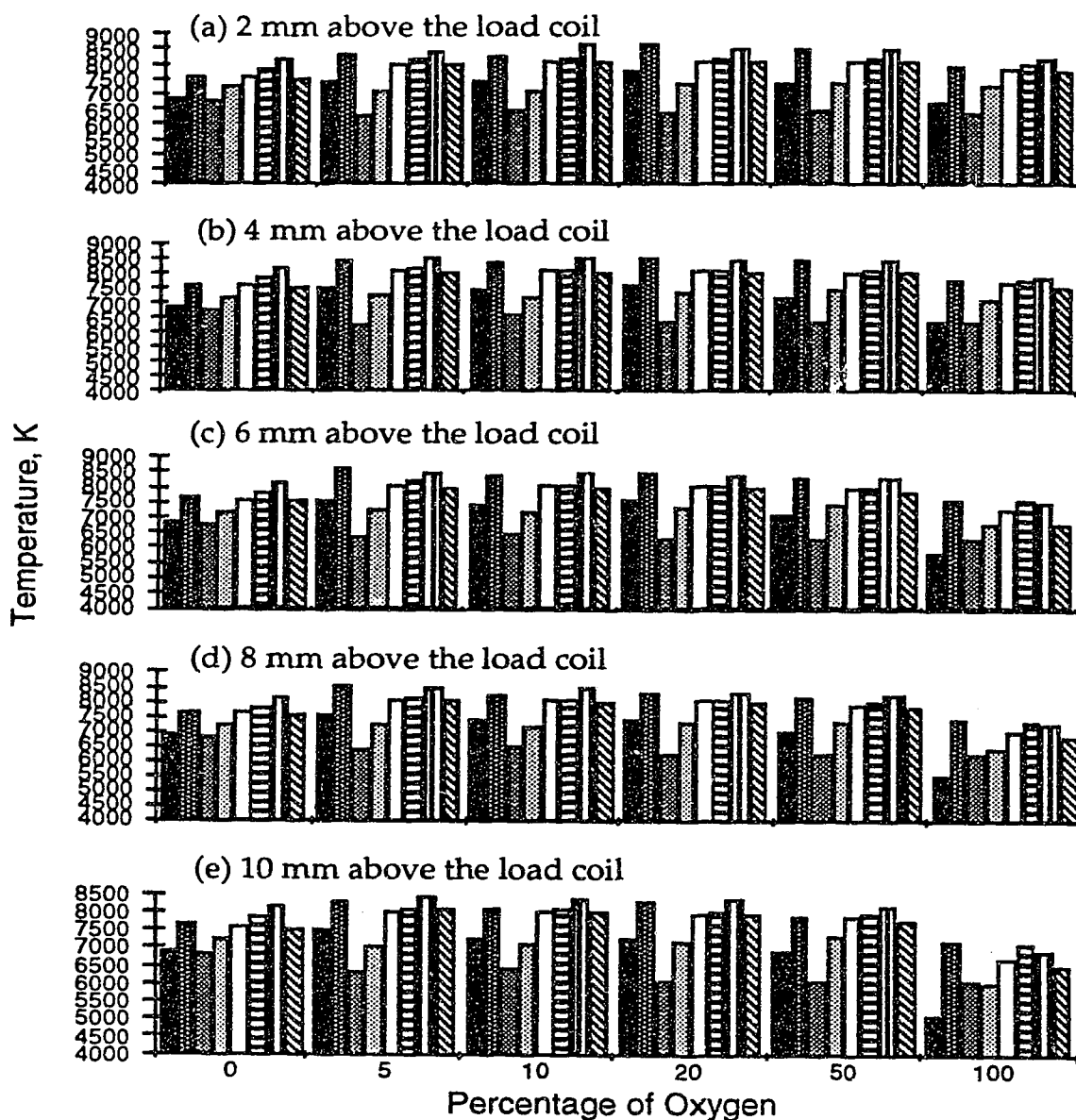
Fig. 44. Effect of increasing the amount of oxygen in the coolant on the temperatures of different thermometric species in argon-oxygen mixed-gas plasma discharges at various heights at 1.5 kW.
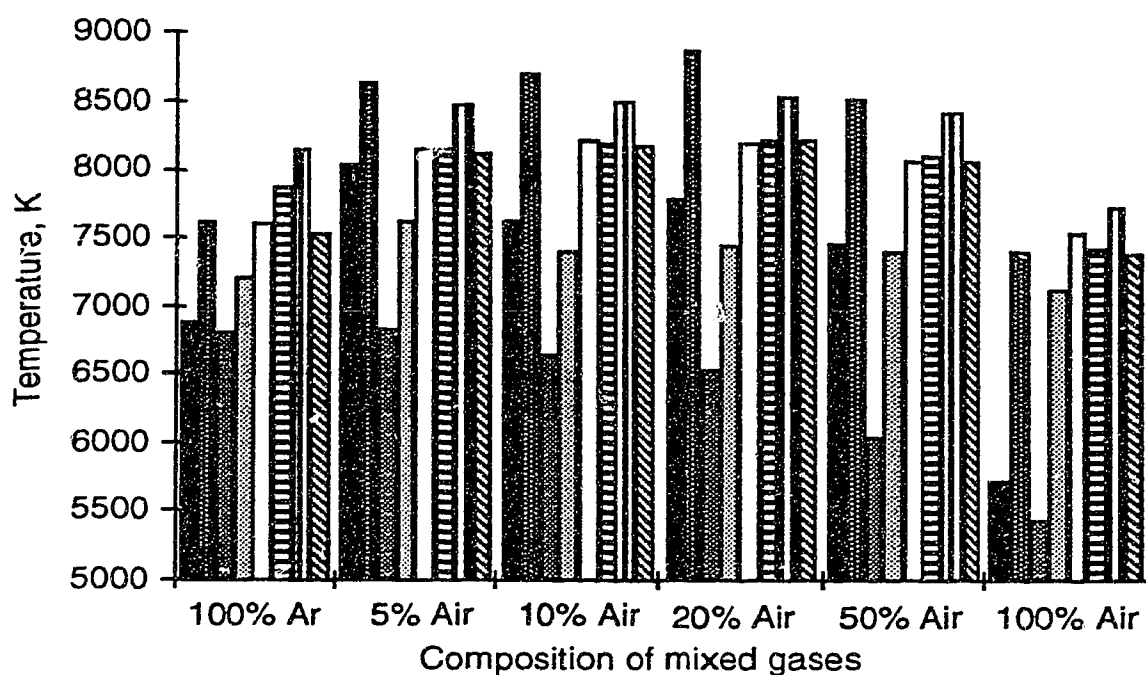
(■) T$_{ex}$ from 6 Fe I lines   (▥) T$_{ex}$ from 8 Fe II lines

(▦) T$_{ex}$ from 11 Ti II lines   (▨) T$_{ion}$ from Ca II/Ca I

(☐) T$_{ion}$ from Cd II/Cd I   (▤) T$_{ion}$ from Fe II/Fe I

(▥) T$_{ion}$ from Mg II/Mg I   (▧) T$_{ion}$ from Zn II/Zn I
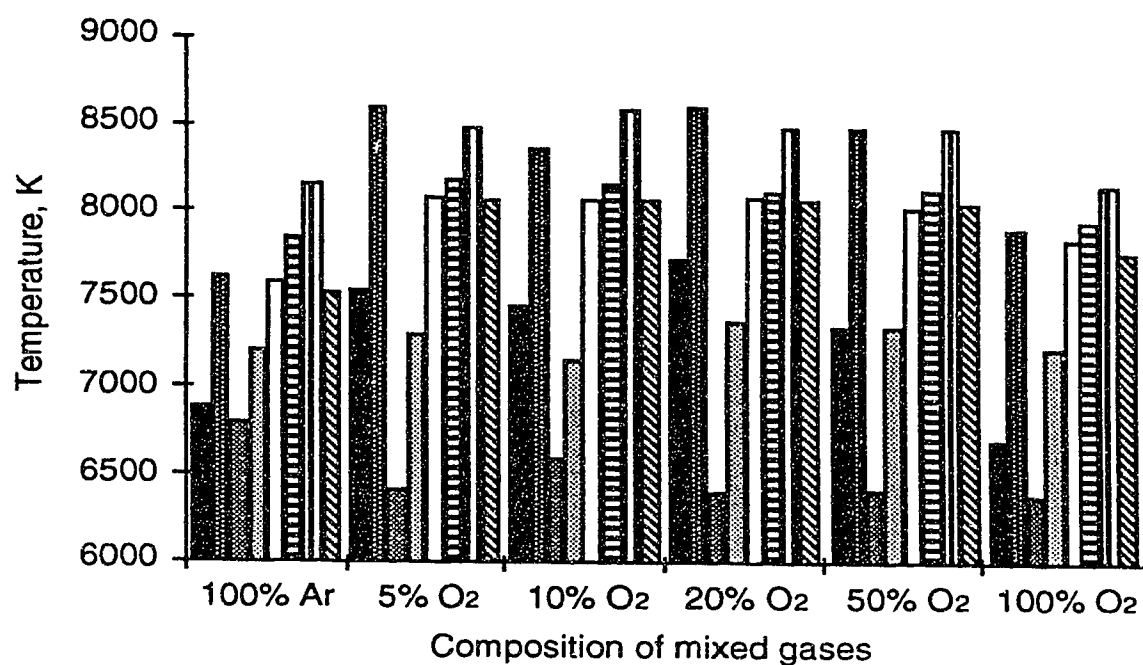
Fig. 45. Effect of increasing the amount of oxygen in the coolant on the maximum temperatures obtainable of different thermometric species in argon-oxygen mixed-gas plasma discharges at 1.5 kW.

(■) T_{ex} from 6 Fe I lines   (▦) T_{ex} from 8 Fe II lines

(▦) T_{ex} from 11 Ti II lines   (▨) T_{ion} from Ca II/Ca I

(□) T_{ion} from Cd II/Cd I   (▤) T_{ion} from Fe II/Fe I

(▥) T_{ion} from Mg II/Mg I   (▧) T_{ion} from Zn II/Zn I

Data in Fig. 45. is the summary of the data in Fig. 44. Because the temperature variations with the amount of oxygen in the coolant are practically the same at all observation heights, Fig. 45 does not show anything new. A temperature boost of up to 1000 K can be achieved by the introduction of not more than 50% oxygen into the coolant stream of an argon plasma discharge.

3-6-5. Summary

Shown in Fig. 46 are the highest possible temperatures that can be achieved regardless of observation height and percentage of nonargon gases in the coolant.

It is observed that temperature increases from 300 K to 1400 K are achievable under suitable operating conditions when not more than 50% air, helium, nitrogen, and oxygen are introduced into the coolant stream of a normal argon-supported plasma discharge. The magnitudes of temperature increase depend on the kinds of nonargon gases mixed into the coolant. The order of temperatures measured in various mixed-gas plasma discharges is: argon-air $\geq$ argon-nitrogen > argon-oxygen > argon-helium > pure argon. The excitation temperatures of Ti II show the following order: argon-helium > argon-air > pure argon > argon-oxygen > argon-nitrogen.

The magnitudes of the temperature increase relative to those achievable in a pure-argon plasma discharge also depend upon the thermometric species used (which it should not). For the excitation temperatures derived from the 6 Fe I lines and from the 8 Fe II lines, these
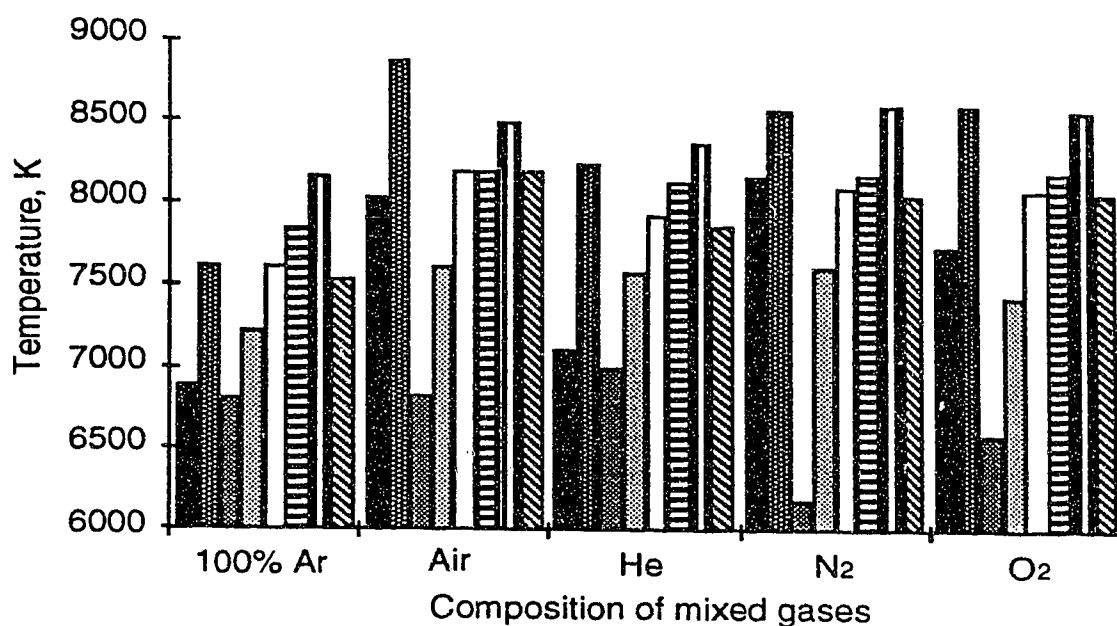
Fig. 46. Maximum temperatures obtainable of different thermometric
species in various mixed-gas plasma discharges at 1.5 kW
regardless of observation height and percentages of nonargon
gases in the coolant.

(■) T_{ex} from 6 Fe I lines   (▨) T_{ex} from 8 Fe II lines
(▨) T_{ex} from 11 Ti II lines   (▨) T_{ion} from Ca II/Ca I
(□) T_{ion} from Cd II/Cd I   (▤) T_{ion} from Fe II/Fe I
(▥) T_{ion} from Mg II/Mg I   (▨) T_{ion} from Zn II/Zn I

increases can be as high as 1000 K to 1400 K as measured in argon-air and argon-nitrogen mixed-gas plasma discharges. For the ionization temperature of Ca, minimal temperature increases of 300 K to 500 K are indicated when various nonargon gases are introduced into the coolant even under the optimized operating conditions. It is even more puzzling to see that the excitation temperatures of Ti II only see very minimal increases in an argon-helium mixed-gas plasma discharge, while in other mixed-gas discharges, decreases in temperatures of up to 600 K are indicated. The lack of consistency between the temperatures measured and temperature increases obtained with different thermometric species can be attributed to, partly, the use of older and/or unreliable gf or gA values from different sources. Similar discrepancies were also observed by other researchers [51, 52, 57]. Most authors blamed heavily on the unreliable gf or gA values used. Faires et al. [57] measured excitation temperatures for seven thermometric species using a high resolution Fourier transform spectrometer, temperatures measured varied from 4392 K to 6142 K depending the thermometric species used. They also compared excitation temperatures derived from the relative intensities of Fe I lines using gf values from six different sources, it was found that the calculated temperature values were critically dependent on the gf values chosen from the literature. In the author's opinion, both the availability and the accessibility of accurate gf or gA values to the analytical chemist still remain to be problems. The assumption of the existence of local thermal equilibrium (LTE) in the source used could be another reason. It was even found that [49, 52] the excitation temperature measured was a function of the excitation energy of the upper states of the spectral transitions used in the calculations, and that higher energy species provided high temperatures. This

suggested deviation from local thermal equilibrium (LTE). From the results obtained from this study, it is reasonable to say that the source used under the operating conditions is not in local thermal equilibrium (LTE). Chemical interference could also be a problem. Excitation temperatures derived from 11 Ti II lines have shown unusual behaviors throughout this chapter. It is thought that the possible formation of Titanium dioxides TiO_2 (melting point: 1892 °C) and/or Titanium nitrides TiN (melting point: 2930 °C) might be one of the problems. The formation of these refractory compounds could lead to erroneous intensity measurements, thus inaccurate temperature values. Further studies are still needed.

All the temperatures measured in this study agree reasonably well with corresponding temperatures reported in the literature [35, 41, 44, 46, 49-53, 55-60, 66, 161].

3-7. Comparison of detection limits determined in mixed-gas plasma discharges for selected elements

Detection limits of 5 elements were determined in a pure-argon plasma discharge and plasma discharges with 5% air, 5% helium, 5% nitrogen, and 5% oxygen in the coolant using both a multielement solution and 5 single-element solutions. The multielement solution contains 100 μg/ml Zn, 1.0 μg/ml Mg, 50.0 μg/ml Cd, 2.0 μg/ml Mn, and 10.0 μg/ml Fe. The single-element solutions are: 10.0 μg/ml Zn, 1.0 μg/ml Mg, 10.0 μg/ml Cd, 5.0 μg/ml Mn, and 10.0 μg/ml Fe. All the measurements were carried out at an auxiliary gas flow rate of 1.1 l/min and at a constant forward power of 1.5 kW. For the pure-argon plasma discharge and the plasma discharge with 5% helium in the coolant, the observation height was set at 14 mm above the load coil, and

the nebulizer flow rate was set at 1.0 l/min. For argon plasma discharges with 5% air, 5% nitrogen, and 5% oxygen in the coolant, the observation height was set at 8 mm above the load coil and the nebulizer flow rate at 1.1 l/min.

The detection limit of an element was calculated as the concentration of this element that will produce a signal three times the standard deviation of the blank. The blank standard deviation (of 50 data points) was calculated from a region of the baseline in the analyte spectrum that was close to the analytical line and the peak height values were used in this study. The spectra used in these calculations were 16 k, 4 time dealiased (4 data points for every He-Ne laser fringe) and 12 scans were co-added. The relative detection limits (relative to the corresponding detection limits measured with the multielement solution aspirated in the pure argon plasma discharge) are provided in Table 8.

It can be seen that the detection limits for the 5 elements obtained in argon-5% air and argon-5% nitrogen mixed-gas plasma discharges are up to 2 to 3 times lower than those achieved in the pure-argon plasma discharge. The detection limits determined in argon-5% helium and argon-5% oxygen mixed-gas plasma discharges are roughly equivalent to those measured in the pure-argon plasma discharge. It is also very obvious that detection limits measured using single element solutions are slightly superior to those measured using multielement solution. This could be explained by the "multiplex disadvantage" mentioned in Chapter 1 when multielement solution was used.

The detection limits could be better if optimized operating conditions

Table 8. Comparison of detection limits determined in various ICP discharges

Element	Wavelength (nm)	Relative detection limits									
		pure Ar		Ar-5% air		Ar-5% He		Ar-5% N2		Ar-5% O2	
		M*	S*	M*	S*	M*	S*	M*	S*	M*	S*
Mg II	279.553	1.0	0.61	0.39	0.27	0.91	0.68	0.52	0.39	0.80	0.70
Fe II	259.940	1.0	0.77	0.52	0.43	1.07	0.85	0.76	0.47	0.86	0.75
Zn I	213.856	1.0	0.58	0.42	0.23	1.17	1.01	0.98	0.60	0.78	0.53
Cd II	226.502	1.0	0.58	0.30	0.25	1.09	0.46	0.41	0.30	0.83	0.42
Mn II	257.610	1.0	0.60	0.52	0.36	1.00	0.81	0.60	0.42	0.80	0.62

M*- multielement solution
S* - single element solutions

for each individual element are used. It is also possible to achieve lower detection limits through longer signal averaging and increasing the interferogram length as these factors increase the measurement time.

3-8. Conclusions

Fourier transform spectrometry has been used in a basic spectrochemical study of the inductively coupled plasma discharges with various amounts of air, helium, nitrogen, and oxygen in the coolant at various observation heights in the middle of the aerosol channel.

Although somewhat lower temperatures were observed in some cases when a "long torch" was used in the study, the real difference a "long torch" makes is to shift the "hottest" spot in the middle of the aerosol channel up by 5 mm.

With the introduction of nonargon gases into the coolant, the "hottest" spot in the middle of the aerosol channel moves toward the load coil. The introduction of helium in the coolant does not have a major effect on the temperature profiles. When less than 50% air, nitrogen, and oxygen are in the coolant, the excitation and ionization temperatures are more uniform along the central aerosol channel than those measured in the pure-argon plasma discharge. Temperature increases from 300 K to 1400 K are achievable when less than 50% air, helium, nitrogen, and oxygen are introduced into the coolant stream. When more than 50% air, helium, nitrogen, and oxygen are introduced, comparable to much lower temperatures are observed in comparison to those measured in the pure-argon plasma discharge.

Under most suitable operating conditions, the order of temperature that can be achieved in mixed-gas plasma discharges with less than 50% nonargon gases in the coolant generally is: argon-air $\geq$ argon-nitrogen > argon-oxygen > argon-helium > pure argon.

Although 11 repetitive temperature measurements for all the 8 thermometric species indicated excellent precision (maximum RSD for excitation temperature: 80 K; maximum RSD for ionization temperature: 30 K), accuracy is still a problem. Even under exactly the same operating conditions, different thermometric species give different temperatures. The discrepancies can be attributed to (1) different sources of the gf or gA values used in the calculations (2) deviation from local thermal equilibrium (LTE) of the ICP source used and (3) possible chemical interferences. Among the 8 thermometric species used in this study, the excitation temperature derived from the 8 Fe II lines and the ionization temperature calculated from the intensity ratio of Mg II to Mg I are always the highest; whereas, the excitation temperature derived from the 11 Ti II lines and the ionization temperature calculated from the intensity ratio of Ca II to Ca I are always the lowest. The ionization temperatures of Cd, Fe, and Zn are always in very close agreement.

Chapter 4

Bandpass preselection ICP-Fourier transform spectrometry

4-1. Introduction

As discussed in Chapter 1, there are two major inherent problems with the FTS technique which are detrimental to the overall performance of the FTS system in the ultraviolet and visible spectral regions. The first one is the multiplex disadvantage which results from the increased amount of noise imposed on one spectral line by other relatively strong emission lines in the same spectral region. The final result is a degradation of the signal-to-noise ratio (S/N) of this particular spectral line. The "extra" noise contributed by other emission lines must be eliminated or at least strongly reduced. The second one is the dynamic range limitation also imposed by strong emission signals, which must be reduced to make the simultaneous observation of weaker signals possible. To eliminate or at least reduce the "trouble making" unwanted strong emission lines, additional filtering, either optical or electronic, must be carried out.

Electronic filtering is already present in the FTS system developed and currently used in our laboratory in the form of low-pass and high-pass electronic filters. In this way, however, all incident radiation and associated noises from the ICP is still collected by the detector in the interferometer.

One alternative approach is to limit the optical bandpass into the interferometer itself. The bandpass is narrowed such that only a small region around the spectral position of the desired information is observed by the

interferometer at a time. In most cases, information about the whole spectrum is not required anyway - rather one or a few selected windows (small spectral regions) would be sufficient for many analytical tasks. The spectral window or windows should be broad enough to include the spectral line or lines of interest and the background and narrow enough to exclude unwanted spectral lines.

The concept of pre-filtering or pre-selecting has been proven in this laboratory. Stubley and Horlick developed a system called "window slew-scan" Fourier transform spectrometry (WSS-FTS) [19]. In their system, a low resolution monochromator was coupled to a Michelson interferometer. By using 2 mm entrance and exit slits the optical bandpass was limited to just 4 nm. The idea was to pass a selectable window of the spectrum and let the FTS part of the system achieve the desired spectral resolution within the window. By appropriately setting the position of the spectral window around the spectral line or lines of interest, unwanted high intensity components of the source radiation could be blocked, prior to entering the interferometer.

Their system was tested with a 16 component multi-element sample. The same solution was run on an ARL 34000 polychromator. A comparison of the detection limits for those elements in the solution, obtained with straight FTS and WSS-FTS, indicated a lowering of the detection limits in the later case by 2 to ten times, indicating some elimination of the multiplex disadvantage.

In this study, variations on this theme are tested and the results will be shown throughout this chapter.

4-2. Instrumental

Instead of a scanning monochromator, a novel pre-dispersion system is used. The pre-disperser or pre-selector is essentially the optical system of a LECO PLASMARRAY™ echelle/photodiode array spectrometer, without the echelle grating and the PDA. The optical arrangement is given in Fig. 47 and the basic operation of this pre-dispersion system is as follows.

The ICP radiation is focussed onto the entrance slit of a 0.5 m polychromator. The spherical grating (G1) disperses the source light and focuses the dispersed components onto the focal plane of the polychromator. Positioned at the focal plane is a mask, which basically is a curved thin metal plate. Slits (127 microns in width, and 17 mm in height) are cut (machined) in the mask at appropriate positions to allow light from preselected narrow wavelength regions to pass through. The slit positions on the mask are centered on spectral lines of choice. The mask is placed at the focal point of a spherical mirror (M1). Since the desired components that pass through the mask are focussed at the position of the slits, each component is collimated by the spherical mirror. The collimated components travel to a plane grating (G2). This is the recombining grating which recombines the narrow wavelength regions transmitted by the mask into a collimated "quasi-white" light beam. This collimated and recombined radiation is folded twice with two plane mirrors (M2 and M3) such that it enters into the interferometer.

By appropriately positioning the slits on the mask, one can choose the components of the source radiation that are desired to enter the
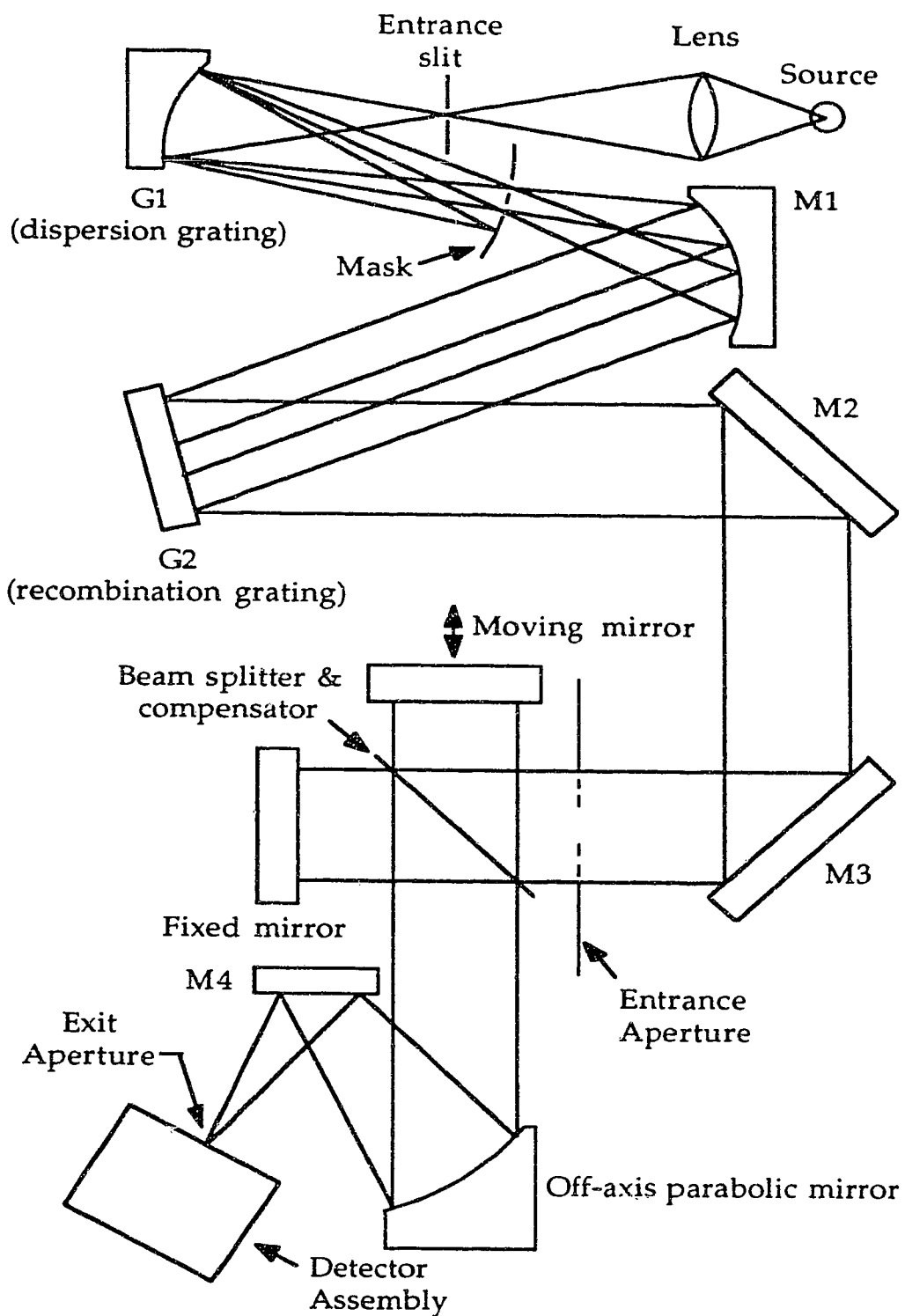
Fig. 47. A simplified schematic diagram of the optical design of the pre-dispersion system.

interferometer, and at the same time, those unwanted large intensity components in the source radiation are removed, thereby allowing small intensity components to be detected.

The ICP assembly and the operating parameters used in this study were the same as listed in Table 6 in Chapter 3 except when indicated otherwise. A constant RF forward power of 1.5 kW is used and an observation height of 14 mm above the load coil is set throughout this work.

4-3. Bandpass pre-selection using optical masks

As mentioned above, with an appropriate mask a set of small wavelength regions can be selected at will. Then the spectral information in these selected wavelength regions can be measured with high resolution and absolute wavelength accuracy in the interferometer.

4-3-1. Single element spectra

The basic spectral characteristics of this pre-dispersion system can be illustrated with a series of mask-out/mask-in measurements for single element solutions.

In Fig. 48.c, the ICP spectrum of 1000 μg/ml Fe solution without any filtering is shown. Two masks designed to select two sets of Fe spectral lines were positioned at the focal plane of the pre-disperser and the spectra measured are shown in Fig. 48.a and Fig. 48.b. The impressive results can be seen more clearly in Fig. 49 - a scale-expanded version of Fig. 48. Fig. 49.c shows the complex spectrum of Fe, Fig. 49.a and Fig. 49.b, with the masks at

Fig. 48. The ICP pectra of a 1000 µg/ml Fe solution with mask 1 in (a) mask 2 in (b) and no mask (c).
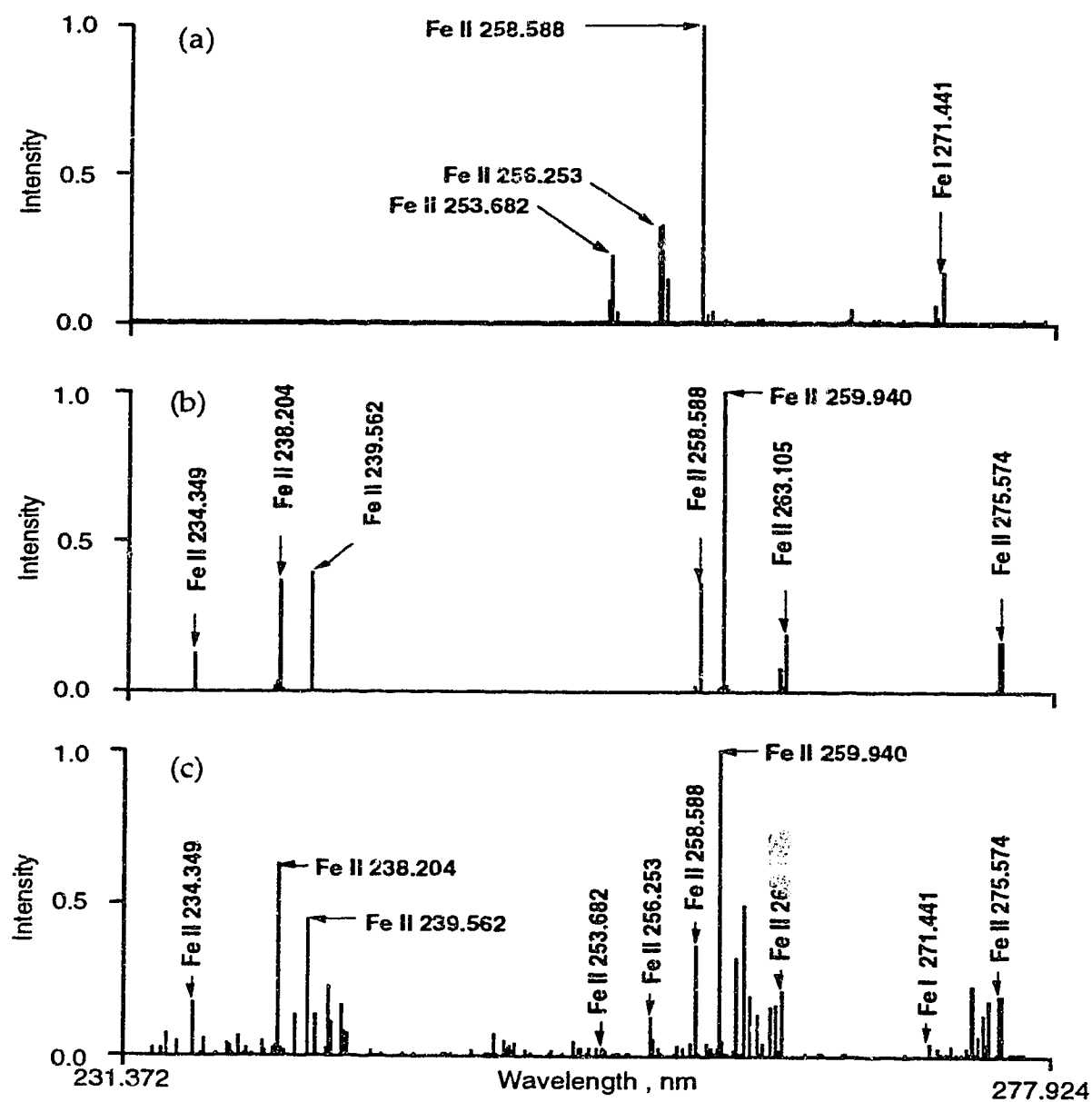
Fig. 49. Scale-expanded plots of the spectra shown in Fig. 48.

the focal plane show practically only the lines that are intended to pass through. Optical leakage in Fig. 49.a is noticeable while in Fig. 49.b it is relatively minimal. The optical masks used in obtaining Fig. 49.a and Fig. 49.b were originally designed to isolated the selected Fe II lines used for the measurement of excitation temperature based on the "Boltzmann plot" method.

The ICP spectrum of a 1000 µg/ml Ni solution without any optical filtering is shown in Fig. 50.b. With a mask designed only to let 5 Ni II lines through placed at the focal plane of the pre-disperser, the desired result is achieved as shown in Fig. 50.a. Details of the two spectra in Fig. 50 can be seen in Fig. 51, which is the scale-expanded version of Fig. 50. The 5 Ni II lines intended to be selected by the mask are designated both in Fig. 51.a and Fig. 51.b.

Shown in Fig. 52.b is the ICP mask-out spectrum of a 1000 µg/ml Cr solution. Fig. 52.a is the ICP mask-in spectrum of the same solution. The details of the difference between the spectra, although quite obvious in Fig. 52, can be seen better in the scale-expanded plots shown in Fig. 53. The lines selected by the mask are all prominent lines, extra lines that got through (optical leakage) are all weak lines, and the extent is also not very severe.

The clear contrast between the ICP mask-in and mask-out spectra of a 1000 µg/ml V solution is illustrated in Fig. 54 and its scale-expanded version Fig. 55. Although the mask picks out the desired 5 lines well, the optical leakage is more severe than previous cases shown above. The ICP mask-in and mask-out spectra of a 1000 µg/ml Si solution and the scale-expanded plots
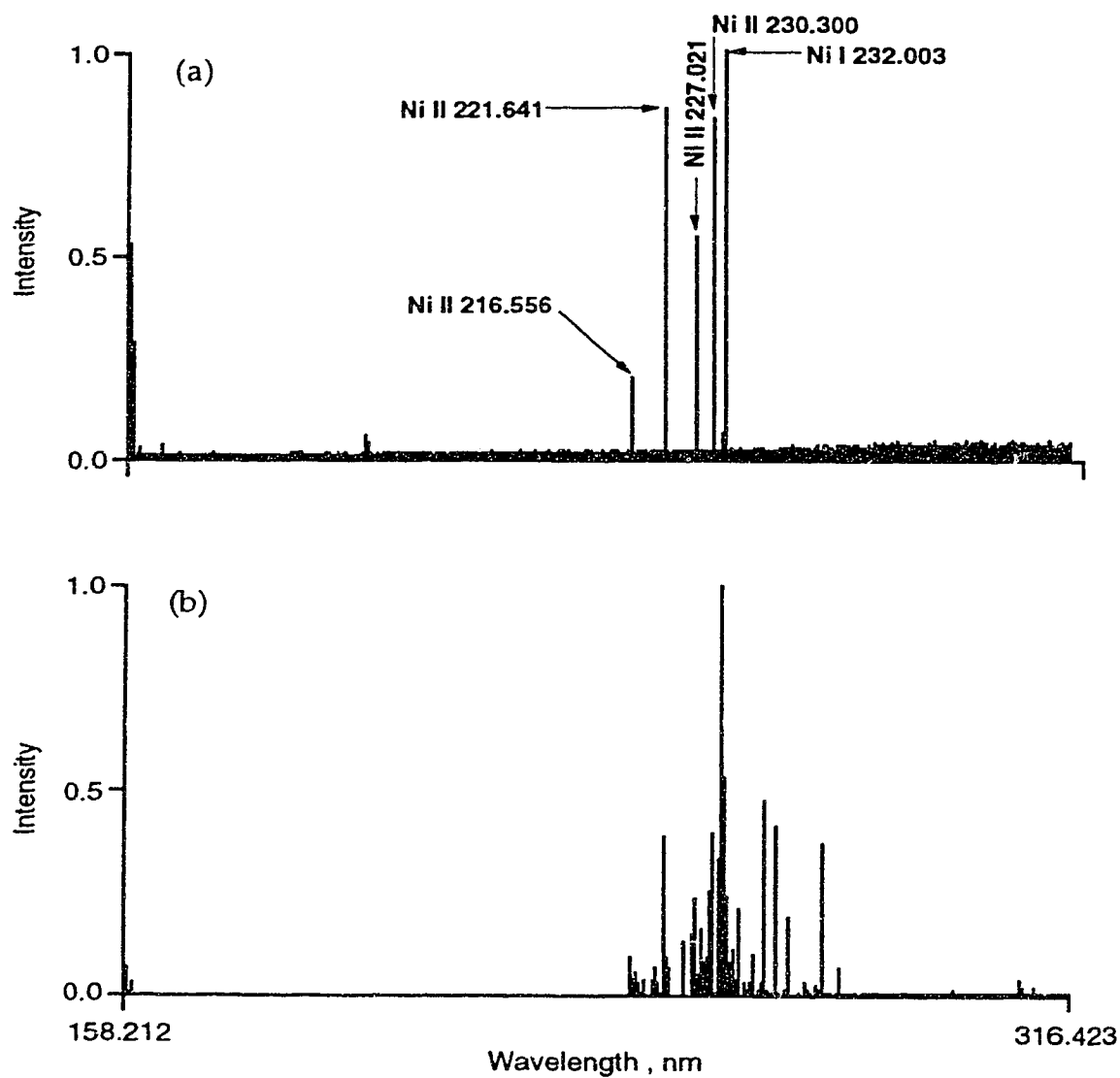
Fig. 50. The ICP pectra of a 1000 μg/ml Ni solution with mask in (a)
and mask out (b).
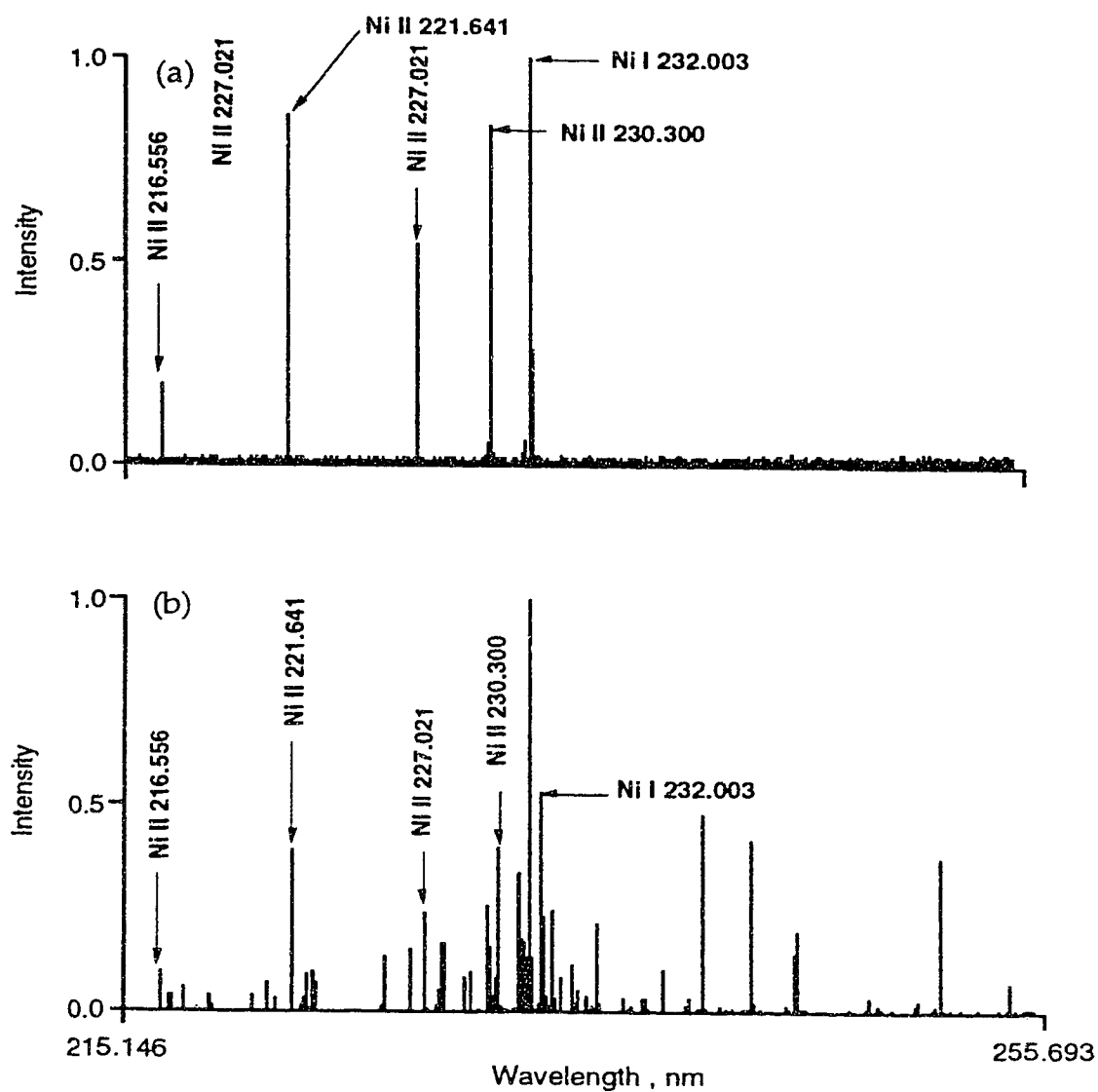
Fig. 51. Scale-expanded plots of the spectra shown in Fig. 50.
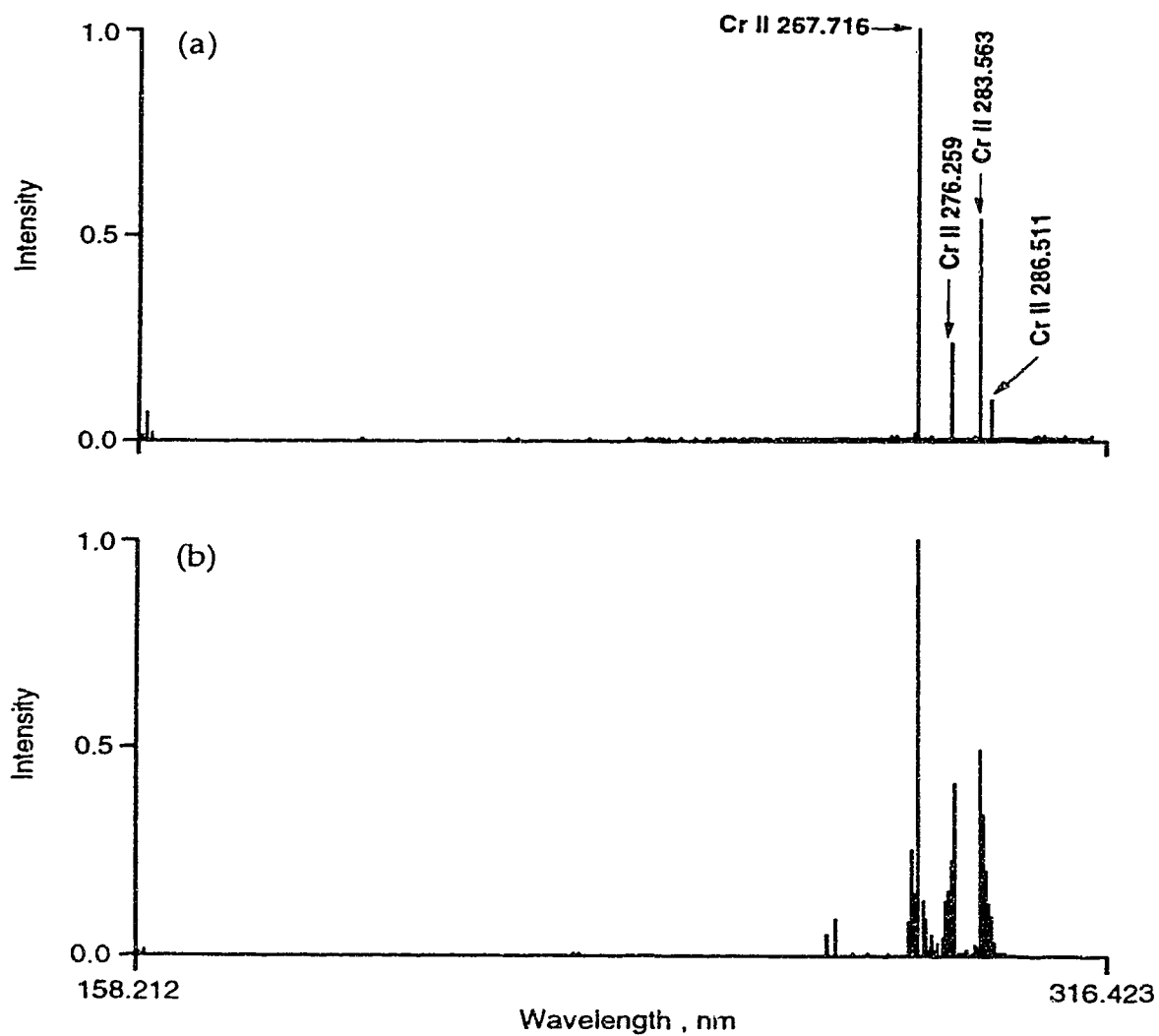
Fig. 52. The ICP pectra of a 1000 µg/ml Cr solution with mask in (a) and mask out (b).
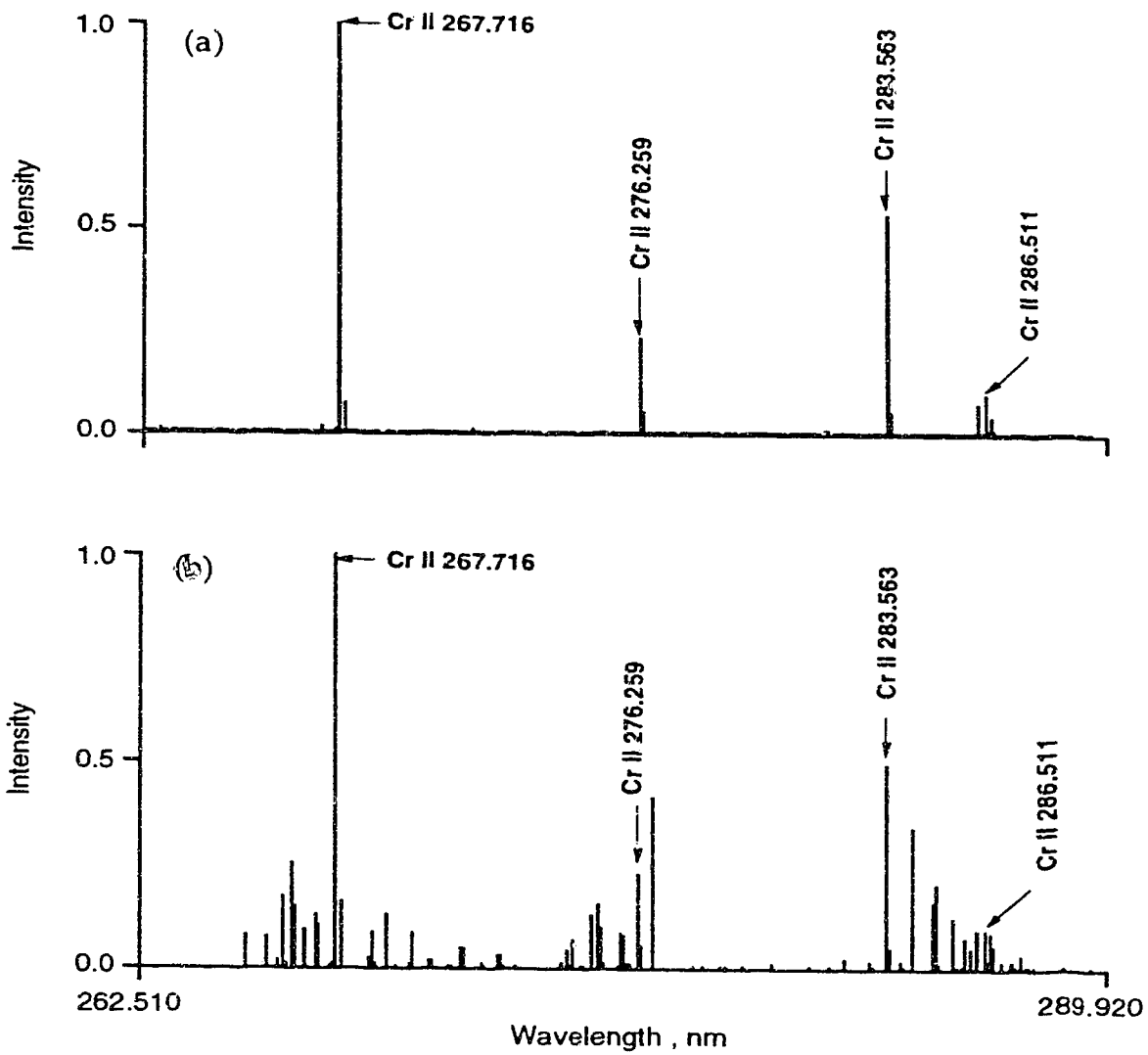
Fig. 53. Scale-expanded plots of the spectra shown in Fig. 52.
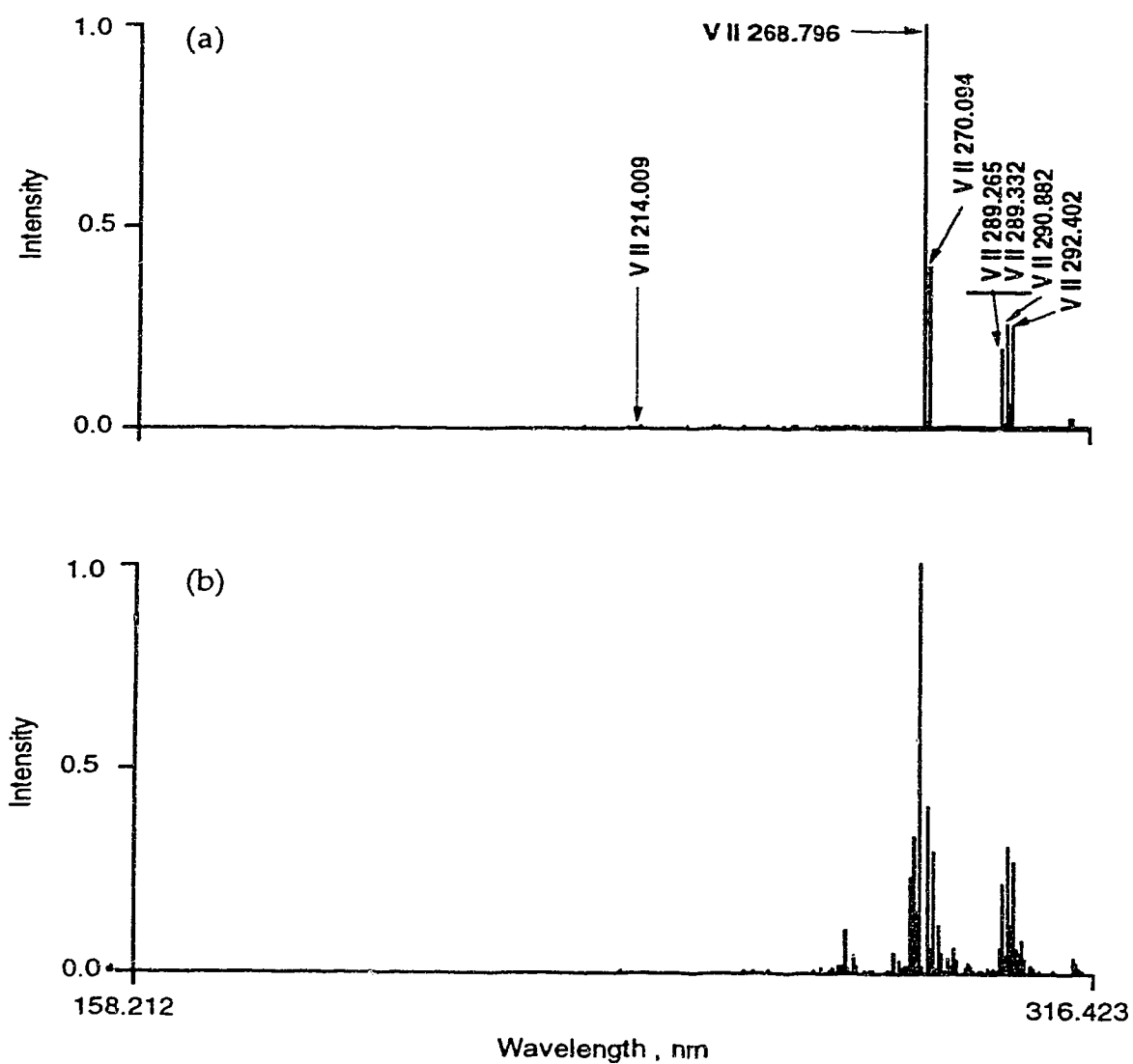
Fig. 54. The ICP pectra of a 1000 μg/ml V solution with mask in (a) and mask out (b).
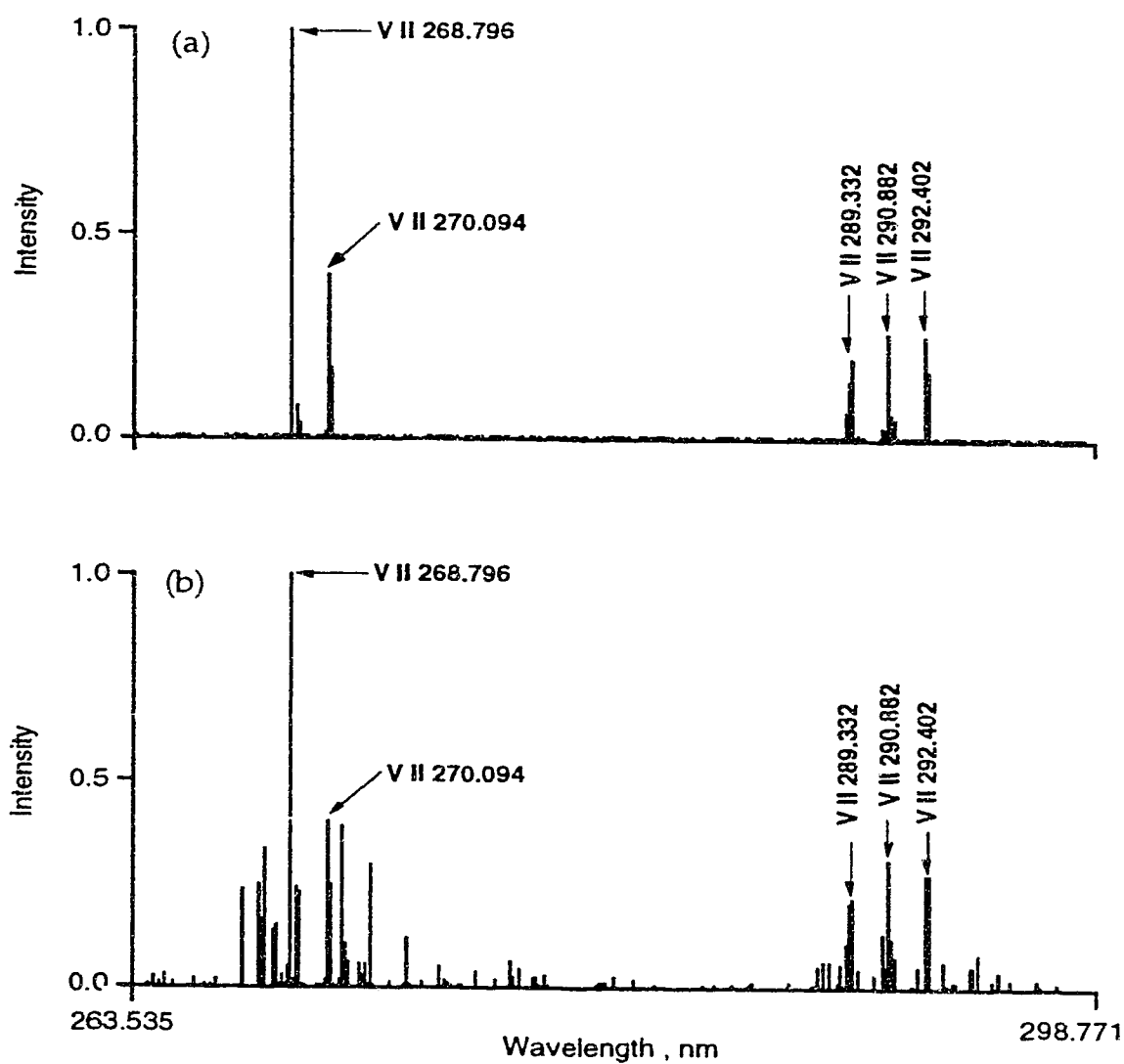
Fig. 55. Scale-expanded plots of the spectra shown in Fig. 54.
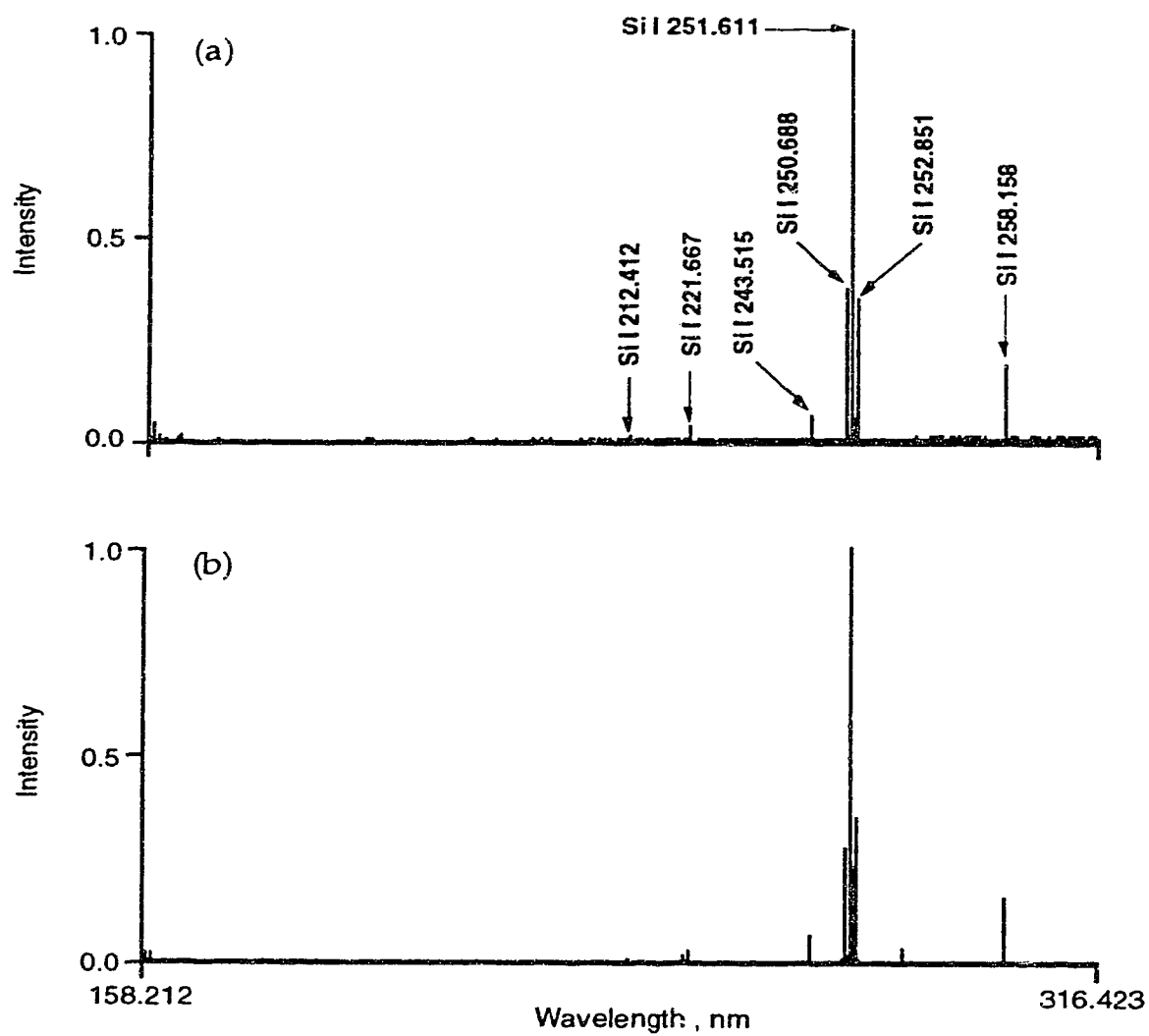
Fig. 56. The ICP spectra of a 1000 μg/ml Si solution with mask in (a) and mask out (b).
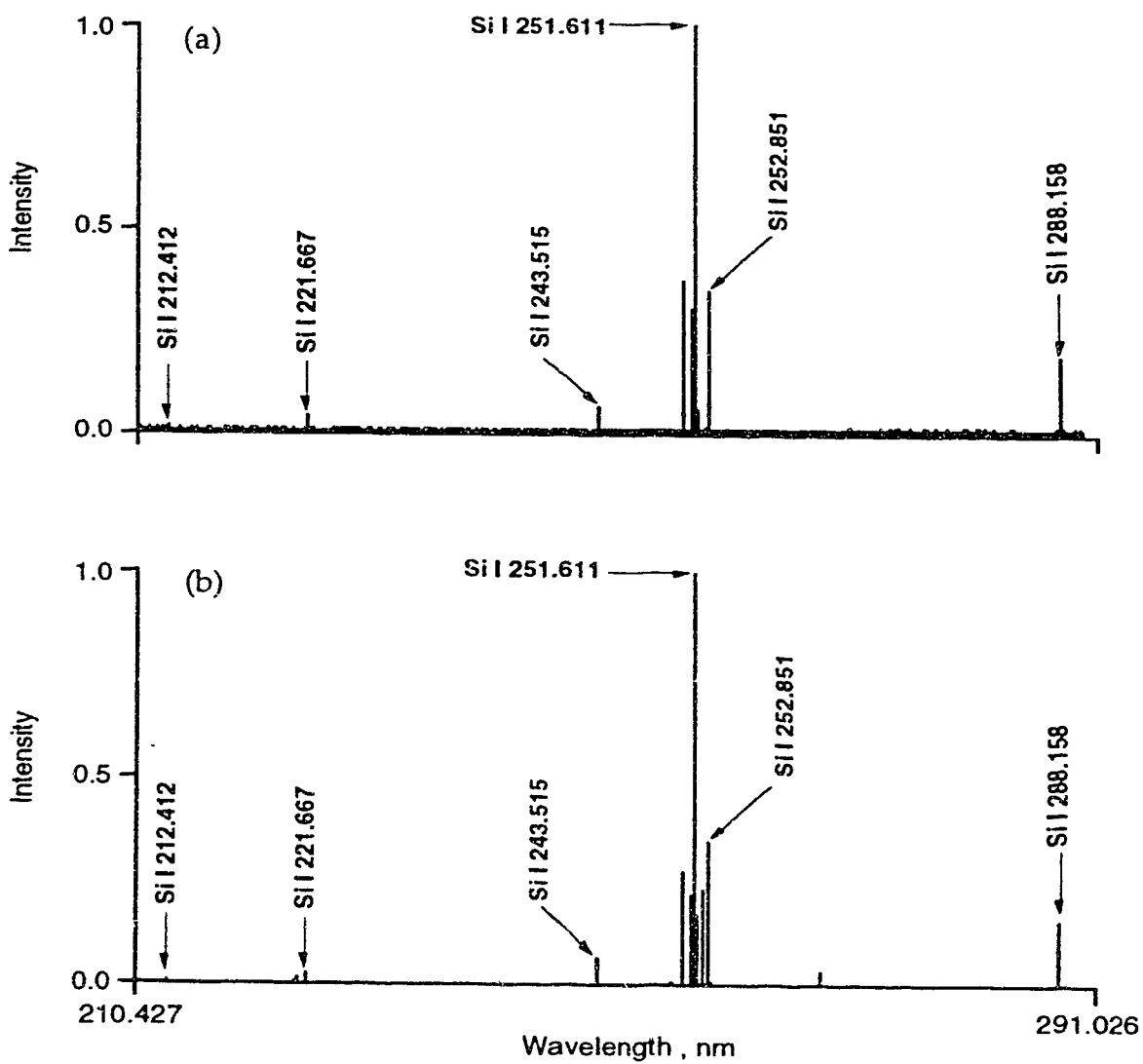
Fig. 57. Scale-expanded plots of the spectra shown in Fig. 56.
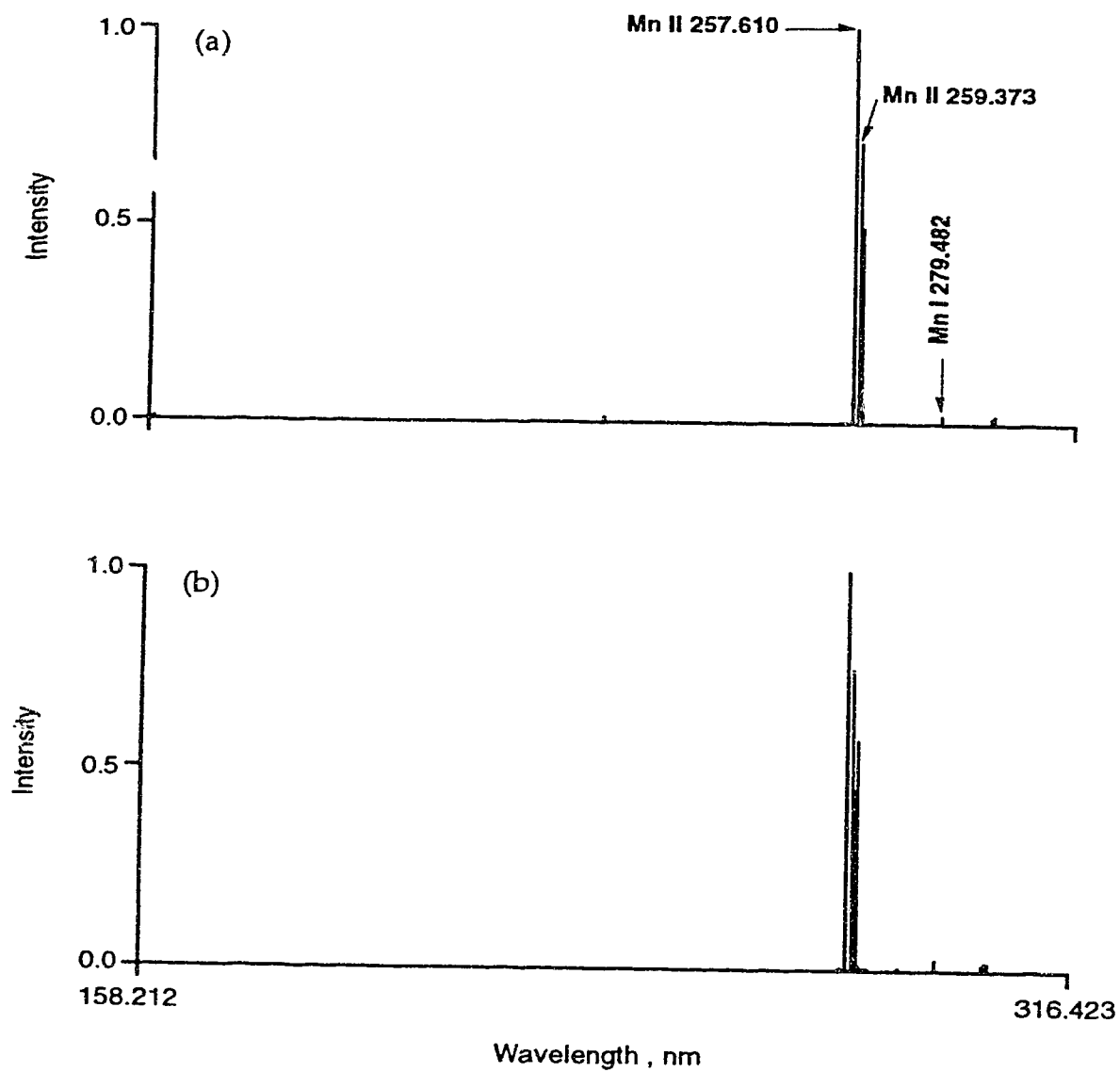
Fig. 58. The ICP spectra of a 1000 μg/ml Mn solution with mask in (a) and mask out (b).
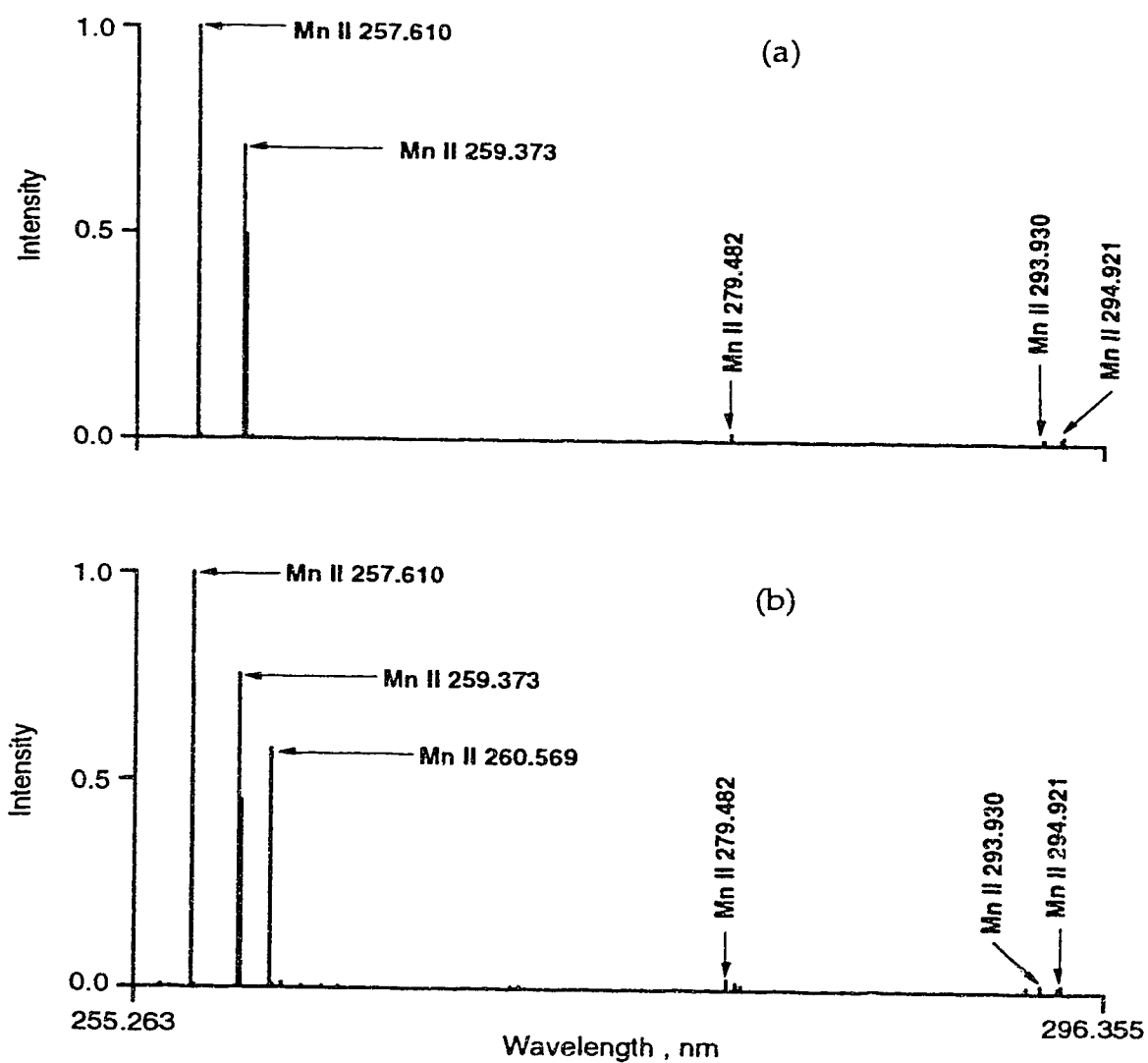
Fig. 59. Scale-expanded plots of the spectra shown in Fig. 58.
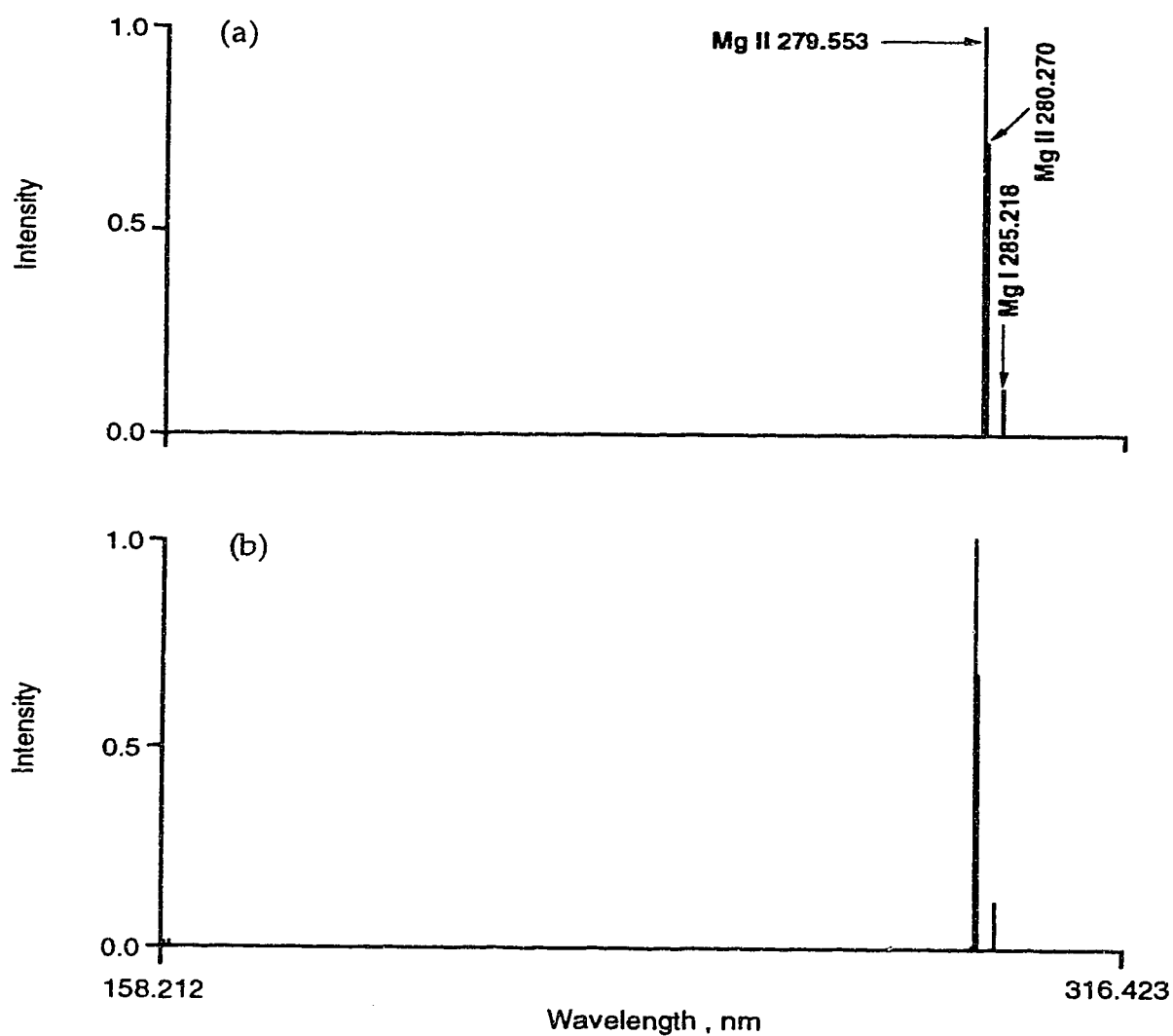
Fig. 60. The ICP spectra of a 1000 µg/ml Mg solution with mask in (a) and mask out (b).
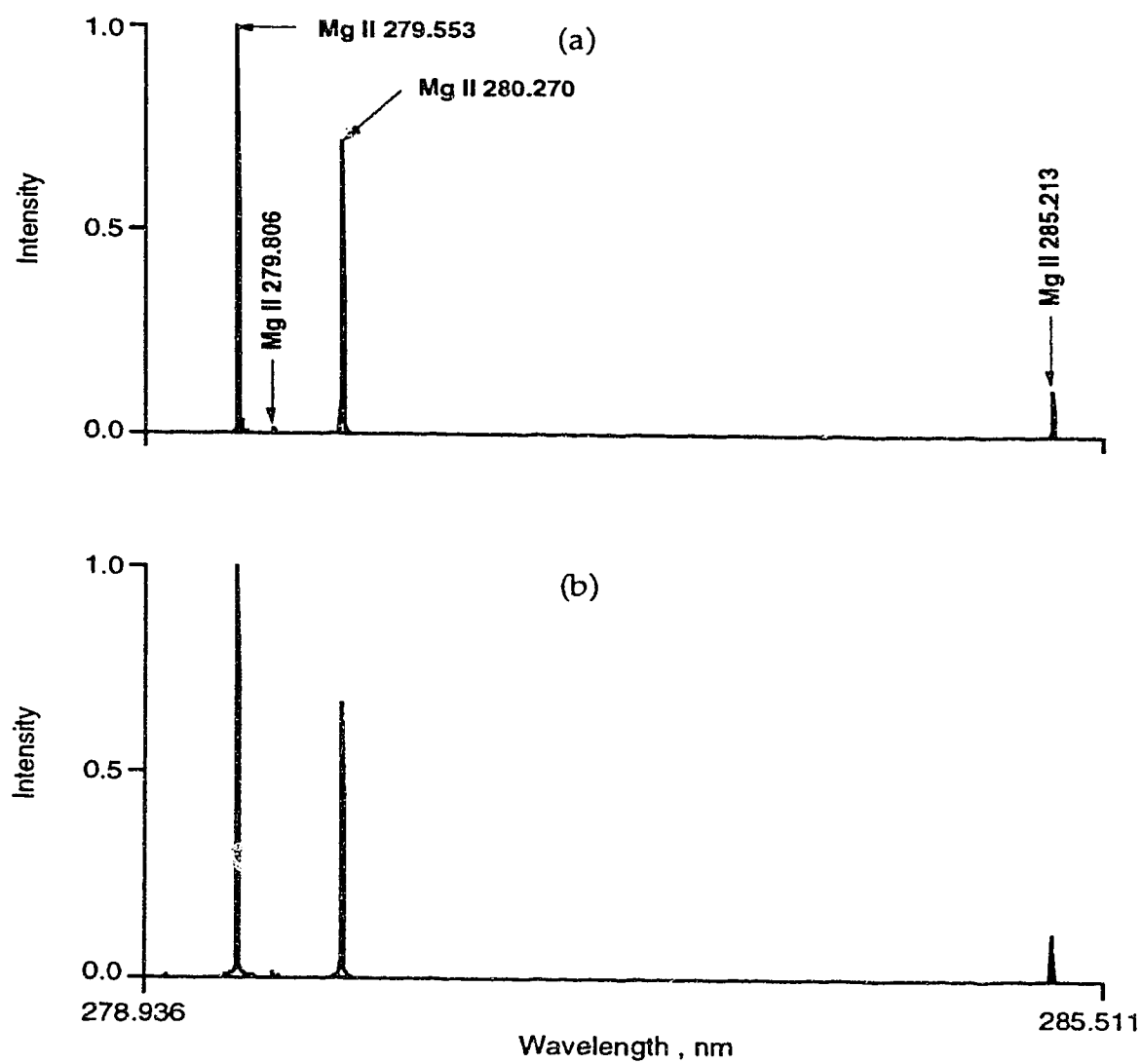
Fig. 61. Scale-expanded plots of the spectra shown in Fig. 60.
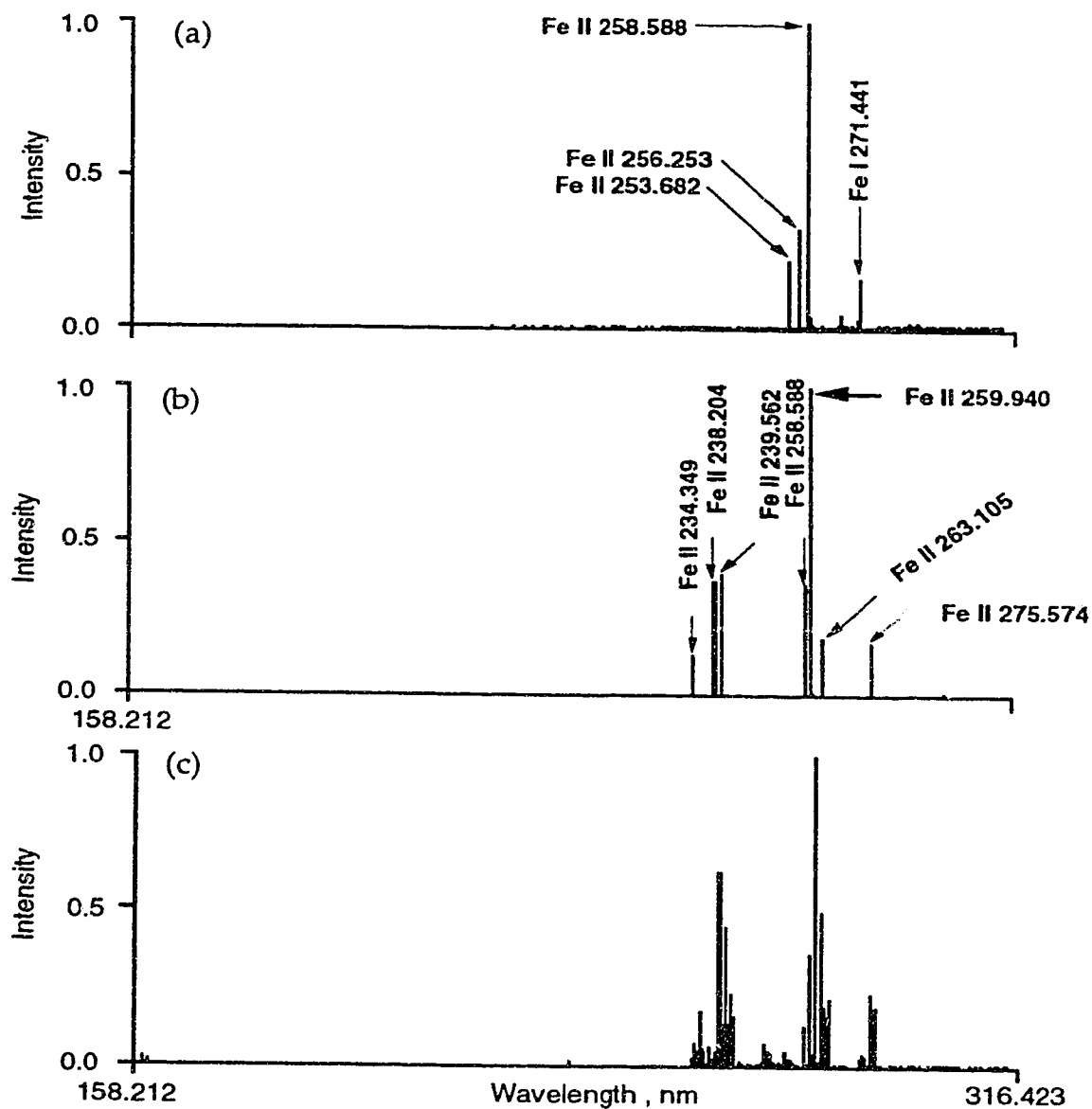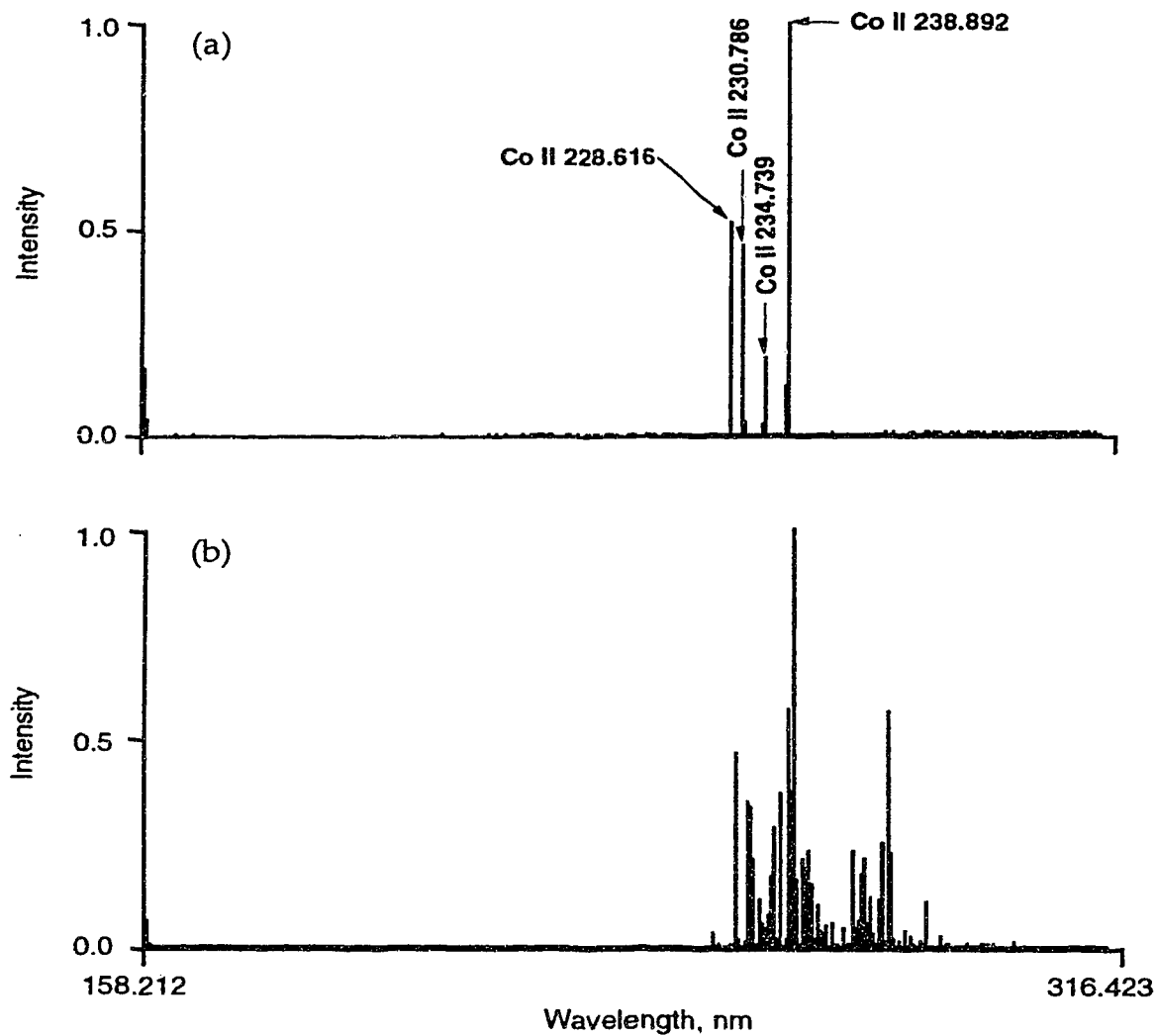
Fig. 62. The ICP spectra of a 1000 µg/ml Co solution with mask in (a) and mask out (b).
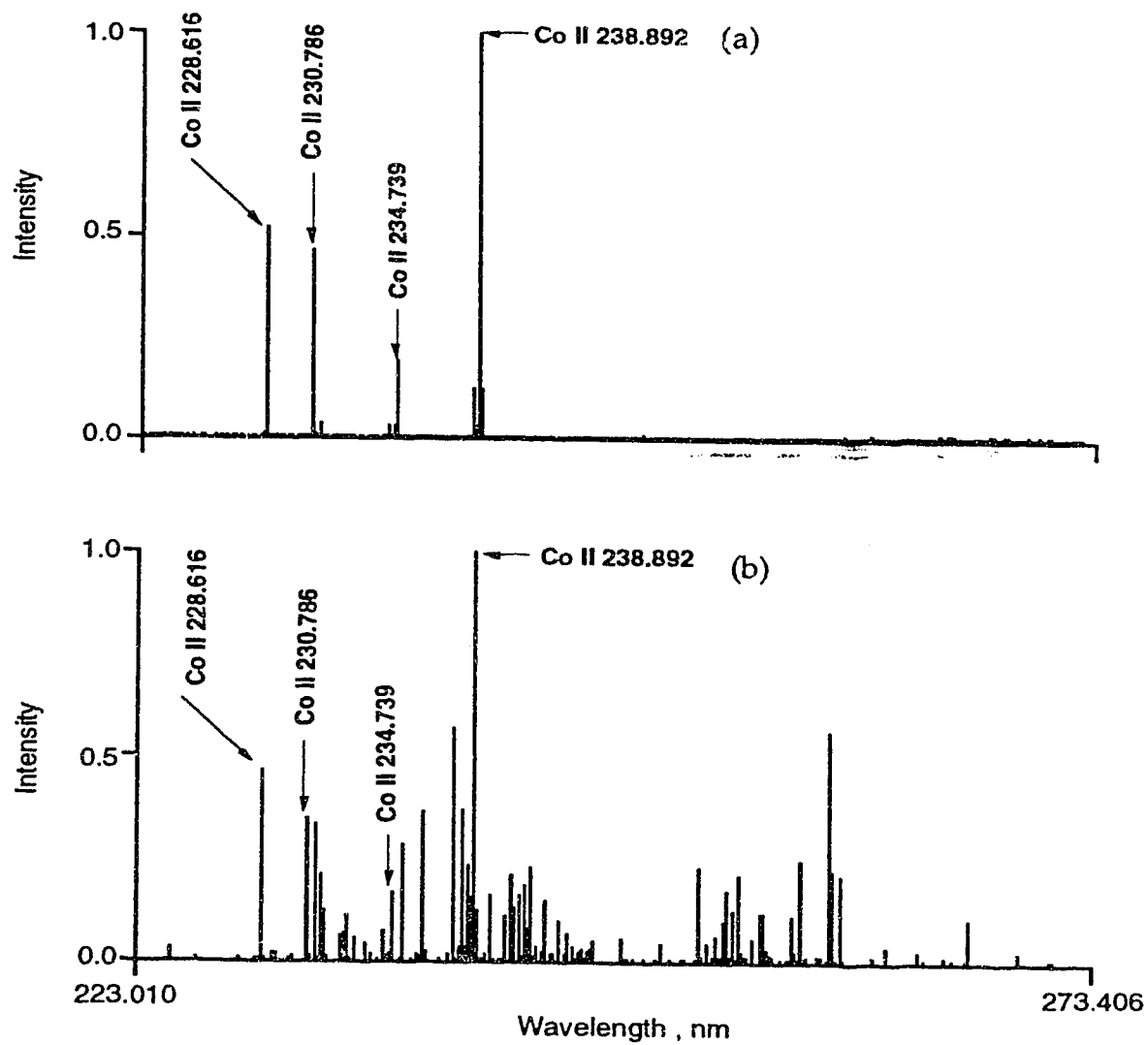
Fig. 63. Scale-expanded plots of the spectra shown in Fig. 62.
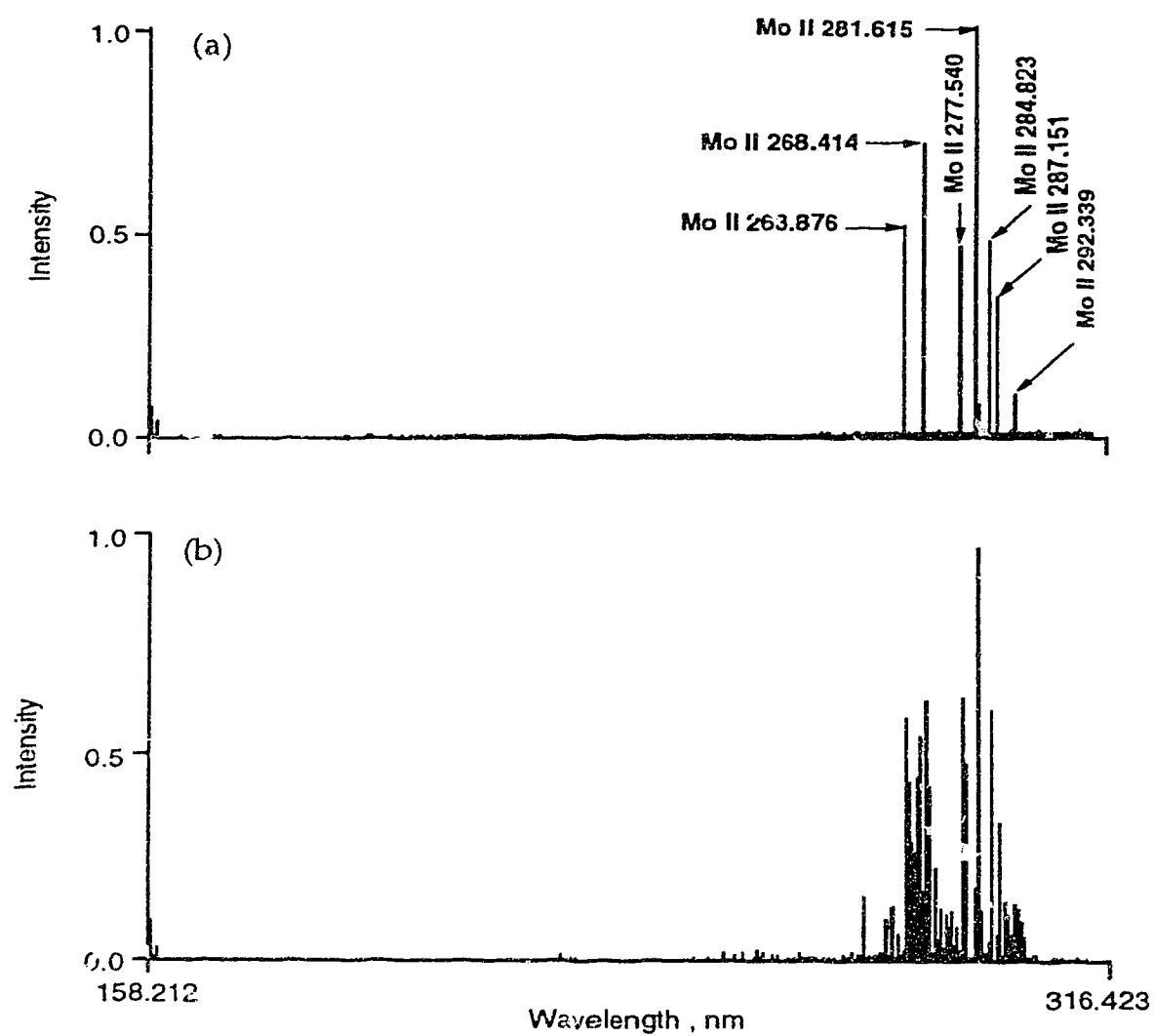
Fig. 64. The ICP spectra of a 1000 μg/ml Mo solution with mask in (a) and mask out (b).
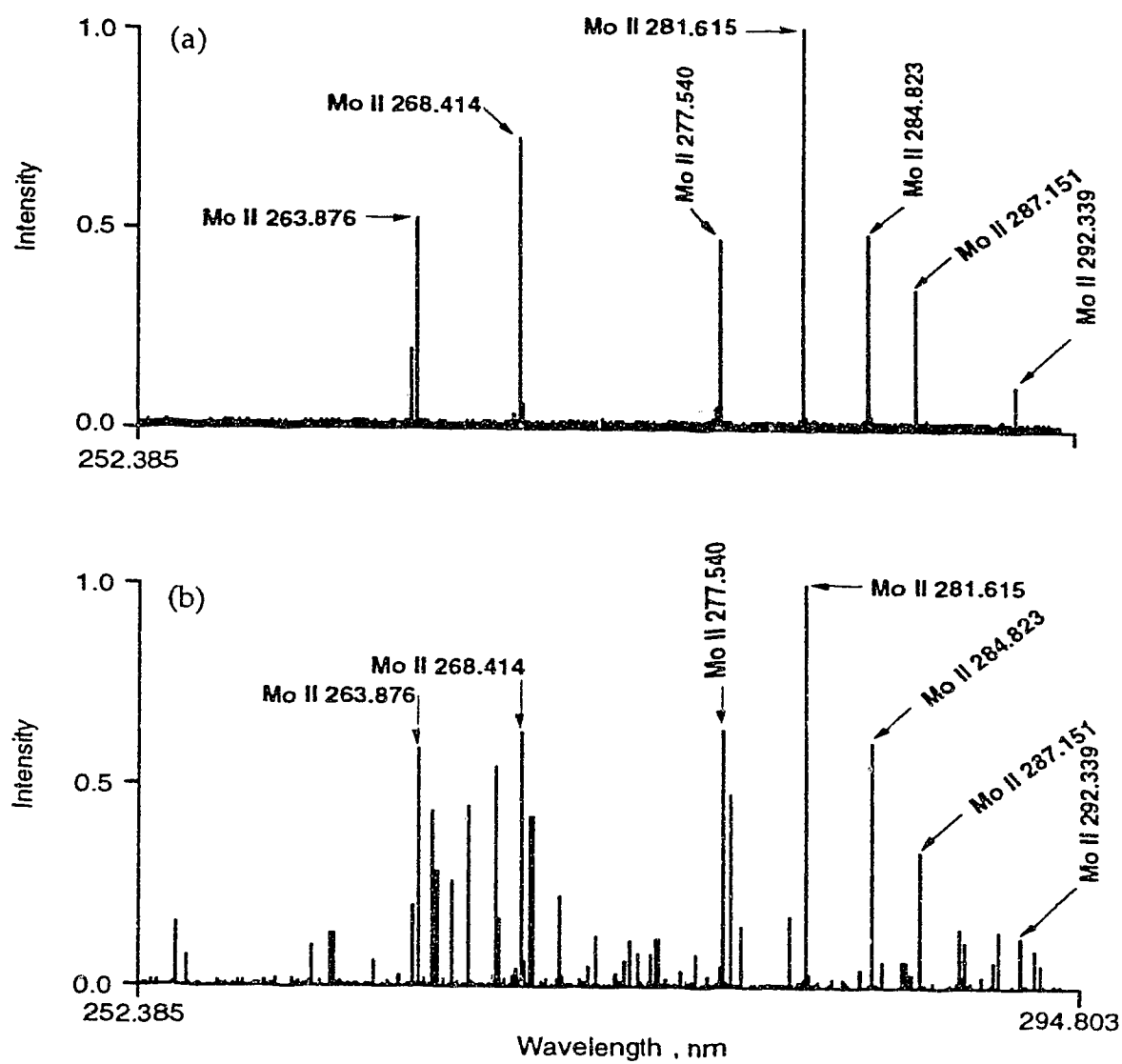
Fig. 65. Scale-expanded plots of the spectra shown in Fig. 64.

are given in Fig. 56 and Fig. 57. Because the mask-out spectrum of Si is already simple enough, the difference between the mask-in and mask-out spectra is not as obvious as those we have seen before. In Fig. 57, the difference is better seen in the vicinity of Si I 251.611 nm line, where spectrum is somewhat simpler in Fig. 57.a than in Fig. 57.b.

The ICP mask-in and mask-out spectra of a 1000 µg/ml Mn solution and the scale-expanded plots are shown in Fig. 58 and Fig. 59. The difference between the mask-in and mask-out spectra can only be seen in Fig. 59. The Mn II 260.569 nm line and some relatively weak lines seen in Fig. 59.b are filtered out by the pre-dispersion system as desired. Although the line designated as Mn II 259.373 nm looks like a doublet, it is actually a single line. The "doublet" is a printing artifact.

Because of the simplicity of the Mg spectrum in this spectral region, the effect of the Mg mask used at the focal plane is also barely noticeable as illustrated by the ICP mask-in and mask-out spectra of the 1000 µg/ml Mg solution and the scale-expanded plots shown in Fig. 60 and Fig. 61.

The dramatic effect of a Co mask in selecting 4 particular lines among dozens of lines is illustrated by the ICP mask-in and mask-out spectra of the 1000 µg/ml Co solution and the scale-expanded plots shown in Fig. 62 and Fig. 63.

Similarly, the ICP mask-in and mask-out spectra for a 1000 µg/ml Mo solution and the scale-expanded plots shown in Fig. 64 and Fig. 65 indicate that the mask used is also quite effective in selecting the designated Mo lines but, once again, some optical leakage (although minimal) also occurs.

4-3-2. Multielement spectra

A multielement no-mask ICP spectrum is shown in Fig. 66.b, which was obtained from a 4-element solution containing 100 μg/ml Zn, 50 μg/ml Cd, 2.0 μg/ml Mn, and 1.0 μg/ml Mg. The spectrum of the same solution with a 4-element mask in place is given in Fig. 66.a and the measurement power of the pre-selection system is very impressive.

The line selection capability of this optical arrangement with mask is also illustrated in Fig. 67. Fig. 67.b is the mask-out ICP spectrum of a 9-element solution containing 100 μg/ml Zn, 50 μg/ml Zn, 50 μg/ml Cd, 50 μg/ml Ni, 200 μg/ml As, 50 μg/ml Si, 10 μg/ml Mn, 10 μg/ml Fe, 20 μg/ml Cr, and 5.0 μg/ml Mg. Clearly the no-mask spectrum is a mess. Despite the complexity of the mask-out spectrum in Fig. 67.b, the mask-in spectrum in Fig. 67.a demonstrates the ability of the pre-selection system using the mask designed to pass the 10 designated lines to discriminate against any unwanted spectral components while selecting all relevant spectral lines. The spectral details of Fig. 67 can be seen in Fig. 68.

4-3-3. Analytical determination of chromium and manganese in the presence of iron

In order to determine the effectiveness of the pre-selection system in reducing the noise and dynamic range problems in the "real world", the effect of a high concentration of iron on the analytical determination of chromium and manganese was studied with and without pre-selection.

Presented in Fig. 69.b is the ICP spectrum of a solution containing 990
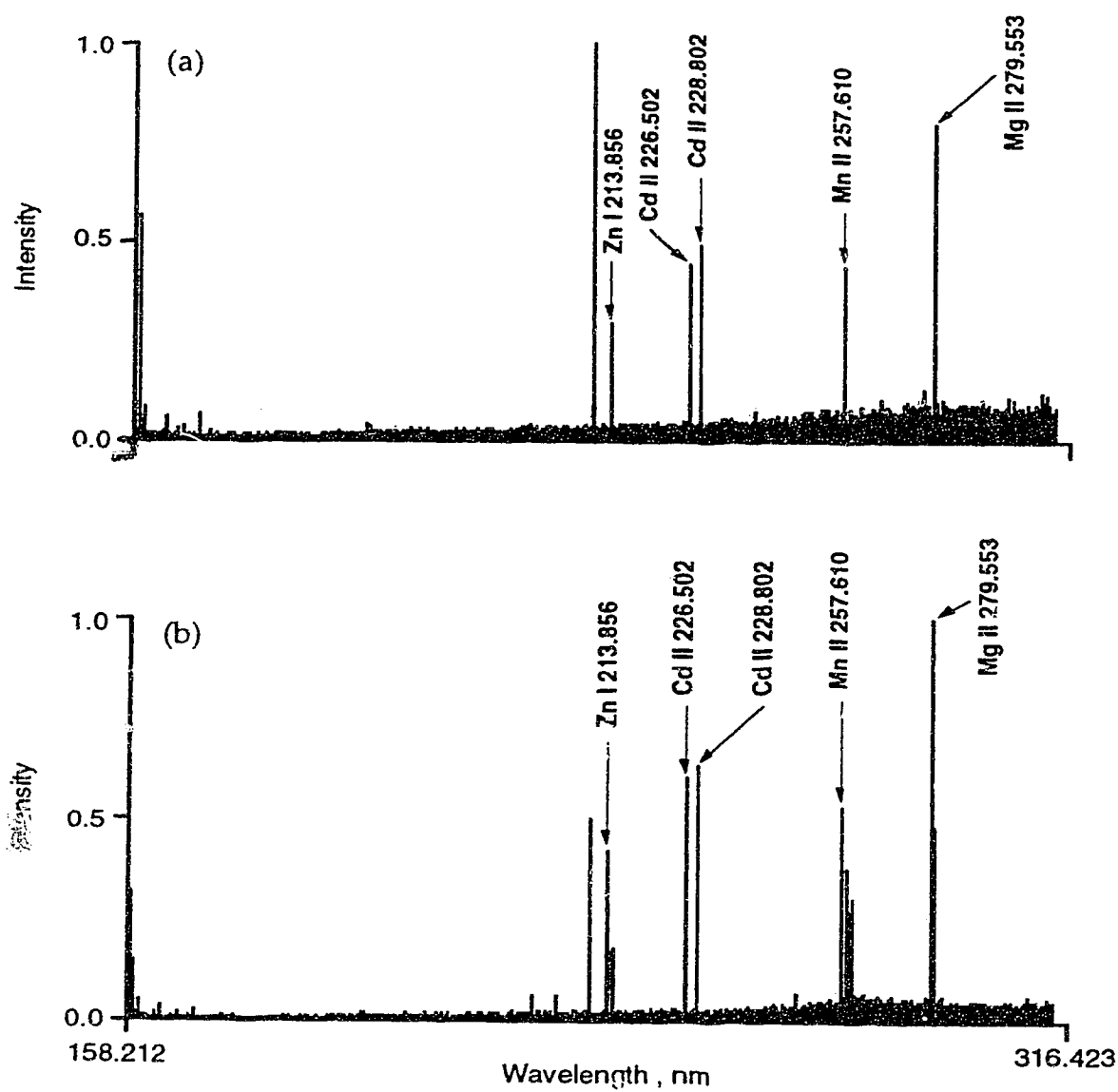
Fig. 66. ICP pectra of a multi-element solution containing 4 elements with mask in (a) and mask out (b).
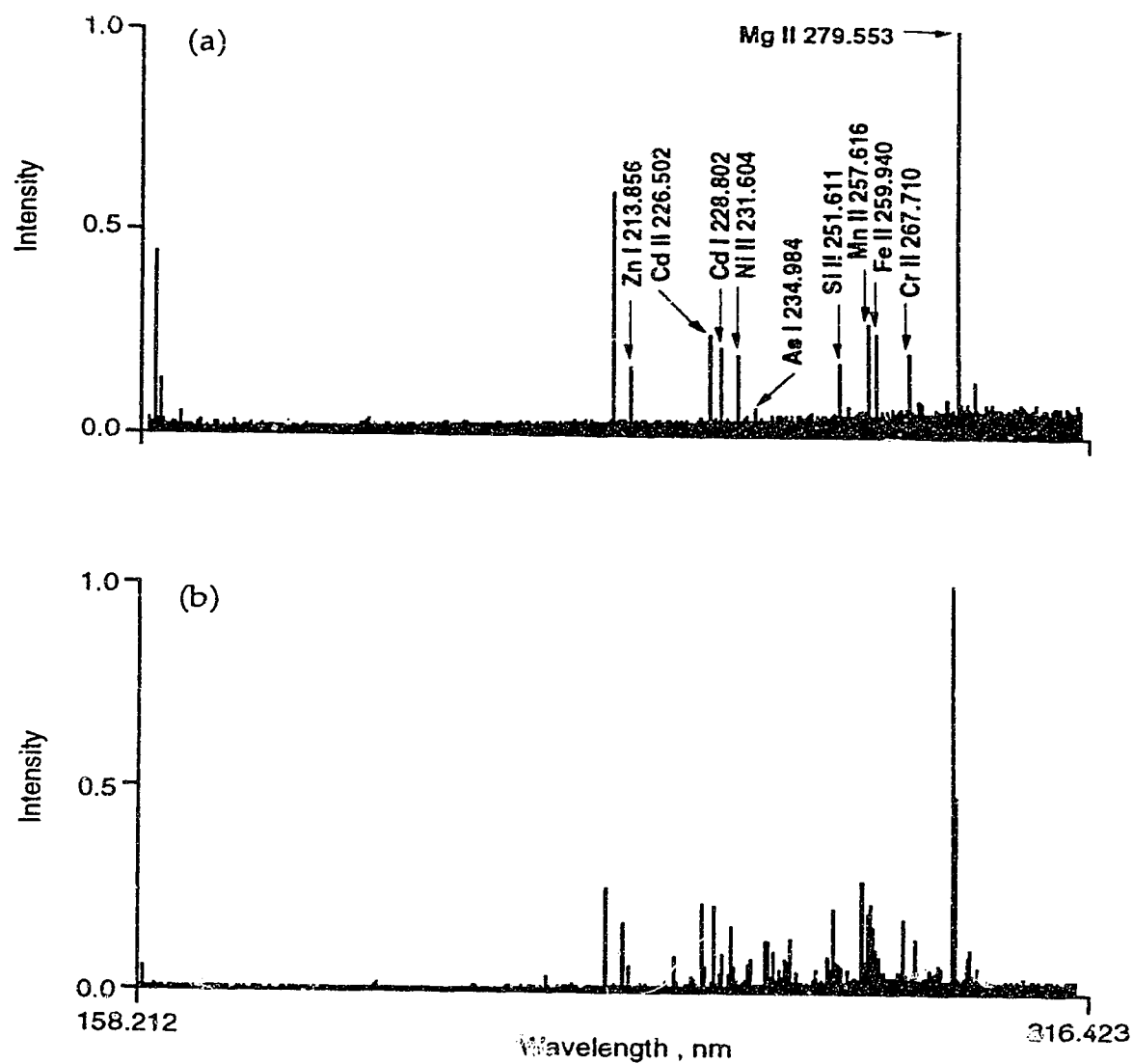
Fig. 67. ICP spectra of a multi-element solution containing 9 elements with mask in (a) and mask out (b).
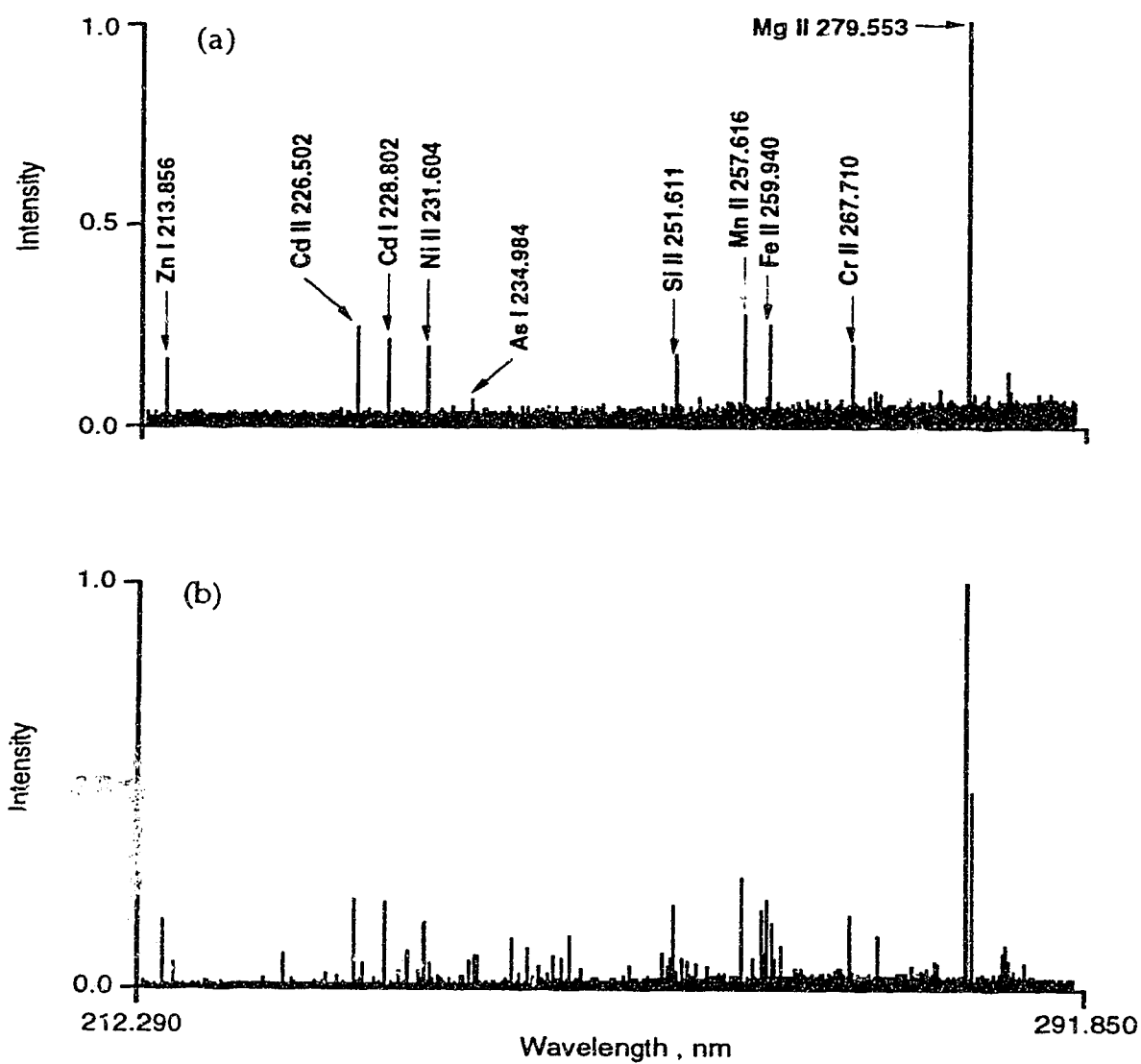
Fig. 68. Scale-ex⸗ ⸗ded plots of the spectra shown in Fig. 67.

μg/ml Fe and 10 μg/ml Cr without any optical pre-filtering. Fig. 69.a is the ICP spectrum of the same solution with a mask designed to let through the Cr II 267.716 nm line, Cr II 276.259 nm line, and Cr II 283.563 nm line positioned at the focal plane of the spectrometer. Clearly, in Fig. 69.a, only the 3 designated Cr II lines are left. In order to see more clearly, we now turn to Fig. 70, the scale-expanded version of Fig. 69. In both Fig. 70.a and Fig. 70.b the spectrum has been expanded vertically. The presence of these 3 Cr II lines could not be reported with much confidence based on the data shown in Fig. 70.b. With a mask designed for these 3 lines placed at the focal plane of the spectrometer, the 3 Cr II lines are clearly present as shown in Fig. 70.a.

Similarly, the ICP spectrum of a solution containing 990 μg/ml Fe and 10 μg/ml Mn without any optical filtering is shown in Fig. 71.b and the ICP spectrum of the same solution with a mask designed to let through the Mn II 257.610 nm line and the Mn II 259.373 nm line positioned at the focal plane of the system is given in Fig. 71.a. Although it is clearly seen that the spectrum shown in Fig. 71.a is simplified compared to that shown in Fig. 71.b, it is still better to look at the scale-expanded plots of the spectra shown in Fig. 72, in which only the spectral portion of interest is displayed. In Fig. 72.b without the mask, the spectral portion chosen is not particularly complex, but the two Mn II lines are weak relative to the Fe lines. In Fig. 72.a with the mask in place, with Fe lines removed, the 2 Mn II lines become the first and second strongest lines in the spectral region.

In summary, the masks designed for both single element and multielement permit only the spectral information of sought analytical
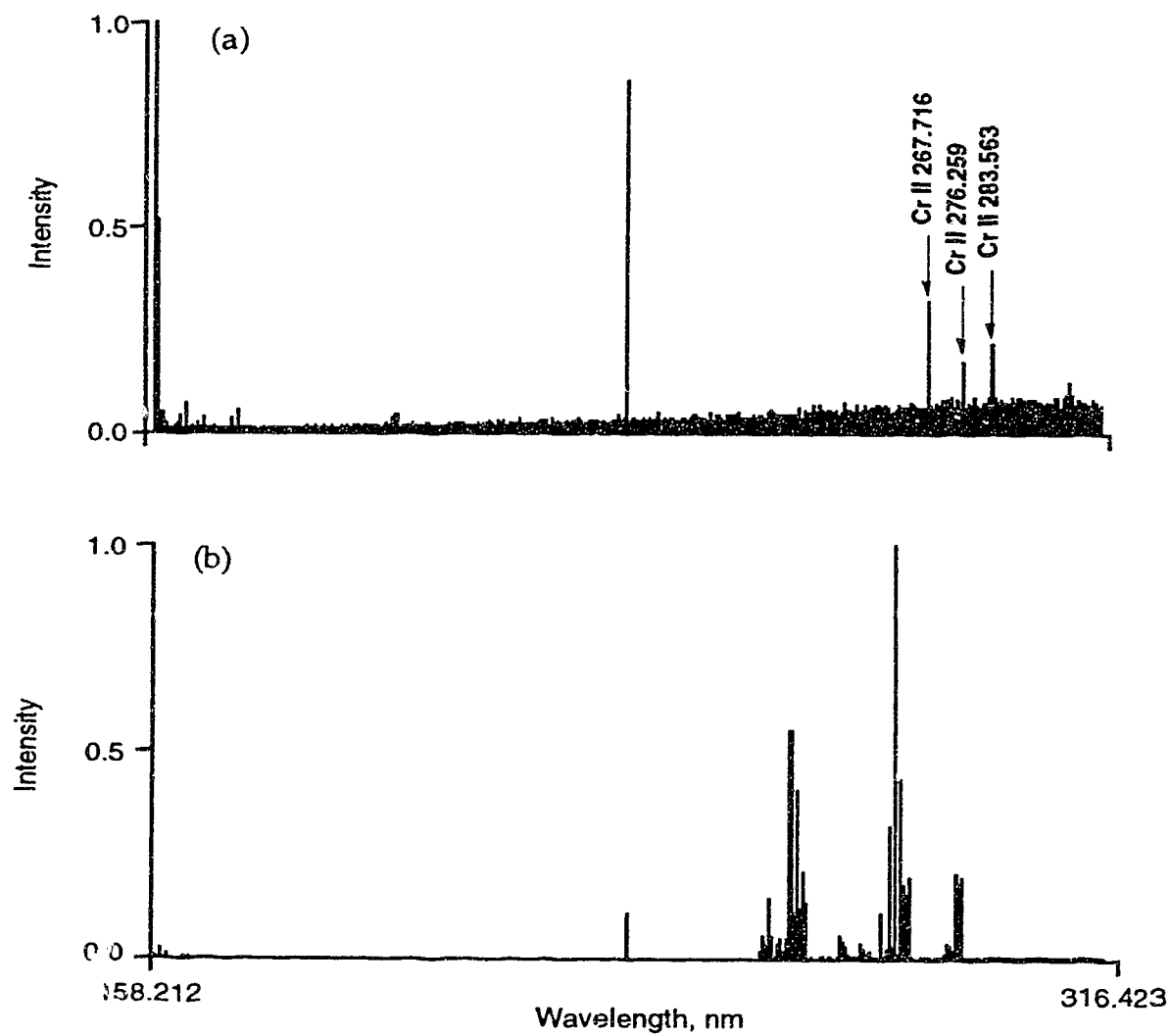
Fig. 69. The ICP spectra of a solution containing 990 µg/ml Fe and 10 µg/ml Cr with mask in (a) and mask out (b).
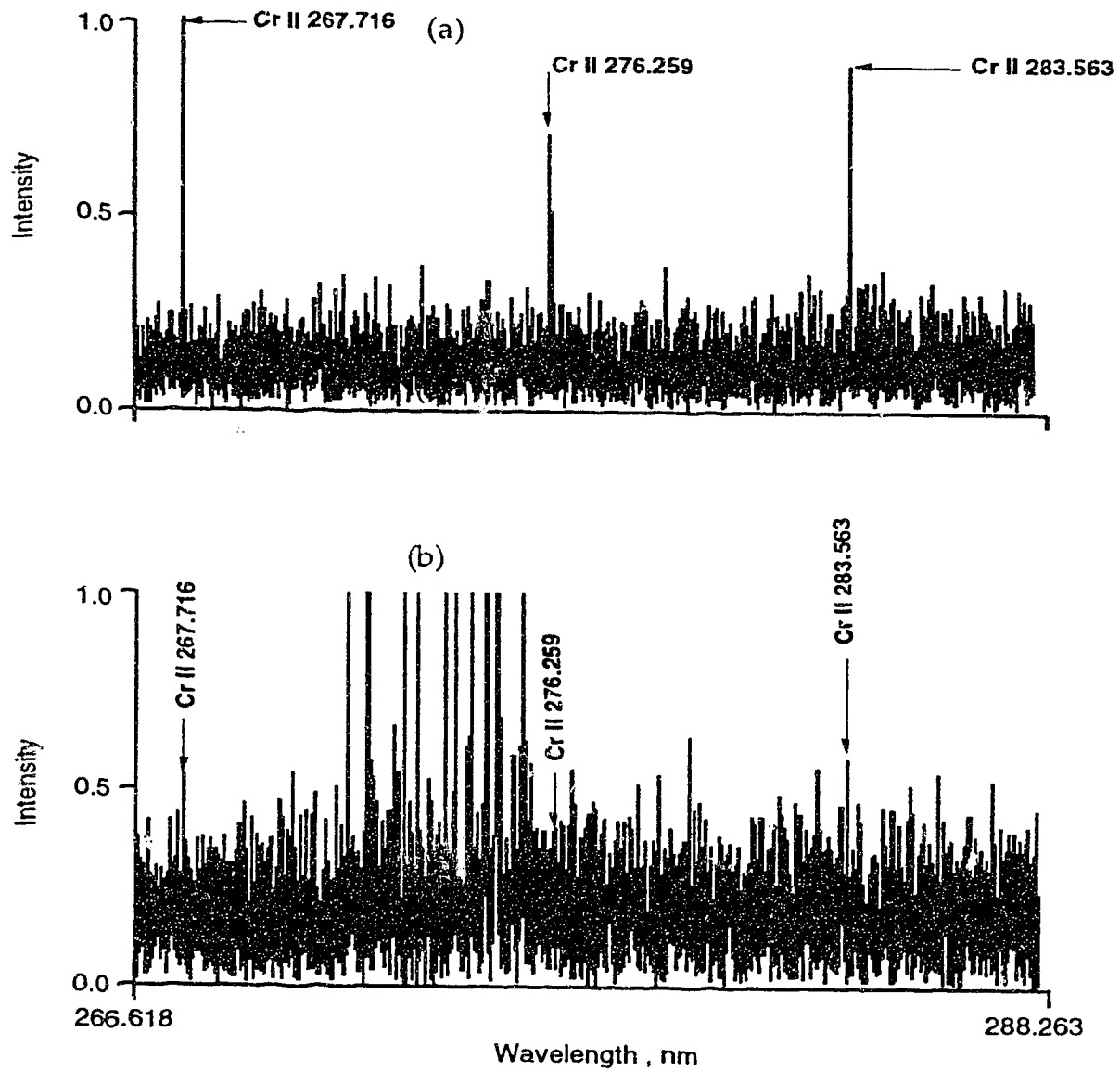
Fig. 70. Scale-expanded plots of the spectra shown in Fig. 69, illustrating the reduction of the multiplex disadvantage.
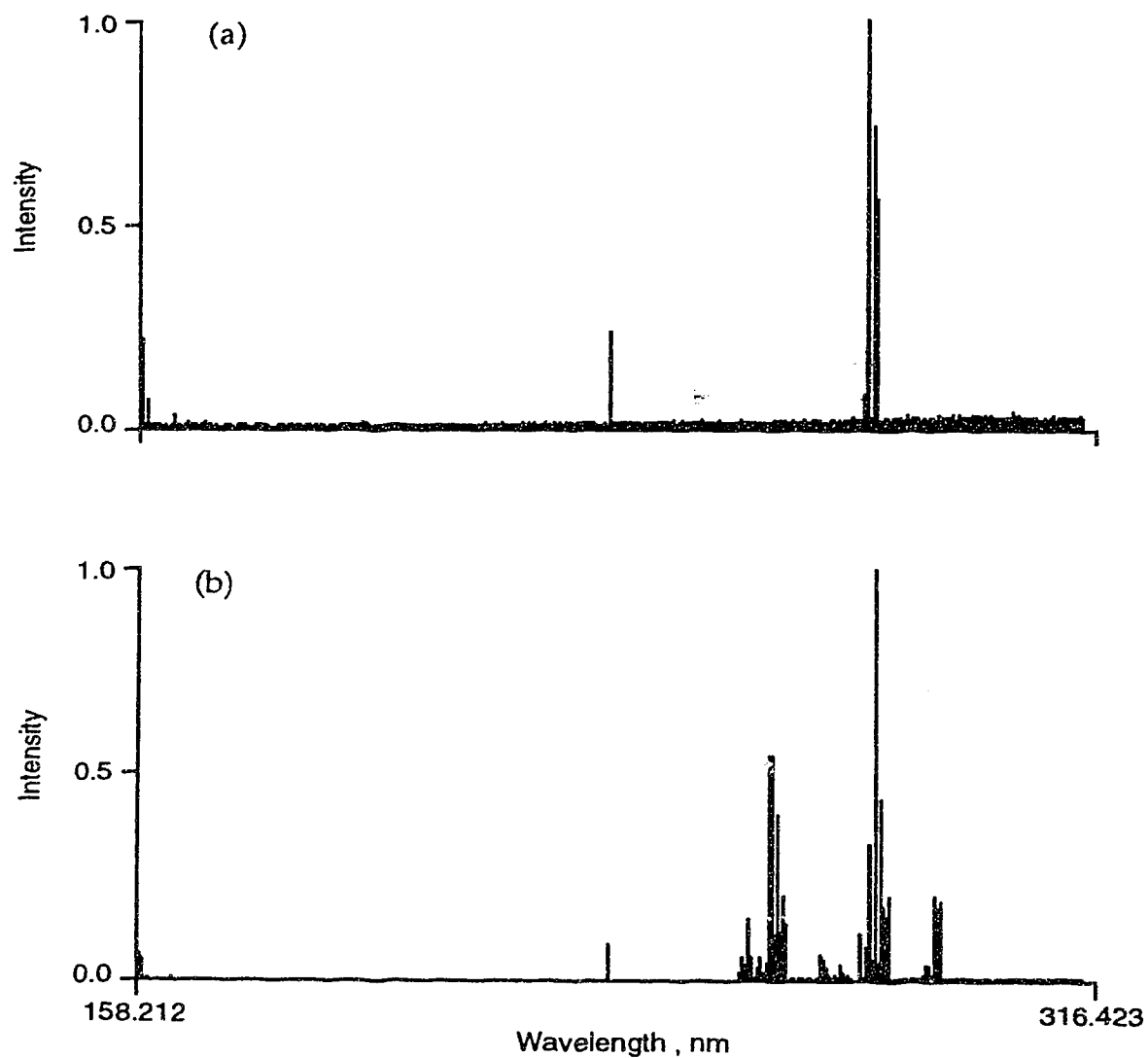
Fig. 71. The ICP spectra of a solution containing 990 μg/ml Fe and 10 μg/ml Mn with mask in (a) and mask out (b).
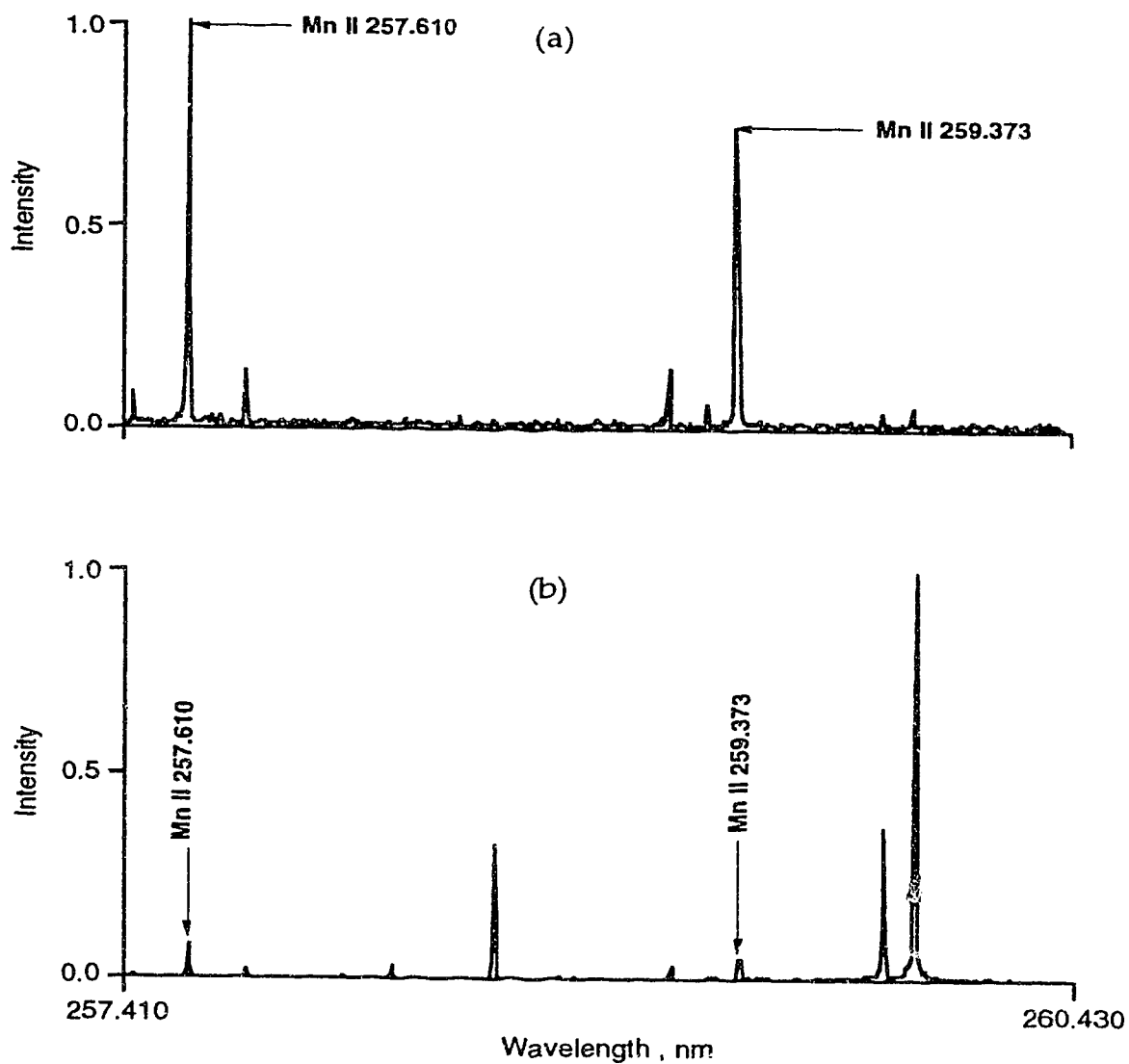
Fig. 72. Scale-expanded plots of the spectra shown in Fig. 71, illustrating the reduction of the multiplex disadvantage.

regions to pass through to the rest of the spectrometer (Michelson interferometer) while blocking all the unwanted information. This "blocking" results in the elimination or reduction of the multiplex disadvantage and the dynamic range limitation. In addition, masks are inexpensive and relatively simple to configure for virtually any arrangement of analytical wavelengths and can be rapidly interchanged depending on analysis conditions.

4-4. Pre-dispersion without recombination - fiber optic coupling

An alternative pre-dispersion arrangement is to "short circuit" the recombination grating (G2) altogether. This can be realized by fiber optic coupling as shown in Fig. 73.

The fiber optic cable was a slit-to-spot, 1 meter quartz cable, obtained from General Fiber Inc. (Cedar, Grove, NJ, 07009). The cable consists of several smaller optical fibers, each 100 μm in diameter. At one end of the cable the individual fibers are grouped together in a circular bundle, 1 mm in diameter. At the other end of the cable, the individual fibers are stacked to form a slit, 100 μm by 5 mm, which is equivalent to a spectral window of 3.0 nm when the slit end of the fiber optic cable is positioned vertically on the focal plane.

In the experiment, the slit end of the fiber optic cable was mounted directly on the focal plane of the spectrometer (spectral range: 190 - 415 nm) such that the slit end of the fiber optic cable can move freely along the focal plane. The idea is that the slit can be positioned to pick up any desired wavelength region. The selected wavelength region is directed through the
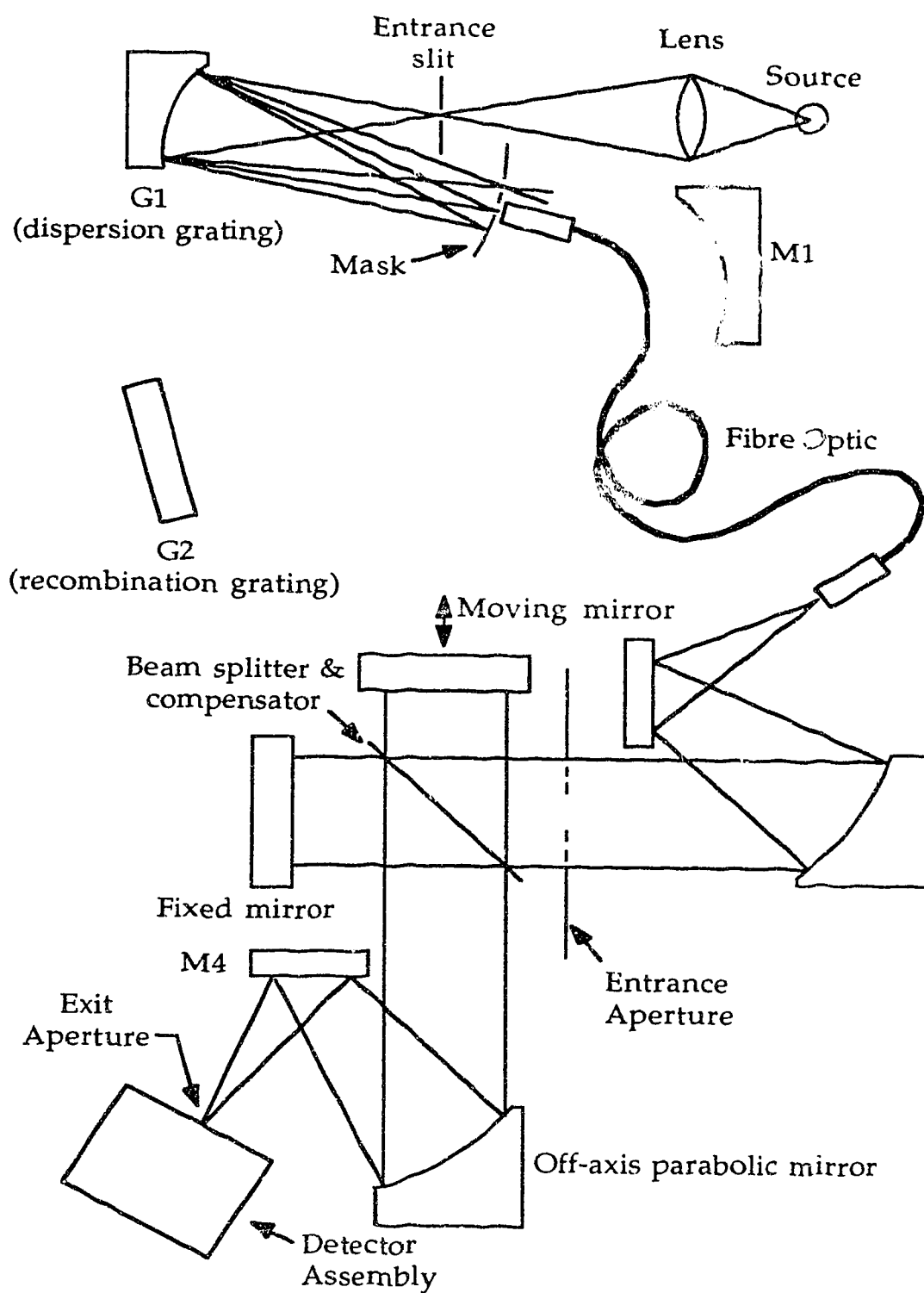
Fig. 73. Pre-dispersion without recombination. Fiber optic coupling .

fiber optic cable. When the selected component from the source radiation comes out of the circular end of the cable, it is folded by a folding mirror onto an off-axis parabolic mirror, which collimates the selected component from the source into the interferometer.

To obtain spectrochemical information with this optical arrangement is straight forward. A particular spectral window can be chosen by simply moving the slit end of the fiber optic cable to the appropriate position on the focal plane. In fact a series of spectral windows could even be sequentially selected.

A complete ICP spectrum of a solution containing 500 μg/ml Fe, 200 μg/ml Mn, and 200 μg/ml Mg is shown in Fig. 74.a. When the fiber optic coupling was put in place and the slit end of the fiber optic cable was moved to select the region around the Mn II 260.569 nm line, the spectrum shown in Fig. 74 is the result. As can be seen in Fig. 74.b, in the spectral region from 158.213 nm to 316.426 nm, there is only one single line - the Mn II 260.569 nm line that has entered the interferometer. When the slit end was moved to another position, only the Mn II 259. 373 nm line and another relatively weak line are observed, as illustrated in Fig. 74.c. Similarly, the Mg II 285.213 nm line and the Mg II 279.553 nm line can be picked off as the slit end of the fiber optic cable is moved to appropriate positions as shown in Fig. 75. The spectrum shown in Fig. 76.a is exactly the same as that shown in Fig. 74.a (the multielement spectrum). Fig. 76.b is the spectrum obtained as the slit end of the fiber optic cable was fixed at another position on the focal plane. Fig. 76.c is the scale-expanded plot of Fig. 76.b, which indicates the detection of the Fe II
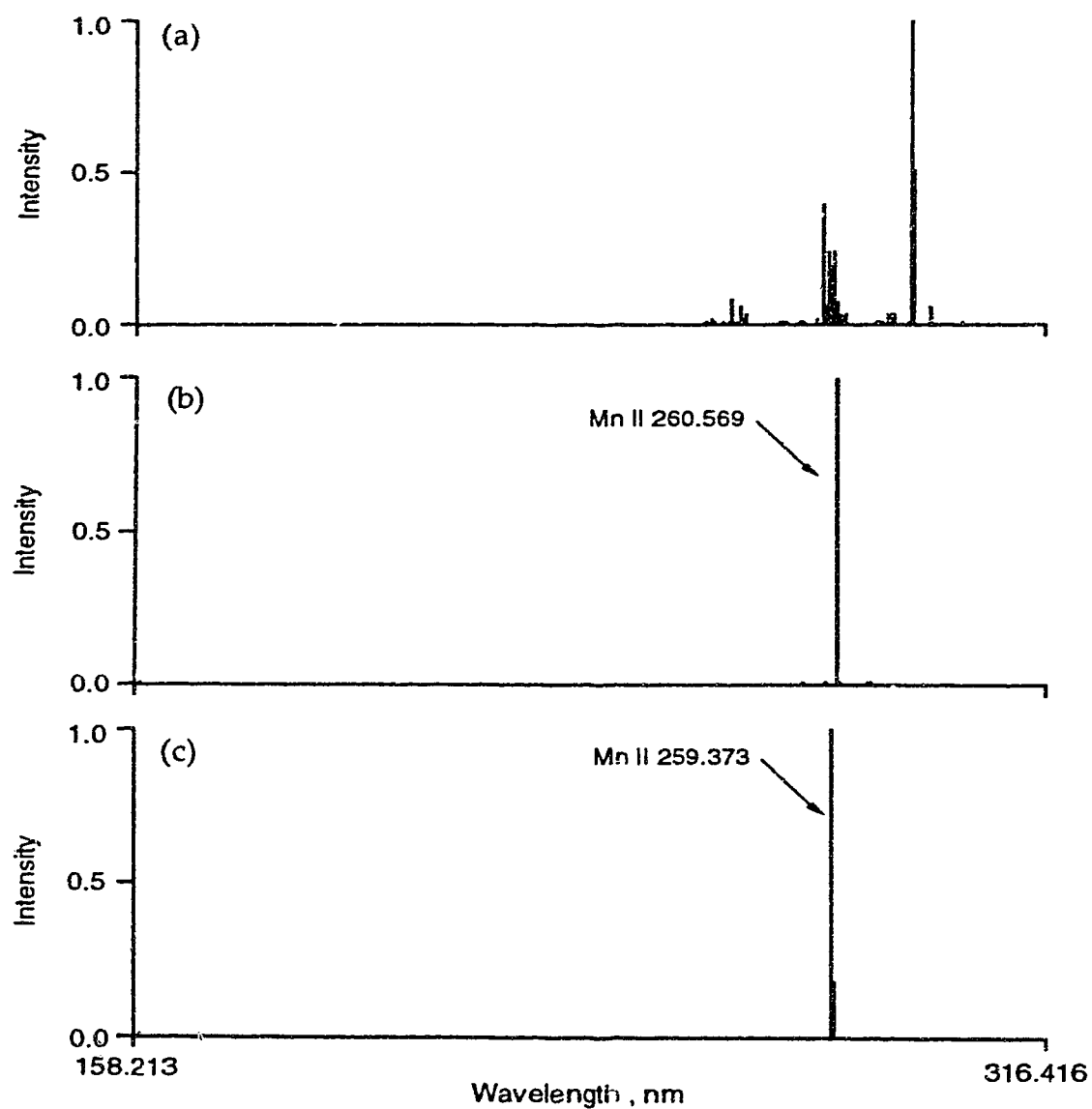
Fig. 74. The ICP spectra of a multielement solution containing 500 μg/ml Fe, 200 μg/ml Mn, and 200 μg/ml Mg without filtering (a) and fiber optic coupling with the slit to circle fiber optic cable positioned at Mn II 260.569 nm line (b) and at Mn II 259.373 nm line (c).
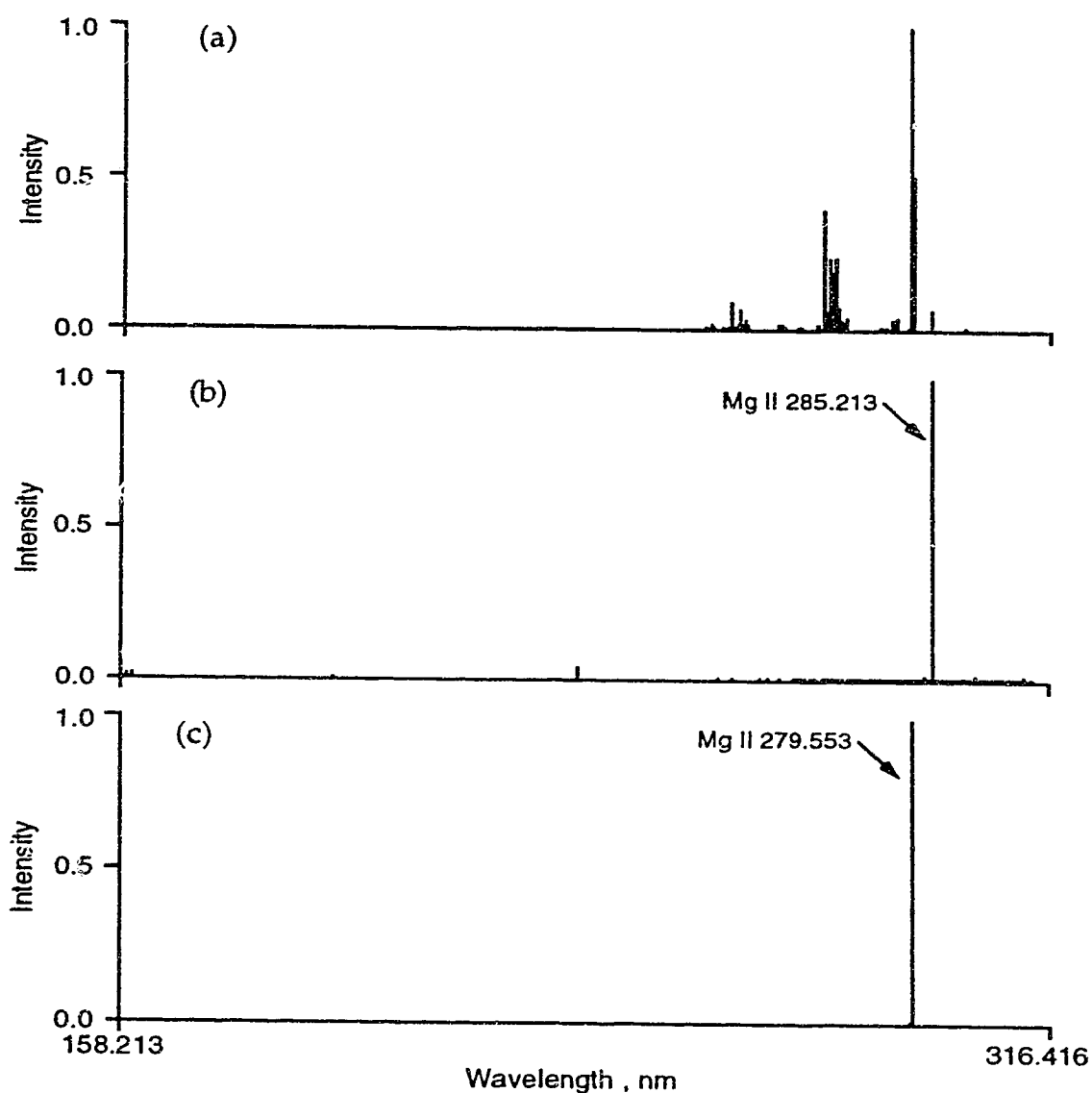
Fig. 75. The ICP spectra of a multielement solution containing 500
µg/ml Fe, 200 µg/ml Mn, and 200 µg/ml Mg without
filtering (a) and fiber optic coupling with the slit to circle
fiber optic cable positioned at Mg II 285.213 nm line (b) and
at Mg II 279.553 nm line (c).
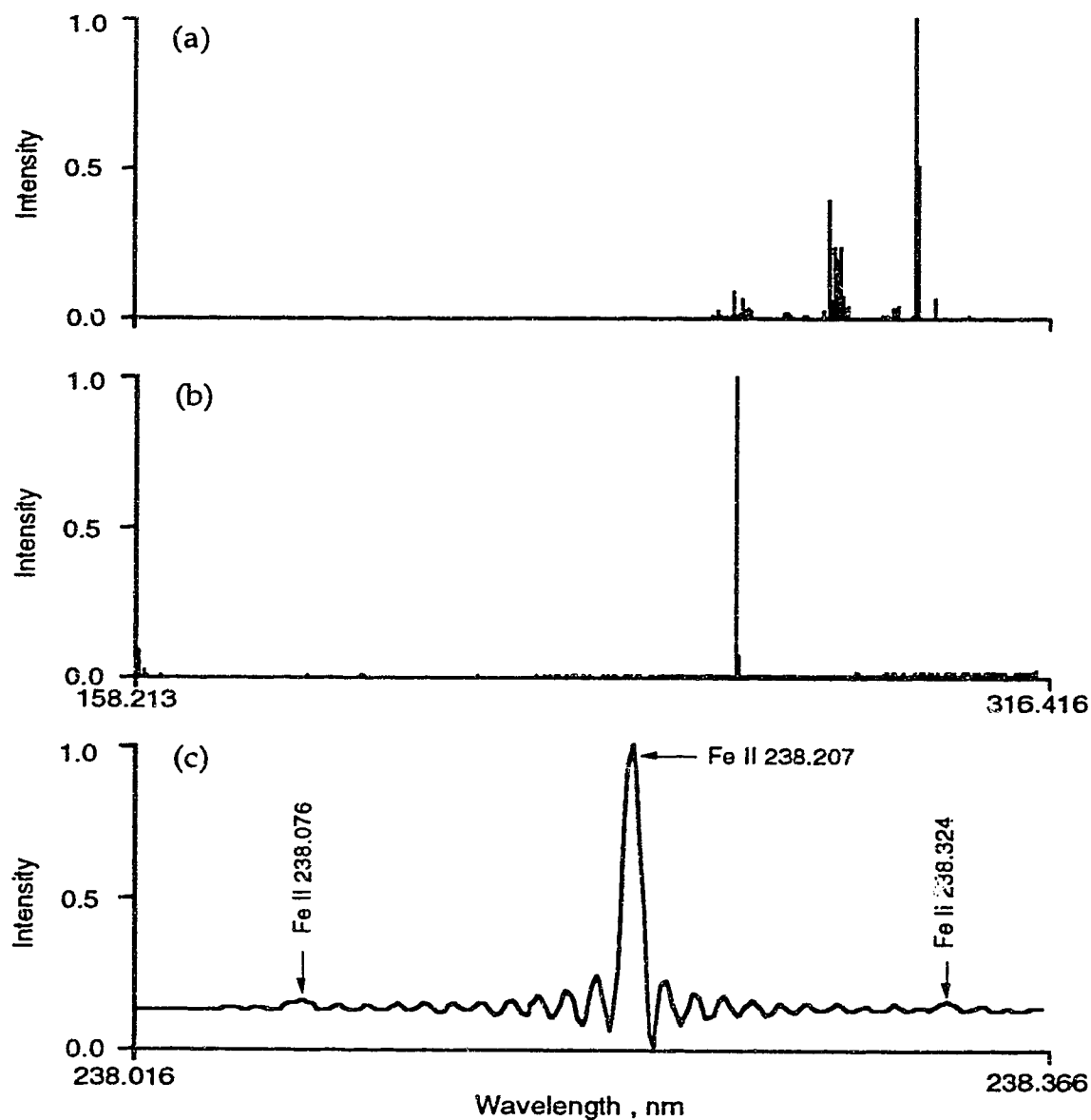
Fig. 76. The ICP spectra of a multielement solution containing 500 μg/ml Fe, 200 μg/ml Mn, and 200 μg/ml Mg without filtering (a) and fiber optic coupling with the slit to circle fiber optic cable positioned at 3 Fe lines (b) and the close-up of the 3 lines (c).
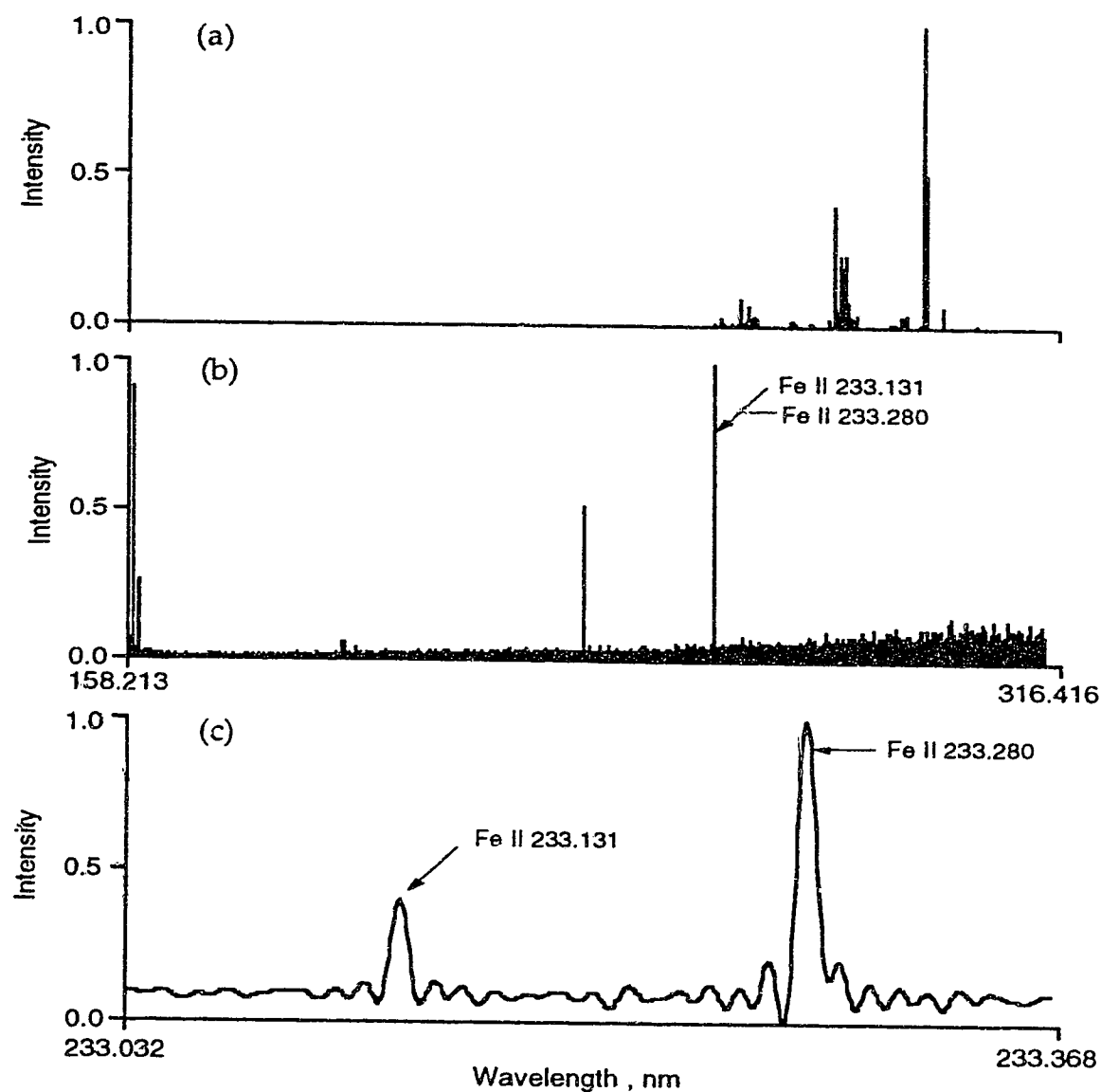
Fig. 77. The ICP spectra of a multielement solution containing 500 µg/ml Fe, 200 µg/ml Mn, and 200 µg/ml Mg without filtering (a) and fiber optic coupling with the slit to circle fiber optic cable positioned at 2 Fe lines (b) and the close-up of the 2 lines (c).
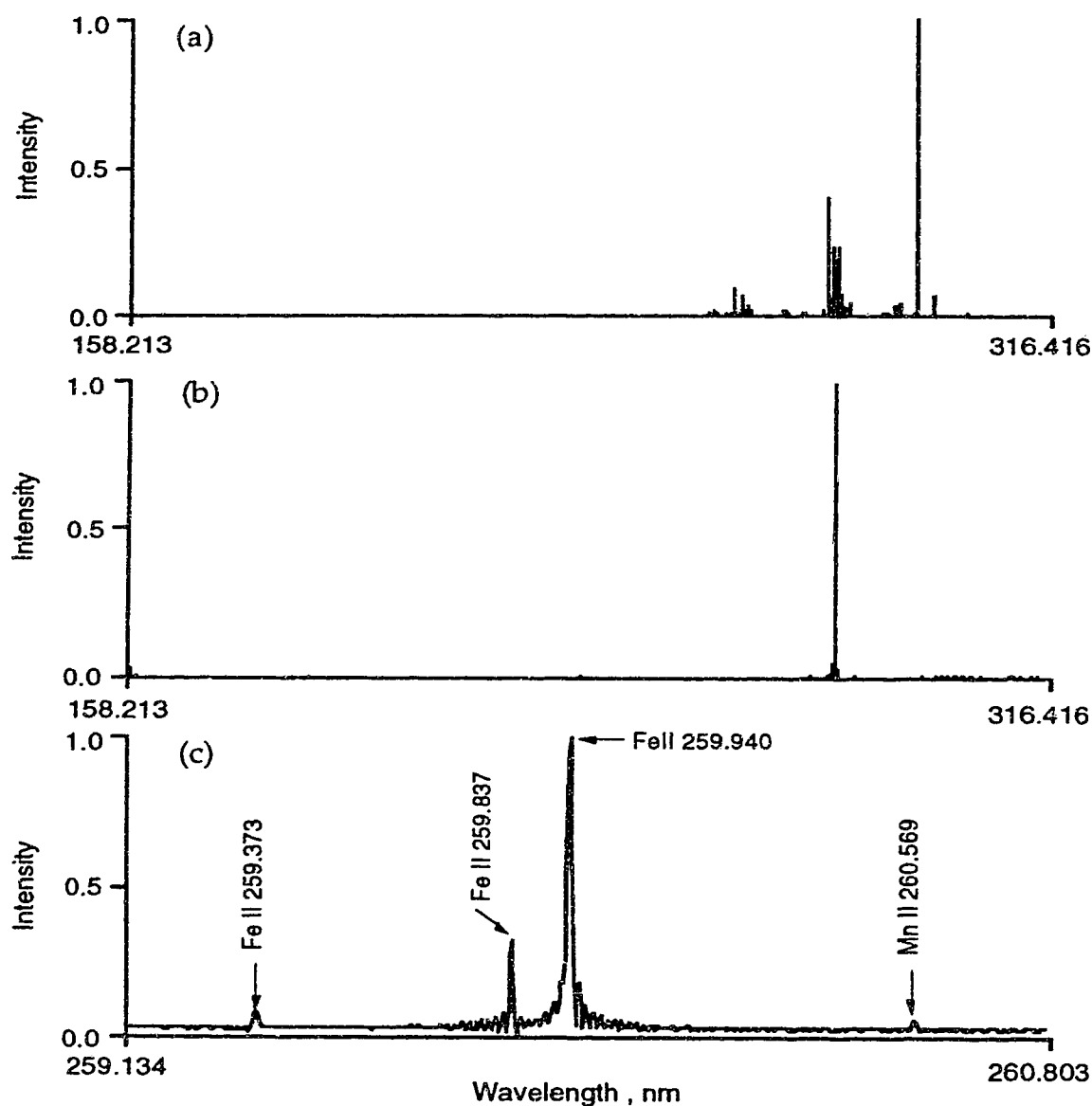
Fig. 78. The ICP spectra of a multielement solution containing 500
μg/ml Fe, 200 μg/ml Mn, and 200 μg/ml Mg without
filtering (a) and fiber optic coupling with the slit to circle
fiber optic cable positioned at 3 Fe lines and 1 Mn line (b)
and the close-up of the 4 lines (c).
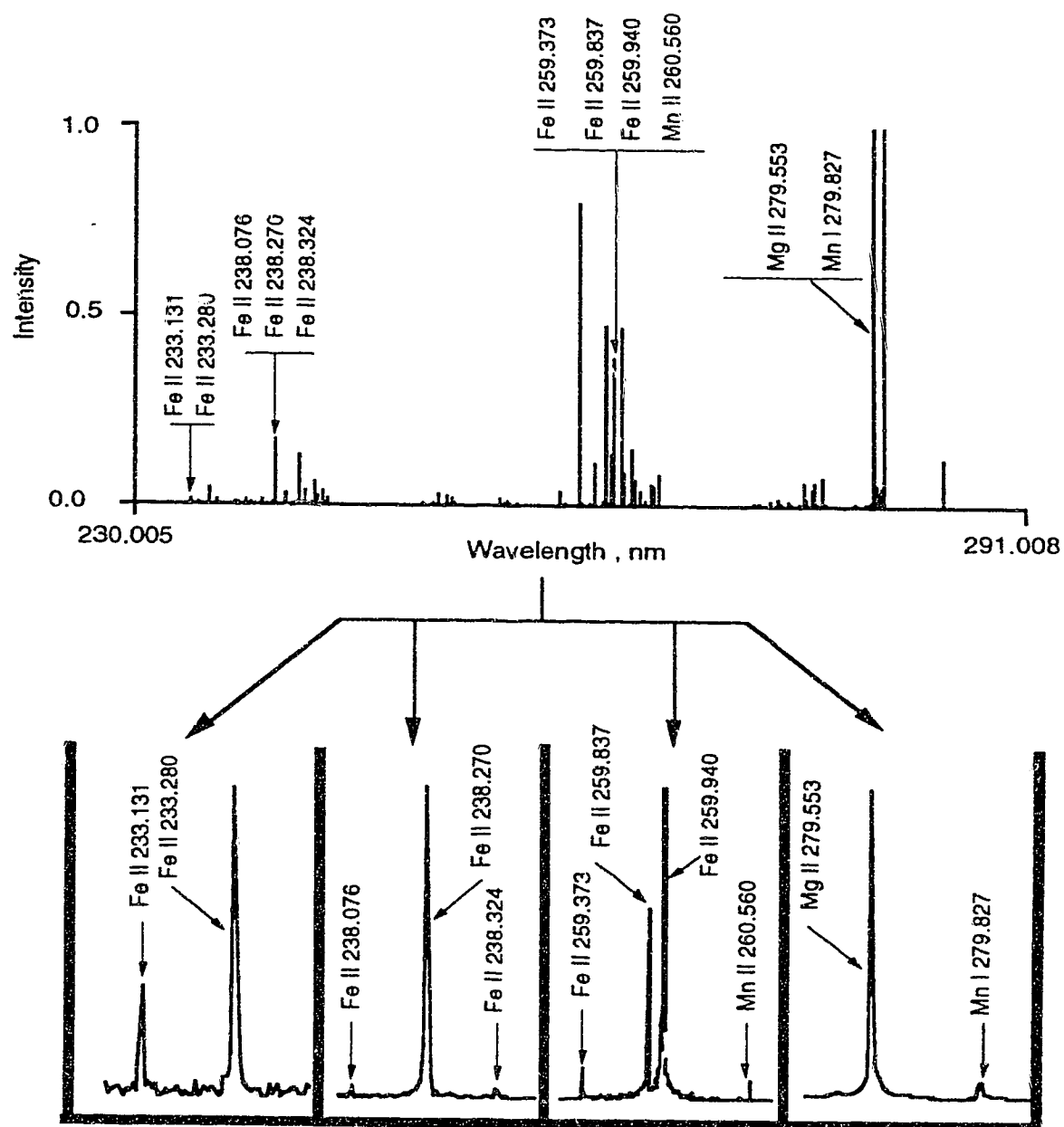
Fig. 79. Summary of the data shown in Fig. 74 - 78.

238.207 nm line and two weak lines: Fe II 238.076 nm and 238.324 nm lines. The data shown in Fig. 77 illustrates the selection of Fe II 233.280 nm line and Fe II 233.131 nm line as shown in Fig. 77.b and its close-up Fig. 77.c as compared to the whole spectrum of the multielement solution mentioned above in the spectral region from 158.213 nm to 316.427 nm. The other line appeared in the middle of Fig. 77.b is the He-Ne reference laser line, leaked into the optical system (likely through electronic cross-talk). It should also be pointed out that those lines appeared at the low end the spectrum in Fig. 77.b in the vicinity of 158.213 nm are not real spectral lines, they are probably caused by the power line interference. Throughout this chapter, these lines also appeared in most of the cases when the whole spectrum from 158 to 316 nm region is shown. When the slit end of the fiber optic cable was moved further along the focal plane, the spectrum shown in Fig. 78.b was obtained. Fig. 78.c - the scale-expanded version of Fig. 78.b, clearly indicates the presence of 4 spectral lines in this small spectral window. A summary of the concepts is given in Fig. 79. The upper part of Fig. 79 is the close-up of the whole ICP spectrum obtained using the multielement solution with the lines to be picked by the pre-selection system indicated. The lower part of Fig. 79 shows the 4 spectral windows actually observed by this fiber optic coupling arrangement.

4-5. Conclusions

The two pre-selection optical arrangements with the current ICP-FTS system proved to be successful in overcoming the multiplex disadvantage and the dynamic range limitation problems. Both systems provide the

capability of choosing any spectral line or lines at will while getting rid of all unwanted spectral components from the source.

The pre-selection system with masks on the focal plane can be considered as a reprogrammable direct reader. It offers the flexibility of being able to change from one set of analytical lines to a completely different set, rapidly and reproducibly. As such, it is a very suitable and versatile spectrometer for simultaneous multielement analysis applications where a variety of sample matrices and types must be dealt with. For instance, a bank of masks (either single element or multielement) can be designed and cut according to the nature and requirements of that particular analytical problem, thus various equivalent "direct readers" can result from a single ICP-FTS system. Whereas, such versatility is not present in the current direct reading spectrometers where focal plane line selection is pre-fixed and cannot easily be changed.

The fiber optic coupling configuration is also quite flexible. The slit end of the fiber optic cable can be moved along the focal plane of the spectrometer to direct the desired narrow spectral windows into the interferometer one after another (i.e., window slew scan), or more than one such fiber optic cables can be positioned along the focal plane and direct more than one spectral windows into the interferometer (i.e., a multiple window direct reader).

While reducing the multiplex disadvantage and the dynamic range limitation, both pre-selection systems provide the capability of conveniently and inexpensively selecting new sets of lines, whenever necessary, to accommodate new applications and sample types. Yet, this flexibility does not

sacrifice simultaneous analytical measurement. Both systems can be optimized for specific simultaneous analysis in specific sample matrices.

It is possible to computerize the two pre-selection systems such that mask-changing or fiber optic movement on the focal plane are programmable in accordance with the nature of the analytical problems and can be performed simply by selecting one of the choices on the screen followed by a single touch of a key on the key board of the computer. There is a lot to be done in this field and the future of the pre-selection system in ICP-FTS looks promising.

Chapter 5

Comparison of the ICP and the GDD

5-1. Introduction

One of the most active current endeavors in analytical chemistry is the search for new methods of multielement analysis. Improvements in many existing methods have been proposed and new methods are being developed. The most significant of these advances has been the emergence of the inductively coupled plasma as a tool for multielement determinations. However, even this powerful source has been found to have limitations (such as high cost, bulkiness) and the search for alternative techniques continues.

Ideally, whatever approach is finally adopted it should be amenable to use with more than one kind of detection technique and be able to handle directly not only liquid samples but also solid samples. One such promising method is the glow discharge device (GDD). The details of this device have been discussed in Chapter 1 and will not be repeated here.

Although the inductively coupled plasma has been the main source in elemental AES and MS, in the last couple of years the glow discharge device has gained more and more popularity. In our laboratory it has been successfully interfaced to the same spectrometers that are currently used for ICP-MS and it has also been coupled to the Fourier transform spectrometer developed in this laboratory. In fact the Fourier transform spectrometer is a very effective spectrochemical measurement system for both the inductively

182

coupled plasma and the glow discharge device. The first part of this study involves a comparison of the emission characteristics of the ICP and the GDD. Spectra measured with the FTS system are presented for brass, stainless steel, and low alloy steel run as solution samples by ICP and run directly as solids by use of a glow discharge device. It should be pointed out that the study of the emission characteristics of the ICP and the GDD in this chapter is only qualitative and further study on the differences between the excitation mechanisms of the ICP and the GDD is in progress in our laboratory by another researcher. In the second part of this chapter, excitation temperatures derived from the "Boltzmann plot" method and the line-pair intensity ratio method in the ICP and the GDD are measured and compared.

5-2. Experimental

Measurements were made using the glow discharge device (GDD) and using the inductively coupled plasma (ICP). The NBS Naval brass B SRM 1107, the NBS stainless steel SRM 1172, and the NBS low alloy steel SRM 1262 samples were machined into sample pins for the GDD, or dissolved into solution using the method described by Fernando [163] for the ICP. The certified compositions of these samples are listed in Tables 9-11. The schematic diagram of the pin-type glow discharge device used in this study is given in Fig. 80. The glow discharge device was run at 1300 V, 7.0 mA, and at an argon pressure of 2.5 torr except when indicated otherwise. It was placed at the focal length distance from a 10 cm focal-length quartz lens , and incident light was directed, through an 8 mm diameter aperture, to the interferometer. The optical coupling between the ICP source and the interferometer was achieved by placing a 30 cm focal-length quartz lens at its focal length distance

Table 9. Certified composition of NBS Naval brass B SRM 1107

Element	Certified composition (nominal weight percent)
Cu	61.21
Zn	37.34
Pb	0.18
Fe	0.037
Sn	1.04
Ni	0.098

Table 10. Certified composition of NBS stainless steel SRM 1172

Element	Certified composition (nominal weight percent)
C	0.056
Mn	1.76
P	0.025
S	0.014
Si	0.59
Cu	0.105
Ni	11.35
Cr	17.4
Mo	0.22
Co	0.12

Table 11. Certified composition of NBS low alloy steel SRM 1262

Element	Certified composition (nominal weight percent)
C	0.163
Mn	1.05
P	0.044
S	0.037
Si	0.40
Cu	0.51
Ni	0.60
Cr	0.30
V	0.041
Mo	0.070
W	0.20
Co	0.30
Ti	0.085
As	0.095
Sn	0.016
Al	0.09
Nb	0.29
Ta	0.20
Zr	0.19
Ca	0.0002
B	0.0025
Pb	0.0004
Sb	0.012
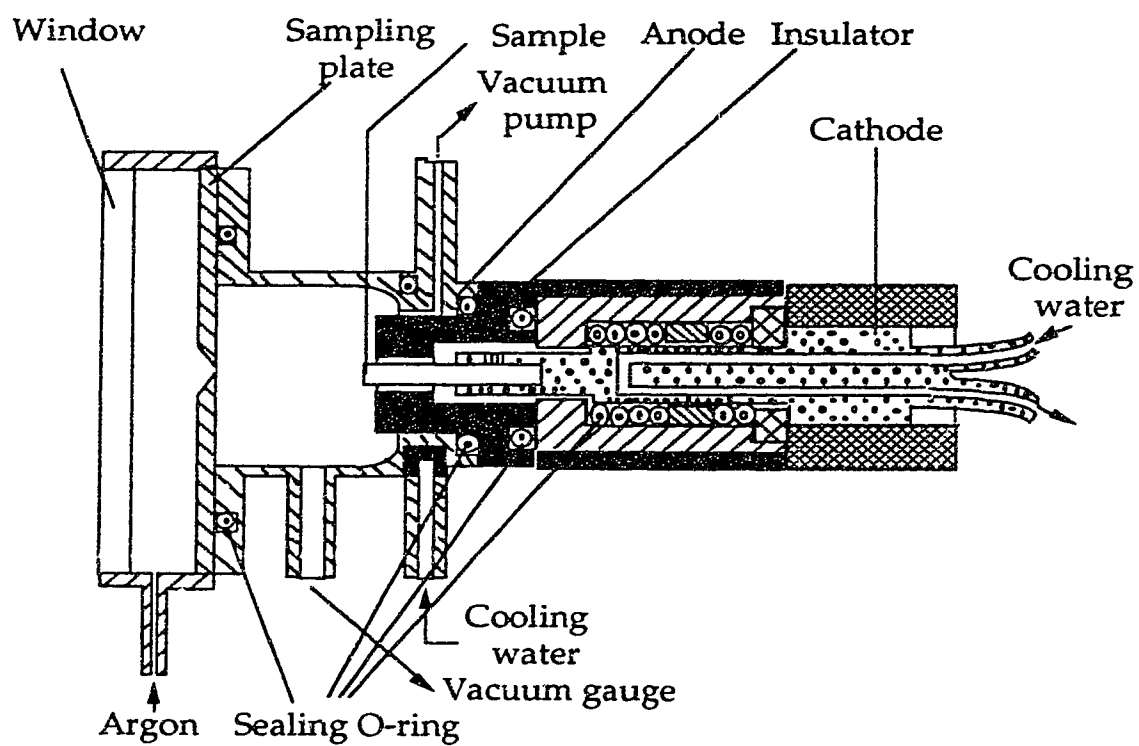
Fig. 80. Schematic diagram of the pin-type glow discharge source.

from the plasma. Collimated light was directed into the interferometer through the same aperture set at a diameter of 8 mm. The detectors used were an R166 solar-blind photomultiplier tube for the ultraviolet spectral region (Hamamatsu photonics K. K.) and 1P21 photomultiplier tube for the visible spectral region (Hamamatsu photonics K. K.). Both were operated at a potential of 660 V. The inductively coupled plasma used was identical to that used in Chapter 3. The plasma was run at a constant forward power of 1.5 kW; coolant, auxiliary, and nebulizer flow rates of 15, 1.0, and 1.0 l/min were used; and the observation height was 14 mm above the load coil.

For each spectrum, 32 interferograms were co-added. All the spectra obtained in this chapter were calculated from 64 k interferograms sampled with a frequency 4 times of that of the clock derived from the He-Ne laser. The acquired interferograms were directly Fourier transformed without any additional processing to yield the resultant spectra.

5-3. Comparative spectra of the ICP and the GDD

In this section some representative spectra will be shown to demonstrate the present capability of our FTS measurement system and to illustrate the differences between the emission from the ICP and the GDD.

5-3-1. Brass sample

The measured emission spectra of brass in the ultraviolet region from the inductively coupled plasma and from the glow discharge source are illustrated in Fig. 81.a and Fig. 81.b, respectively. Although both spectra show
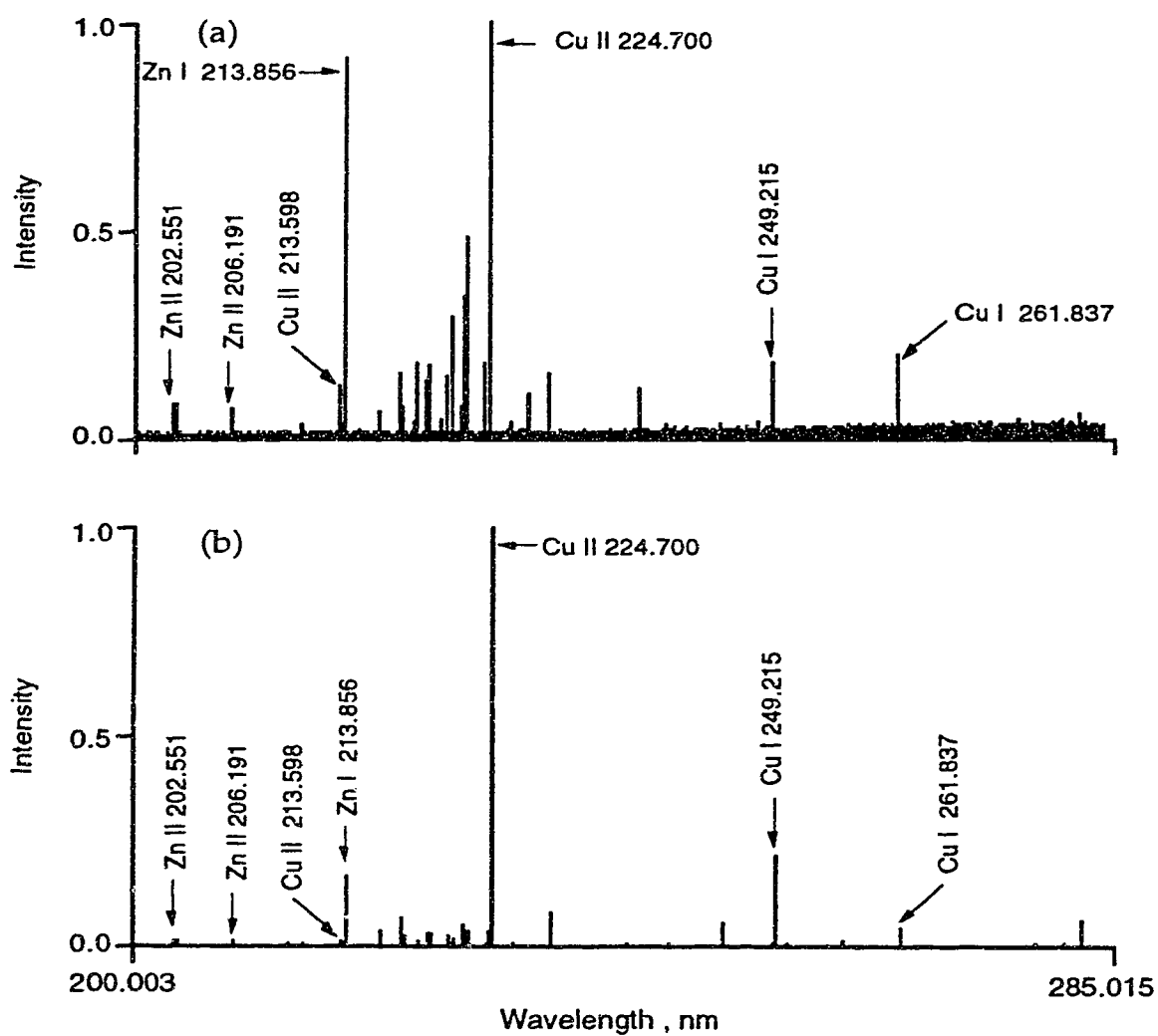
Fig. 81. Emission spectra of brass in the ultraviolet region from the ICP
(a) and from the GDD (b).
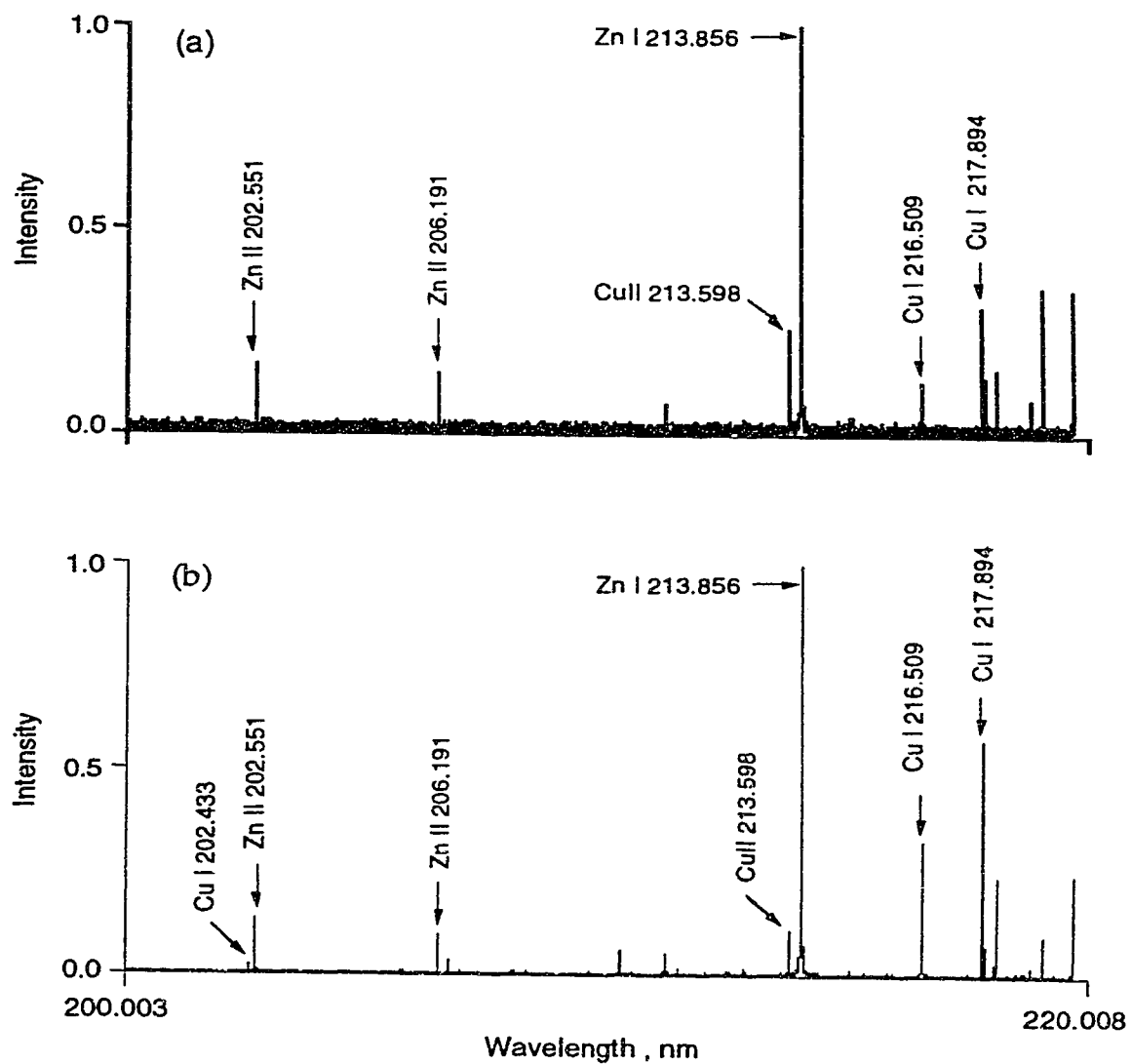
Fig. 82. Expanded plot of Fig. 81 in the vicinity of the Zn I 213.856 nm
line.
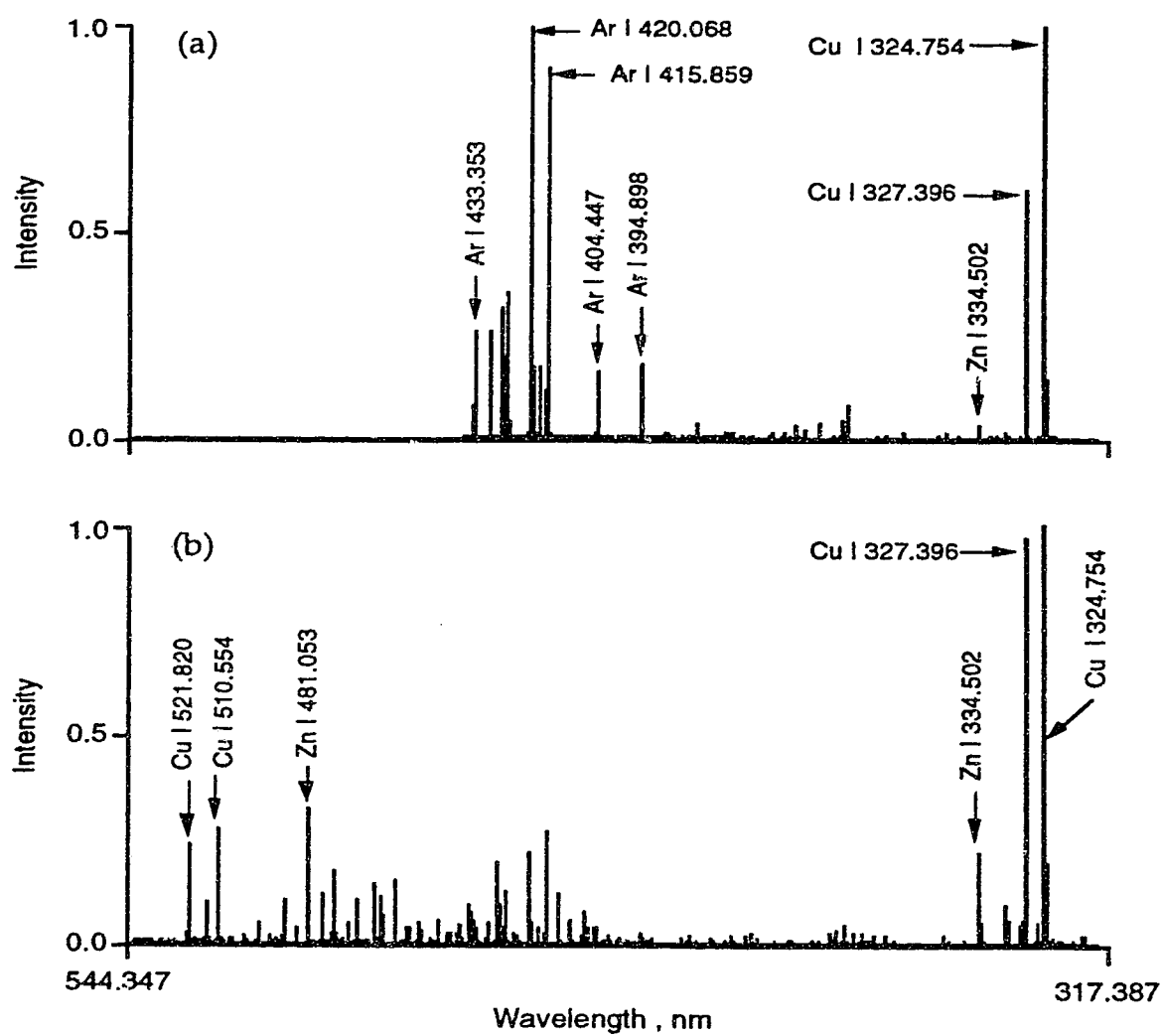
Fig. 83. Emission spectra of brass in the visible region from the ICP (a) and from the GDD (b).

the same set of most prominent lines, some differences can be seen between the two spectra. First, the intensity of the Zn I 213.856 nm line from the GDD (Fig. 81.b) is only about one fifth of that of the Cu II 224.700 nm line; whereas, the intensity of the Zn I 213.856 nm line from the ICP (Fig. 81.a) is almost as strong as that of the Cu II 224.700 nm line. Second, those lines between the Zn I 213.856 nm and the Cu II 224.700 nm lines from the ICP (Fig. 81.a), which are either copper neutral atom lines or copper ionic lines, are quite strong relative to these two lines; in clear contrast, the corresponding lines from the GDD (Fig. 81.b) are quite weak.

Fig. 82 is an expanded plot of Fig. 81 in the vicinity of the Zn I 213.856 nm line. It can be seen that the emission spectrum from the glow discharge device (Fig. 82.b) has more observable lines in this spectral region than the spectrum from the inductively coupled plasma (Fig. 82.a). For instance, in the GDD (Fig. 82.b) the Cu I 202.433 nm line can be seen very clearly, but in the ICP (Fig. 82.a), not a trace of the Cu I 202.433 nm line can be detected. In the ICP (Fig. 82.a), between the Zn II 206.200 nm line and Cu II 213.598 nm line, the only distinguishable line is the He-Ne reference laser line "leaked" into the system; in the same region of the GDD spectrum (Fig. 82.b), Zn II 206.425 nm, Zn II 209.986 nm and Cu II 211.209 nm lines can also be distinguished from the baseline. The relative intensities of the lines are also different: Cu I 216.509 nm and Cu I 217.894 nm lines from the GDD (Fig. 82.b) look much stronger than the two lines from the ICP (Fig. 82.a) relative to the Zn I 213.856 nm line.

Shown in Fig. 83 are the emission spectra of the same brass sample in the visible region. More lines are present in the GDD emission spectrum (Fig.

83.b). In the ICP spectrum (Fig. 83.a), from 433 nm to 544 nm, not even a single line is observable; whereas, in the same region of the GDD spectrum (Fig. 83.b), in addition to the two copper lines and one zinc line, a huge number of ionic argon lines can also be observed (the details will be seen later in section 5-3-5 and in Chapter 6). The appearance of the copper lines in the GDD can be explained by the radiative deexcitation of the copper atoms in excited state Cu^* [164]. These copper atoms in excited state could result from the following ion-electron recombination process:

$$Cu^+ + e^- \rightarrow Cu^* + hv$$
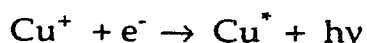
While in the ICP, these copper atoms in excited state are collisionally deexcited due to the relatively high pressure (1 atm) compared to the low pressure (2.5 torr) used in the GDD, thus no emission can be observed.

Also, in the ICP (Fig. 83.a), Ar I 420.068 nm and Ar I 415.859 nm lines are two of the most prominent lines; in the GDD (Fig. 83.b), they are relatively weak. In the ICP (Fig. 83.a), the intensity ratio of the Cu I 324.754 nm line to Cu I 327.396 nm line is roughly 2:1; in the GDD (Fig. 83.b), this ratio becomes almost 1:1.

5-3-2. Stainless steel sample

Portions of the emission spectra for a stainless steel sample in the ultraviolet region from an ICP and a GDD are presented in Fig. 84. One thing in common about the ICP and the GDD spectra (Fig. 84.a, Fig. 84. b) is that they both have the same most prominent line: the Fe II 259.940 nm line. The relative intensities of the rest of the lines are all quite different. The three iron lines in the vicinity of Fe I 248.327 nm line are very strong in the GDD

(Fig. 84.b); while the same three lines in the ICP (Fig. 84.a) are very small. The Ni I 231.097 nm line in the GDD (Fig. 84.b) can be easily seen, but in the ICP (Fig. 84.a), this line simply does not exist.

The emission spectra of stainless steel in the visible region from an ICP and a GDD are shown in Fig. 85. Needless to say, the emission spectra from the ICP (Fig. 85.a) and the GDD (Fig. 85.b) are different. Similar to Fig. 83, in the ICP (Fig. 85.a), the spectral region from 428 nm to 552 nm is simply empty; while in the GDD (Fig. 85.b), a few dozen lines (mostly ionic argon lines) are present in the same spectral region. For the ICP (Fig. 85.a), the dominant lines are the Ar I 420.068 nm and the Ar I 415.859 nm lines; for the GDD (Fig. 85.b), the dominant lines are the Fe I 374.994 nm and the Fe I 385.991 nm lines.

The characteristic emission triplets of Cr in the vicinity of 360 nm and 427 nm from the ICP and the GDD are illustrated in Fig. 86 and Fig. 87 as expanded versions of Fig. 85.

5-3-3. Low alloy steel sample

The emission spectra of low alloy steel in the ultraviolet region from the ICP and the GDD are illustrated in Fig. 88. The difference between the ICP (Fig. 88.a) and the GDD (Fig. 88.b) spectra is roughly the same as that shown earlier for the stainless steel sample (Fig. 84). In general, there are more lines present in the GDD emission spectrum (Fig. 88.b), and the intensities of the Fe I lines relative to the Fe II lines are stronger in the GDD spectrum compared to the ICP emission spectrum (Fig. 88.a).
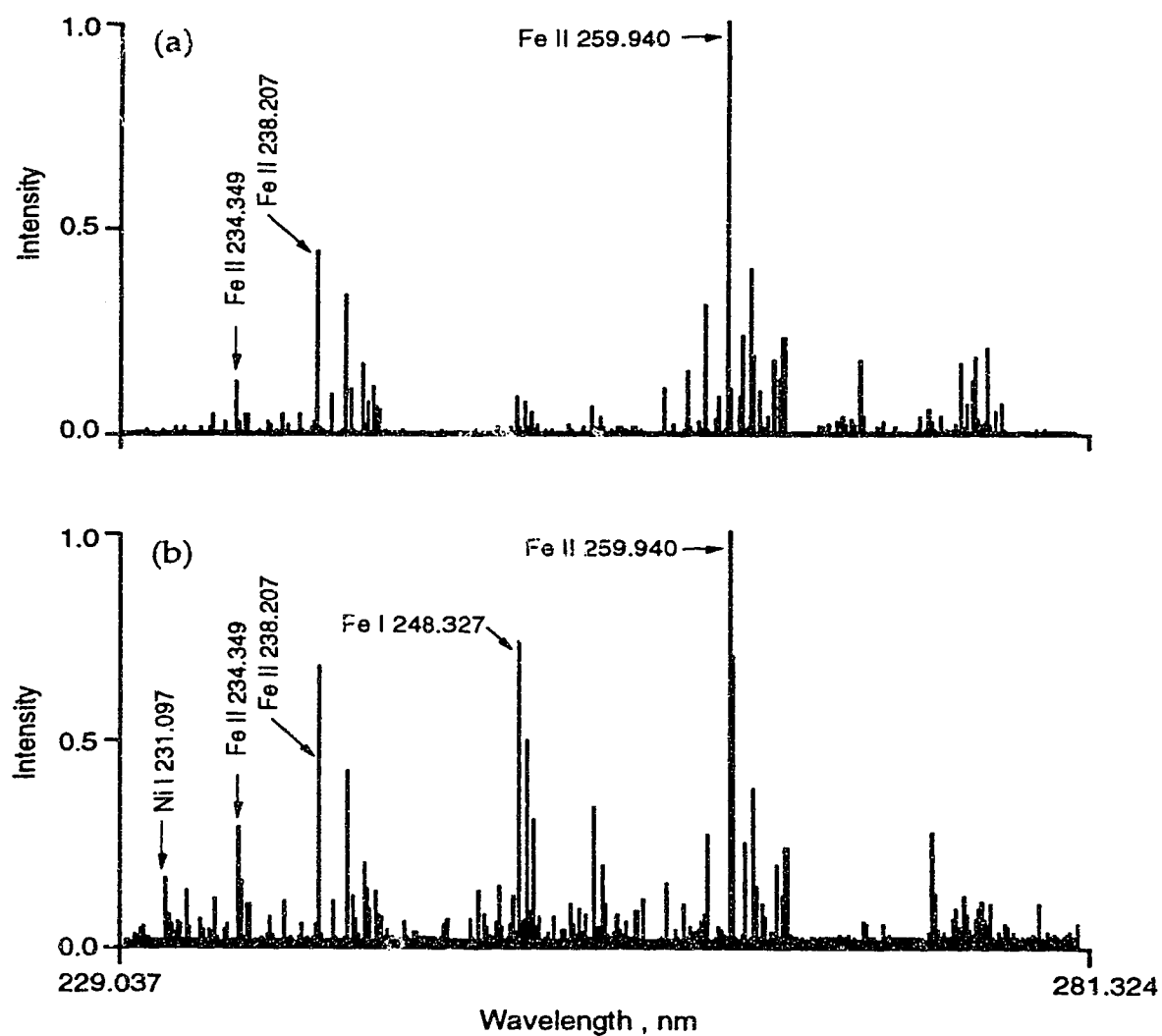
Fig. 84. Emission spectra of stainless steel in the ultraviolet region from an ICP (a) and from a GDD (b).
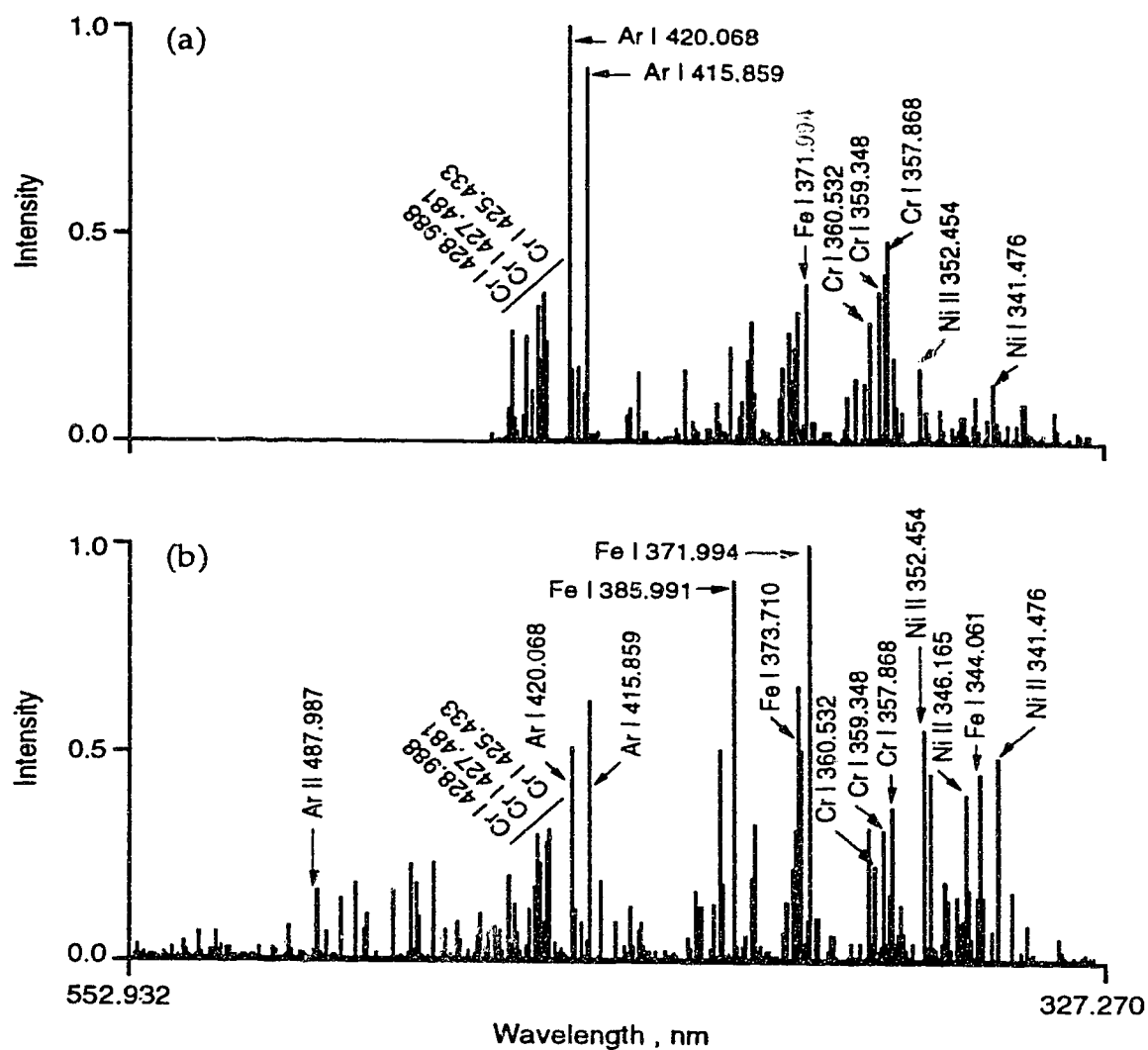
Fig. 85. Emission spectra of staineless steel in the visible region from an ICP (a) and from a GDD (b).
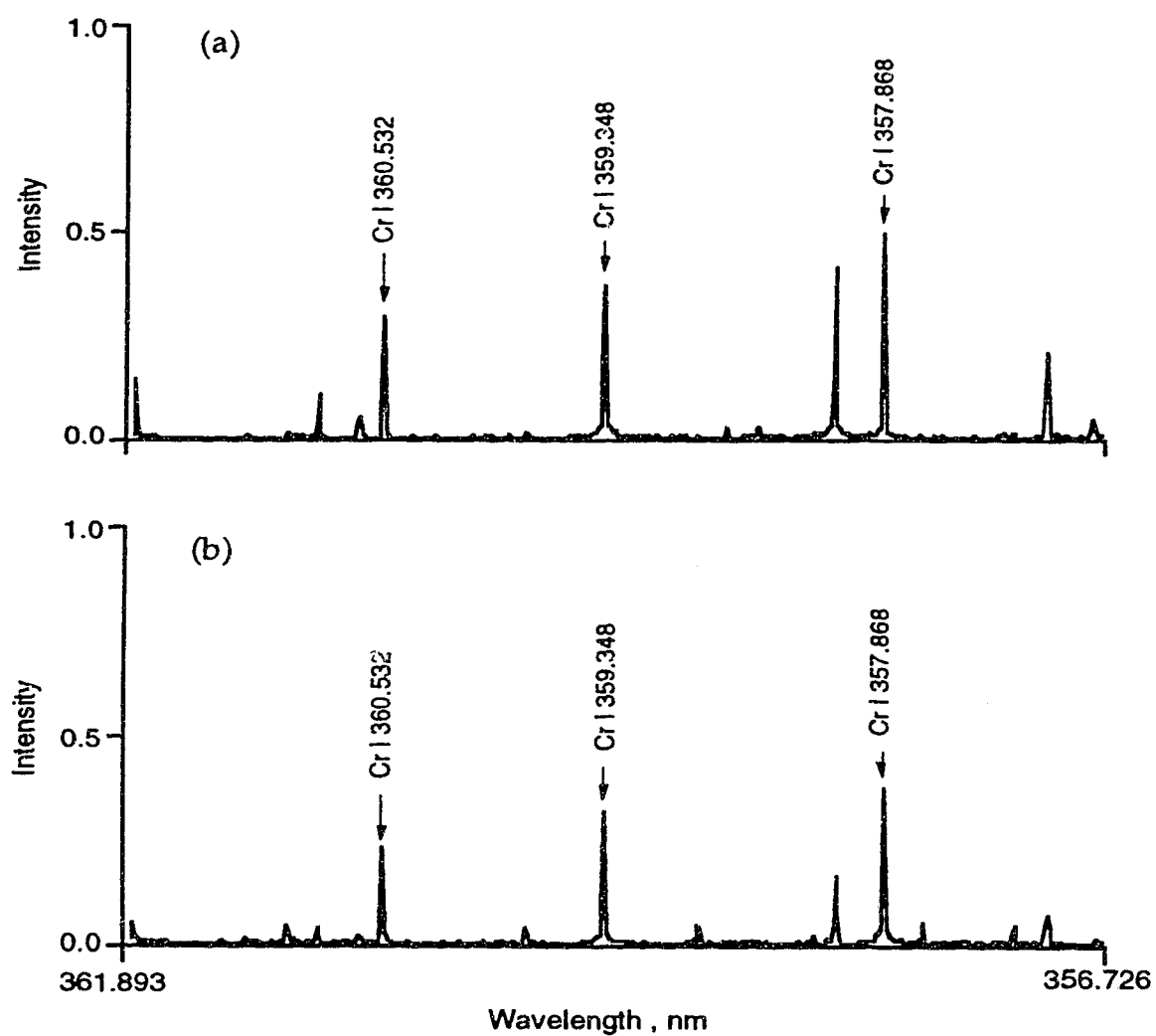
Fig. 86. Expanded plot of Fig. 85 showing the characteristic emission triplet of Cr in the vicinity of 360 nm from the ICP (a) and from the GDD (b).
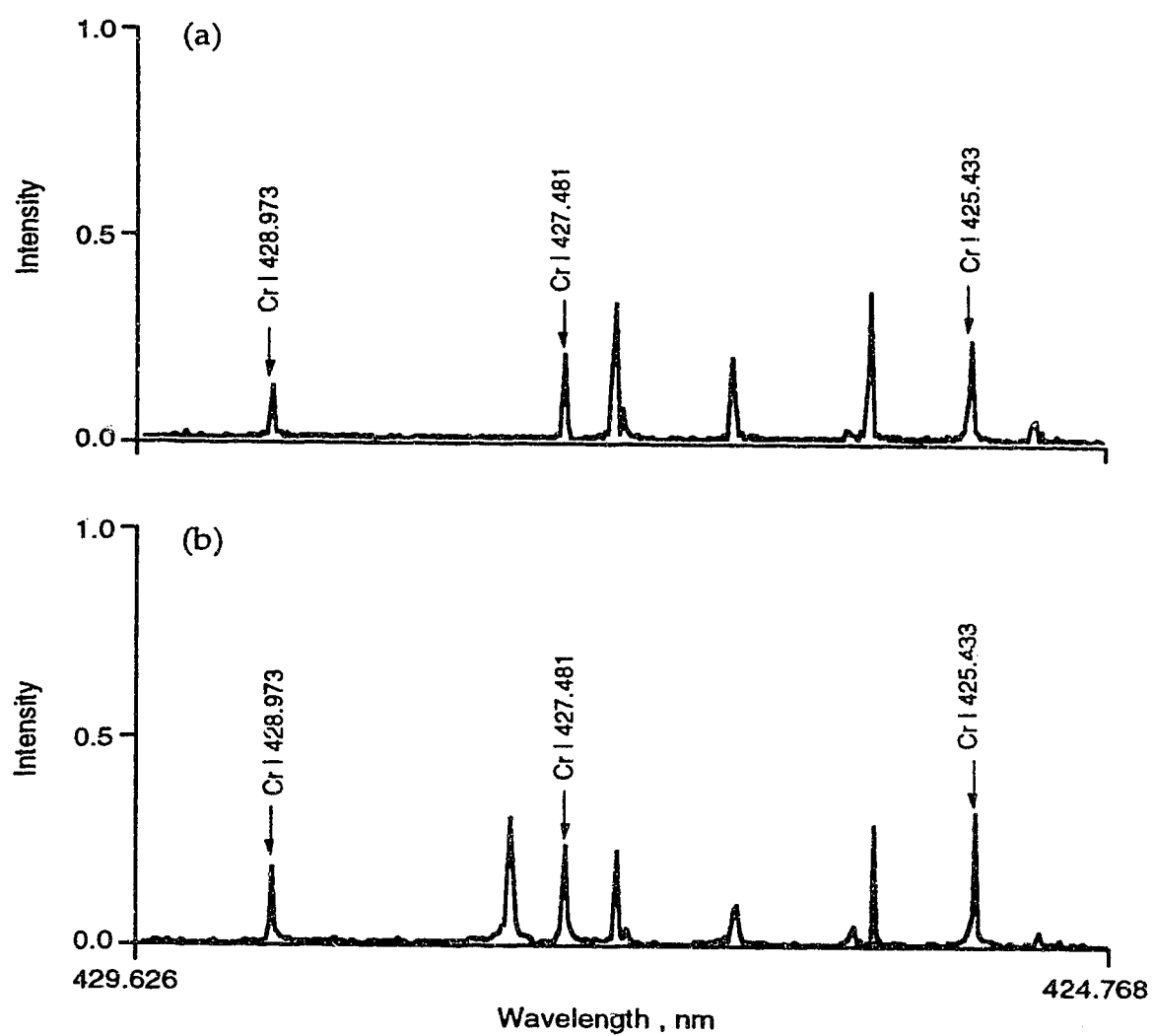
Fig. 87. Expanded plot of Fig. 85 showing the characteristic emission triplet of Cr in the vicinity of 427 nm from the ICP (a) and from the GDD (b).
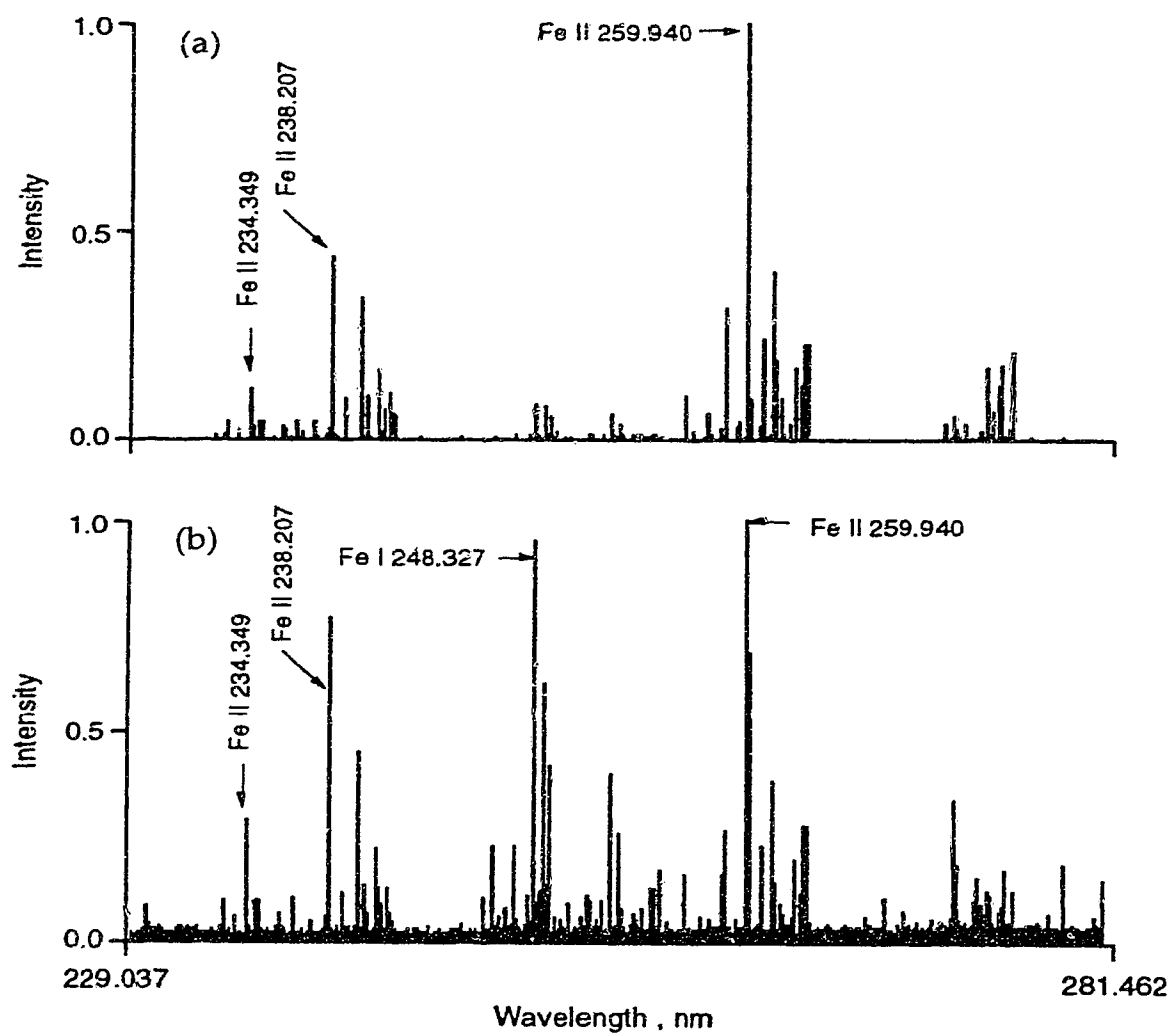
Fig. 88. Emission spectra of low alloy steel in the ultraviolet region from the ICP (a) and from the GDD (b).
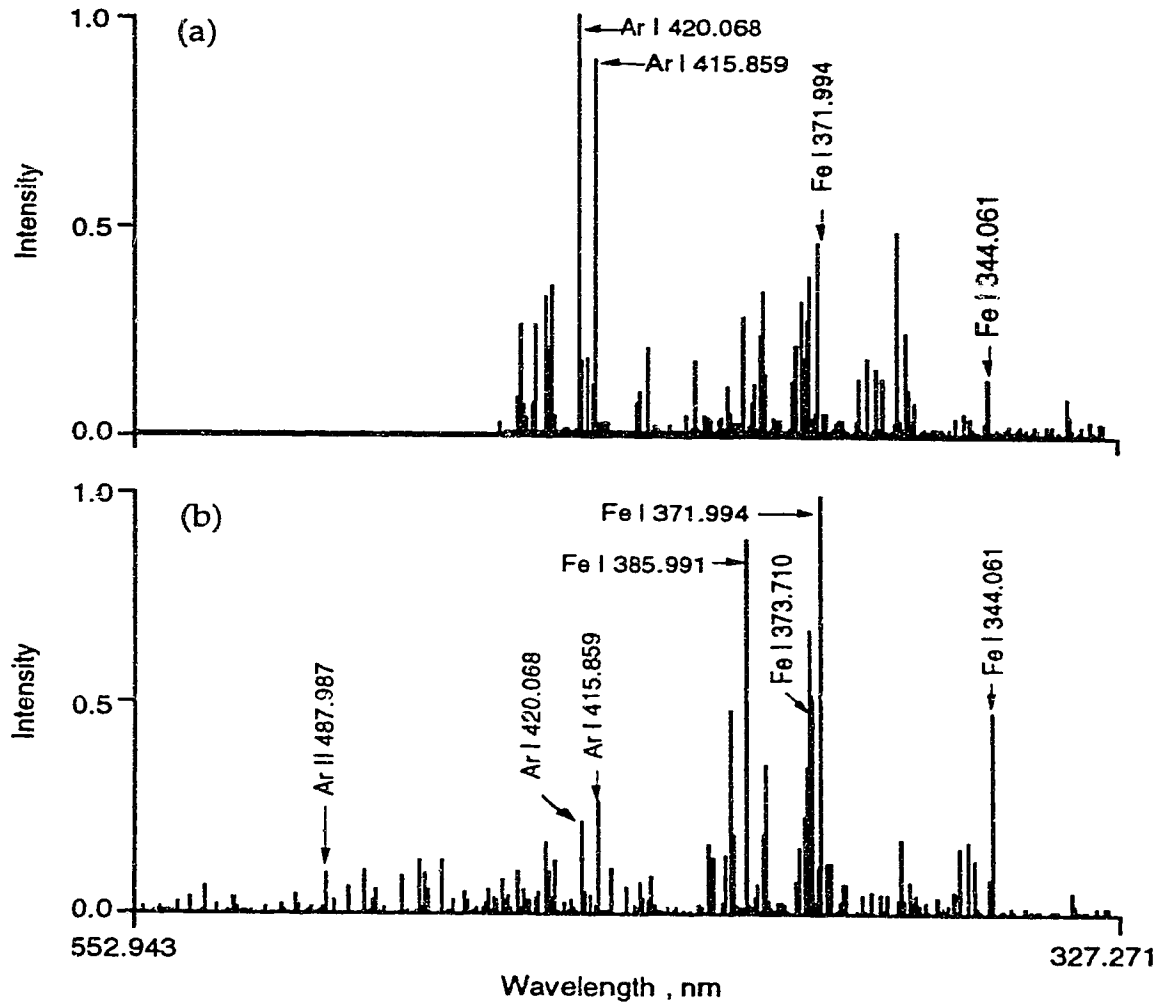
Fig. 89. Emission spectra of low alloy steel in the visible region from the ICP (a) and from the GDD (b).

The emission spectra of the low alloy steel sample in the visible region from the ICP and the GDD are presented in Fig. 89. The difference between the spectra from the ICP (Fig. 89.a) and the GDD (Fig. 89.b) is almost identical to that between Fig. 85.a and Fig. 85.b, with half of the spectral region empty in the ICP (Fig. 89.a) and very densely filled with lines in the GDD (Fig. 89.b). Also in the ICP (Fig. 89.a), the Ar I 420.068 nm and Ar I 415.859 nm lines are dominant; while in the GDD (Fig. 89.b), they are not, where half a dozen prominent lines are Fe I lines.

5-3-4. Stainless steel vs low alloy steel

The emission spectra of stainless steel and low alloy steel in the ultraviolet spectral region from the ICP are presented in Fig. 90. Fig. 90.a and Fig. 90.b are almost exactly the same, except in the vicinity of 267 nm, where some Cr II lines are present in Fig. 90.a the spectrum of the stainless steel sample.

The emission spectra of stainless steel and low alloy steel from a GDD in the ultraviolet region are shown in Fig. 91. The stainless steel spectrum and the low alloy steel spectrum are almost identical except for the presence of the Ni II 231.097 nm line in the stainless steel spectrum.

Fig. 92 is an expanded version of Fig. 91, illustrating the presence of 5 Ni lines in stainless steel (Fig. 92.a), and the absence of these lines in the spectrum of the low alloy steel (Fig. 92.b).

The emission spectra of stainless steel and low alloy steel from an ICP
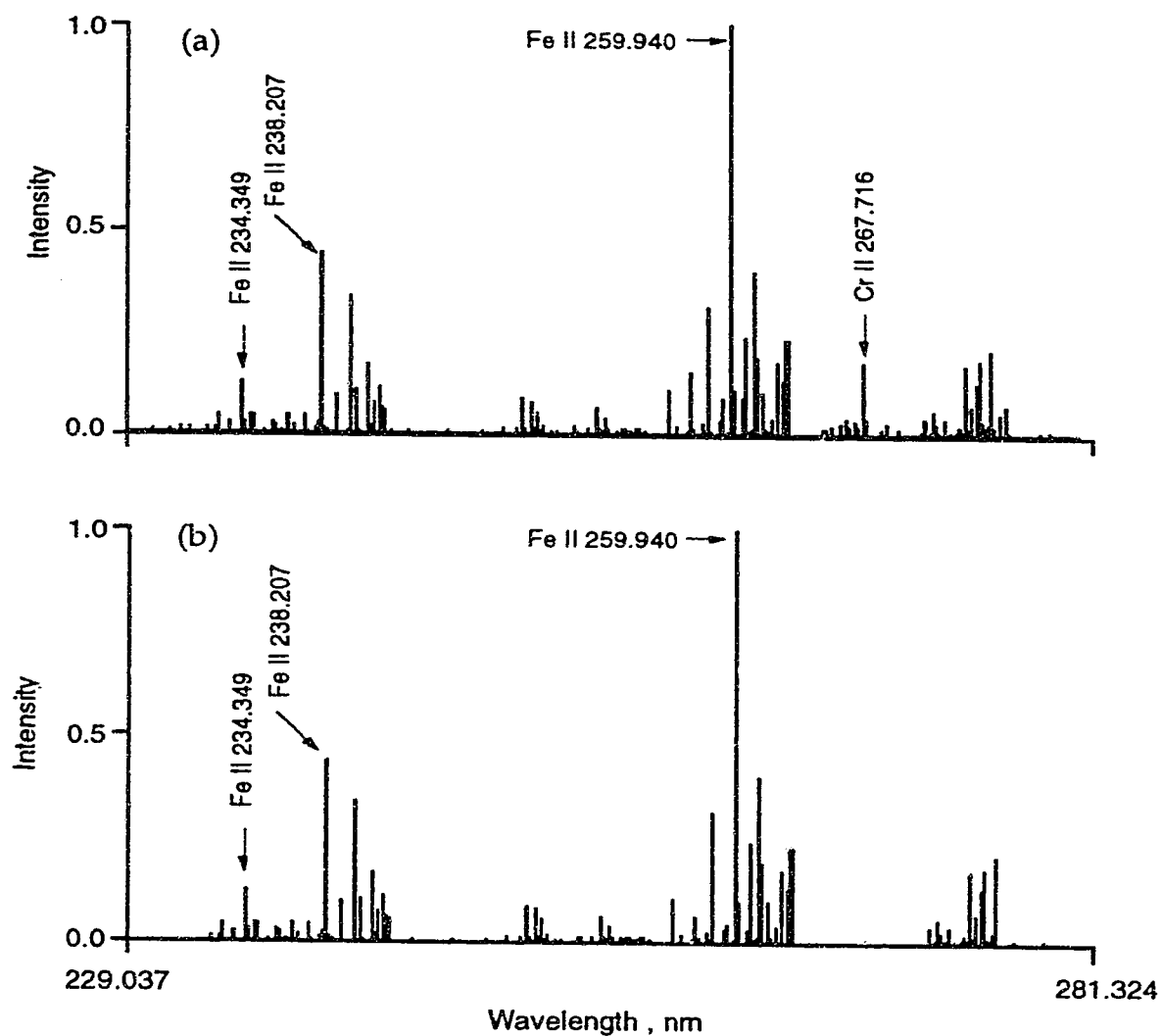
Fig. 90. Emission spectra of stainless steel (a) and low alloy steel (b) from the ICP in the ultraviolet region.
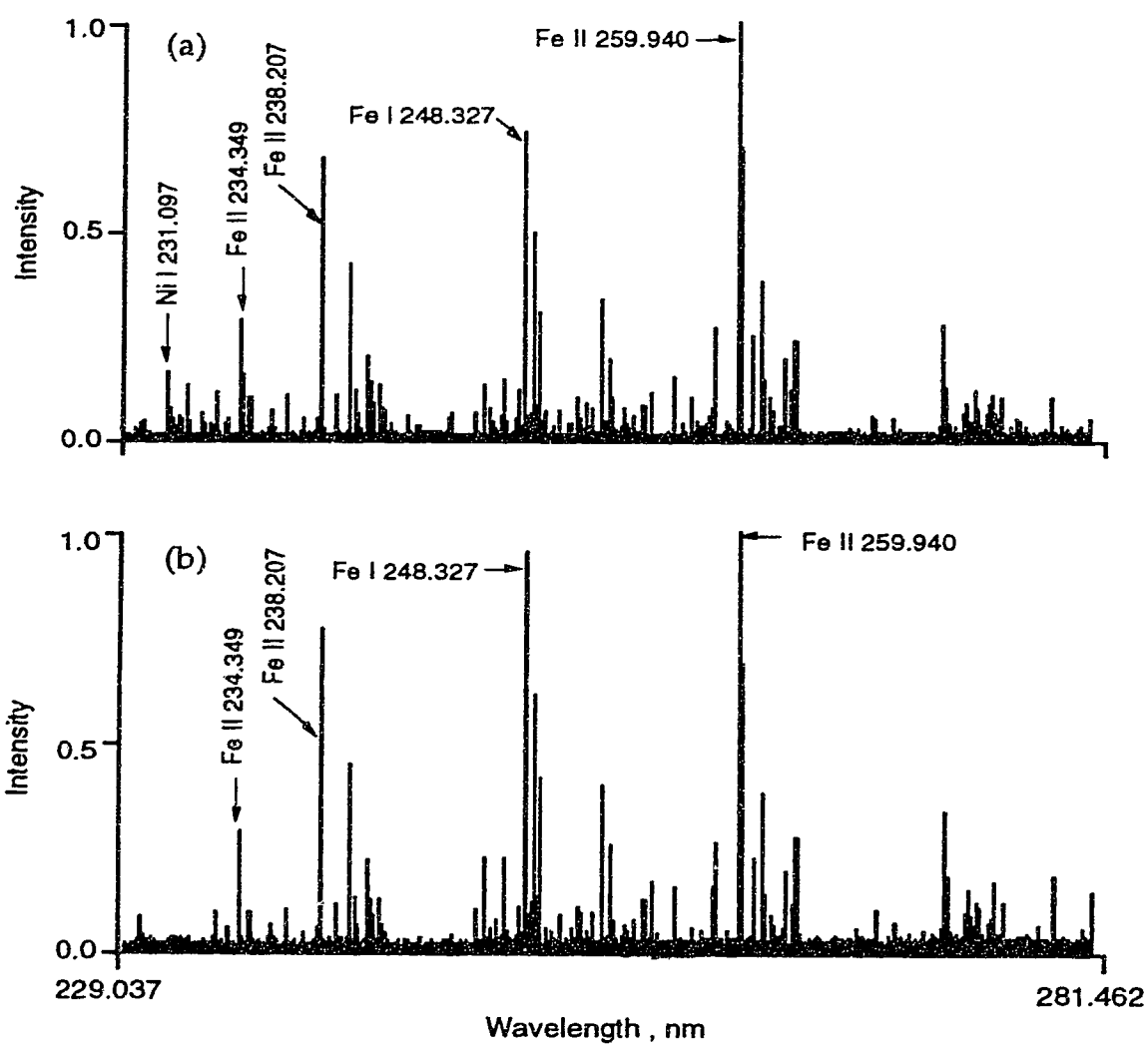
Fig. 91. Emission spectra of stainless steel (a) and low alloy steel (b) from the GDD in the ultraviolet region.
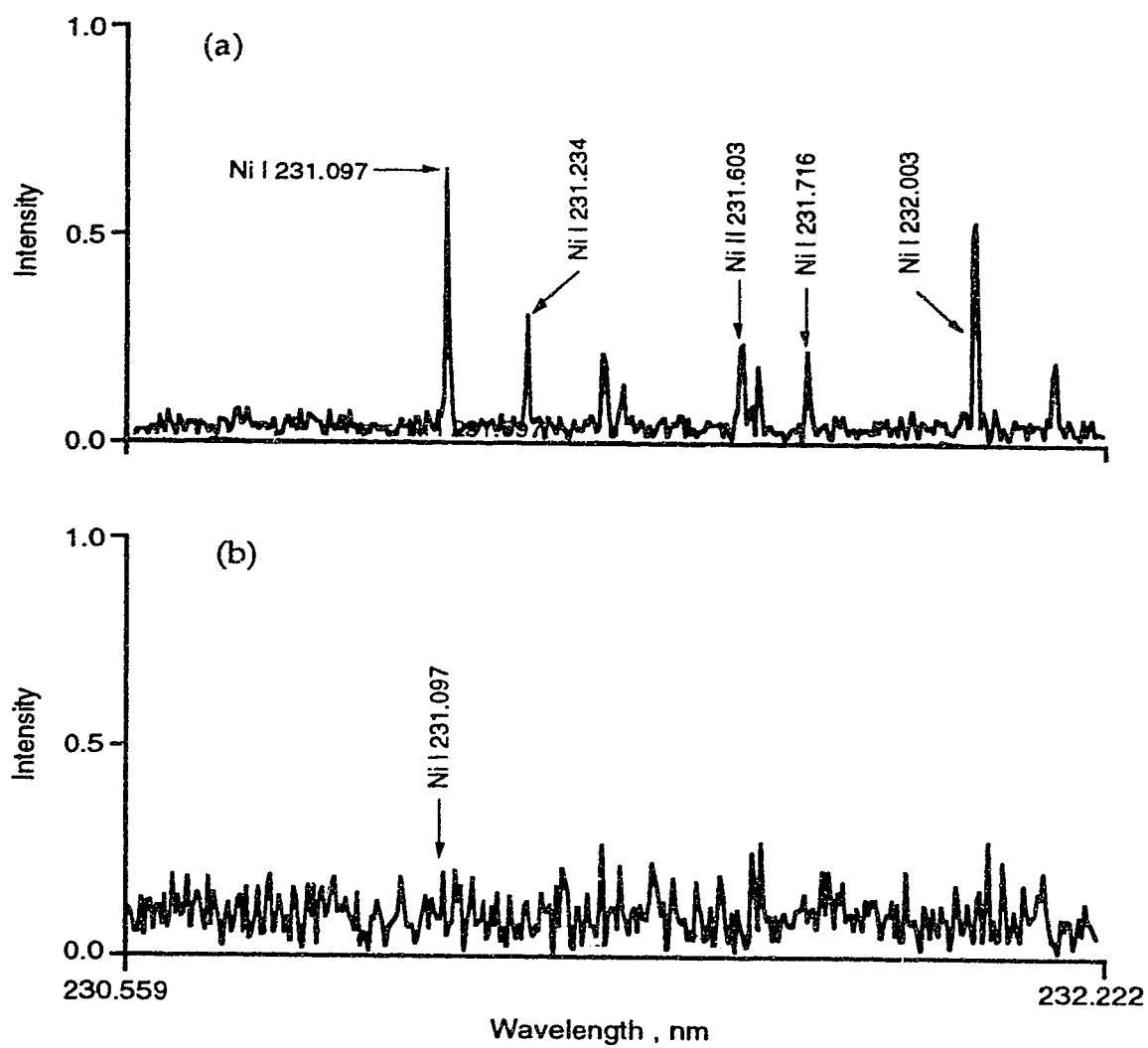
Fig. 92. Expanded plots of Fig. 91 showing Ni lines.
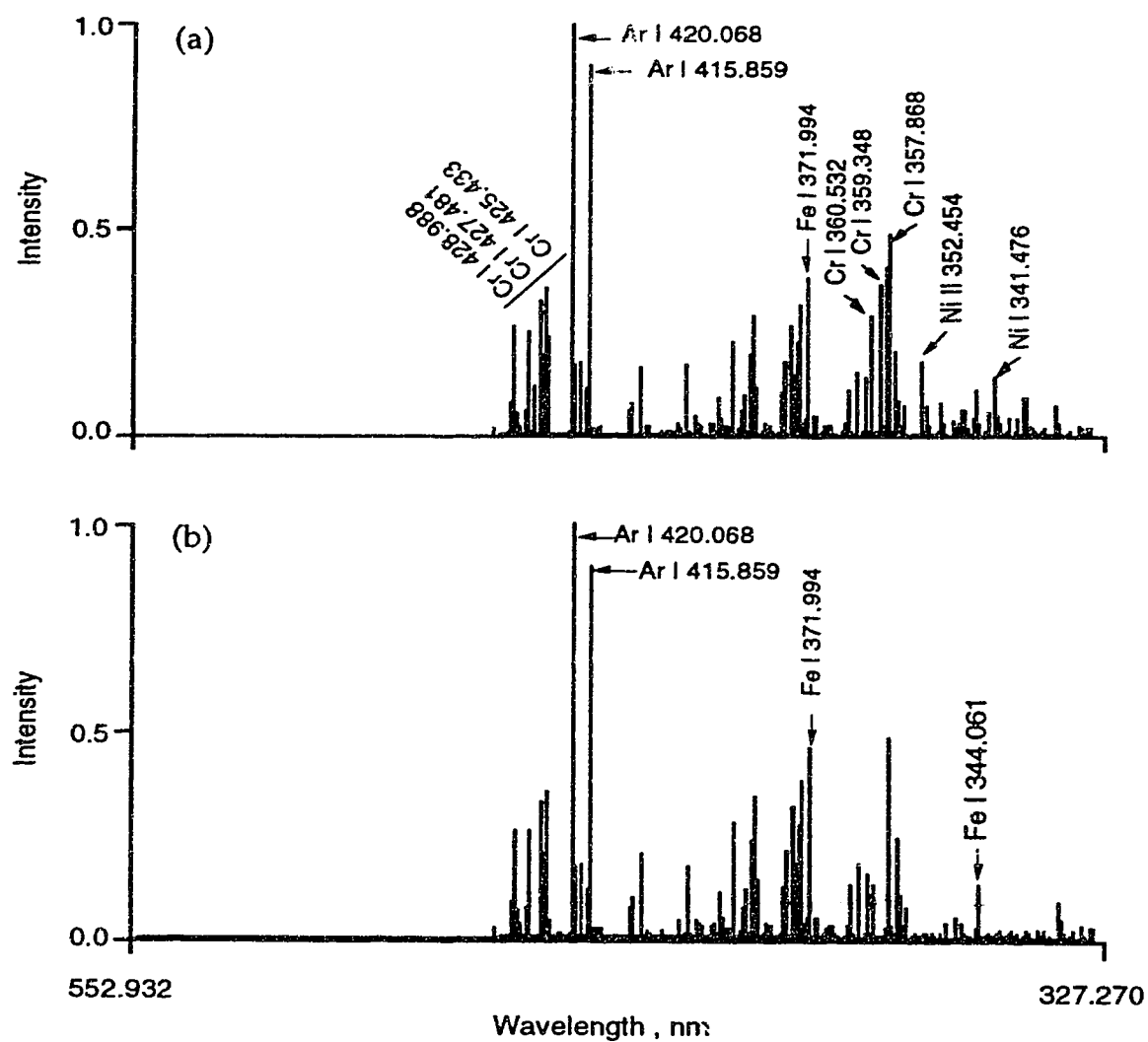
Fig. 93. Emission spectra of stainless steel (a) and low alloy steel (b) from the ICP in the visible region.
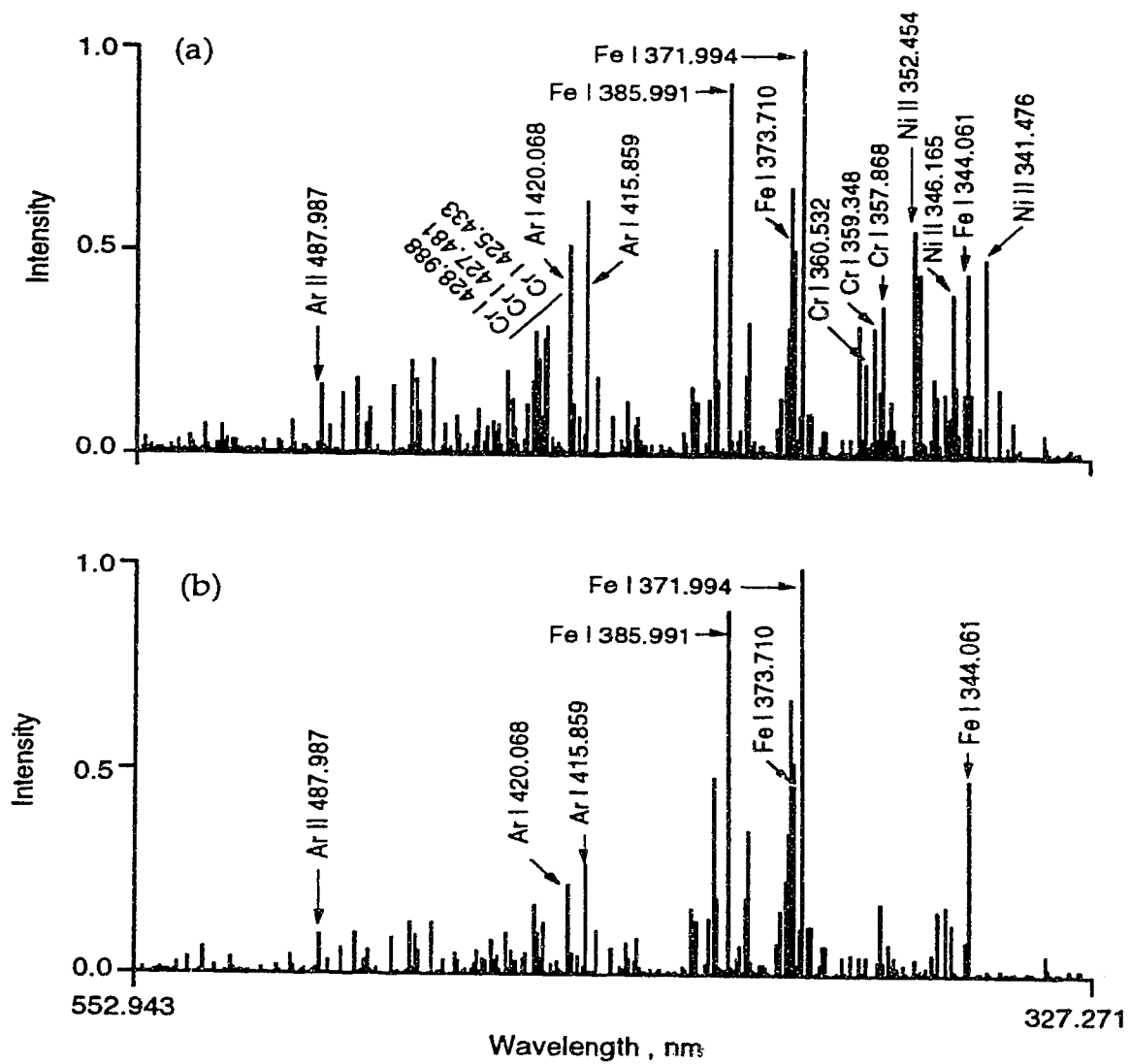
Fig. 94. Emission spectra of stainless steel (a) and low alloy steel (b) from the GDD in the visible region.

in the visible region are shown in Fig. 93. The existence of the Cr triplets and the Ni lines in Fig. 93.a indicates a relatively higher percentage of chromium and nickel in stainless steel compared to low alloy steel as shown from the low alloy steel emission spectrum in Fig. 93.b.

Similar to Fig. 93, the emission spectra of stainless steel and low alloy steel from the glow discharge device in the visible region are given in Fig. 94. The differences between Fig. 94.a and Fig. 94.b are the same as those between Fig. 93.a and Fig. 93.b, that is, Cr and Ni lines are clearly prominent in the spectrum of the stainless steel sample.

The results observed from Fig. 90 to Fig. 94 should not be surprising considering that this stainless steel sample contains 17.4% chromium and 11.35% nickel (Table 10), while the low alloy steel sample only contains 0.3% chromium and 0.6% nickel (Table 11).

5-3-5. Comparison of argon emission from the ICP and the GDD

Portions of the emission spectra of brass, stainless steel, and low alloy steel from the GDD and the ICP are illustrated in Fig. 95, Fig. 96, and Fig. 97, respectively. All the emission spectra from the ICP (Fig. 95.b, Fig. 96.b, and Fig. 97.b) have been scale expanded on the vertical axis. The presence of ionic argon lines in the glow discharge device spectra is absolutely conclusive as indicated in Fig. 95.a, Fig. 96.a, and Fig. 97.a. The absence of any ionic argon lines from the ICP as indicated in Fig. 95.b, Fig. 96.b, and Fig. 97.b is also quite evident even with the intensity axis expanded.
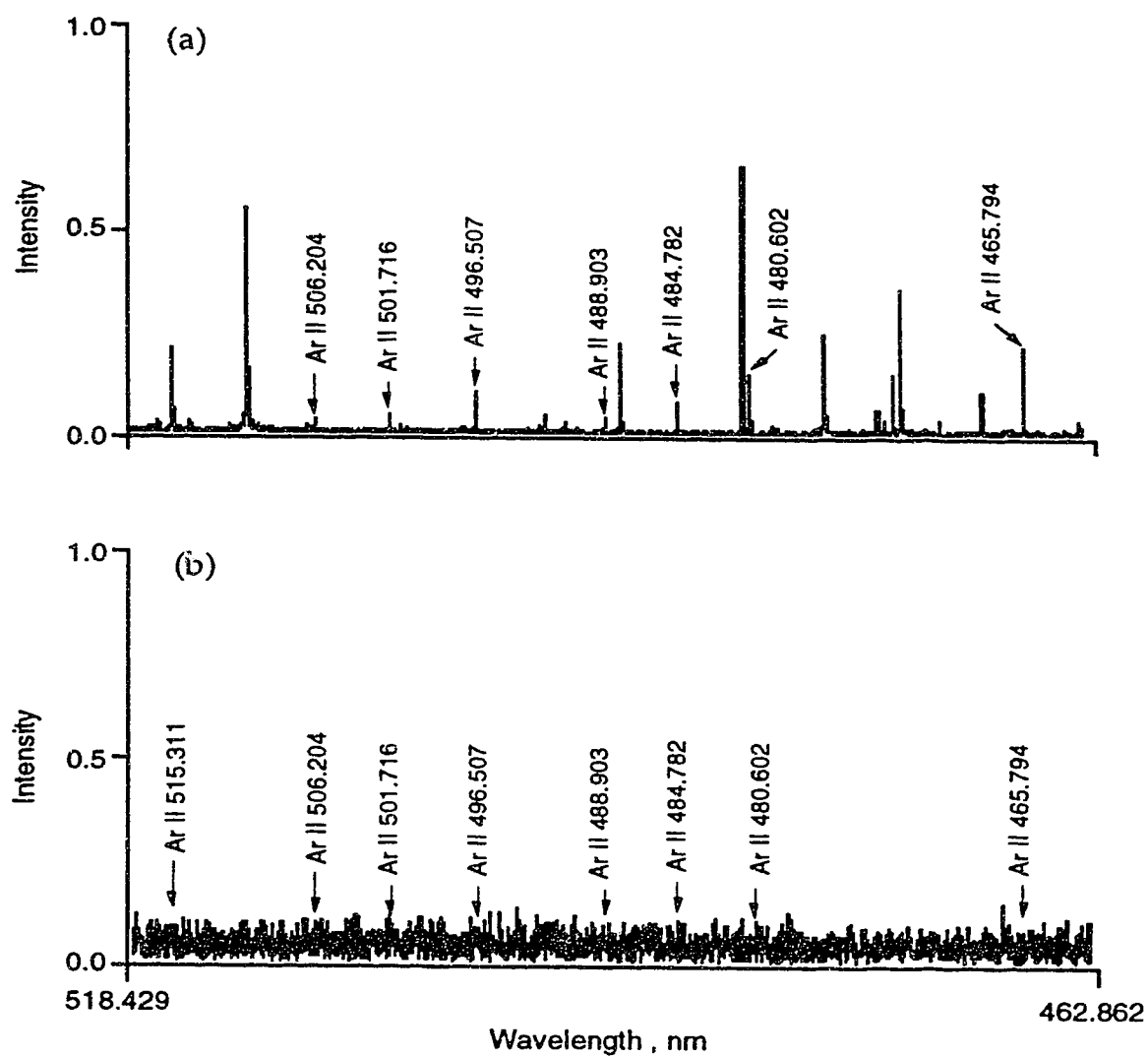
Fig. 95. One portion of the emission spectra of brass from the GDD (a) and from the ICP (b) showing ionic argon lines.
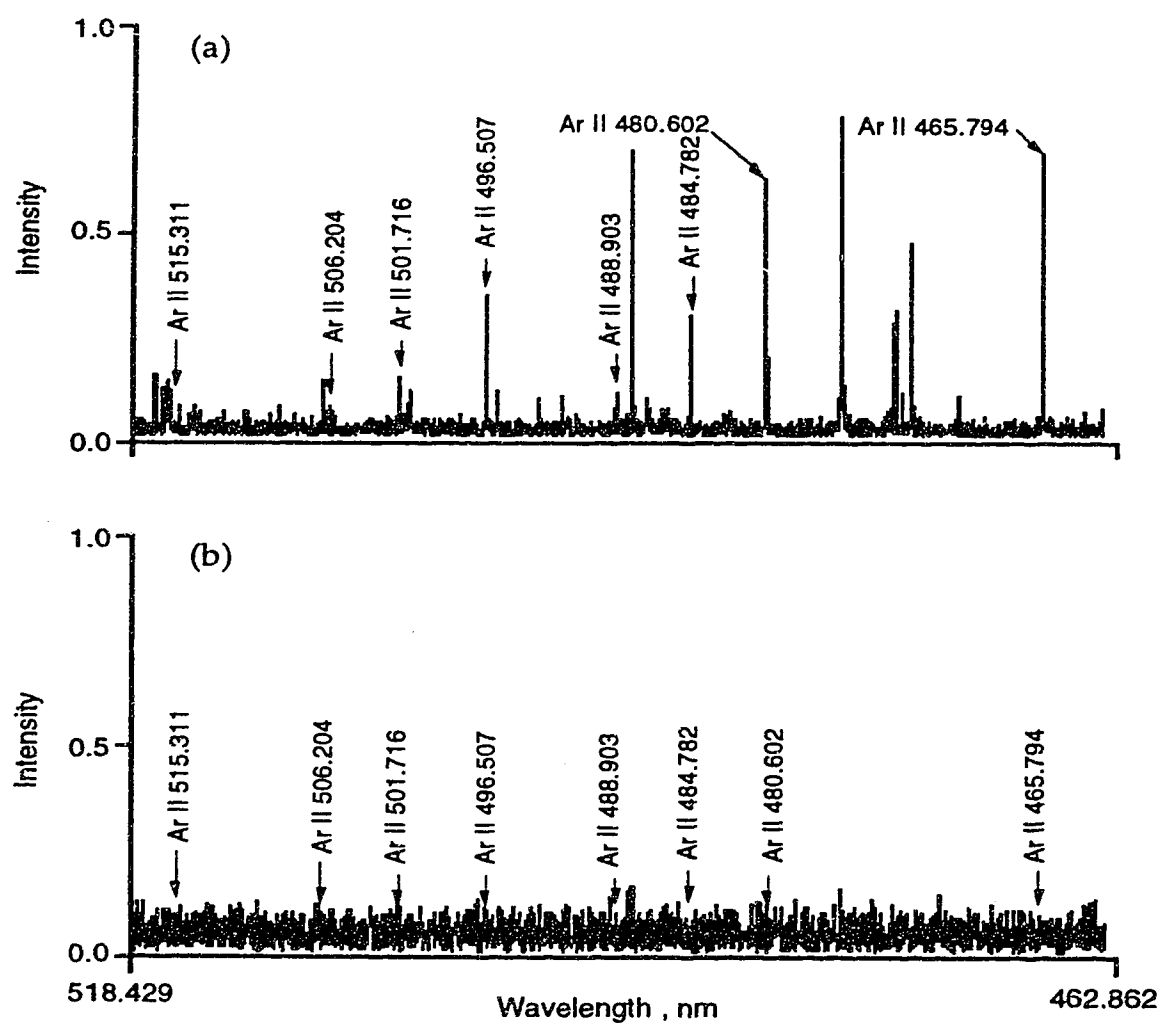
Fig. 96. One portion of the emission spectra of stainless steel from the GDD (a) and from the ICP (b) showing ionic argon lines.
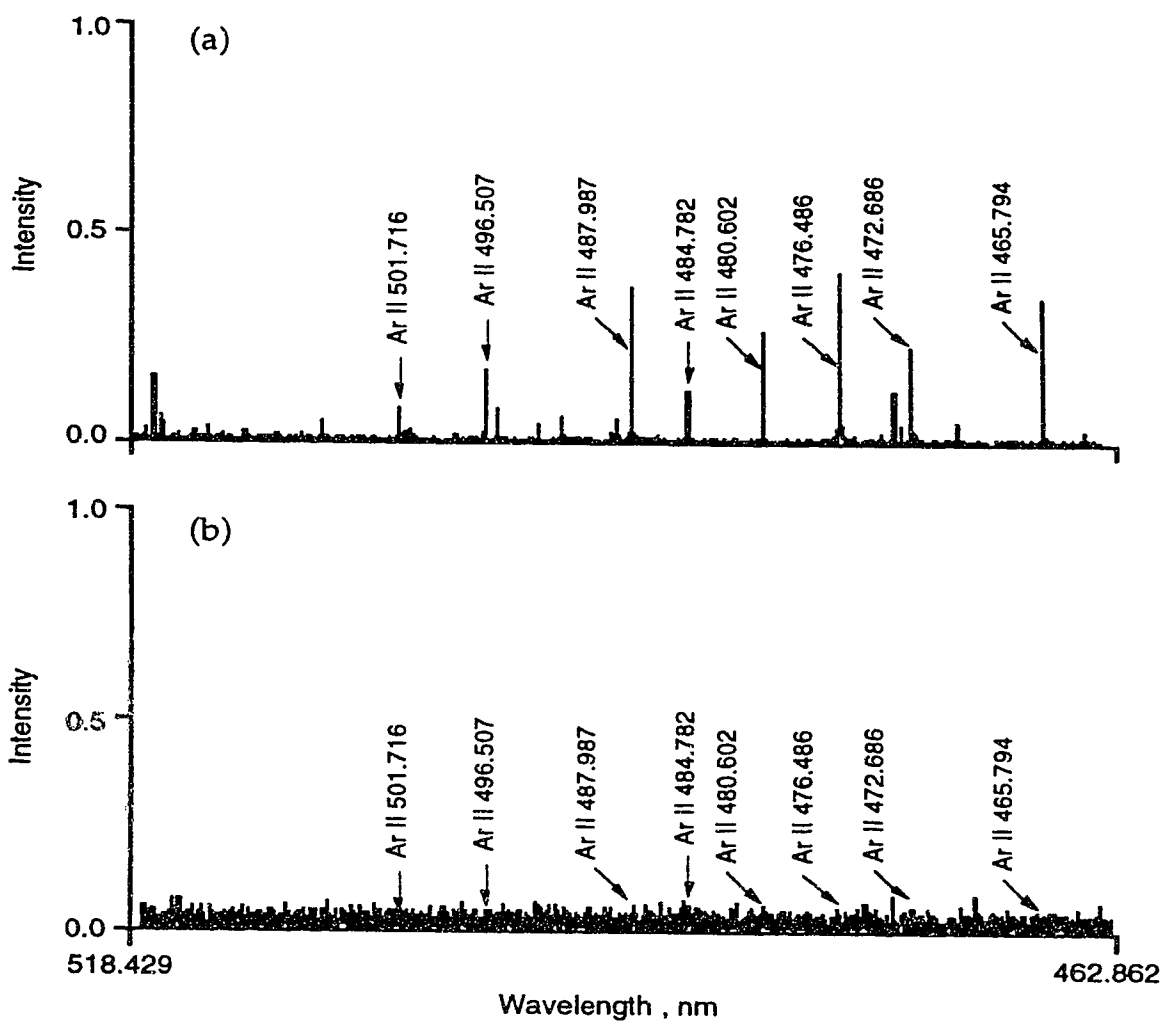
Fig. 97. One portion of the emission spectra of low alloy steel from
the GDD (a) andfrom the ICP (b) showing ionic argon lines.

The contrast between the emission spectra from the ICP and the GDD indicates that different spectrochemical excitation mechanisms are operative in the ICP and the GDD. The following processes are probably responsible for the ionic argon emission in the GDD:

$$Ar^{2+} + e^- \rightarrow Ar^{+*}$$

$$Ar^{+*} \rightarrow Ar^+ + h\upsilon$$
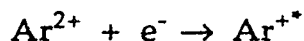
The product of the recombination reaction is the ionic argon in the excited state Ar^{+*}, and the radiative deexcitation of Ar^{+*} leads to the ionic argon emission. In fact, the presence of Ar^{2+} in the GDD and the absence of Ar^{2+} in the ICP have been proven in our laboratory by interfacing the two sources to the mass spectrometer.

Studies are in progress in our laboratory to better understand the two sources and explain the differences observed [164]. For example, it is observed that in Fig. 81.b the Cu II 224.700 nm line is particularly strong relative to other ionic copper lines (say the Cu II 213.598 nm line) in the GDD compared to the ICP spectrum in Fig. 81.a. It is thought that charge exchange process is responsible for the relatively strong emission of the Cu II 224.700 nm line:

$$Ar^+ + Cu \rightarrow Ar + Cu^{+*} + \Delta E$$
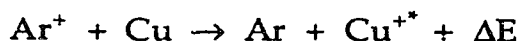
The radiative deexcitation of the copper ion in excited state Cu^{+*} results in the Cu II 224.700 nm line. One requirement for the charge exchange process to occur is an almost direct overlap of the Ar^+ and metal energy levels [165-166]. The upper energy level of the Cu II 224.700 nm transition (15.96 eV) almost directly overlaps the Ar^+ level (15.94 eV), $\Delta E = - 0.02$ eV, providing an

effective pathway for a charge exchange process to occur, and thus selectively enhancing the Cu II 224.700 nm transition.

He and Ne were also used as discharge gases in the GDD [164] to study the charge exchange process. Observation of selectively enhanced lines whose upper energy levels closely overlap the He^+ and Ne^+ energy levels could provide evidence for the existence of the charge exchange process in the GDD. The details of these studies will be reported by Y. Zhao [164].

5-4. Temperature measurements in the ICP and the GDD

Excitation temperatures in the inductively coupled plasma and the glow discharge device are measured and compared with various thermometric species using the "Boltzmann plot" method and the line pair intensity ratio method. The effect of forward power on the excitation temperatures of the ICP has been studied in Chapter 3. In this section, the effect of power on the excitation temperatures of a glow discharge device is studied. The gf values and other parameters used in the calculations of excitation temperatures are identical to those listed in Chapter 2 except when indicated otherwise.

5-4-1. Comparison of excitation temperature in the ICP and the GDD

One section of the emission spectrum of 1000 μg/ml Fe from the ICP used in the calculation of excitation temperature and the corresponding Boltzmann plot are given in Fig. 98. The excitation temperature derived from the intensities of 5 Fe II lines as indicated in Fig. 98.a is 7700 K.

The same section of the emission spectrum of 1000 µg/ml Fe from the ICP showing the 8 Fe II lines used in the temperature calculation and the corresponding Boltzmann plot are shown in Fig. 99. The excitation temperature derived from these 8 Fe II line intensities is 7500 K.

Similarly, a section of the emission spectrum of 1000 µg/ml Fe from the ICP showing 6 Fe I lines and the corresponding Boltzmann plot are provided in Fig. 100. The excitation temperature calculated based on the intensities of these 6 Fe I lines is 6100 K.

The excitation temperature in the ICP derived from the intensities of 11 Ti II lines and 8 Ar I lines are 5000 K and 4900 K, respectively. The spectra showing lines used in these calculations and their Boltzmann plots are illustrated in Fig. 101 and Fig. 102.

A section of the GDD emission spectrum of stainless steel showing the 6 Fe I lines used the calculation of the excitation temperature and the corresponding Boltzmann plot are shown in Fig. 103. An excitation temperature of 3100 K was obtained.

An attempt was also made to use the 8 Ar I lines from the GDD emission to calculate the excitation temperature of the glow discharge source, but the log ($I\lambda/gA$) versus Energy plot was not a straight line, indicating possible self-absorption of these Ar I lines in the GDD. One section of the GDD emission spectrum used and the log ($I\lambda/gA$) versus Energy plot are given in Fig. 104. Note, however, the values of the Boltzmann plot are very scattered.
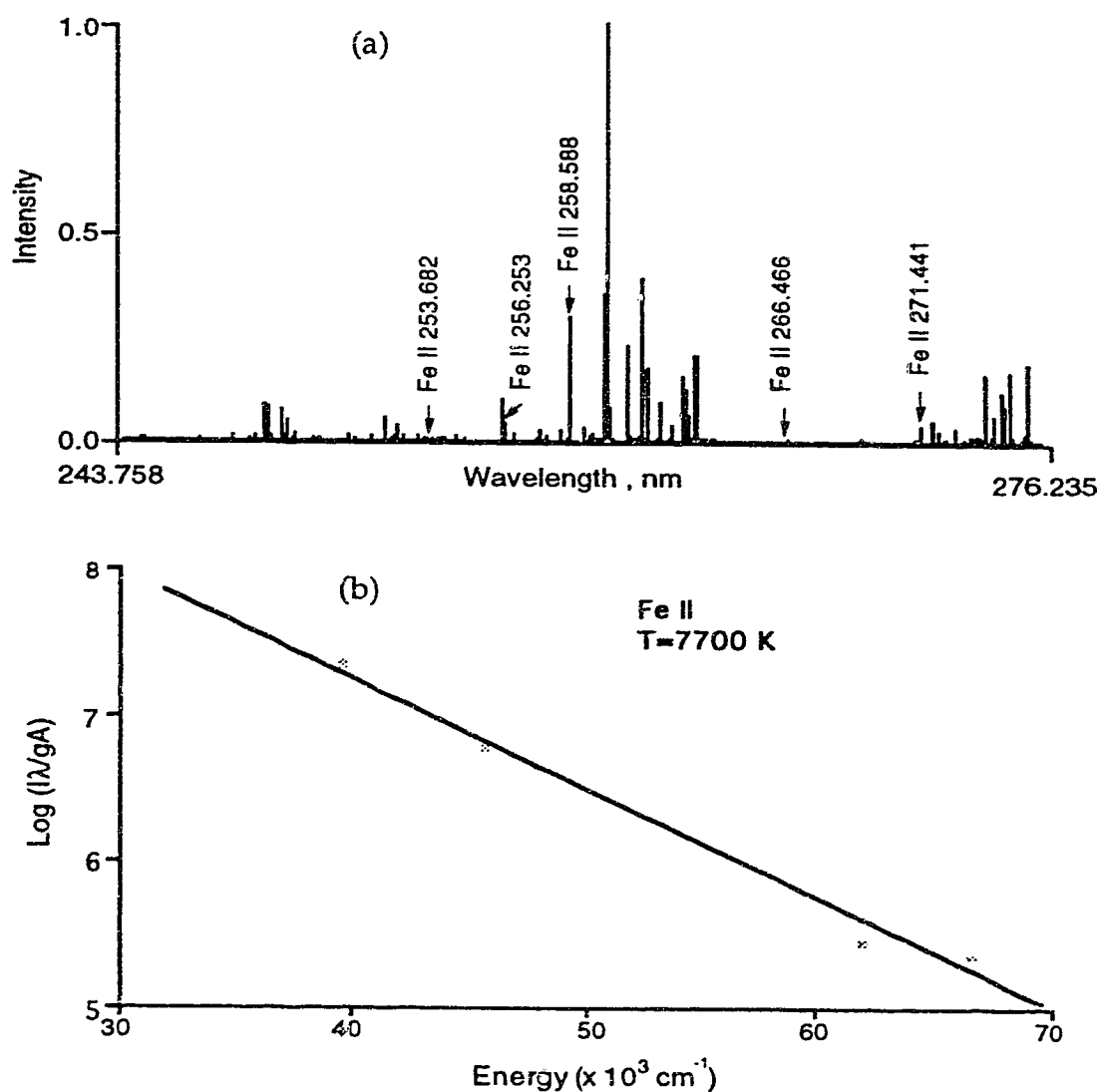
Fig. 98. Section of the emission spectrum of 1000 µg/ml Fe from the ICP showing the 5 Fe II lines (a) used in the calculation of the excitation temperature and the corresponding Boltzmann plot (b).
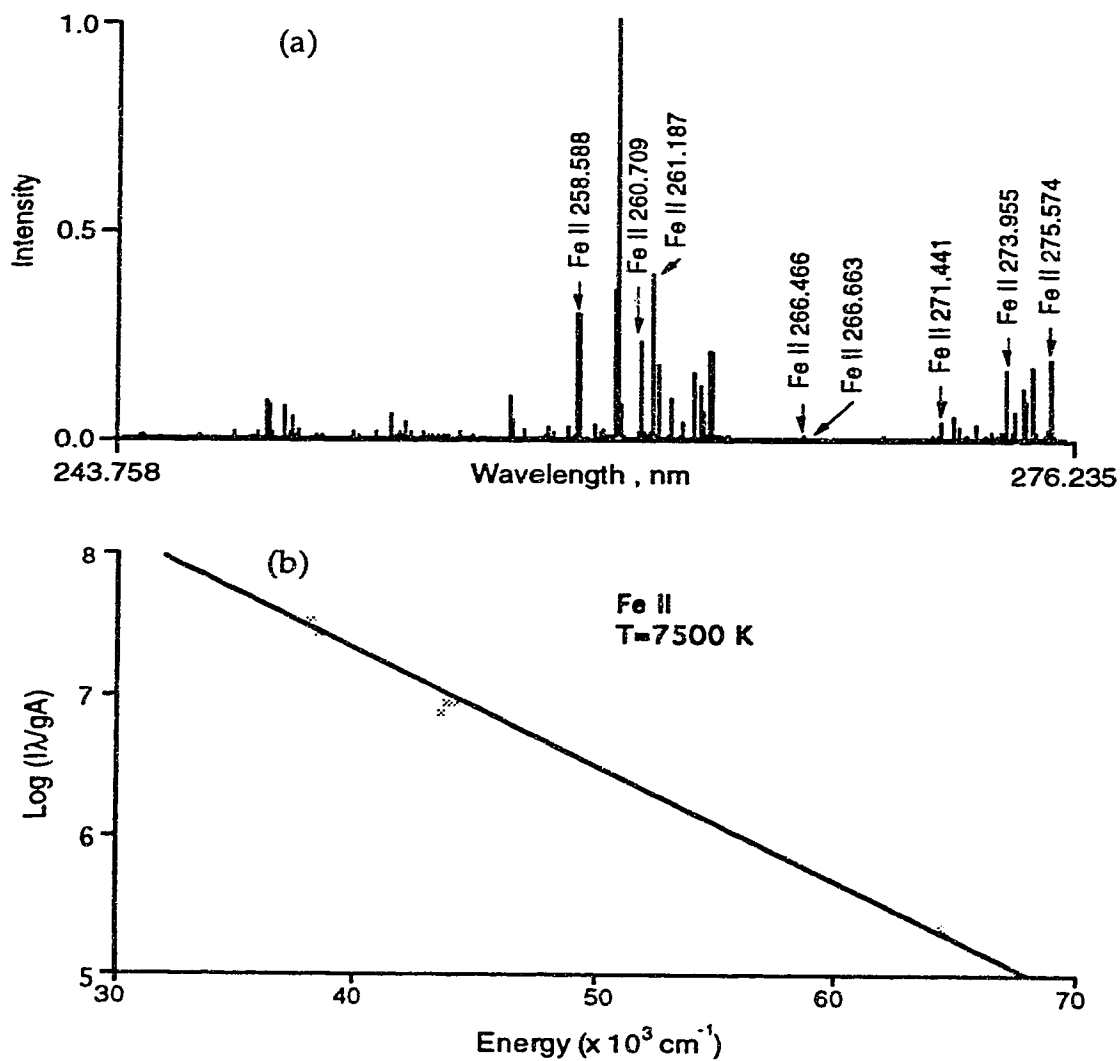
Fig. 99. Section of the emission spectrum of 1000 μg/ml Fe from the ICP showing the 8 Fe II lines (a) used in the calculation of the excitation temperature and the corresponding Boltzmann plot (b).
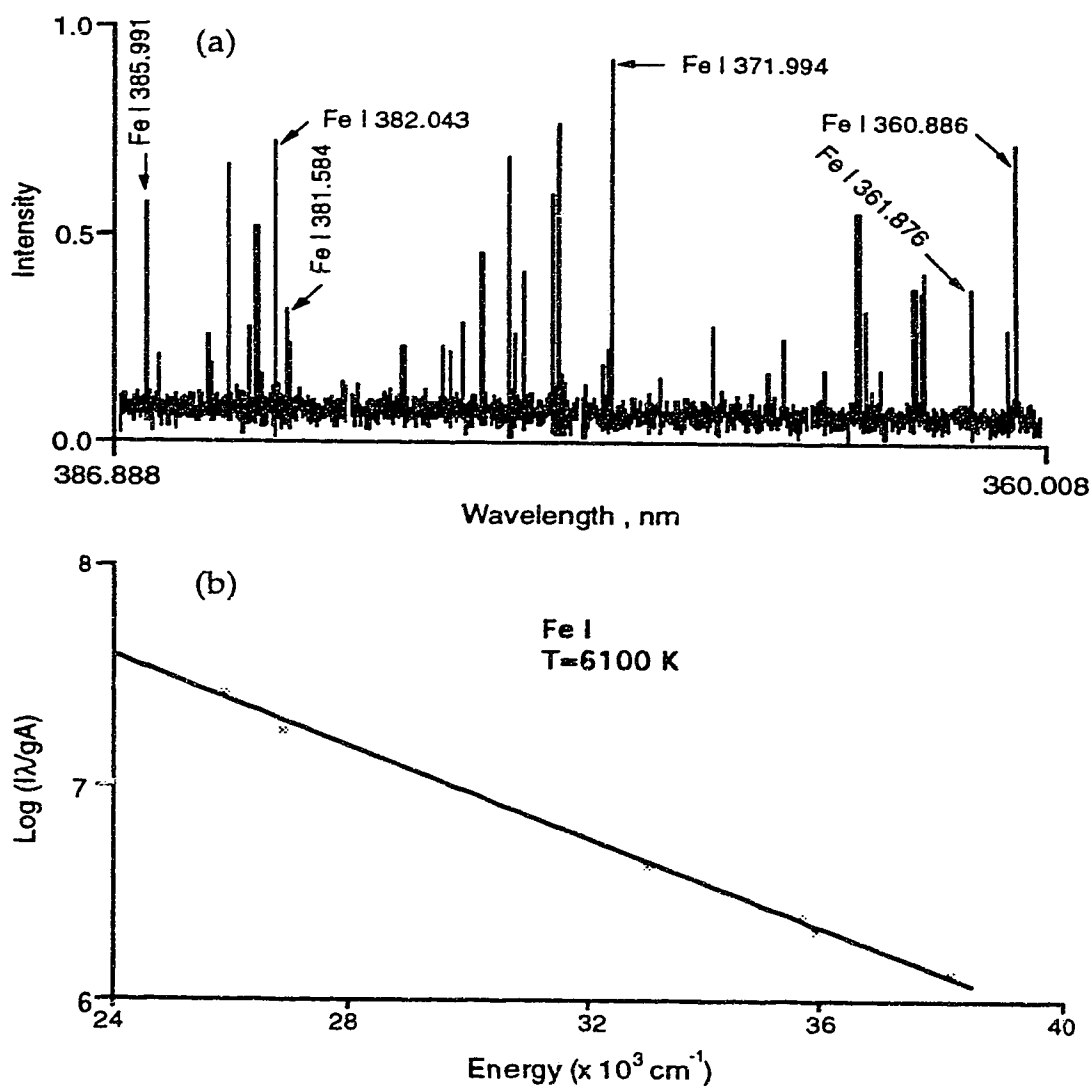
Fig. 100. Section of the emission spectrum of 1000 µg/ml Fe from the
ICP showing the 6 Fe I lines (a) used in the calculation of the
excitation temperature and the corresponding Boltzmann plot
(b).
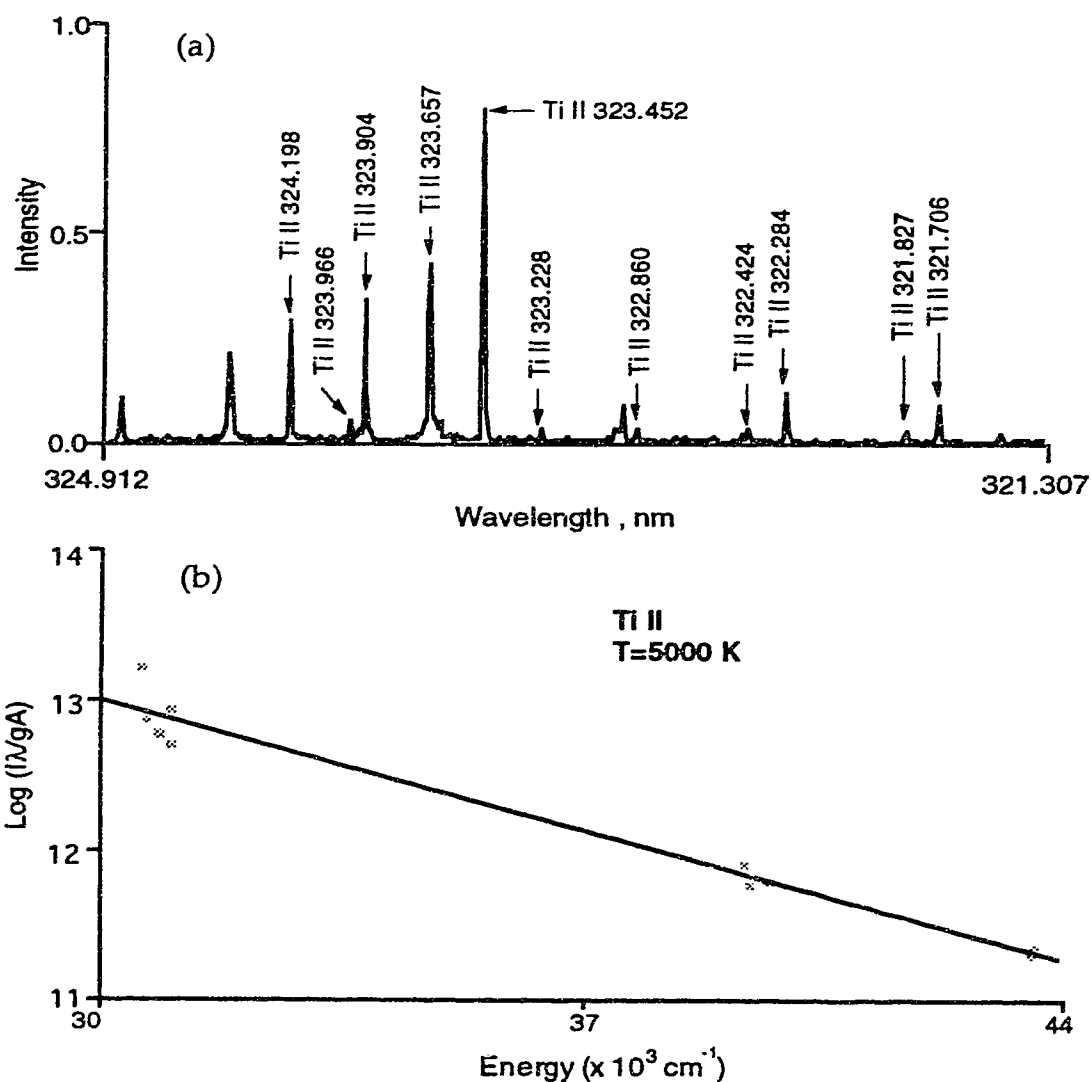
Fig. 101. Section of the emission spectrum of 1000 μg/ml Ti from the ICP showing the 11 Ti II lines (a) used in the calculation of the excitation temperature and the corresponding Boltzmann plot (b).
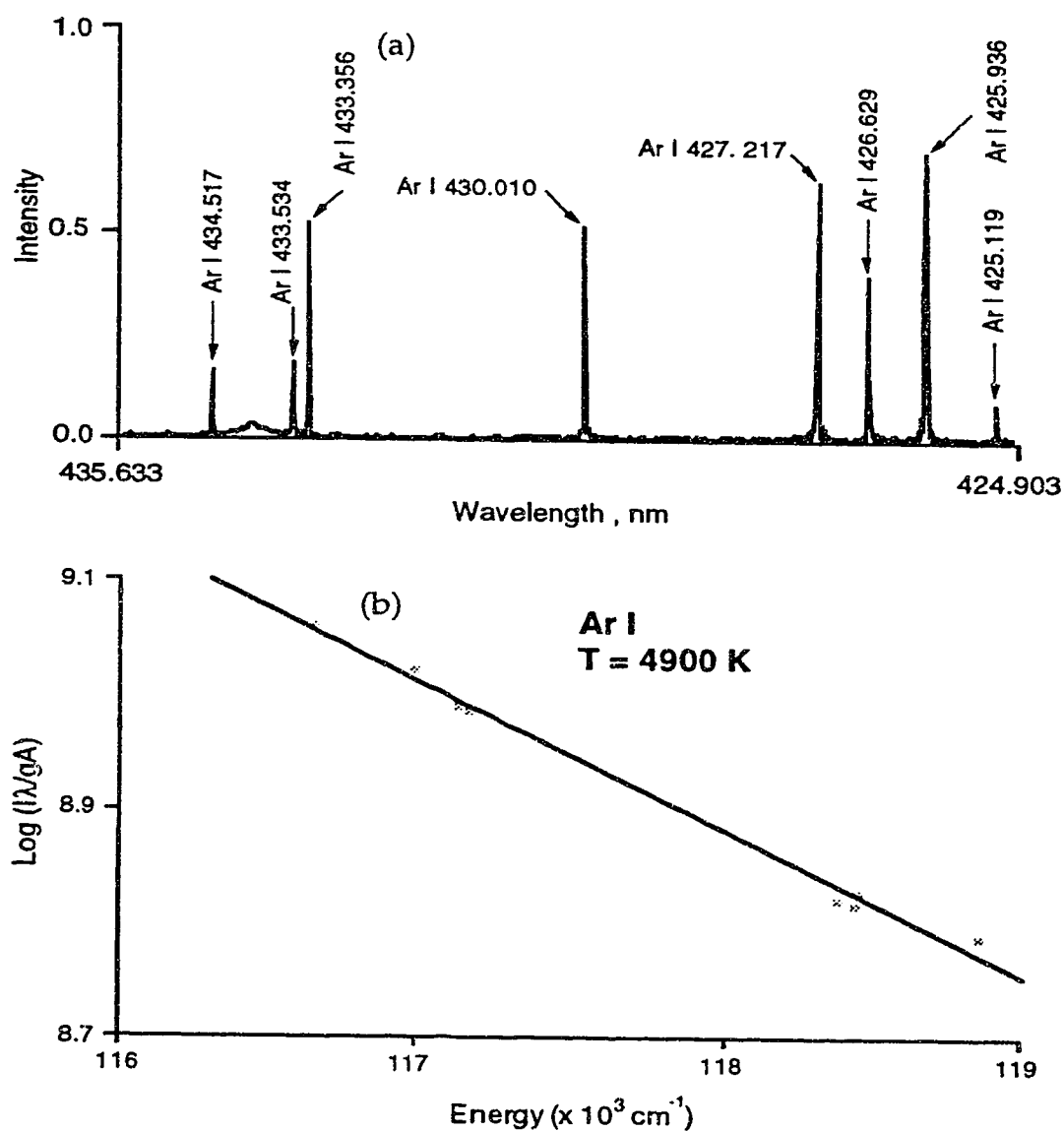
Fig. 102. Section of the emission spectrum of brass from the ICP showing the 8 Ar I lines (a) used in the calculation of the excitation temperature and the corresponding Boltzmann plot (b).
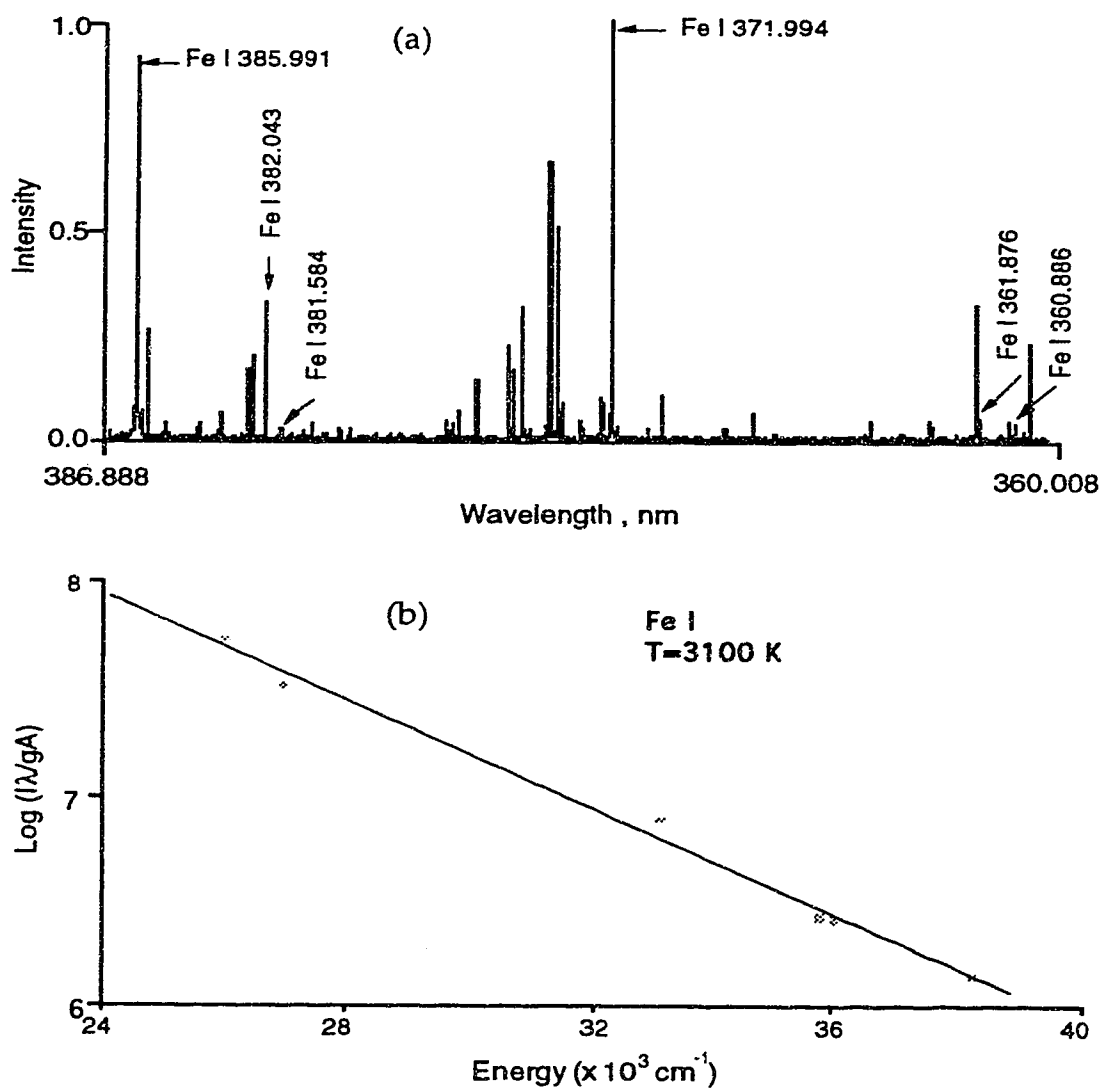
Fig. 103. Section of the emission spectrum of stainless steel from the GDD showing the 6 Fe I lines (a) used in the calculation of the excitation temperature and the corresponding Boltzmann plot (b).
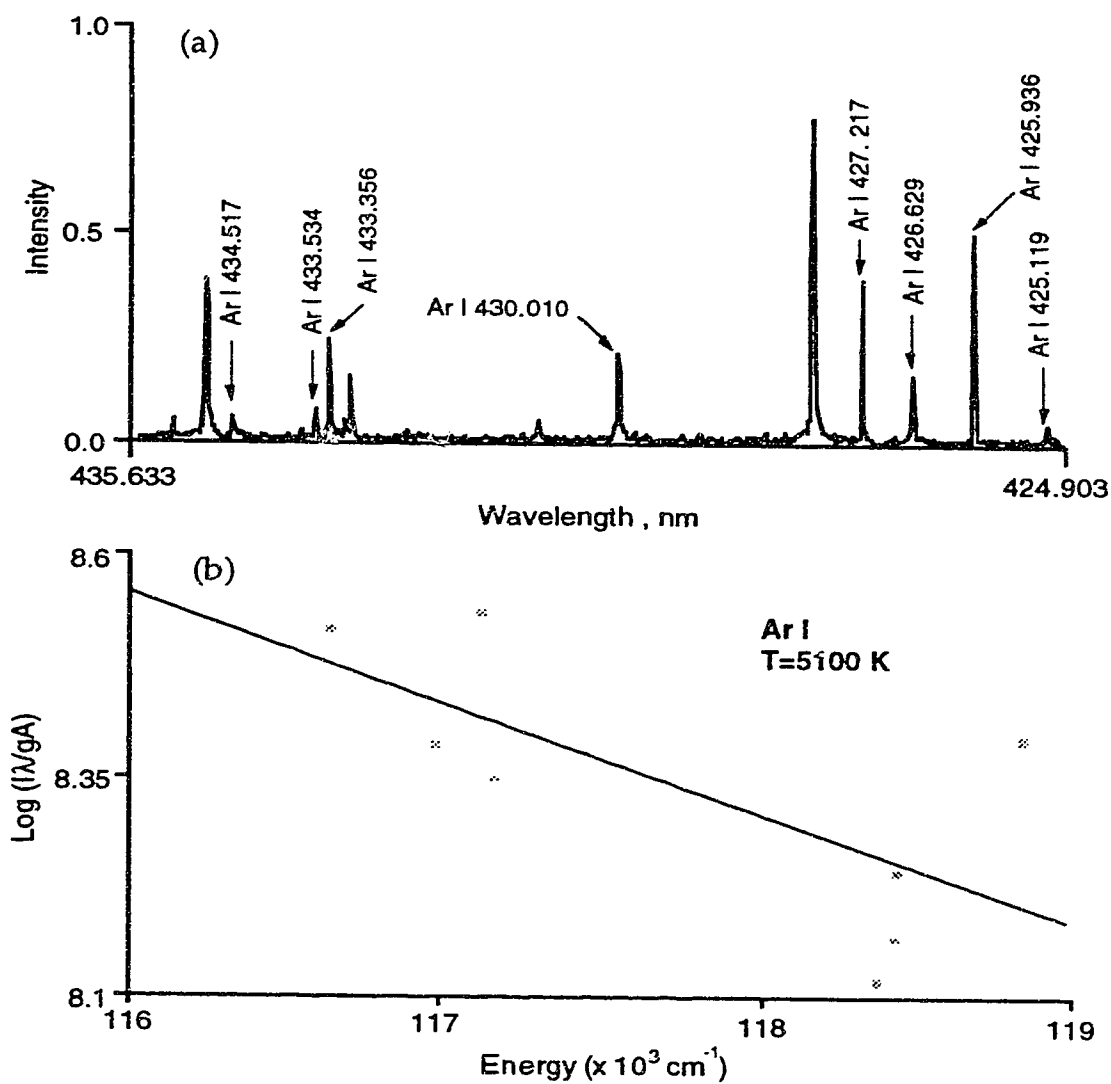
Fig. 104. Section of the emission spectrum of brass from the GDD
showing the 8 Ar I lines (a) used in the calculation of the
excitation temperature and the corresponding Boltzmann
plot (b).

Sections of the ICP emission spectrum of a 1000 µg/ml Ti solution showing two line-pairs are given in Fig. 105. The excitation temperature based on the intensity ratio of the Ti II 322.424 nm line to Ti II 322.284 nm line ranges from 5500 K to 7400 K depending on the gf values used [167-171]. An excitation temperature of 5900 K is obtained using the line intensity ratio of the Ti II 334.034 nm line to Ti II 333.211 nm line if the gA values of Triche et al. [172] are used.

Using the intensity ratio of the FeI 382.444 nm line to the FeI 381.584 nm line, excitation temperatures of 6100 K and 5200 K are obtained for the ICP if the gA values of Reif [173] and Banfield et al. [174] are used, while excitation temperatures of 3200 K and 3000 K are obtained in a GDD using stainless steel as the cathode if the gA values of Reif [173] and Banfield et al. [174] are used. Excitation temperatures of 3300 K and 3000 K are obtained in a GDD using low alloy steel as the cathode if the gA values of Reif [173] and Banfield et al. [174] are used. Sections of the spectra used in these calculations showing the Fe I 382.444 nm/ Fe I 381.584 nm line pair are illustrated in Fig. 106.

If the line intensity ratio of FeI 382.588 nm to FeI 382.444 nm is used, ICP excitation temperatures of 5800 K and 5900 K are obtained if the gA values of Reif [173] and Banfield et al. [174] are used; GDD excitation temperatures of 2600 K and 2500 K are observed using stainless steel as the cathode when the gA values of Reif [173] and Banfield et al. [174] are used and GDD excitation temperatures of 3500 K and 3400 K are measured using low alloy steel as the cathode when gA values of Reif [173] and Banfield et al. [174] are used. Sections of the spectra used in these calculations showing the Fe I 382.588 nm/Fe I 382.444 nm line pair are given in Fig. 107.
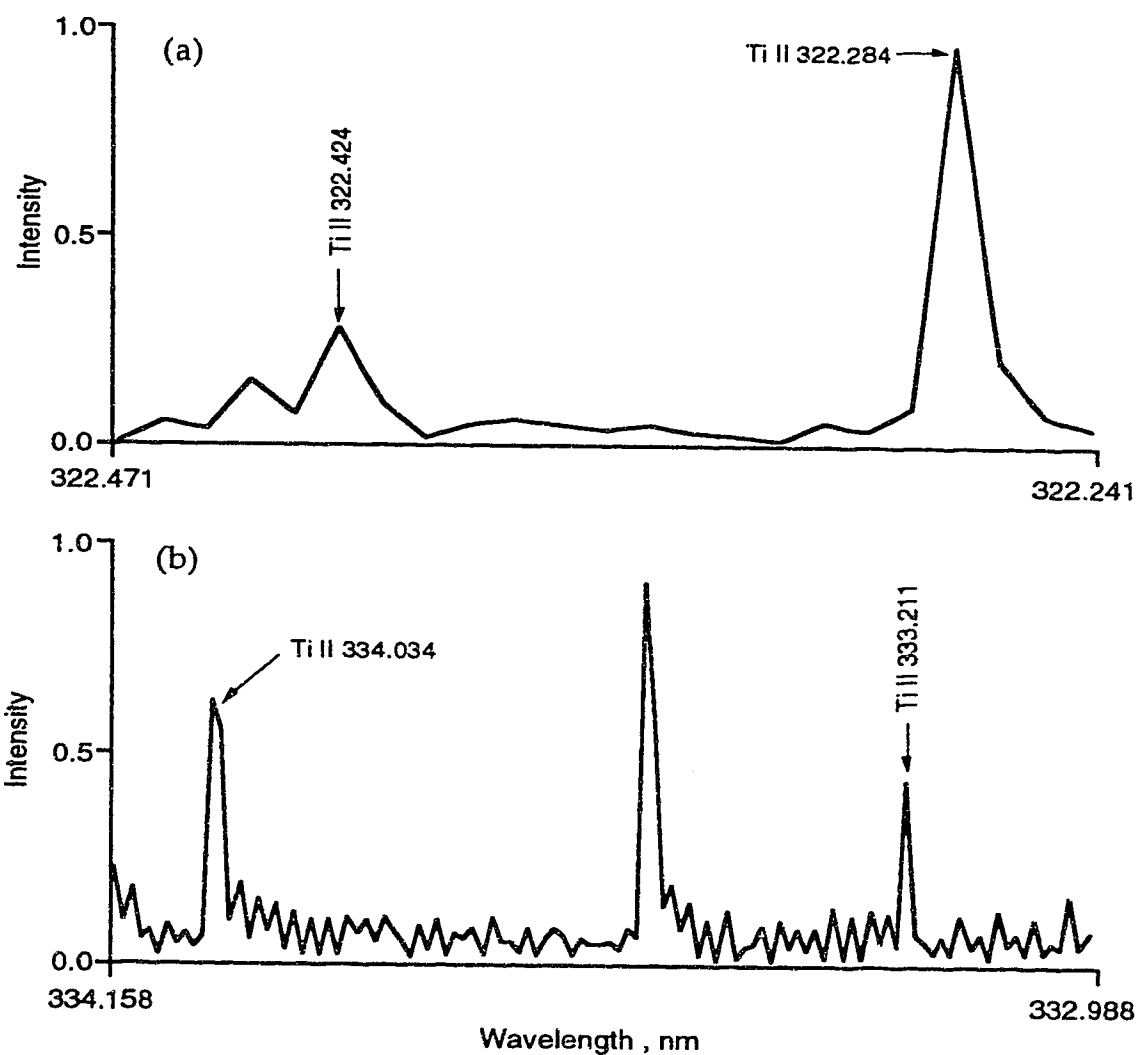
Fig. 105. Sections of the emission spectra of 1000 µg/ml Ti from the
ICP showing the 322.424 nm/322.284 nm line pair (a) and
the 334.034 nm/333.211 nm line pair (b).
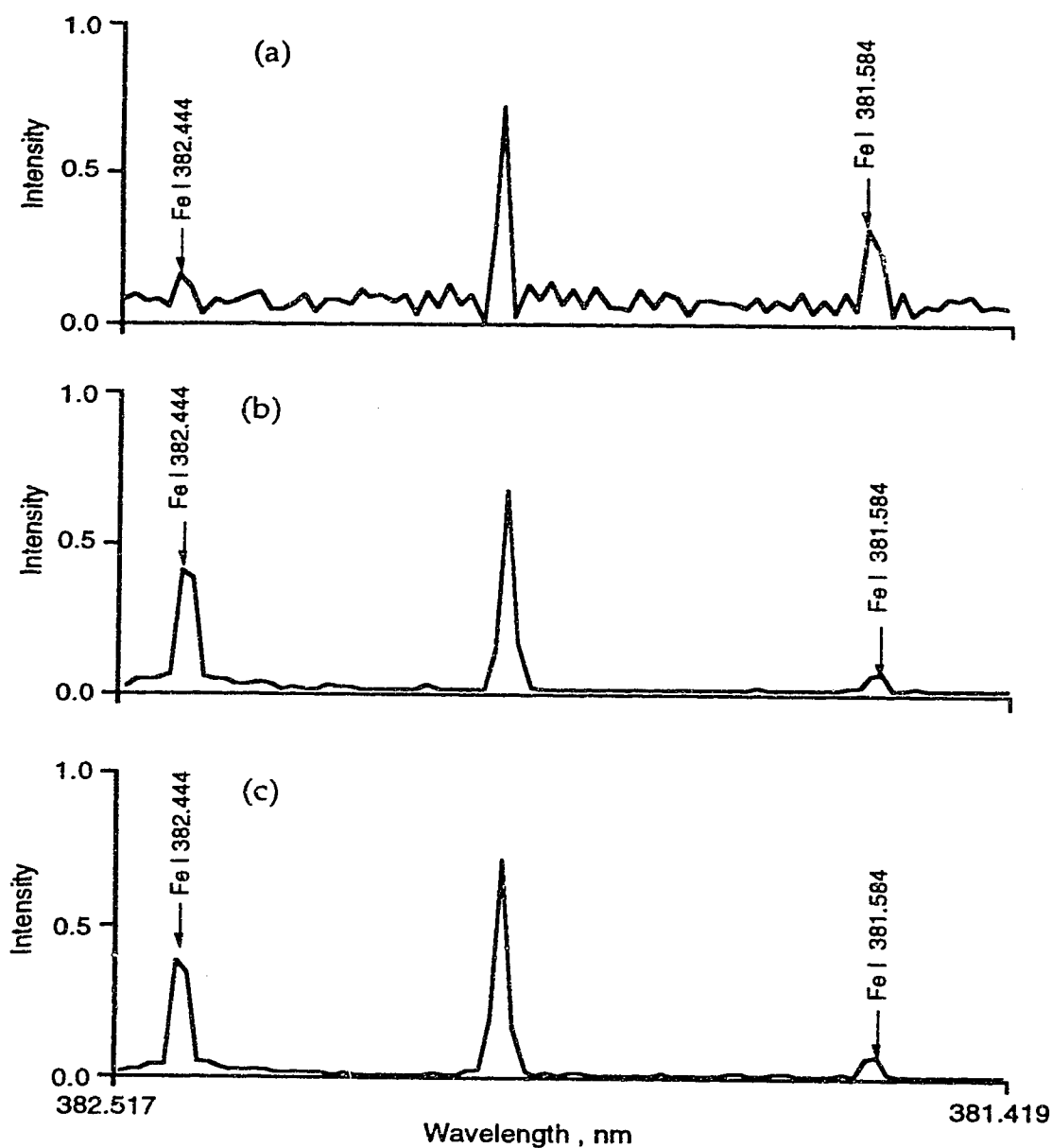
Fig. 106. Sections of the emission spectra of 1000 µg/ml Fe from the
ICP (a) of stainless steel from the GDD (b) and of low alloy
steel from the GDD (c) showing the Fe I 382.444 nm/381.584
nm line pair.
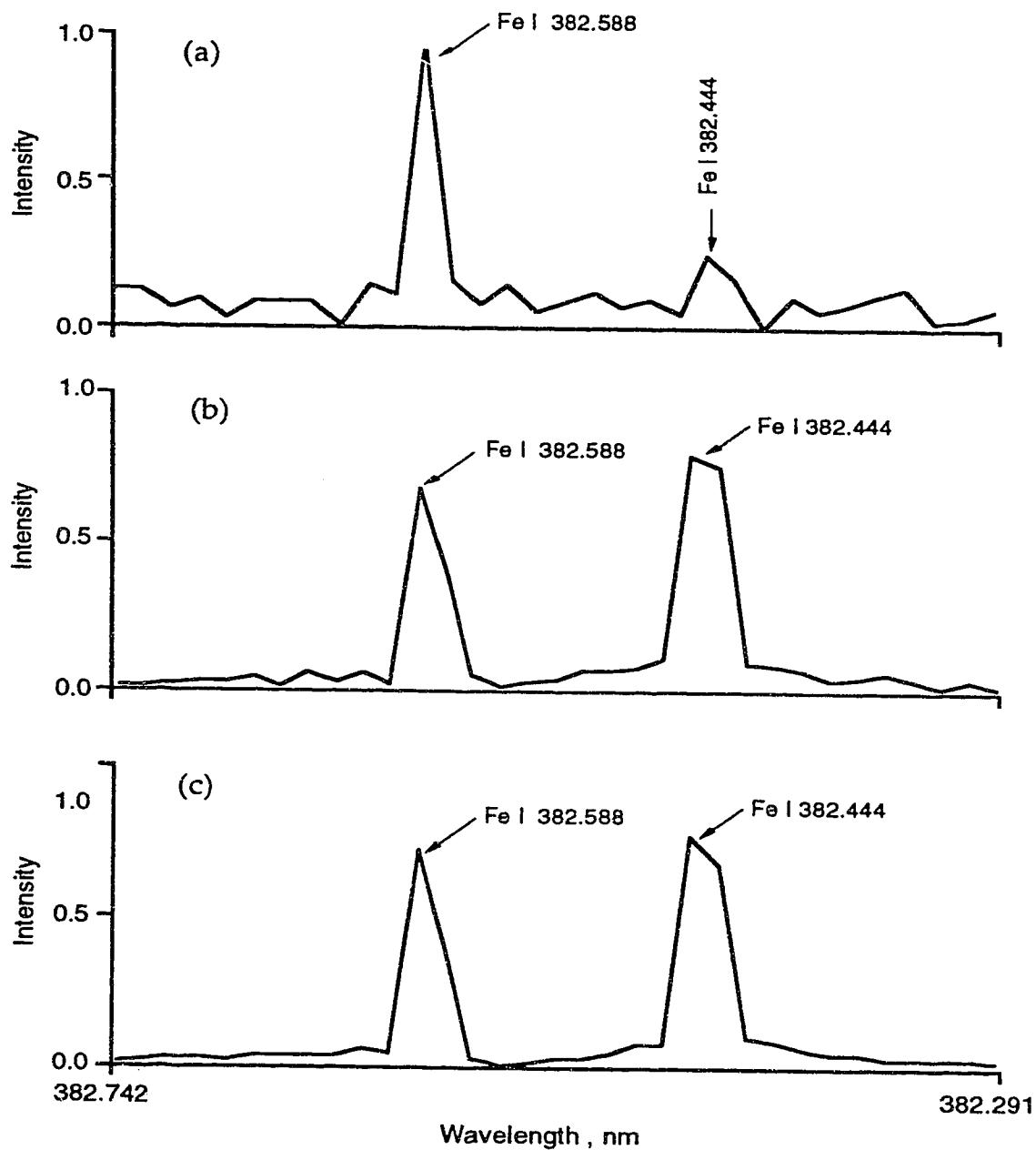
Fig. 107. Sections of the emission spectra of 1000 µg/ml Fe from the ICP (a) of stainless steel from the GDD (b) and of low alloy steel from the GDD (c) showing the Fe I 382.588 nm/382.444 nm line pair.

In summary, depending on the thermometric species chosen, line-pairs selected, and the gA values used, GDD excitation temperatures range from 2500 K to 3500 K and ICP excitation temperatures range from 4900 K to 7700 K.

5-4-2. Effect of power on the excitation temperature of the GDD

As observed in the inductively coupled plasma in Chapter 3, excitation temperature increases with increasing RF forward power. Similar results are obtained for the glow discharge device. Three Boltzmann plots with their corresponding excitation temperatures calculated under three different operating conditions are provided in Fig. 108. The glow discharge device was run at a constant voltage of 900 V and the argon gas pressure was varied such that the current can be set at 5.0 mA, 10 mA, and 15 mA. Excitation temperature increases from 3600 K to 4400 K when the current applied increases from 5.0 mA to 15.0 mA as indicated in Fig. 108.

5-5. Conclusion

The FTS system proved to be particularly powerful in obtaining a measurement of the inductively coupled plasma and the glow discharge source. Detailed high resolution spectra of both sources covering a wide spectral region can be obtained very quickly. This allows the detailed study of the spectrochemical characters of both sources such as the assessment of relative line intensities over a range of experimental conditions.

Totally different spectral characteristics are observed for the ICP and the GDD for the same sample in the same spectral region. Overall, neutral atom
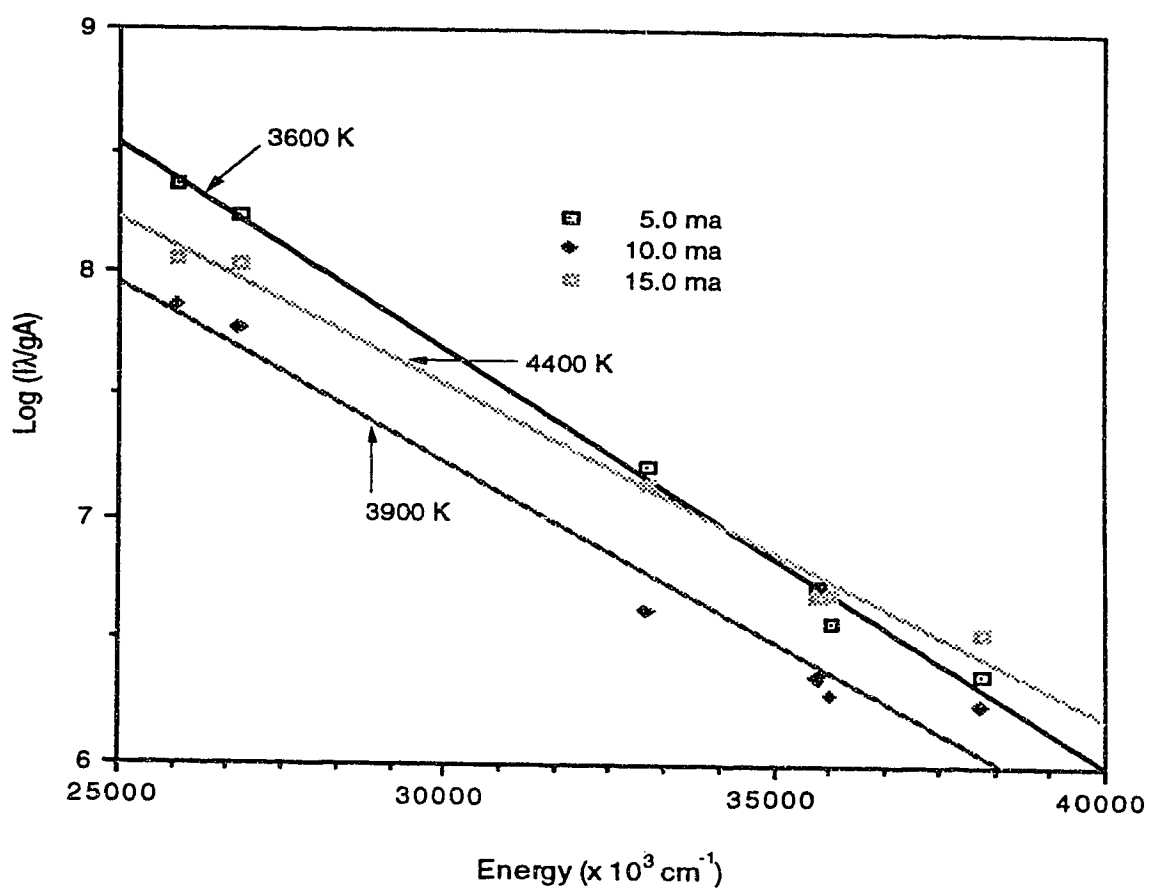
Fig. 108. Effect of power on the excitation temperature in a glow
discharge source.

lines are generally more prominent in the GDD spectra than they are in the ICP spectra. Ionic argon emission lines are dominant in the GDD in the visible spectral region, while the ionic argon emission in the ICP simply does not happen, indicating different ionization and excitation mechanisms in the ICP and the GDD.

The inductively coupled plasma is 3000 - 4000 K higher in excitation temperature than the glow discharge device under the operating conditions used in this study. The excitation temperature of the glow discharge device increases with increasing power.

Chapter 6

Interferometric observation of Ar emission from an ICP and a GDD in the region 300-1300 nm

6-1. Introduction

The emission spectrum of argon is one of the most useful sources of standard wavelengths. The first and most extensive analysis of the argon spectrum was by Meissner and reported in a series of articles beginning in 1926 [175-177]. Observations by Meggers and Humphreys [178] in 1934 covered the entire range between 394.8 and 1047.0 nm. Following this, Humphreys reported [179] new measurements mostly in the ultraviolet and visible regions in 1938. Fifteen years then elapsed before any significant additional interferometric observations of argon emission were reported. Then, several precision measurements were performed with different equipment. In 1953, Burns and Adams [180], working with Fabry-perot etalons in air and electrodeless tubes filled with 3 torr of argon, published a very extensive list of interferometrically determined wavelengths between 317.2 and 1047.0 nm. Almost simultaneously, working with reflecting echelons in vacuum, and a liquid-air cooled Geissler tube containing about 0.4 torr of argon as the light source, Littlefield and Turnbull [181] reported interferometric observations of nearly all the strong lines between 355.5 and 653.9 nm. In 1967, Norlen [182] reported interferometric observations of both Ar I and Ar II lines, excited in a water-cooled hollow cathode source. Norlen's observations included the region from 515.2 nm to 695.3 nm. In 1973, Norlen [183] published his observations of Ar I and Ar II lines in the region 340.0 to 980.0 nm, measured

by means of Fabry-perot etalons in vacuum and a water-cooled hollow cathode discharge in argon at a pressure of 0.2 torr. Li and Humphreys [184] reported the argon emission spectrum from 317.3 to 1167.2 nm originating in a microwave-excited electrodeless source. Faires et al. [185] were the first to report argon emission from an inductively coupled plasma discharge. They covered the spectral region from 900 to 2000 nm using a high resolution Fourier transform spectrometer.

Analytical atomic spectrometry generally utilizes the strong atomic and ionic lines of metallic elements in the ultraviolet and visible regions of the spectrum. However, since the early 1980's, emission spectra of the inductively coupled plasma in the near infrared and beyond [186-196] have been investigated as a means of extending the analytical capabilities of the ICP to nonmetallic elements such as oxygen, nitrogen, fluorine, chlorine, bromine, carbon, hydrogen, and sulfur.

As more interest develops in possible analytical applications of the ICP and other sources in wider and wider spectral regions, the need for a comprehensive and accurate survey of the spectral background characteristics is evident. Fourier transform spectroscopy is especially well suited to this kind of survey because of its high resolution, absolute wavelength accuracy, simultaneous and comprehensive coverage of the entire spectral region, and speed of acquiring entire spectra.

From a survey of the literature, it was found that few, if any, detailed measurements of the argon emission from the ICP discharge in the spectral region from 300 to 900 nm have been reported, let alone any studies of argon emission from glow discharge devices (GDD's) in the same region. In this

study, argon emission in the region 300 - 1300 nm from an inductively coupled plasma discharge and from a glow discharge device (GDD) were recorded with the use of Fourier transform spectrometry. This spectral region was found to be quite rich in atomic argon lines for the ICP, and rich in both atomic and ionic argon lines for the GDD. This information is useful for determining spectral interferences and assessing the degree of interferences to be expected in the development of analytical applications for the ICP and the GDD in this spectral region.

6-2. Experimental

The optical arrangement in this study is identical to that shown in Fig. 8 in Chapter 3. A 1P21 photomultiplier tube (PMT) was utilized for the 300 to 650 nm spectral region. For wavelengths longer than 650 nm, a silicon photodiode was used.

6-2-1. ICP

The same ICP assembly as in Chapter 3 was employed. The ICP RF forward power was set at 1.5 kW and the argon gas flows were 15 l/min (coolant), 0.9 l/min (auxiliary), and 1.1 l/min (nebulizer). The observation height was set at 14 mm above the load coil.

6-2-2. GDD

The same glow discharge device as described in Chapter 5 was utilized. It was operated at 900 V, 15.0 ma, and at an argon pressure of about 1000 millitorr. Pure copper was used as the cathode.

6-2-3. Method

The emission spectra of distilled-deionized water from the inductively coupled plasma and the emission spectra of copper from a glow discharge device were recorded on the Fourier transform spectrometer. Data were acquired as 32 scans, 16 K, 4 times de-aliased interferograms which were co-added to improve the signal-to-noise ratio in the resulting spectra. The acquired interferograms were directly transformed without any additional processing.

6-3. Results and discussion

The argon emission spectra from the inductively coupled plasma and from the glow discharge device are shown in Fig. 109 and Fig. 110. Because of the scale, the spectra are highly compressed and individual lines are not discernible. Individual argon emission lines appeared in Fig. 109.a, Fig. 109.b, Fig. 110.a, and Fig. 110.b are summarized in Table 12, Table 13, Table 14, and Table 15, respectively. Before the wavelength measurements, the 4 spectra shown in Fig. 109 and Fig. 110 were all 16 times zero filled in order to improve the readout resolution. Initial line lists with tentative wavelengths were automatically generated by computer from the calculated spectra. Further calibrations and identifications were based on the extensive compilation of argon emission lines by Li and Humphreys [184], Norlen [183], and by Zaidel et al [197]. Wavelength values given in Table 12 are obtained by calibrating spectrum shown in Fig. 109.a with 3 evenly-spaced Ar I lines (Ar I 331.935 nm, Ar I 394.898 nm, and Ar I 434.517 nm) in order to establish an
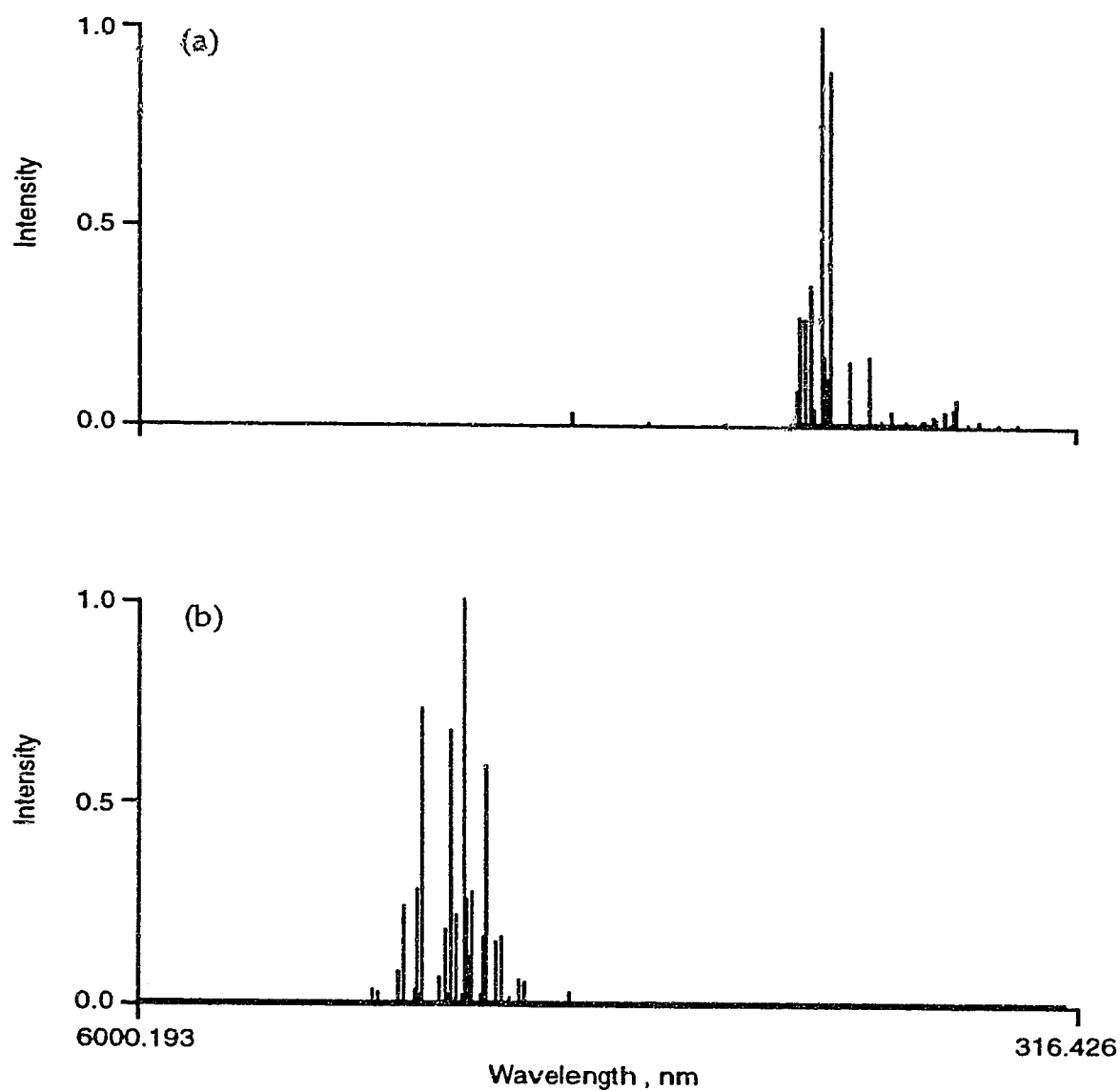
Fig. 109. Argon emission from the inductively coupled plasma measured by Fourier transform spectrometry using a 1P21 PMT (a) and a silicon photodiode (b) as the detectors.
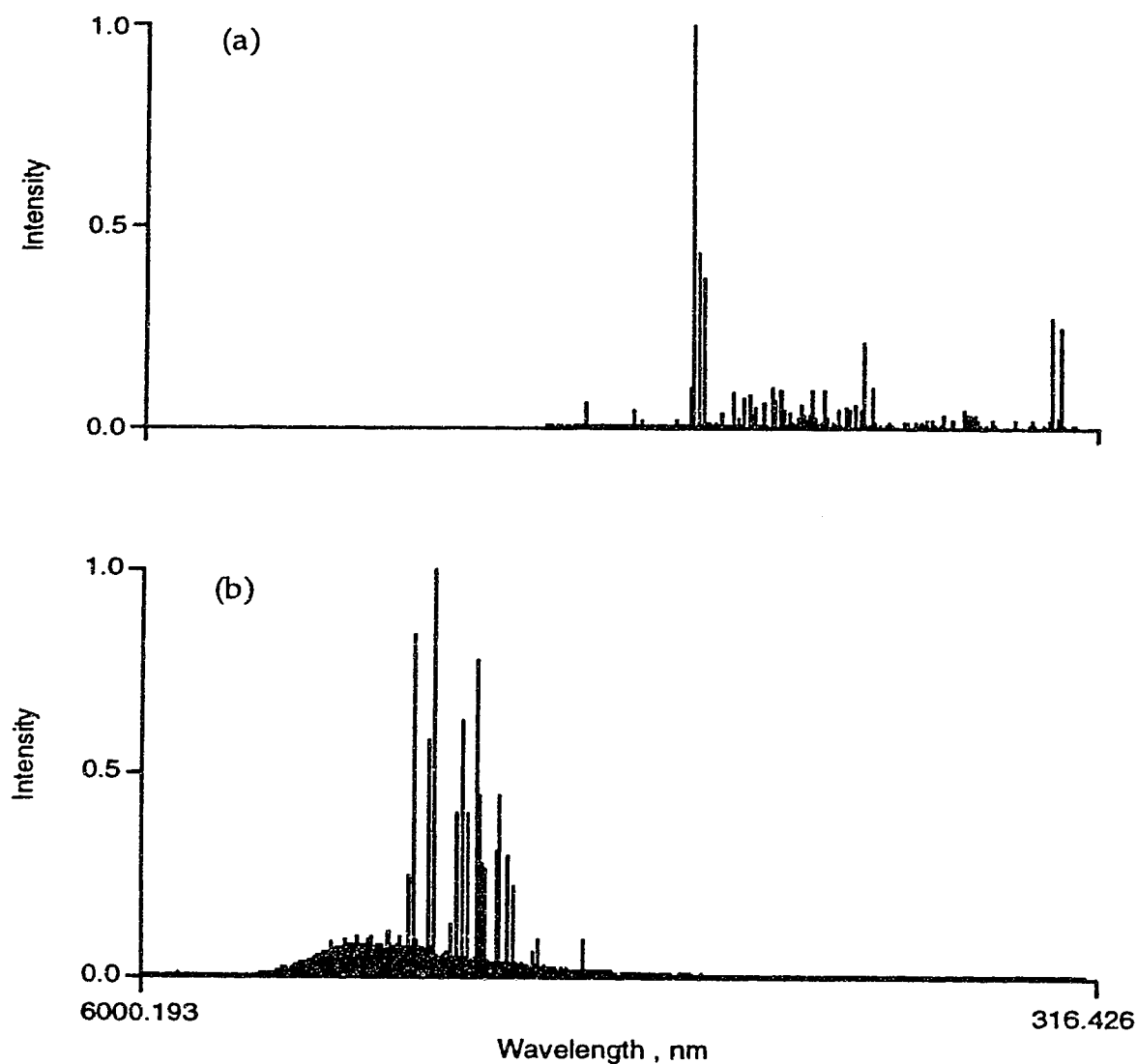
Fig. 110. Argon emission (Cu cathode) from a glow discharge device
(GDD) measured by Fourier transform spectrometry using
a 1P21 PMT (a) and a silicon photodiode (b) as the detectors.

Table 12. Ar ICP emission lines in the region 331.935-434.517 nm

Wavelength (nm)	Relative intensity	State	Reference wavelength (nm)	Reference
331.942	0.0069	I	331.935	ZPSS
332.556	0.0049	I	332.550	ZPSS
338.759	0.0044	I	338.760	ZPSS
339.278	0.0065	I	339.278	ZPSS
339.374	0.0117	I	339.375	ZPSS
346.107	0.0139	I	346.108	ZPSS
350.645	0.0095	I	350.649	ZPSS
355.431	0.0724	I	355.431	ZPSS
355.604	0.0110	I	355.601	ZPSS
356.326	0.0169	I	356.329	ZPSS
356.430	0.0112	II ?	356.434	ZPSS
356.766	0.0437	I	356.766	ZPSS
357.238	0.0113	I	357.229	ZPSS
360.653	0.0401	I	360.652	ZPSS
363.268	0.0203	I	363.268	ZPSS
363.446	0.0228	I	363.446	ZPSS
364.310	0.0099	I	364.312	ZPSS
364.984	0.0030	I	364.983	ZPSS
365.953	0.0086	I	365.953	ZPSS
367.067	0.0115	I	367.067	ZPSS
367.523	0.0088	I	367.524	ZPSS
369.084	0.0147	I	369.089	N
377.036	0.0140	I	337.037	N
378.136	0.0113	I	378.136	N
383.469	0.0377	I	385.468	N
394.744	0.0451	I	394.750	N
394.895	0.1752	I	394.898	N
404.438	0.1642	I	404.442	N
404.597	0.0173	I	404.597	N
415.854	0.8898	I	415.859	N
416.415	0.1235	I	416.418	N
418.187	0.1783	I	418.188	N
419.065	0.1743	I	419.071	N
419.101	0.1377	I	419.103	N
419.827	0.3592	I	419.832	N
420.063	1	I	420.067	N
425.115	0.0447	I	425.118	N
425.931	0.3559	I	425.936	N
426.625	0.2075	I	426.628	N
427.212	0.3227	I	427.217	N
430.006	0.2696	I	430.010	N
433.351	0.2733	I	433.351	N
433.531	0.0988	I	433.534	N
434.512	0.0872	I	434.517	N

Table 13. Ar ICP emission lines in the region 603.212-1166.786 nm, part 1

Wavelength (nm)	Relative intensity	State	Reference wavelength (nm)	Reference
603.224	0.0017	I	603.212	N
641.642	0.0014	I	641.630	N
675.280	0.0037	I	675.283	N
687.125	0.0024	I	687.123	N
688.837	0.0005	I	688.816	N
693.760	0.0011	I	693.766	N
696.527	0.0498	I	696.543	N
703.039	0.0044	I	703.025	N
706.717	0.0607	I	706.721	N
706.837	0.0043	I	706.873	N
710.731	0.0009	I	710.747	N
712.582	0.0008	I	712.582	N
714.703	0.0060	I	714.704	N
715.906	0.0011	I	715.884	N
720.699	0.0015	I	720.698	N
727.286	0.0185	I	727.294	N
731.178	0.0016	I	731.171	N
731.591	0.0009	I	731.600	N
735.326	0.0033	I	735.329	N
737.208	0.0083	I	737.212	N
738.383	0.1616	I	738.398	N
743.546	0.0019	I	743.629	N
750.373	0.0966	I	750.387	N
751.447	0.1484	I	751.465	N
763.500	0.5914	I	763.510	N
772.394	0.1651	I	772.376	N
794.809	0.2735	I	794.818	N
800.589	0.1112	I	800.616	N
801.459	0.2575	I	801.478	N
810.346	0.4352	I	810.369	N
811.524	1	I	811.531	N
826.433	0.1776	I	826.453	N
840.813	0.3321	I	840.821	N
842.466	0.6749	I	842.464	N
852.129	0.1829	I	852.144	N
860.567	0.0033	I	860.578	N
866.777	0.0674	I	866.794	N
867.997	0.0081	I	867.840	N
876.157	0.0037	I	876.168	N
912.294	0.7335	I	912.296	N
919.448	0.0119	I	919.463	N

Table 13. Ar ICP emission lines in the region 603.212-1166.786 nm, part 2

Wavelength (nm)	Relative intensity	State	Reference wavelength (nm)	Reference
922.444	0.2771	I	922.450	N
929.145	0.0087	I	929.153	N
935.416	0.0329	I	935.421	N
965.759	0.2344	I	965.778	N
978.427	0.0751	I	978.450	LH
1046.989	0.0272	I	1047.005	LH
1047.829	0.0098	I	1047.803	LH
1050.642	0.0050	I	1050.650	LH
1067.353	0.0361	I	1067.357	LH
1068.129	0.0060	I	1068.177	LH
1088.074	0.0022	I	1088.094	LH
1139.627	0.0009	I	1139.702	LH
1144.747	0.0018	I	1144.832	LH
1168.913	0.0019	I	1168.871	LH

Table 14. Ar GDD emission lines in the region 347.672-570.080 nm, part 1

Wavelength (nm)	Relative intensity	State	Reference wavelength (nm)	Reference
347.673	0.0203	II	347.674	ZPSS
349.123	0.0252	II	349.124	ZPSS
349.154	0.0481	II	349.154	ZPSS
350.978	0.0181	II	350.978	ZPSS
351.440	0.0250	II	351.439	ZPSS
354.554	0.0451	II	354.558	ZPSS
354.586	0.0358	II	354.584	ZPSS
355.953	0.0757	II	355.951	ZPSS
356.101	0.0624	II	356.104	ZPSS
357.661	0.0775	II	357.662	ZPSS
358.157	0.0220	II	358.161	ZPSS
358.235	0.0293	II	358.235	ZPSS
358.846	0.0557	II	358.844	ZPSS
371.821	0.0227	II	371.821	ZPSS
372.930	0.0448	II	372.931	ZPSS
373.790	0.0373	II	373.789	ZPSS
376.527	0.0472	II	376.527	ZPSS
376.617	0.0177	II	376.612	ZPSS
378.084	0.0333	II	378.084	ZPSS
380.318	0.0175	II	380.319	ZPSS
380.944	0.0303	II	380.946	ZPSS
385.060	0.0222	II	385.057	ZPSS
386.855	0.0293	II	386.853	ZPSS
392.569	0.0275	II	392.572	ZPSS
392.863	0.0198	II	392.860	ZPSS
393.256	0.0289	II	393.255	ZPSS
394.605	0.0232	II	394.610	ZPSS
397.934	0.0150	II	397.936	ZPSS
401.383	0.0293	II	401.386	ZPSS
403.385	0.0212	II	403.382	ZPSS
404.290	0.0237	II	404.290	ZPSS
404.440	0.0225	I	404.442	ZPSS
405.290	0.0262	II	405.292	ZPSS
407.201	0.1062	II	407.201	ZPSS
407.237	0.0405	II	407.239	ZPSS
410.392	0.1318	II	410.391	ZPSS
413.173	0.1078	II	413.173	ZPSS
415.610	0.0141	II	415.609	ZPSS
415.858	0.1214	I	415.859	ZPSS
418.194	0.0135	I	418.188	ZPSS
419.070	0.0212	I	419.071	ZPSS
419.831	0.0691	I	419.832	ZPSS
420.069	0.1061	I	420.068	ZPSS
421.865	0.0135	II	421.867	ZPSS
422.261	0.0160	II	422.261	ZPSS
422.814	0.0266	II	422.816	ZPSS

Table 14. Ar GDD emission lines in the region 347.672-570.080 nm, part 2

Wavelength (nm)	Relative intensity	State	Reference wavelength (nm)	Reference
423.721	0.0310	II	423.722	ZPSS
425.937	0.0606	I	425.936	ZPSS
426.652	0.0220	II	426.653	ZPSS
427.218	0.0416	I	427.217	ZPSS
427.749	0.2234	II	427.752	ZPSS
430.014	0.0295	I	430.010	ZPSS
433.122	0.0650	II	433.120	ZPSS
433.199	0.0236	II	433.203	ZPSS
433.357	0.0331	I	433.356	ZPSS
433.529	0.0179	I	433.534	ZPSS
434.809	0.2211	II	434.806	ZPSS
435.214	0.0220	II	435.220	ZPSS
436.774	0.0156	II	436.783	ZPSS
437.070	0.0770	II	437.075	ZPSS
437.120	0.0351	II	437.133	ZPSS
437.968	0.0522	II	437.967	ZPSS
440.093	0.0804	II	440.099	ZPSS
442.597	0.1332	II	442.601	ZPSS
443.023	0.0703	II	443.019	ZPSS
443.104	0.0378	II	443.100	ZPSS
443.384	0.0383	II	443.384	ZPSS
447.475	0.0291	II	447.476	ZPSS
448.177	0.0932	II	448.181	ZPSS
454.503	0.2160	II	454.505	ZPSS
457.936	0.0996	II	457.937	ZPSS
458.990	0.1668	II	458.990	ZPSS
460.952	0.2297	II	460.956	ZPSS
465.793	0.1539	II	465.794	ZPSS
472.689	0.0957	II	472.686	ZPSS
473.216	0.0229	II	473.206	ZPSS
473.589	0.0782	II	473.591	ZPSS
476.484	0.1949	II	476.486	ZPSS
480.604	0.1771	II	480.602	ZPSS
484.785	0.0647	II	484.782	ZPSS
487.981	0.2112	II	487.987	ZPSS
496.510	0.0898	II	496.507	ZPSS
500.922	0.0244	II	500.935	ZPSS
501.771	0.0066	II	501.763	ZPSS
515.318	1	I	515.311	ZPSS
570.090	0.0191	I	570.087	ZPSS

Table 15. Ar GDD emission lines in the region 696.536-978.449 nm

Wavelength (nm)	Relative intensity	State	Reference wavelength (nm)	Reference
696.540	0.1008	I	696.543	N
706.730	0.0683	I	706.722	N
738.406	0.2512	I	738.398	N
750.380	0.3359	I	750.387	N
751.464	0.2896	I	751.465	N
763.520	0.0295	I	763.511	N
772.400	0.3490	I	772.376	N
794.830	0.3037	I	794.818	N
800.606	0.3185	I	800.615	N
801.476	0.5090	I	801.478	N
810.371	0.6270	I	810.369	N
811.521	0.8926	I	811.531	N
826.455	0.4572	I	826.452	N
840.809	0.7248	I	840.821	N
842.457	0.6979	I	842.465	N
852.133	0.4599	I	852.144	N
866.812	0.1472	I	866.794	N
912.306	1	I	912.296	N
922.472	0.3994	I	922.450	N
965.788	0.9664	I	965.779	N
978.456	0.2782	I	978.450	N

averaged He-Ne calibration wavelength. For Table 12, this value is 632.8343 nm. Wavelength values given in Table 13 are obtained by calibrating spectrum shown in Fig. 109.b with 3 evenly-spaced Ar I lines (Ar I 603.212 nm, Ar I 876.168 nm, and Ar I 1067.357 nm) in order to establish an averaged He-Ne calibration wavelength. For Table 13, this value is 632.8326 nm. Wavelength values given in Table 14 are obtained by calibrating spectrum shown in Fig. 110.a with 3 evenly-spaced Ar lines (Ar II 347.674 nm, Ar II 460.956 nm, and Ar I 515.311 nm) in order to establish an averaged He-Ne calibration wavelength. For Table 14, this value is 632.8482 nm. Wavelength values given in Table 15 are obtained by calibrating spectrum shown in Fig. 110.b with 3 evenly-spaced Ar I lines (Ar I 696.543 nm, Ar I 801.478 nm, and Ar I 978.450 nm) in order to establish an averaged He-Ne calibration wavelength. For Table 15, this value is 632.8552 nm. Interested reader should refer to reference [198] for the details of the calibration and zero filling procedures. All the argon lines are listed with (measured) wavelength, relative intensity, state, reference wavelength, and the literature reference. ZPSS denotes Zaidel et al [197], LH for Li and Humphreys [184], and N for Norlen [183]. The relative intensities were calculated relative to the most intense line in each spectrum.

From Tables 12-15, degrading accuracy of the measured wavelengths with increasing wavelength is obvious. This can be easily understood by measuring point spacing (pm/point) in the region 300-1300 nm. The result is listed in Table 16. The point spacing is not constant across the spectrum and increases from 9.7 pm at 300 nm to 163 pm at 1300 nm. The discrete nature of the spectra limits the accuracy of a measured line to ± 1/2 point, that is why

Table 16. Point spacing in the region 300-1300 nm

Wavelength (nm)	pm/point	± 1/2 point (pm)
300	9.7	4.9
400	15.4	7.7
500	24.2	12.1
600	34.8	17.4
700	47.3	23.7
800	61.7	30.9
900	78.1	39.1
1000	96.0	48.0
1100	117	58.5
1200	139	69.5
1300	163	81.5

this value is also given in Table 16. Zero filling 16 times, which was performed to the 4 spectra used in this chapter, means that the data point density is increased by a factor of 16, thus better wavelength accuracy can be achieved.

From Tables 12-15, the complete absence of ionic argon emission in the ICP and the dominant ionic argon emission in the GDD is easily seen and the possible mechanisms involved have been discussed in Chapter 5.

6-4. Conclusions

The powerful information gathering capability of the Fourier transform spectrometry (FTS) in the visible and near-IR spectral regions is demonstrated in this chapter. The disadvantages of using FTS to compile spectral lines are the multiplex disadvantage and the dynamic range limitation. The increased baseline noise obscures some weak lines, especially those near prominent lines. Although quite time-saving, the FTS provides fewer lines than conventional scanning methods because of the dynamic range limitation.

The main purpose of this study was to provide a general survey of the argon emission over the spectral range from 300 to 1300 nm from both the ICP and the GDD under operating conditions most commonly used for analytical purposes. The information provided in this chapter could be used to assess spectral interferences in this region and thus it should provide a useful reference for the future development of analytical applications of the ICP and the GDD in this spectral region.

Chapter 7

Summary and future work

The Fourier transform spectrometer has been proven by the work in this thesis to be a very powerful tool for the measurement of spectrochemical information.

The foremost advantages of FTS in the ultraviolet-visible spectral region: comprehensive wavelength coverage; simultaneous observation of the entire spectrum within a selected instrumental bandpass; absolute wavelength axis accuracy; the relatively easy accomplishment of high resolution; have been demonstrated by the reported measurements.

An obvious application of the FTS technique which combines all three of these major advantages is the fundamental study of an atomic emission source, such as the ICP and the GDD. Since the knowledge of the temperature and the electron number density, which are important parameters governing various mechanisms, is vital for understanding the desolvation, dissociation, atomization, ionization, and excitation processes occurring in the source. These parameters can be used to follow the variations of the source when one or more of the operating conditions are modified. Excitation temperature and electron number density were determined by Gunter et al. [199] in a 9, 27, and 50 MHz inductively coupled argon plasma. Their experimental evidence indicated a general decrease in excitation temperature and electron number density with increasing generator frequency. Using a photodiode array spectrometer, spatially resolved excitation temperatures and electron number

densities were measured by Blades and Caughlin [200] for an ICP with both water and xylene solution introduction. Both the excitation temperature and the electron number density were found to be lower in the ICP with organic aerosol than in the ICP with aqueous aerosol at a fixed power and observation height. As a result, they explained the reason why an ICP with organic aerosol required about 0.5 kW of additional r.f. power to achieve performance similar to that exhibited by an ICP with aqueous aerosol. The knowledge of excitation temperature and electron number density can also be used to facilitate the selection of optimum operating conditions, such as the type and the composition of the mixed-gas ICP discharge to perform direct solid sample analysis. In addition, this knowledge can also be used directly to evaluate the extent to which LTE prevails in the source. It was found in this study that both the excitation and ionization temperatures in the middle of aerosol channel measured in the mixed-gas ICP discharges were more uniform than those measure in a pure-argon plasma discharge, thus it is reasonable to say that mixed-gas ICP discharges are closer to LTE than a pure-argon ICP. It is also helpful for the understanding of interelement effects.

In this study, excitation temperatures for 3 thermometric species and ionization temperatures for 5 thermometric species were determined in a pure-argon ICP as well as in argon-air, argon-helium, argon-nitrogen, and argon-oxygen mixed-gas plasma discharges with 5 to 100% of these non-argon gases mixed into the coolant stream. This is the first systematic temperature measurement for 8 thermometric species under exactly the same experimental conditions in various mixed-gas ICP's. It was found that with less than 50% air, nitrogen, and oxygen in the coolant, temperature increases from 300 to 1500 K relative to a pure-argon plasma discharge can be achieved

at an appropriate observation height. With more than 50% air, nitrogen, and oxygen in the coolant stream, particularly with the complete replacement of the coolant by these 3 gases, dramatic decreases in temperatures relative to a pure-argon plasma discharge were observed. The introduction of various amounts of helium into the coolant did not make too much difference in terms of temperatures in comparison with temperatures measured in a pure-argon plasma discharge.

In this work, the excitation temperatures were calculated using the Macintosh software package "Microsoft Excel". In each column, a single calculation is performed using the data entered into this column or previous column(s) such that the result obtained in this column is used to perform the calculations in the next column, in this way, step by step the final column gives the excitation temperature. All parameters except the intensities of all the spectral lines are constants in the calculation. In each new calculation, what the operator needs to do is to enter the new set of intensity data into the first column. Upon the completion of the entry of all the intensities data, a new excitation temperature value will appear instantly in the last column. Although this calculation is quite time efficient, it is necessary to pick out each individual spectral line manually from each spectrum and enter (type in) the intensity of each line into the computer each time a new excitation temperature is to be calculated under a new operating condition. If, for instance, the excitation temperature change with increasing amount of nitrogen in the coolant stream is being measured, a lot of data has to be extracted after obtaining the interferograms under different operating conditions.

The ionization temperatures measured in this thesis were calculated using a separate program based on "Microsoft Basic". In each calculation, the intensities of the neutral atom line and the ion line of the thermometric species must be entered. As above, the line intensities have to be extracted before hand from each spectrum.

As a future development step, a separate software package should be developed as a temperature probe, in which the data acquisition, Fourier transformation, zero-filling the spectra, and temperature calculation steps are integrated. Ideally, the goal is for the system to display the excitation temperature and ionization temperature for selected thermometric species directly without "manually" extracting the frequency and intensity information. The selection of the thermometric species should be performed by clicking the appropriate dialog boxes on the screen, and the rest of the task should be carried out by the punch of a single key on the keyboard of the computer after the source is ready.

The two pre-dispersion configurations studies in this thesis proved to be successful in combatting the multiplex disadvantage and the dynamic range limitation problems by only picking up the spectral components of interests while blocking out all unwanted spectral components. These two optical arrangements were both based on the front-end of a LECO PLASMARRAY™ spectrometer. This spectrometer consists of a 0.5 meter polychromator. As mentioned before, the resolution of the Fourier transform spectrometer depends on the distance the moving mirror travels and not the size of the pre-dispersion polychromator, thus a polychromator of 0.5 meter is not really necessary. In addition, the front-end of the LECO PLASMARRAY™

spectrometer is too bulky and not easy to manoeuvre. As a future development step, a more compact version (say, 0.25 meter) of the polychromator should be built as the pre-disperser (or, may be, post-disperser) using mirrors and gratings such that it can be mounted or removed very easily. Further more, the mask-changing and slit-moving steps in the two pre-dispersion arrangements should be computer-software controlled such that the right mask is placed on the focal plane of the polychromator according to the nature of the analytical problems at hand, or the slit-end of the fiber optic cable(s) is moved to the appropriate position(s) (wavelength(s)) at the will of the operator.

The Fourier transform spectrometer coupled to the inductively coupled plasma (ICP) and the glow discharge device (GDD) has also proven to be effective in performing massive qualitative analytical work in the spectral range from 180 nm to 1300 nm in Chapter 5 and Chapter 6. It is possible and desirable in the near future to compile a comprehensive spectral atlas for ICP and GDD using the FTS measurement system.

The study of the excitation mechanisms of glow discharge device (GDD) is under way in this laboratory. By monitoring the changes in the intensities of some particular spectral lines simultaneously as a function of power applied to the GDD, and as a function of the types and composition of the filler gases with different excitation energies, it may be possible to elucidate the excitation mechanisms in glow discharges and explain the qualitative spectral characteristics observed here in this work.

Due to its wide, simultaneous wavelength coverage capability, the utilization of the Fourier transform spectrometry will make the study of

easily and noneasily ionizable element (EIE and NON-EIE) matrix effects in the inductively coupled plasma much easier. Since the magnitude and the direction (enhancement or suppression) of the matrix effect depend upon both the matrix elements and the spectral lines of the analytes, by monitoring the changes in the intensities of the spectral lines originating from states with different excitation energies of different elements caused by various matrix elements at various concentrations, further and better understanding of matrix effects and the findings of remedies should be possible. Work in this field with the ICP-FTS system is planned in the near future.

Thus, with the work reported on here and in progress, it can be seen that UV-VIS-FTS provides a powerful technique for the development and further fundamental characterization of analytical atomic emission sciences.

Bibliography

1.   C. ? Alkamade, J. M. W. Milatz, Appl. Sci. Res., 4B, 289(1955).

2.   A. Walsh, Spectrochim. Acta 7, 108(1955).

3.   G. F. Box, A. Walsh, Spectrochim. Acta 16, 255(1960).

4.   J. D. Winefordner, T. J. Vickers, Anal. Chem. 36, 161(1964).

5.   S. Greenfield, I. L. Jones, Analyst 89, 713(1964).

6.   R. Wendt, V. A. Fassel, Anal. Chem. 37, 920(1965).

7.   P. W. J. M. Boumans, M. Bosveld, Spectrochim. Acta 34B, 59(1979).

8.   R. K. Winge, V. J. Peterson, V. A. Fassel, Appl. Spect. 33, 206(1979).

9.   W. Grimm, Spectrochim. Acta 23B, 443(1968).

10.   G. Horlick, Ph.D. Thesis, University of Illinois, 1969.

11.   G. Horlick, W. K. Yuen, Anal. Chem. 775A, 47(1975).

12.   W. K. Yuen, Ph. D. Thesis, University of Alberta, 1978.

13.   R. H. Hall, Ph. D. Thesis, University of Alberta, 1979.

14.   S. Marra, G. Horlick, Appl. Spectrosc., 40, 804(1986).

15.   R. C. L. Ng, G. Horlick, Appl. Spectrosc., 39, 834(1985).

16.   R. C. L. Ng, G. Horlick, Appl. Spectrosc., 39, 841(1985).

17.   E. A. Stubley, G. Horlick, Appl. Spectrosc., 39, 800(1985).

18. E. A. Stubley, G. Horlick, Appl. Spectrosc., **39**, 805(1985).

19. E. A. Stubley, G. Horlick, Appl. Spectrosc., **39**, 811(1985).

20. G. King, Ph. D. Thesis, University of Alberta, 1989.

21. A. P. Thorne, C. J. Harris, I. Wynne-Hones, R. C. M. Learner, and G. Cox, J. Phys. E., **20**, 54(1987).

22. A. P. Thorne, J. Anal. At. Spectrom., **2**, 227(1987).

23. B. R. Todd, and G. Horlick, Spectrochim. Acta **47B**, 275(1992).

24. L. M. Faires, J. Anal. At. Spectrom. **2**, 585(1987).

25. T. B. Reed, J. Appl. Phys. **32**, 821(1961).

26. T. B. Reed, J. Appl. Phys. **32**, 2534(1961).

27. P. D. Johnston, Phys. Lett. **20**, 499(1966)

28. B. S. Malone and W. H. Corcoran, J. Quant. Spectrosc. Radiat. Transfer **4**, 443(1966).

29. D. W. Hughes and E. R. Wooding, Phys. Lett. **24A**, 70(1967).

30. H. U. Eckert, F. L. Kelly, and H. N. Olsen, J. Appl. Phys. **39**, 1846(1968).

31. P. D. Scholz and T. P. Anderson, J. Quant. Spectrosc. Radiat. Transfer **8**, 1411(1968).

32. S. V. Desai and W. H. Corcoran, J. Quant. Spectrosc. Radiat. Transfer **8**, 1721(1968).

33. S. V. Desai and W. H. Corcoran, J. Quant. Spectrosc. Radiat. Transfer 9, 1371(1969).

34. W. B. Barnett, V. A. Fassel and R. N. Kniseley, Spectrochim. Acta 25B,139(1970).

35. I. Kleinmann and J. Cajko, Spectrochim. Acta 25B, 657(1970).

36. H. U. Eckert, J. Appl. Phys. 41, 1520(1970).

37. H. U. Eckert and D. C. Pridmore-Brown, J. Appl. Phys. 42, 5051(1971).

38. B. Talayrach, J. Besombes-Vailhe, and H. Triche, Analusis 1, 132(1972).

39. H. Triche, A. Saadate, B. Talayrach and J. Bescombes-Vailhe, anlusis 1,413(1972).

40. S. L. Leonard, J. Quant. Spectrosc. Radiat. Transfer 12, 619(1972).

41. J. F. Alder and J. M. Mermet, Spectrochim Acta 28B, 421(1973).

42. G. R. Kornblum and L. De Galan, Spectrochim. Acta 29B, 249(1974).

43. R. H. Scott, V. A. Fassel, R. N. Kniseley and D. E. Nixon, Anal. Chem. 46, 75(1974).

44. J. M. Mermet, Spectrochim. Acta 30B, 383(1975).

45. R. M. Barnes and R. G. Schleicher, Spectrochim. Acta 30B, 109(1975).

46. D. J. Kalnicky, R. N. Kniseley and V. A. Fassel, Spectrochim. Acta 30B, 511(1975).

47.   K. Visser, F. H. Hamm and P. B. Zeeman, Appl. Spectrosc. 30, 34(1976).

48.   D. J. Kalnicky, V. a. Fassel, and R. N. Kniseley, Appl. Spectrosc. 31, 137(1977).

49.   G. R. Kornblum and L. De Galan, Spectrochim. Acta 32B, 71(1977).

50.   M. H. Abdallah and J. M. Mermet, J. Quant. Spectrosc. Radiat. Transfer 19, 83(1978).

51.   J. Jarosz, J. M. Mermet, and J. P. Robin, Spectrochim. Acta 33B, 55(1978).

52.   J. F. Alder, R. M. Bombelka, G. F. Kirkbright, Spectrochim. Acta 35B, 163(1981).

53.   H. Kawaguchi, J. Ito, A. Mizuike,Spectrochim. Acta 36B, 615(1981).

54.   H. Uchida, K. Tanabe, Y. Nojiri, H. Haraguchi, K. Fuwa, Spectrochim. Acta 36B, 711(1981).

55.   M. H. Abdallah and J. M. Mermet, Spectrochim. Acta 37B, 391(1982).

56.   W. H. Gunter, K. Visser, P. B. Zeeman,Spectrochim. Acta 38B, 949(1983).

57.   L. M. Faires. B. A. Palmer, R. Engleman, T. M. Niemczyk, Spectrochim. Acta 39B, 819(1984).

58.   M. W. Blades and C. L. Caughlin, Spectrochim. Acta 40B, 579(1985).

59.   N.Furuta, Spectrochim. Acta 40B, 1013(1985).

60.   A. Goldwasser, J. M. Mermet, Spectrochim. Acta 41B, 725(1986).

61.	B. Raeymaekers, J. A. C. Broekaert and F. Leis, Spectrochim. Acta **43B,** 941(1988).

62.	Izumi Ishii, Akbar Montaser, J. Anal. At. Spectrom. **5,** 57(1990).

63.	P. W J. M. Boumans, Theory of Spectrochemical Excitation, Adam Hilger/London, Plenum/New York (1966).

64	P. W J. M. Boumans, Excitation Spectral, in "Analytical Emission Spectrometry." E. L. Grove, Ed. Marcel Dekker, New York, 1972.

65.	A. P. Thorne, "Spectrophysics." Chapman & Hall, London, 1974.

66.	M. Kubota, Y. Fujishiro, and R. Ishida, Spectrochim. Acta.**36B,** 697(1981).

67.	C. H. Corliss and J. L. Tech, NBS Monograph 108(1968).

68.	C. H. Corliss and J. L. Tech, J. Res. Natn. Bur. Stand. **80A,**787(1976).

69.	T. Gary and M. Kock, Astro. and Astrophys. **2,** 274(1969).

70.	J. M. Bridges and W. L. Wiese, Astrophys. J. **161,** L71(1970).

71.	S. J. Wolnik, R. O. Berthel and G. W. Wares, Astrophys. J. **162,** 1037(1970).

72.	M. C. E. Huber and W. h. Parkinson, Astrophys. J. **172,** 229(1972).

73.	F. P. Banfield and M. C. E. Huber, Astrophys. J. **186,** 335(1973).

74.	J. M. Bridges and R. L. Kornblith, Astrophys. J. **192,** 793(1974).

75.   I. Reif, V. A. Fassel, R. N. Kniseley and D. J. Kalnicky, Spectrochim. Acta **33B**, 807(1978).

76.   D. E. Blackwell and B. S. Collins, Mon. Not. R. Astr. Soc. **157**, 255(1972).

77.   J. Besombes-Vailhe, J. Chim. Phys. Phys. Chim. Biol. **64**, 370(1967).

78.   H. Triche. A. Saadate, B. Talayrach, and J. Besomes-Vailhe, Analusis **1**, 413(1972).

79.   P. A. M. Ripson, L. de Galan, and J. W. de Ruiter, Spectrochim. Acta **37B**, 733(1982).

80.   J. P. Rybarczyk, C. P. Jester, D. A. Yates, and S. R. Koirtyohann, Anal. Chem. **54**, 2162(1982).

81.   P. W. J. M. Boumans, H. Wagenaar, and F. J. de Boer, Preprints, 17th Coll. Spectrosc. Intern., Florence, Vol. **1**, 114(1973).

82.   W. H. Gunter, K. Visser, and P. B. Zeeman, Spectrochim. Acta **37B**, 571(1982).

83.   W. H. Gunter, K. Visser, and P. B. Zeeman, Spectrochim. Acta **40B**, 617(1985).

84.   W. L. Wiese, M. W. Smith and B. M. Miles, Atomic Transition Probabilities, Vol II, NSRDS-NBS 22(1969).

85.   S. R. Baumann and W. H. Smith, J. Opt. Soc. Am. **60**, 345(1970).

86.   T. Andersen and g. Sorensen, J. Quant. Spectrosc. Radiat, Transfer **13**, 369(1973)

87.   S. J. Wolnik and R. O. Berthel, Astrophys. J. **179**, 665(1973).

88.   J. R. Roberts, T. Andersen and G. Sorensen, Astrophys. J. **181**, 567(1973).

89.   B. M. Miles and W. L. Wiese, Critically Evaluated Transition Probabilities for BaI and BaII, NBS Technical note 474(1969).

90.   G. E. Assousa and W. H. Smith, Astrophys. J. **176**, 259(1972).

91.   M. C. E. Huber, Astrophys. J. **190**, 237(1972).

92.   G. Herzberg, Spectra of Diatomic Molecules, Van Nostrand, Princeton (1950).

93.   W. H. J. Childs, Proc. R. Soc. London Ser. A **137**, 641(1932).

94.   D. Coster and F. Brons, Z. Physik **73**, 747(1932)

95.   H. Dieke and H. M. Crosswhite, J. Quant. Spectrosc. Radiat. Transfer **2**, 97(1962).

96.   A. K. Hui, m. R. Mckeever, and J. Tellinghuisen, J. Quant. Spectrosc. Radiat. Transfer **21**, 387(1979).

97.   J. M. Mermet and J. Robin, Rev.. Intern Htes Temp. Refract. **10**, 133(1973).

98.   N. Furuta, Y. Nokiri, and K Fuwa, Spectrochim. Acta **40B**, 423(1985).

99.   L. J. M. Raaijmakers, P. W. J. M. Boumans, B. van der sijde, and D. C. Schram, Spectrochim. Acta **36B**, 697(1983).

100.   R. J. Lovett, Spectrochim. Acta **37B**, 969(1982).

101. T. Hasegawa and H. Haraguchi, Spectrochim. Acta **40B**, 1505(1985).

102. H. R. Griem, "Plasma Spectroscopy." McGraw-Hill, New York, 1964.

103. W. L. Wiese, Line Broadening, in "Plasma Diagnostic Technique," R. H Huddlestone and S. L. Leonard, Eds,. Academic press, New York, 1965.

104. H. R. Griem, "Spectral Line Broadening by Plasma." Academic Press, New York, 1974.

105. P. Kepple and H. R. Griem, Phys. Rev. **137**, 317(1968).

106. H. R. Griem, A. C. Knolb, and K. Y. Shen, Astrophys. J. **135**, 272(1962).

107. C. R. Vidal, J. Cooper, ane E. W. Smith, Astrophys. J. Suppl. Series No.**214**, 37(1973).

108. P. Kepple and H. R. Griem, Phys. Rev. **137**, 317(1968).

109. J. R. Greig, C. P. Lim, G. A. Moo-Yourig, G Palumpo, and H. R. Griem, Phys. Rev. **172**, 148(1968).

110. A. Czernikowski and J. Chapelle, Acta Phys. Plo. **63A**, 67(1983).

111. G. J. Bastiaans and R. A. Mangold, Spectrochim. Acta **40B**, 885(1985).

112. D. R. Inglis and E. Teller, Astrophys. J. **90**, 434(1939).

113. R. E. Rovinskii, V. A. Gruzdev, T. M. Gutenmakher, and A. P. Sobolev, High Temp. (USSR) **5**, 502(1967).

114. A. Montaser, V. A. Fassel, and G. Larson, Appl. Spectrosc. **35**, 385(1981).

115.   A. Montaser, V. A. Fassel, Appl. Spectrosc. **36**, 613(1982).

116.   J. M. Mermet, and C. Trassy, Spectrochim. Acta, **36B**, 269(1981).

117.   R. K. Winge, V. A. Fassel, V. G. Peterson, and M. A. Floyd, Appl. Spectrosc., **36**, 210(1982).

118.   E. A. Stubley, and G. Horlick, Appl. Spectrosc., **38**, 162(1984).

119.   J. M. Keane, D. C. Brown, and R. C. Fry, Anal. Chem., **57**, 2526(1985).

120.   A. Montaser, G. R. Huse, R. A. Wax, S. Chan, D. W. Golightly, J. S. Kane, and A. F. Dorrzapf Jr., Anal. Chem. **56**, 283(1984).

121.   R. Rezaaiyaan, and G. M. Heiftje, Anal. Chem., **57**, 412(1985).

122.   R. M. Dagnall, D. J. Smith, T. S. West, and S. Greenfield, Anal. Chem., **57**, 412(1985).

123.   A. Aziz, J. A. C. Broekaert, K. Laqua, and F. Leis, Spectrochim. Acta, **39B**, 1091(1984).

124.   G. A. Meyer, and R. M. Barnes, Spectrochim. Acta, **40B**, 893(1985).

125.   S. Greenfield, I. L, Jones, H. M. McGeachin, and P. B. Smith, Anal. Chim. Acta, **74**, 225(1975).

126.   S. Greenfield, H. M. McGeachin, and P. B. Smith, Talanta, **23**, 1(1976).

127.   E. H. Choot, and G. Horlick, Spectrochim. Acta, **41B**, 935(1986).

128.   D. Truitt, and J. W. Robinson, Anal. Chim. Acta, **51**, 61(1970).

129. S. Greenfield, Metron, 3, 224(1971).

130. S. Greenfield, and P. B. Smith, Anal. Chim. Acta, 59, 341(1972).

131. S. Greenfield, and H. M. McGeachin, Anal. Chim. Acta, 100, 101(1978).

132. S. Greenfield, and D. T. Burns, Anal. Chim. Acta, 113, 205(1980).

133. S. Greenfield, and P. B. Smith, Anal. Chim. Acta, 57, 209(1971).

134. I. B. Brenner, A. E. Watson, G. M. Russell, and M. Goncalves, Chem. Geol., 28, 321(1980).

135. J. A. C. Broekaert, F. Leis, and K. Laqua, Talanta, 28, 745(1981).

136. A. E. Watson, ICP Inform. Newsl., 5, 553(1980).

137. I. B. Brenner, E. A. Jones, A. E. Watson, and T. W. Steele, Chem. Geol., 45, 135(1984).

138. I. B. Brenner, A. E. Watson, T. W. Steele, E. A. Jones, and M. Goncalves, Spectrochim. Acta, 36B, 785(1981).

139. L. Ebdon, M. R. Cave, and D. J. Mowthorpe, Anal. Chim. Acta, 115, 179(1980).

140. K Ohls, ICP Inform. Newsl., 7, 6(1981).

141. D. Sommer, and K. Ohls, Fresenius Z. Anal. Chem., 295, 337(1979).

142. K. Ohls, and D. Sommer, Fresenius Z. Anal. Chem., 296, 241(1979).

143. K. Ohls, and D. Sommer, ICP Inform. Newsl., 4, 532(1979).

144.   A. Montaser, V. A. Fassel, and J. Zalewski, Appl. Spectrosc., **35**, 292(1981).

145.   A. Montaser, and J. M. Mortazavi, Anal. Chem., **52**, 255(1980).

146.   A. Montaser, S. Chan, G. R. Huse, P. A. Vieira, and R. L. Van Hoven, Appl. Spectrosc., **40**, 473(1986).

147.   E. H. Choot, Ph. D. Thesis, University of Alberta, 1982.

148.   E. H. Choot, and G. Horlick, Spectrochim. Acta, **41B**, 889(1986).

149.   E. H. Choot, and G. Horlick, Spectrochim. Acta, **41B**, 907(1986).

150.   E. H. Choot, and G. Horlick, Spectrochim. Acta, **41B**, 925(1986).

151.   ZhiZhuang He, Fenxi Huaxue, **11**, 181(1983).

152.   ZhiZhuang He, Fenxi Huaxue, **11**, 401(1983).

153.   S. Greenfield, Proc. anal. Div. Chem. Soc., **13**, 279(1976).

154.   S. Greenfield, and H. M. McGeachin, and P. B. Smith, Anal. Chim. Acta, **84**, 67(1976).

155.   A. E. Watson, and G. M. Russell, ICP Inform. Newsl., **4**, 441(1979).

156.   ZhiZhuang He, ICP Inform. Newsl., **9**, 150(1983).

157.   G. M. Russell, and A. E. Watson, ICP Inform. Newsl., **5**, 548(1980).

158.   S. Greenfield, and H. M. McGeachin, and P. B. Smith, ICP Inform. Newsl., **2**, 167(1976).

159. S. Greenfield, ICP Inform. Newsl., **1**, 3(1975).

160. J. A. C. Broekaert, B. Wopenka, and H. Puxbaum, Anal. Chem., **54**, 2174(1982).

161. A. Montaser, CRC Critical Reviews in Analytical Chemistry, **18**, 45(1987).

162. G. King, and G. Horlick, Spectrochim. Acta Electronica **47B**, E353(1992).

163. L Fernando, Anal. Chem., **56**, 1970(1984).

164. Y. Zhao, Personal communication.

165. A. R. Turner-Smith, J. M. Green, and C. E. Webb, J. Phys. B. **6**, 114(1973).

166. J. M. Green, and C. E. Webb, J. Phys. B. **7**, 1698(1974).

167. J. B. Tatum, Mon. Not. R. Astron. Soc. **122**, 331(1961).

168. C. H. Corliss and J. B. Shumaker Jr. J. Res. Nat. Bur. Std. **71A**, 575(1967).

169. B. Wagner, Mem. R. Astron. Soc. **70**, 165(1967).

170. J. R. Roberts and P. A. Voight, Astrophys. J. **181**, 587(1975).

171. W. L. Wiese and J. R. Furh, J. Chem. Ref. data **4**, 263(1975)

172. H. Triche, A. Saadate, B. Talayrach, and J. Besombes-Vailhe, Analusis **1**, 431(1972).

173. I. Reif, "Spectroscopic temperature measurements of flames and their physical significance," Ph.D thesis, Iowa state University, Iowa (1971).

174. F. P. Banfield and M. C. E. Huber, Atrophys. J., **186**, 335(1973).

175. K. W. Meissner, Z. Phys. **37**, 238(1926).

176. K. W. Meissner, Z. Phys. **39**, 172(1926).

177. K. W. Meissner, Z. Phys. **40**, 839(1926).

178. W. F. Meggers, and C. J. Humphreys, J. Res. Natl. Bur. Stand. (US) **13**, 393(1934).

179. C. J. Humphreys, J. Res. Natl. Bur. Stand. (US) **20**, 17(1938).

180. K. Burns and K. B. Adams, J. Opt. Soc. Am. **43**, 1024(1953).

181. T. A. Littlefield and D. T. Turnbull, Proc. Roy. Soc. A **218**, 577(1953).

182. C. Roslen, Ark. Fys. **35**, 119(1967).

183. G. Holden, Phys. Scr. **8**, 249(1973).

184. H. H. Li, and C. J. Humphreys, J. Opt. Soc. Am. **64**, 1072(1974).

185. L. M. Faires, B. A. Palmer, and R. Engleman,Jr., Spectrochim. Acta **40B**, 545(1985).

186. S. J. Northway, and R. C. Fry, Appl. Spec. **34**, 332(1980).

187. S. J. Northway, R. M. Brown, and R. C. Fry, Appl. Spec. **34**, 338(1980).

188. R. C. Fry, S. J. Northway, R. M. Brown, and S. K. Hughes, Anal. Chem. **52**, 1716(1980).

189. R. M. Brown, and R. C. Fry, Anal. Chem. **53**, 532(1981).

190. R. M. Brown, S. J. Northway, and R. C. Fry, Anal. Chem. 53, 934(1981).

191. S. K. Hughes, and R. C. Fry, Anal. Chem. 53, 1111(1981).

192. S. K. Hughes, R. M. Brown, and R. C. Fry, Appl. Spec. 35, 396(1981).

193. S. K. Hughes, and R. C. Fry, Appl. Spec. 35, 493(1981).

194. M. W. Blades, and P. Hauser, Anal. Chim. Acta 157, 163(1984).

195. A. J. J. Schleisman, W. G. Fateley, and R. C. Fry, J. Phys. Chem. 88, 398(1984).

196. E. A. Stubley, and G. Horlick, Appl. Spec. 38, 162(1984).

197. A. Zaidel, V. Prokofjev, V. Slavnyi, and E. Shreider, "Tables of Spectral Lines", IFI/Plenum, New York, 1970.

198. G. King, B. R. Tood, and G. Horlick, Spectrochim. Acta Electronica 47B, E333(1992).

199. W. H. Gunter, K. Visser, and P. B. Zeeman, Spectrochim. Acta 38B, 949(1983).

200. M. W. Blades, B. L. Caughlin, Spectrochim. Acta 40B, 579(1985).